Fall 2011

# Effects of headwinds on towing tank resistance and PMM tests for ONR Tumblehome

Shane Stuart Cook
*University of Iowa*

# EFFECTS OF HEADWINDS ON TOWING TANK RESISTANCE AND PMM TESTS FOR ONR TUMBLEHOME

by

Shane Stuart Cook

A thesis submitted in partial fulfillment
of the requirements for the Master of
Science degree in Mechanical Engineering
in the Graduate College of
The University of Iowa

December 2011

Thesis Supervisor: Professor Frederick Stern

Graduate College
The University of Iowa
Iowa City, Iowa

CERTIFICATE OF APPROVAL

_____

MASTER'S THESIS

_____

This is to certify that the Master's thesis of

Shane Stuart Cook

has been approved by the Examining Committee
for the thesis requirement for the Master of Science
degree in Mechanical Engineering at the December 2011 graduation.

Thesis Committee: _____
Frederick Stern, Thesis Supervisor

_____
Pablo Carrica

_____
James Buchholz

# ACKNOWLEDGMENTS

The Office of Naval Research sponsored this research under Grant N00014-10-1-0017 administered by Dr. Pat Purtell. The author expresses thanks for continual support and contributions to the ship hydrodynamics program at IIHR.

The unrivaled vision and guidance of thesis supervisor Dr. Fred Stern contributed to a profound learning experience. The author is honored to serve under the tutelage of one of the most prominent figures in ship hydrodynamics.

The author is grateful to individuals who contributed to efficient and quality execution of research support. These include undergraduate mechanical engineering students who co-endured tedious rounds of data acquisition and IIHR mechanical and electrical shop staff who committed time to help with technical support.

Dr. Joe Longo provided considerable mentoring and training during phases of test design and implementation. The author is extremely thankful for Dr. Joe Longo's patience and willingness to help with development of data processing software. Under no other person could an experiment of such daunting proportions be undertaken with such smoothness.

Utmost thanks must be expressed to great friend and mentor Dr. Hyunse Yoon who constantly provided new levels of understanding within the vast and complex world of ship model testing. Dr. Hyunse Yoon's background, wisdom, and extensive development of data processing tools guided the author's success and ensured the quality of the research.

# ABSTRACT

Calm water towing tank experiments consisting of resistance tests and static and dynamic planar motion mechanism (PMM) tests are performed for a surface combatant with primary focus on the effects of hurricane scale headwinds. The experiments are designed to gain a better understanding of the physics of ship response to wind and to provide a validation dataset for an unsteady Reynolds-averaged Navier Stokes (RANS)-based computational fluid dynamics (CFD) code used for computing both air and water flow around a ship. Hurricane scale wind speeds are chosen to maximize the measurable effect of wind on ship forces and motions for a more definitive analysis and comparison with CFD. The geometry is the 1/48.9 scale fully appended ONR Tumblehome model 5613, which has length $L$ = 3.147 m and is equipped with a superstructure. Tests are performed in a 3.048 × 3.048 × 100 m towing tank with wind generated by a custom built wind carriage towed ahead of the ship model. Air-stream velocity measurements indicate a maximum relative wind speed magnitude of 9.38 m/s with 6 - 7% uniformity and $RMS$ values of approximately 4.5%. The effects of three wind speeds on static and dynamic forces, moment, and motions are analyzed. Results show that wind contributes significantly to surge force (approximately 46% at $Fr$ = 0.2). Resistance data shows agreement with CFD computations with errors averaging approximately 4%. The drag coefficient above water is approximately 0.3 and generally decreases with increasing ship speed. Sway force and yaw moment are largely affected when the ship experiences oblique orientation to the flow. Forces and moment exhibit quadratic scaling with wind speed. Roll is the most sensitive motion to wind and is counteracted by it up to 1.8° for PMM test conditions. In addition, harmonic amplitudes of forces and moment data from dynamic tests are used to determine hydrodynamic derivatives for all three wind conditions following a mathematical model. The effect of wind on hydrodynamic derivatives is significant with changes on the order of 10 - 100%.

TABLE OF CONTENTS

LIST OF TABLES

Table

LIST OF FIGURES

Figure

# CHAPTER 1. INTRODUCTION

Wind impacts the three traditional disciplines of ship hydrodynamics including aerodynamic loading (resistance and propulsion), vessel response motions (seakeeping), and course stability (maneuvering). Wind can compromise ship survivability and also affects ship-ship and ship-aircraft interactions. Studies on wind effects were recently reviewed by the 25th International Towing Tank Conference (ITTC) Resistance Committee (ITTC, 2008). Most studies involve experimental fluid dynamics (EFD) investigations emphasizing measurements of forces and moments and velocity fields with scale models. Computational fluid dynamics (CFD) studies have a comparatively shorter history and mainly focus on prediction of the airwake flows with relatively simple geometry and conditions, applying either no-slip or symmetry plane conditions on the calm water plane. Thus, most EFD studies were performed in wind tunnels and using only the above-water portion of the ship for analysis. Due to the recent availability of powerful computing environments it is now possible to perform extremely detailed and encompassing CFD analysis concerning ship performance. Computations such as those performed by Mousaviraad et al. (2008) allow for full six-degrees-of-freedom (6DOF) ship motions imparted by wind and waves and thus warrant the use of more advanced EFD techniques for validation. A simple wind tunnel is not capable of replicating the dynamic behavior realized by such computations and therefore a more comprehensive experimental plan is necessary in order to obtain adequate validation. Subjecting a ship model to a controllable and uniform wind source in a free-model basin may prove impractical. Fujiwara et al. (2008) managed to perform free running model tests on a container ship with wind and waves at the National Maritime Research Institute, Japan to study the effects of wind on ship speed and thrust and to verify a computational model for maneuvering. An array of fans suspended from an overhead carriage was used as the wind source, however, wind speeds were low with little attention paid to flow control.

In nature wind is generally always accompanied by waves with wave spectra depending on fetch and the type of weather pattern. In a towing tank experiment without waves the wind source can be idealized on a more manageable scale and is potentially more effective at isolating measured variables. Maneuvering and other free-model testing generally cannot be performed but standard towing tank resistance and planar motion mechanism (PMM) tests can provide significant insight into ship response due to wind and can serve as a basis for 6DOF CFD validation. Hurricane scale wind speeds are of interest because effects of wind on ship response are maximized. Exaggerating the effects of wind allows for more definitive measurements and analysis. Additionally, large wind speeds are more consequential to ship performance. Unsteady Reynolds-averaged Navier Stokes (RANS) studies of the effects of head and following winds on forces, moments, and motions of the Office of Naval Research (ONR) Tumblehome for static and dynamic PMM maneuvering in calm water and pitch and heave in regular head waves have been carried out using CFDShip-Iowa V4.5 (Mousaviraad et al., 2008). The results show that for the strong hurricane winds and small $Fr$ = 0.2 simulated, static forces are affected up to 28% whereas motions are affected up to 7%. For pure yaw the wind effects on $0^{th}$, $1^{st}$, and $2^{nd}$ harmonics are more significant than for pure sway, especially for roll motion and sway force. The current objective is a complimentary EFD investigation of effects of hurricane scale headwinds on forces, moments, and motions of ONR Tumblehome model 5613 for calm water resistance and static and dynamic PMM tests using the IIHR – Hydroscience & Engineering towing tank. Note that the goal of the experiment is not to simulate an accurate hurricane wind environment, but to create a validation regime appropriate for direct CFD comparison and to observe general wind effects. Different wind speeds and Froude numbers are included, EFD data and standard deviations are provided, hydrodynamic derivatives are obtained, and the effects of wind are analyzed.

# CHAPTER 2. EXPERIMENTAL METHODS

## 2.1 Facility, Model, and Conditions

The IIHR – Hydroscience & Engineering towing tank has dimensions of 3.048 × 3.048 × 100 m and is equipped with side wave dampers, wave dampening beach, instrumented drive carriage, wind carriage, and PMM carriage. A layout of the facility is shown in Fig. 2-1. The drive carriage is outfitted with all test control and data acquisition systems. Both the attached wind and PMM carriages are collaboratively designed and constructed by Sanshin Seisakusho Ltd. and Mori Engineering Ltd. for the mechanical and electrical systems, respectively. The wind carriage is custom made for the experiment and is used to impart uniform and steady headwinds up to approximately 10 m/s to the model as it is towed. It consists of eight axial flow fans, a contraction, a combination elbow contraction with guide vanes, honeycomb section, and 0.6 × 2.3 m outlet. The outlet is positioned just above the free surface. Fig. 2-2 shows a cutaway view of the wind carriage construction. The PMM carriage is used to tow the model as well as providing lateral sway and yaw motions for applicable PMM test conditions using a built-in scotch-yoke type mechanism. The model is towed via a 6-component load cell capable of measuring the three principle forces and moments. The load cell is mounted to a strongback which is affixed to the yaw platter that provides lateral motion. The strongback is used as a rigid foundation to mount measurement devices and support hardware for various stages of the experiment. Fig. 2-3 shows the experimental setup and model arrangement in relation to the wind carriage. Conventional towing tank experiments only focus on effects of water flow around the hull of the ship and thus most mounting systems are designed without regard to their aerodynamics. A custom three-degrees-of-freedom (3DOF) mount made by Sanshin Seisakusho Ltd. is designed to allow for pitch, heave, and roll motions while minimizing the effect on air flow over the ship superstructure. The mount also contains integrated rotary potentiometers for pitch,

heave, and roll measurements. A schematic is shown in Fig. 2-4. The mount is attached to the load cell and consists of a cylindrical hollow post protruding into the roof of the model which ensures predicable airflow and drag effects which is shown in yellow in Fig. 2-4. The hole in which the 3DOF mount enters the ship is clearanced to allow for pitch and roll motion but does not extend beyond the horizontal surface of the roof, allowing for a maximum roll of $\pm 7°$. The aerodynamic drag of the 3DOF mount is added to the measured forces on the ship due to the load cell's external placement. The load cell is not positioned within the ship due to its required size and capacity. A correction is applied during data reduction to account for the effect of the 3DOF mount drag which is obtained through measurements explained in Appendix A. The mount post contains a heave staff with a gimbal assembly on the end allowing for pitch and roll shown in grey in Fig. 2-4. The tow point is the gimbal center of rotation which defines the pitch and roll centers of rotation and is positioned to coincide with the model's center of gravity. The mass of the heave staff (1.15 kg) is considered to be a point-mass at the ship center of gravity because it does not pitch or roll with the ship and only contributes to the displacement of the ship. The blue mounts shown in Fig. 2-4 locate the tow point at the vertical center of gravity ($VCG$) which is defined relative to the static waterline on the model. The longitudinal center of gravity ($LCG$) is defined relative to the forward perpendicular (FP) of the model. Due to the construction of the gimbal the pitch axis is fixed horizontally relative to Earth regardless of the ship's roll angle. The roll axis is fixed in relation to the ship so that the roll axis pitches with the ship. The orientation of pitch and roll axis are thus constrained and not arbitrary as they would be if using a spherical ball type joint at the tow point. The gimbal method, however, allows for convenient integration of pitch and roll potentiometers. The low profile and light construction of the 3DOF mount prevents the use of a large high strength gimbal. As a result, the gimbal alone will not support the ship in yaw. A secondary mount referred to as the 'yaw guide' branches off the main post once inside the model and reaches up into the fore section of the ship. It attaches to

the ship with a pantograph-type linkage that consists of a counter-weighted link with a slide-bearing about a longitudinal rail mounted to the ship floor. This component is shown in red in Fig. 2-4. The rail and linkage mechanism ensures proper yaw support without any binding when the ship pitches, heaves, and rolls. The counterweight mass only balances the mass of the rotating component and not the rail.

The present study focuses on ONR Tumblehome model 5613 with $L$ = 3.147 m which is a 1/48.9 scale version of the full scale model ($L$ = 154 m). Model 5613 is a pre-contract design for the U.S. Navy's DDG 1000 Zumwalt class destroyer ($L$ = 180 m). Due to the importance of wind effects the model is equipped with a deckhouse superstructure and lowered helicopter flight deck. The model has a wave piercing hull design with 10° tumblehome sides and transom stern. Appendages include skeg, bilge keels, shafts, struts, and rudders but no propulsors. The rudders remain fixed straight for all tests. Installation of pin-type turbulence stimulators at the bow in accordance with ITTC standards and guidelines ensures fully turbulent flow. The geometric and mass properties of model 5613 are presented in Table 2-1 with values from tests performed at the Department of Naval Architecture & Ocean Engineering at Osaka University (OU), Italian Ship Model Basin (INSEAN), IIHR CFD cases, and full scale.

Table 2-1 Geometric and Mass Properties of Model 5613.

| | IIHR | OU | INSEAN | IIHR CFD | Full Scale |
|---|---|---|---|---|---|
| $L$ (m) | 3.147 | 3.147 | 3.305 | 3.147 | 154 |
| $B$ (m) | 0.384 | 0.384 | 0.403 | 0.384 | 18.78 |
| $T$ (m) | 0.112 | 0.112 | 0.1201 | 0.112 | 5.494 |
| $LCG$ (m aft FP) | 1.6265 | 1.6265 | 1.708 | 1.626 | 79.587 |
| $VCG$ (m) | 0.0443 | 0.0443 | i) 0.0549 ii) 0.0499 iii) 0.0449 | 0.0443 | 2.42 |
| $k_{xx}/L$ | 0.054 | i) 0.053 ii) 0.054 | i) 0.038 ii) 0.038 iii) 0.037 | 0.054 | i) 0.053 ii) 0.054 |
| $k_{yy}/L=k_{zz}/L$ | 0.246 | i) 0.254 ii) 0.246 | i) 0.22 ii) 0.22 iii) 0.22 | 0.246 | i) 0.025 ii) 0.025 |
| Displacement | 72.6 kg | 72.6 kg | 84.7 kg | | 8507 ton |
| $\overline{GM}$ (m) | 0.0423 | i) 0.0364 ii) 0.0423 | i) 0.033 ii) 0.038 iii) 0.043 | | i) 1.781 ii) 2.068 |

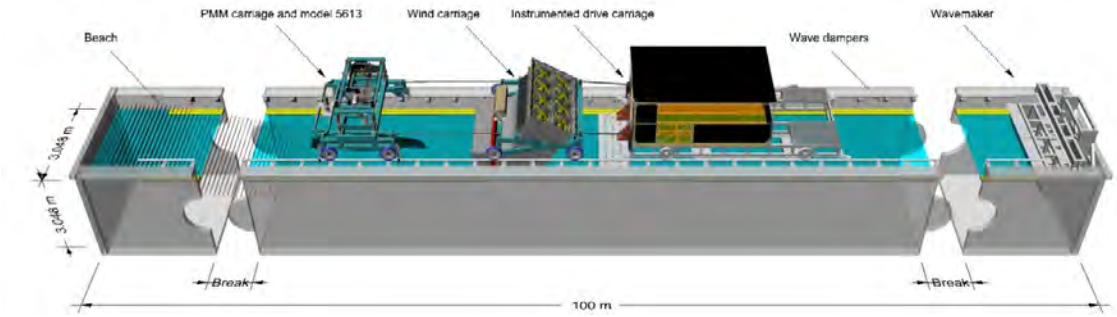


Figure 2-1 Schematic of IIHR towing tank with drive, wind, and PMM carriages.

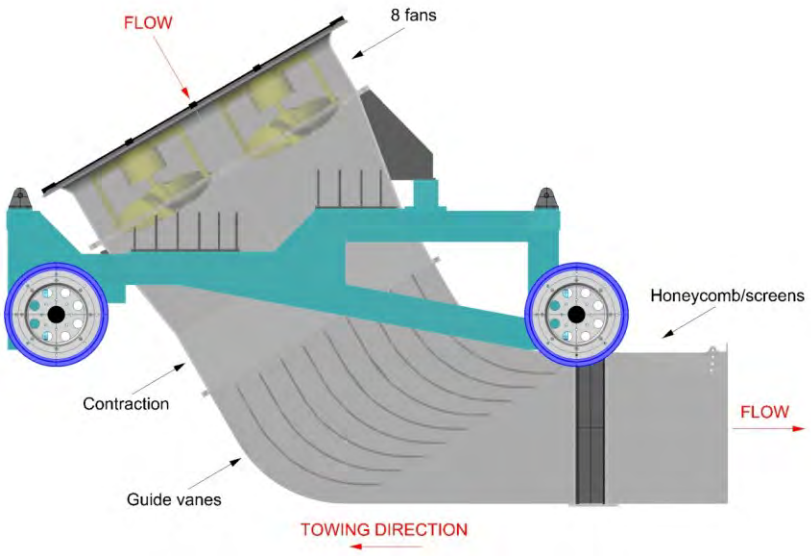


Figure 2-2 Schematic of custom built wind carriage.

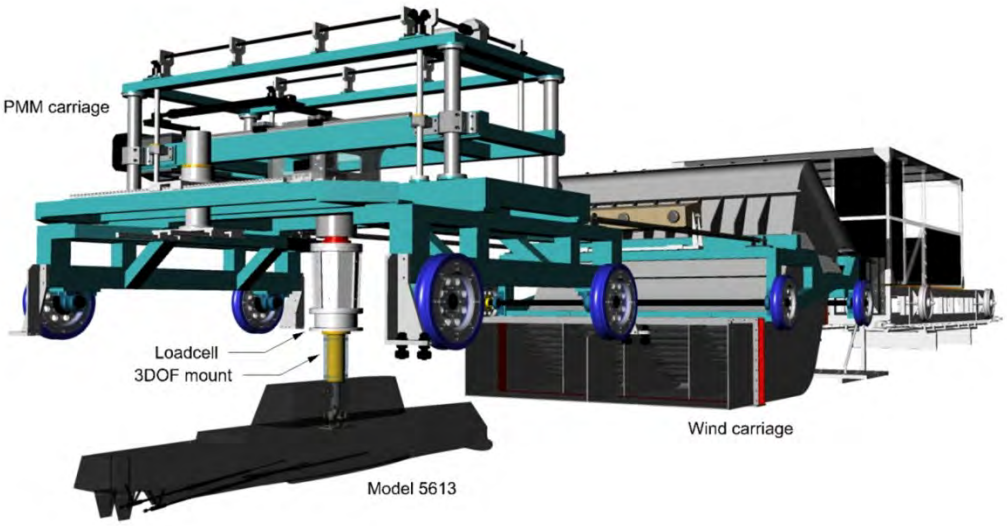


Figure 2-3 Schematic of test setup showing drive, wind and PMM carriages; model 5613 is attached to the load cell on the PMM carriage with a 3DOF mount. Strongback is not shown.

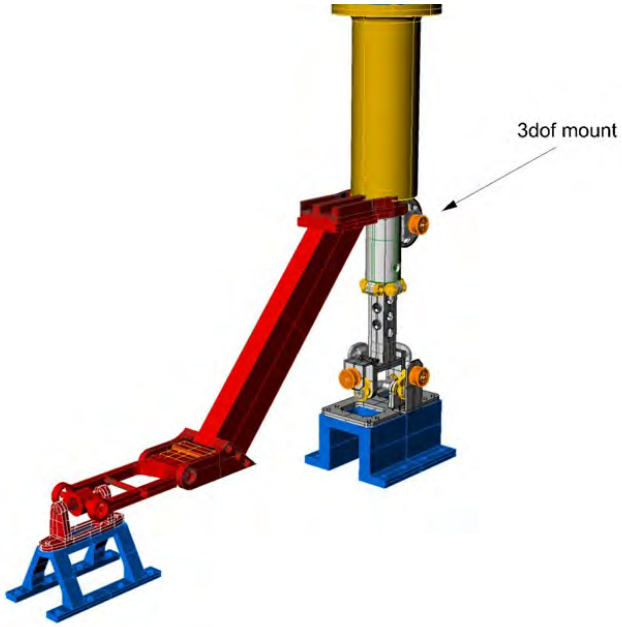


Figure 2-4 3DOF mount assembly. Heave staff and gimbal assembly shown in grey restrain the model in surge and sway with integrated potentiometers for measuring pitch, heave and roll. Pantograph with slide roller link shown in red supports model in yaw but allows for pitch, heave, and roll. Floor mounts shown in blue define elevation of model center of rotation and roll axis.

### 2.1.1 Free-stream Air Velocity Distribution

Model testing is conducted using three wind conditions for all static and dynamic tests. One wind condition utilizes the wind carriage running at full flow capacity in order to observe the maximum possible effects of wind within the machine's capability. This condition is referred to as 'full wind.' Another wind condition subjects the model to headwinds with velocity equal to about half the velocity of headwinds from the full wind tests and is referred to as 'half wind.' The remaining wind condition is that of no wind in which the wind carriage is still towed in front of the model but the fans are not powered. This condition is referred to as 'no wind' or 'w/o wind.' Due to recent installation of the wind carriage, no detailed free-stream velocity data is available. Therefore characterization of the free-stream air velocity distribution output by the wind carriage is needed for full wind and half wind conditions. This characterization also serves to quantify headwind velocities as a function of fan controller dial setting. The wind carriage is towed with the model so wind velocity relative to Earth changes with carriage speed. Surveying the free-stream air velocity distribution is performed at two carriage speeds to determine if the moving carriage causes changes to the air stream and at three different stream-wise planes to determine how the air stream evolves at it exits the wind carriage and approaches the model. The coordinate system used for free-stream air velocity distribution surveys follows the CFD convention for convenience and is shown in Fig. 2-5 while test conditions are summarized in Table 2-2. The coordinate system is nondimensionalized by $L$ = 3.147 m. $U_C$ is dimensional carriage speed and Froude number $Fr$ is nondimensional carriage speed. The model is not installed during surveys.

Table 2-2 Test Conditions for Free-stream Air Velocity Distribution Surveys.

| $x$ | $U_C$ | $Fr = \frac{U_C}{\sqrt{gL}}$ | Wind condition |
|---|---|---|---|
| (-) | (m/s) | (-) | |
| 0.00 (model FP) | 0 | 0 | half, full |
| -0.13 | 0, 1.111 | 0, 0.2 | half, full |
| -0.33 (wind carriage outlet) | 0 | 0 | full |


Figure 2-5 Coordinate system for free-stream air velocity distribution surveys. The origin resides at the FP.

### 2.1.2 Straight Ahead Test

Thirteen ship speeds are chosen in the range of $Fr = 0 – 0.41$ in increments of 0.05 to obtain adequately realized resistance, sinkage, and trim curves. Off incremental values correspond to overlap data from other facilities. All speeds are performed with all three wind conditions. Roll is locked in order to monitor and confirm zero roll moment. Conditions for straight ahead tests are summarized in Table 2-3. CFD sign conventions are used as shown in Fig. 2-5.

Table 2-3 Straight Ahead Test Conditions.

| Test | $Fr = \frac{U_C}{\sqrt{gL}}$ | $U_C$ (m/s) | $\beta$ (°) | Wind condition | Motions | Data acquired |
|---|---|---|---|---|---|---|
| Straight ahead | 0.000 | 0.000 | 0 | half, full | *z, θ* | *z, θ, X, Y, K, N* |
| | 0.050 | 0.278 | 0 | none, half, full | *z, θ* | *z, θ, X, Y, K, N* |
| | 0.100 | 0.555 | 0 | none, half, full | *z, θ* | *z, θ, X, Y, K, N* |
| | 0.138 | 0.766 | 0 | none, half, full | *z, θ* | *z, θ, X, Y, K, N* |
| | 0.150 | 0.833 | 0 | none, half, full | *z, θ* | *z, θ, X, Y, K, N* |
| | **0.200** | **1.111** | **0** | **none, half, full** | ***z, θ*** | ***z, θ, X, Y, K, N*** |
| | 0.250 | 1.389 | 0 | none, half, full | *z, θ* | *z, θ, X, Y, K, N* |
| | 0.280 | 1.555 | 0 | none, half, full | *z, θ* | *z, θ, X, Y, K, N* |
| | **0.300** | **1.666** | **0** | **none, half, full** | ***z, θ*** | ***z, θ, X, Y, K, N*** |
| | 0.350 | 1.944 | 0 | none, half, full | *z, θ* | *z, θ, X, Y, K, N* |
| | 0.364 | 2.022 | 0 | none, half, full | *z, θ* | *z, θ, X, Y, K, N* |
| | **0.400** | **2.222** | **0** | **none, half, full** | ***z, θ*** | ***z, θ, X, Y, K, N*** |
| | 0.410 | 2.277 | 0 | none, half, full | *z, θ* | *z, θ, X, Y, K, N* |

**Bold**: UA cases with 10 repeat tests.

### 2.1.3 Static and Dynamic PMM Tests

Included as part of the System Based Simulation method category of maneuvering prediction methods by The Maneuvering Committee of the 24th International Towing Tank Conference, PMM tests are designed to isolate certain measured hydrodynamic forces and moments by imparting prescribed ship velocities and accelerations. Using appropriate mathematical modeling to solve the motion equations allows for the calculation of hydrodynamic derivatives of forces and moments (maneuvering coefficients) that describe the fundamental response characteristics of the particular ship geometry. Static and dynamic PMM tests are performed without wind, with half wind, and with full wind to investigate the effect of wind on static and dynamic ship forces, moments, and motions. Tables 2-4 and 2-5 summarize static and dynamic PMM test conditions, respectively, which closely follow test conditions of prior PMM tests for DTMB model 5512 performed by Yoon (2009) at the IIHR towing tank. Maximum tested drift angles for static drift tests are restricted by the maximum roll angle allowed by the 3DOF mount clearance hole in the roof of the ship. The following is a description of static drift, pure sway, pure yaw, and yaw and drift PMM tests. The ship-fixed, non-inertial reference frame $xyz$ that moves relative to an Earth-fixed, inertial reference frame $x_E y_E z_E$ is shown in Fig. 2-6. The origin of the ship-fixed reference frame is located at the ship center of gravity which coincides with the tow point. Note that sign conventions for $x$ and $z$ are inverted compared to CFD sign conventions. Three basic prescribed motions $x_E$, $y_E$, and $\psi$ make up the model trajectories of PMM motions in the $x_E y_E$-coordinate system, with $Fr$ defined using carriage speed:

$$x_E = U_C t \tag{2.1a}$$

$$y_E = -y_{max} \sin \omega t \tag{2.1b}$$

$$\psi = -\arctan\left(\frac{y_{max}\omega}{U_C}\cos \omega t\right) + \beta \tag{2.1c}$$

$$Fr = \frac{U_C}{\sqrt{gL}} \tag{2.1d}$$

where $y_{max}$ is the amplitude of the sinusoidal lateral motion with frequency $\omega$, $\psi$ is the sinusoidal yaw motion (or heading) oriented relative to $x_E$, and $\beta$ is a constant drift angle oriented with respect to advance speed, $U$, which is then

$$U = \sqrt{u_E^2 + v_E^2} \tag{2.2}$$

A more detailed view of the coordinate system as it pertains to general PMM motions is shown in Fig. 2-7. For static drift the ship is merely towed at an oblique angle $\beta$ without lateral motions as illustrated in Fig. 2.8 (a) and results in respective ship-fixed surge and sway velocities

$$u = \dot{x} = U_C \cos\beta \tag{2.3a}$$

$$v = \dot{y} = -U_C \sin\beta \tag{2.3b}$$

With PMM motions $U$ is time dependent due to constant carriage speed $U_C$ and $y_E$ time dependence as seen in (2.1). For small PMM motions and small $\beta$, however, $U$ may be approximated as $U \approx u \approx U_C$. For pure sway tests heading is kept straight ($\psi = 0$) while $y_E$and $\omega$ are non-zero, thus causing a continuously changing drift angle $\beta$ which is illustrated in Fig. 2.8 (b). Pure sway motions are described as

$$y = -y_{max} \sin\omega t \tag{2.4a}$$

$$v = \dot{y} = -v_{max} \cos\omega t \qquad v_{max} = y_{max}\omega \tag{2.4b}$$

$$\dot{v} = \ddot{y} = \dot{v}_{max} \sin\omega t \qquad \dot{v}_{max} = y_{max}\omega^2 \tag{2.4c}$$

$$\beta = \beta_{max} \cos\omega t \qquad \beta_{max} = \frac{y_{max}\omega}{U_C} \tag{2.4d}$$

Pure yaw tests maintain non-zero $y_E$ and $\omega$ as in pure sway but drift angle is kept zero ($\beta = 0$) causing the model orientation to always be tangent to its trajectory as shown in Fig. 2.8 (c). Pure yaw motions are described as

$$y_E = -y_{max} \sin\omega t \tag{2.5a}$$

$$\psi = -\psi_{max}\cos\omega t \qquad \psi_{max} = \frac{y_{max}\omega}{U_C} \tag{2.5b}$$

$$r = \dot{\psi} = r_{max}\sin\omega t \qquad r_{max} = \psi_{max}\omega \tag{2.5c}$$

$$\dot{r} = \ddot{\psi} = \dot{r}_{max}\cos\omega t \qquad \dot{r}_{max} = \psi_{max}\omega^2 \tag{2.5d}$$

Yaw and drift tests are a combination of pure yaw and static drift tests. Yaw and drift maintains non-zero $y_E$, $\omega$, and $\psi$ as in pure yaw but a constant non-zero drift angle $\beta$ kept as shown in Fig 2.8 (d). Thus $y_E$, $r$, and $\dot{r}$ are the same as in (2.5a), (2.5c), and (2.5d) while

$$\psi = -\psi_{max}\cos\omega t + \beta \qquad \psi_{max} = \frac{y_{max}\omega}{U_C} \tag{2.6a}$$

$$v = -U_C\sin\beta \tag{2.6b}$$

Table 2-4 Static PMM Test Conditions.

| Test | *Fr* | $U_C$ (m/s) | $\beta$ (°) | Wind condition | Motions | Data acquired |
|---|---|---|---|---|---|---|
| Static drift | 0.000 | 0.000 | -11.7, -9.3, -7, -4.7, -2.3, 0, 2.3, 4.7, 7, 9.3, 11.7 | half, full | *z, θ, ϕ* | *z, θ, ϕ, X, Y, N* |
| | 0.200 | 1.111 | -11.7, **-9.3**, -7, -4.7, -2.3, 0, 2.3, 4.7, 7, 9.3, 11.7 | none, half, full | *z, θ, ϕ* | *z, θ, ϕ, X, Y, N* |
| | 0.300 | 1.666 | -7, -4.7, -2.3 0, 2.3, 4.7, 7 | none, half, full | *z, θ, ϕ* | *z, θ, ϕ, X, Y, N* |
| | 0.400 | 2.222 | **-3.7**, -2.3, -0.9, 0, 0.9, 2.3, 3.7 | none, half, full | *z, θ, ϕ* | *z, θ, ϕ, X, Y, N* |

**Bold**: UA cases with 10 repeat tests.

Table 2-5 Dynamic PMM Test Conditions.

| Test | $Fr$ | $U_C$ | $\beta$ | $\frac{y_{max}}{L}$ | $\frac{v_{max}}{U_C}$ | $\frac{\dot{v}_{max}L}{U_C^2}$ | $\beta_{max}$ | $\psi_{max}$ | $\frac{r_{max}L}{U_C}$ | $\frac{\dot{r}_{max}L^2}{U_C^2}$ | $\frac{\omega L}{U_C}$ | Wind condition | Motions |
|---|---|---|---|---|---|---|---|---|---|---|---|---|---|
| | | (m/s) | (°) | (-) | (-) | (-) | (°) | (°) | (-) | (-) | (-) | | |
| Pure sway | 0.200 | 1.111 | - | 0.0210 | 0.035 | 0.057 | 2 | 0 | 0 | 0 | 1.655 | none, half, full | *z, θ, ϕ* |
| | | | - | 0.0419 | 0.070 | 0.117 | 4 | 0 | 0 | 0 | 1.673 | none, half, full | *z, θ, ϕ* |
| | | | **-** | **0.1040** | **0.174** | **0.291** | **10** | **0** | **0** | **0** | **1.673** | **none, half, full** | ***z, θ, ϕ*** |
| Pure yaw | 0.200 | 1.111 | 0 | 0.0124 | 0 | 0 | - | 1.4 | 0.05 | 0.10 | 1.994 | none, half, full | *z, θ, ϕ* |
| | | | 0 | 0.0400 | 0 | 0 | - | 4.5 | 0.15 | 0.29 | 1.940 | none, half, full | *z, θ, ϕ* |
| | | | **0** | **0.0804** | **0** | **0** | **-** | **8.9** | **0.30** | **0.59** | **1.940** | **none, half, full** | ***z, θ, ϕ*** |
| | | | 0 | 0.1204 | 0 | 0 | - | 13.4 | 0.45 | 0.88 | 1.940 | none, half, full | *z, θ, ϕ* |
| | | | 0 | 0.0972 | 0 | 0 | - | 13.9 | 0.60 | 1.50 | 2.492 | none, half, full | *z, θ, ϕ* |
| | | | 0 | 0.1274 | 0 | 0 | - | 17.7 | 0.75 | 1.81 | 2.421 | none, half, full | *z, θ, ϕ* |
| | 0.300 | 1.666 | 0 | 0.0194 | 0 | 0 | - | 1.8 | 0.05 | 0.08 | 1.602 | none, half, full | *z, θ, ϕ* |
| | | | 0 | 0.0540 | 0 | 0 | - | 5.1 | 0.15 | 0.25 | 1.661 | none, half, full | *z, θ, ϕ* |
| | | | **0** | **0.1080** | **0** | **0** | **-** | **10.3** | **0.30** | **0.50** | **1.661** | **none, half, full** | ***z, θ, ϕ*** |
| | | | 0 | 0.0950 | 0 | 0 | - | 11.9 | 0.45 | 0.99 | 2.183 | none, half, full | *z, θ, ϕ* |
| | | | 0 | 0.1296 | 0 | 0 | - | 16.0 | 0.60 | 1.28 | 2.149 | none, half, full | *z, θ, ϕ* |
| | 0.400 | 2.222 | 0 | 0.0346 | 0 | 0 | - | 2.4 | 0.05 | 0.06 | 1.201 | none, half, full | *z, θ, ϕ* |
| | | | 0 | 0.1169 | 0 | 0 | - | 7.6 | 0.15 | 0.17 | 1.130 | none, half, full | *z, θ, ϕ* |
| | | | **0** | **0.0725** | **0** | **0** | **-** | **8.4** | **0.30** | **0.61** | **2.029** | **none, half, full** | ***z, θ, ϕ*** |
| | | | 0 | 0.1077 | 0 | 0 | - | 12.6 | 0.45 | 0.92 | 2.047 | none, half, full | *z, θ, ϕ* |
| Yaw and drift | 0.200 | 1.111 | -2 | 0.0804 | - | 0 | - | 8.9* | 0.30 | 0.59 | 1.940 | none, half, full | *z, θ, ϕ* |
| | | | -4 | 0.0804 | - | 0 | - | 8.9* | 0.30 | 0.59 | 1.940 | none, half, full | *z, θ, ϕ* |
| | | | **-10** | **0.0804** | **-** | **0** | **-** | **8.9*** | **0.30** | **0.59** | **1.940** | **none, half, full** | ***z, θ, ϕ*** |

**Bold**: UA cases with 10 repeat tests.

***** Represents heading amplitude rather than maximum heading.

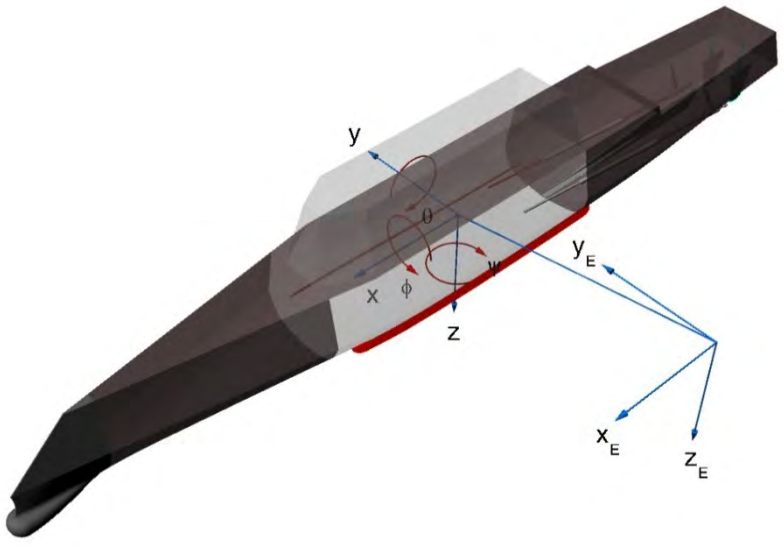


Figure 2-6 Earth- and ship-fixed coordinate systems for PMM tests.

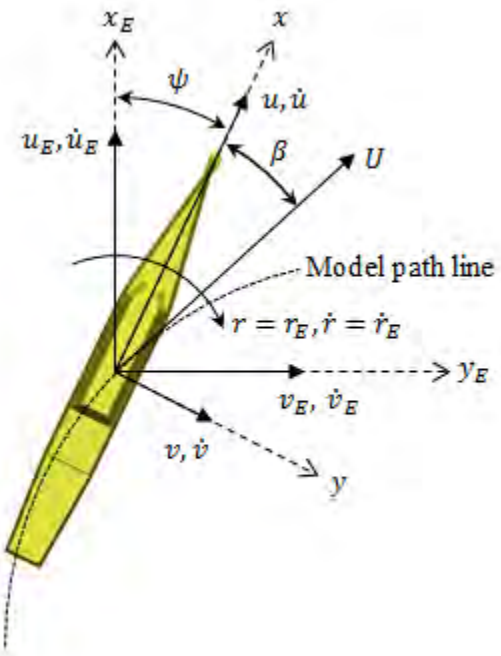


Figure 2-7 General coordinate system and motion parameters for PMM tests.

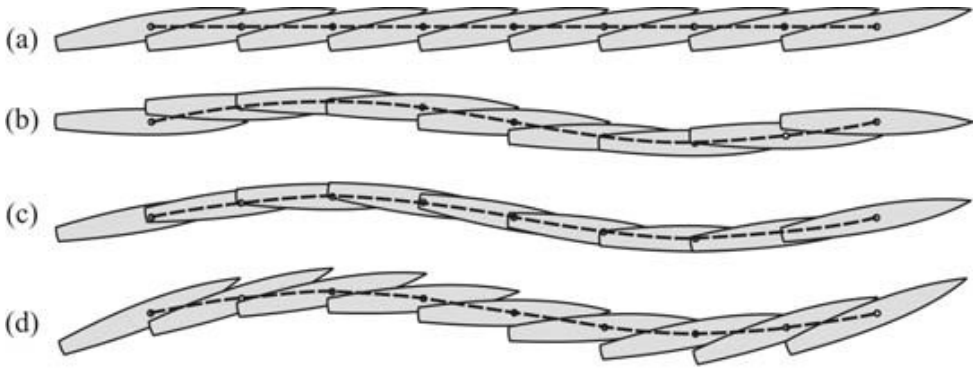


Figure 2-8 Illustrations of (a) static drift, (b) pure sway, (c) pure yaw, and (d) yaw and drift tests.

## 2.2 Ballasting Procedures

This section describes the procedures performed in ballasting model 5613 to maintain dynamic similitude to full scale and CFD. Mass is strategically placed within the model to satisfy specified displacement $\nabla$, $LCG$, $VCG$ (and thus $\overline{GM}$), pitch gyradius $k_{yy}$, and roll gyradius $k_{xx}$. The ship is considered a long slender object for which $k_{zz} \approx k_{yy}$ thus yaw gyradius $k_{zz}$ need not be set.

Model displacement is set by enforcing the total mass of the model rather than adding mass until desired waterline is achieved. This ensures consistency with scaling and CFD. Pre-cut lengths of square steel rod stock are used as ballast pieces and lumped together in such a way that they can be split apart in equal portions in all three principle directions while iteratively setting location of ballast pieces. To trim the model, the $LCG$ is roughly defined by placing ballast fore and aft in such a way to maintain even keel and to ensure the keeled edge of the model's static waterline coincides with the observed waterline when placed in water. This occurs only if the model is constructed within geometric specifications and correct mass is added. Dummy weights representing the mass of the heave staff and front yaw guide rail mount are placed on their respective floor mounts so that the influence of their weight is considered when trimming the model because the 3DOF mount is not installed at this time for convenience. $LCG$ is further refined by then placing the model in a moment-of-inertia swing which can be seen in Fig. 2-9 (a). Ballast is fine-tuned so that the model is level when its desired $LCG$ location is directly underneath the swing pivot point. While the model is still on the swing, $VCG$ and $k_{yy}$ are both set in an iterative fashion by distributing ballast vertically and lengthwise, respectively, while performing the procedure that will hence be described. The swing is fitted with a rotary potentiometer that is used to capture oscillatory swing motion. LabView is used to display the calibrated output of the potentiometer which allows for easy swing and ship leveling as well as acquiring swing and ship oscillation period. A precision angle finder is used to calibrate the potentiometer and to confirm ship levelness.

The accuracy of the swing method is confirmed by measuring the known $VCG$ and $k_{yy}$ of a large rectangular aluminum slab prior to ship measurements.

In measuring ship $VCG$ and $k_{yy}$ the distance from the swing's center of gravity to the pivot point, $\overline{OG_0}$, and the swing's moment of inertia about its pivot, $I_0$, must be measured before placing the ship on the swing. A movable weight $W_b$ is placed at the edge of the swing at distance $d$. Refer to step 1 in Fig 2-9 (b). The resulting swing angle $\theta_0$ is then recorded and the distance $\overline{OG_0}$ is obtained by the moment balance

$$W_0\overline{OG_0}\tan\theta_0 = W_b d \tag{2.7}$$

where $W_0$ is the total weight of the swing and movable weight. Next, the swing's moment of inertia about its pivot, $I_0$, is measured. The movable weight is placed back to level condition and the swing is perturbed into oscillation as seen in step 2 of Fig. 2-9 (b). Solving the ODE for pendulum motion gives

$$I_0 = \frac{W_0\overline{OG_0}T_0^2}{4\pi^2} \tag{2.8}$$

where $T_0$ is natural swing period recorded by the DA. Next, the distance from the ship's center of gravity to the pivot point, $\overline{OG_M}$, and thus $VCG$ is measured. The ship is placed and leveled on the swing with $LCG$ below the pivot point. The dummy weight for the heave staff is removed because the heave staff does not roll or pitch with the ship and is considered to be a point mass at the center of gravity - tow point and therefore its mass only contributes to ship displacement and does not contribute to the center of gravity location or moments of inertia. The dummy weight for the yaw guide rail mount is left in place because this particular component of the yaw guide portion of the 3DOF mount moves with the ship at a considerable distance from the ship center of gravity therefore its mass cannot be ignored. The yaw guide rail linkage and counterweight assembly add to the ship pitching moment of inertia but are not considered due to infeasibility of installation while performing the swing test. Its effect is nonetheless considered to be

small. The movable weight is then moved distance $d$ and the angle $\theta'$ is recorded as shown in step 3 of Fig. 2-9 (b). The distance from the combined ship and swing center of gravity to the pivot point, $\overline{OG'}$, is obtained by the moment balance

$$\overline{OG'} = \frac{W_b d}{(W_0+W_M)\tan\theta'} \tag{2.9}$$

where $W_M$ is the weight of the ship model (minus the weight of heave staff). The definition of center of gravity allows for the separation of $(W_0 + W_M)\overline{OG'}$:

$$(W_0 + W_M)\overline{OG'} = W_0\overline{OG_0} + W_M\overline{OG_M} \tag{2.10}$$

The distance from the ship's center of gravity to the pivot point is then

$$\overline{OG_M} = \frac{(W_0+W_M)\overline{OG'} - W_0\overline{OG_0}}{W_M} \tag{2.11}$$

Pieces of ballast are moved vertically until the desired $\overline{OG_M}$ is obtained. The desired $\overline{OG_M}$ is simply found by subtracting the target $VCG$ from the ship waterline to pivot distance. The natural period of the ship and swing system, $T'$, is found by setting the swing into motion as shown in step 4 of Fig. 2-9 (b). Following (2.8) the total moment of inertia of the ship and swing system about the pivot point is

$$I' = \frac{(W_0+W_M)\overline{OG'}T'^2}{4\pi^2} \tag{2.12}$$

Splitting $I'$ into components due to the swing and ship gives

$$I' = I_0 + I_{MO} \tag{2.13}$$

where $I_{MO}$ is the ship's moment of inertia about the swing pivot point. The parallel axis theorem relates $I_{MO}$ to the ship moment of inertia about its own center of gravity, $I_y$:

$$I_{MO} = I_y + m_M(\overline{OG_M})^2 \tag{2.14}$$

where $m_M$ is the mass of the ship. Combining (2.13) and (2.14) gives

$$I_y = I' - I_0 - m_M(\overline{OG_M})^2 \tag{2.15}$$

The following relation defines the pitch radius of gyration, $k_{yy}$:

$$I_y = m_M k_{yy}^2 \tag{2.16}$$

And thus

$$k_{yy} = \sqrt{\frac{I_y}{m_M}} \tag{2.17}$$

Fore and aft ballast groupings are moved toward or away from ship center of gravity until the desired $k_{yy}$ is obtained. The $LCG$ is maintained by monitoring and ensuring ship levelness while altering ballast distribution.

Once $VCG$ is set, so then is $\overline{GM}$. Using a swing to determine $VCG$ by displacing the ship about the pitch axis, however, is less accurate than the standard inclining test which displaces the ship about the roll axis to determine $\overline{GM}$. This is due to the swing's low sensitivity to vertical movements of individual ballast pieces, when displacing about the pitch axis. Any error in $\overline{OG_M}$ would be relatively large error in $VCG$ due to $VCG$ being much smaller than $\overline{OG_M}$. Therefore the standard inclining test must be performed to verify and fine-tune $\overline{GM}$ and is most straight forward when performed in water. Refer to Fig. 2-10 for an explanation of inclining test parameters. The simplest inclining method is to use ballast that is normally transversely centered on the ship as the displacement weight $W_b$so that when removed the ship does not heel. Only when the weight is placed to the side of the ship at distance $d$ from the ship centerline will the ship heel at some angle $\phi$. The 3DOF mount is not installed during the inclining test so for convenience the heave staff dummy weight is chosen to be the displacement weight. A precision angle finder whose mass is neglected is placed on the deck of the model to acquire heel angle, shown in Fig 2-11 (a). A moment balance relates the moment of the displacement weight and the righting arm, $\overline{GZ}$:

$$W_b d \cos\phi = W_M \overline{GZ} \tag{2.18}$$

where, again, $W_b$ is displacement weight (in this case the heave staff dummy weight) and $W_M$ is model weight (minus the weight of heave staff). Where

$$\overline{GZ} = \overline{GM} \sin \phi \tag{2.19}$$

The metacentric height, $\overline{GM}$, is then

$$\overline{GM} = \frac{W_b d}{W_M \tan \phi} \tag{2.20}$$

The procedure is performed for many values of $d$ while maintaining $\phi < 4°$ to keep $\overline{GM}$ near constant. $\overline{GZ}$ is then plotted against $\phi$ for each value of $d$ to ensure a near linear trend. The displacement weight placement for $d$ = 0, 40, 65, 123, and 165 mm is shown in Fig. 2-11 (b), (c), (d), (e), and (f), respectively. Massless foam inserts are used to extend the flat surface of the heave staff and gimbal assembly mount for which the displacement weight rests on at varying $d$.

The remaining mass property to satisfy is roll gyradius, $k_{xx}$, in which ballast must be adjusted transversely to obtain the correct mass distribution about the roll axis. It is possible to perform this measurement by using the swing method to obtain the model's roll moment of inertia. Due to the model's small roll moment of inertia about its own center of gravity compared to the total ship and swings' moment of inertia about the swing pivot, however, the measurement would be highly dominated by the latter and thus the swing method is not the preferred choice. Instead, the model's natural roll frequency in water is measured and set to the target value which can be obtained from the following analysis. Free roll motion can be describe as

$$(I_x + J_x)\ddot{\phi} + N_x\dot{\phi} + C_x\phi = 0 \tag{2.21}$$

where $I_x$ is the model's roll moment of inertia, $J_x$ is the added roll moment of inertia due to motion imparted to the surrounding water, $N_x$ is the damping coefficient, and $C_x$ is the righting moment coefficient. With damping neglected and $C_x = W_M\overline{GM}$, (2.21) becomes

$$\ddot{\phi} + \frac{W_M\overline{GM}}{I_x+J_x}\phi = 0 \tag{2.22}$$

which has natural frequency

$$\omega_\phi = \sqrt{\frac{W_M \overline{GM}}{I_x + J_x}} \tag{2.23}$$

with

$$I_x + J_x = m_M k_{xx}^2 \tag{2.24}$$

where $m_M$ is the model's mass. In this instance the target natural roll frequency is calculated to be $\omega_\phi$ = 3.79 rad/s. This value matches the value given by Umeda et al. (2008) in which the very same model was used for free model testing. The ship model is placed in the water with the 3DOF mount installed and attached to the PMM carriage so that the roll potentiometer can be used with the DA to record the roll motion. With the water being calm upon visual inspection the model is released at the maximum roll angle allowed by the 3DOF mount in order to record as many oscillation periods as possible. Once the frequency is determined ballast is adjusted transversely inward or outward and the procedure is repeated until the measured natural roll frequency matches $\omega_\phi$ = 3.79 rad/s.

The above procedures involve frequent movement of ballast pieces in the pursuit of satisfying mass properties. The vertical movement of ballast when fine tuning $\overline{GM}$ changes $k_{yy}$ a slight amount. Therefore the last step of the ballasting process is to re-perform the swing test and fine tune $k_{yy}$ back to the target value. It is important to refrain from moving ballast vertically when doing so, even if the swing method indicates $\overline{OG_M}$ (and thus $VCG$) has changed slightly after setting $\overline{GM}$ with the inclining test. Discrepancy between the two methods is likely due to inconsistent swing loading deformations from foam cushioning pads that hold the model in place as well as error from difficulty in measuring the distance from the swing pivot to the ship water line, from which, $VCG$ is measured relative to. Recall that setting $\overline{GM}$ with the inclining test is a more reliable way of fixing $VCG$ so the current vertical positioning of ballast must be trusted. Final ballast placement throughout the model is shown in Fig. 2-12.

(a) (b)

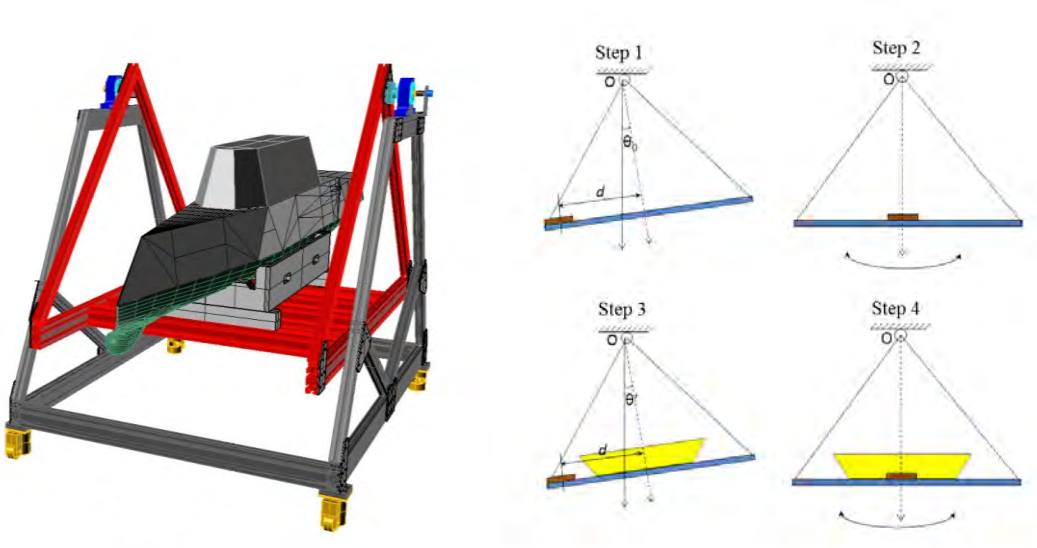


Figure 2-9 Test setup for model $k_{yy}$ acquisition with (a) swing used for measurement and (b) illustration of procedure to acquire $k_{yy}$.

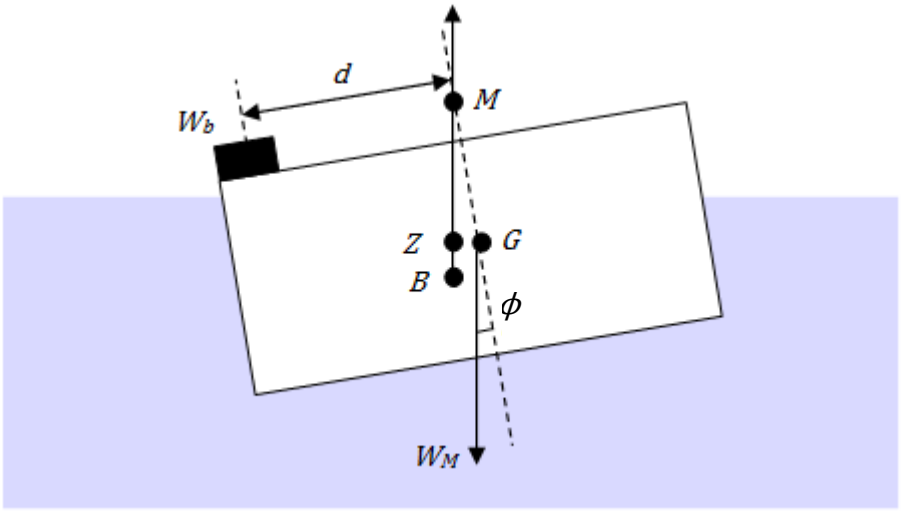


Figure 2-10 Illustration of inclining test.

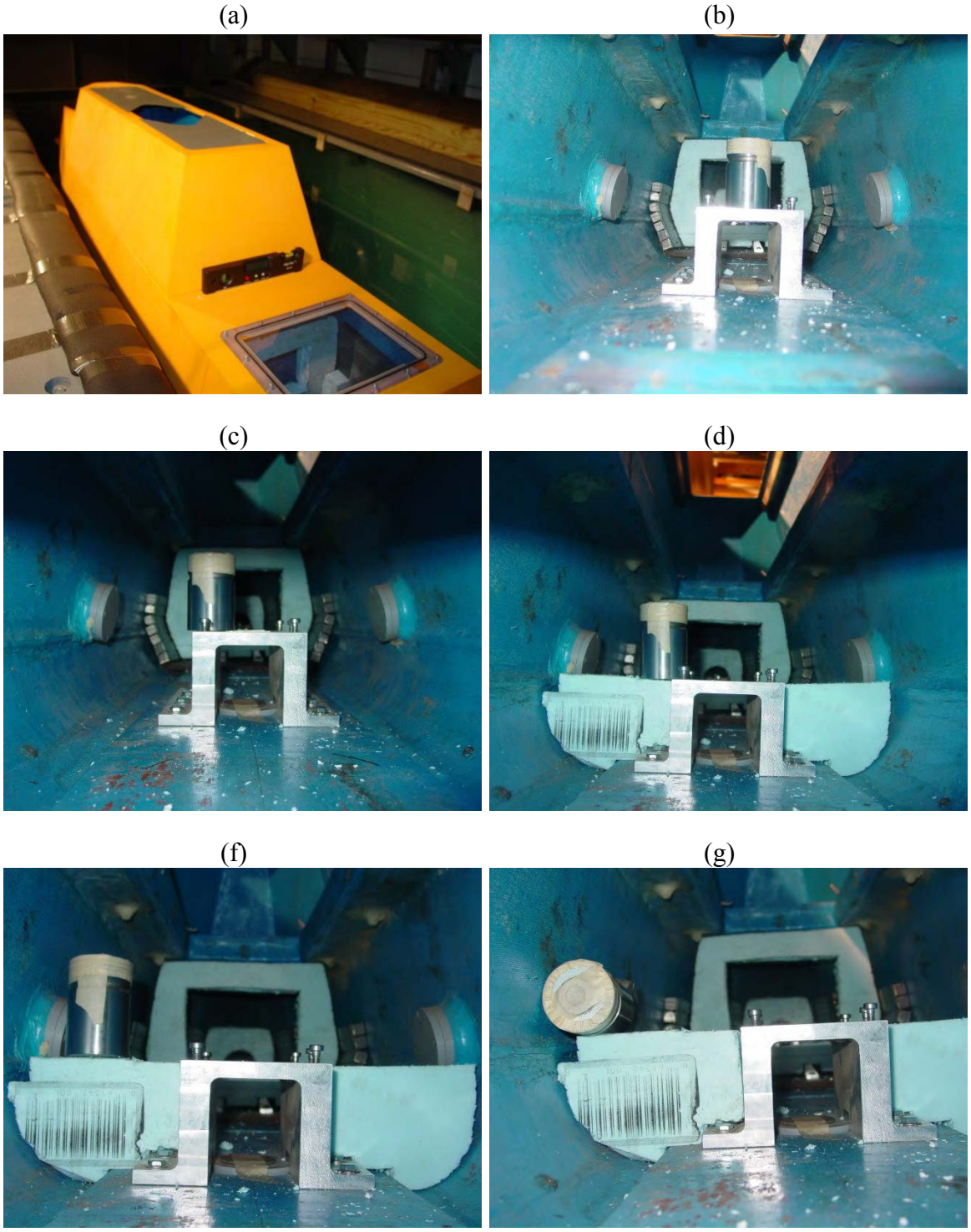


Figure 2-11 Setup for inclining test showing (a) placement of angle finder and displacement weight at (b) $d$ = 0, (c) $d$ = 40, (d) $d$ = 65, (e) $d$ = 123, and (f) $d$ = 165 mm.

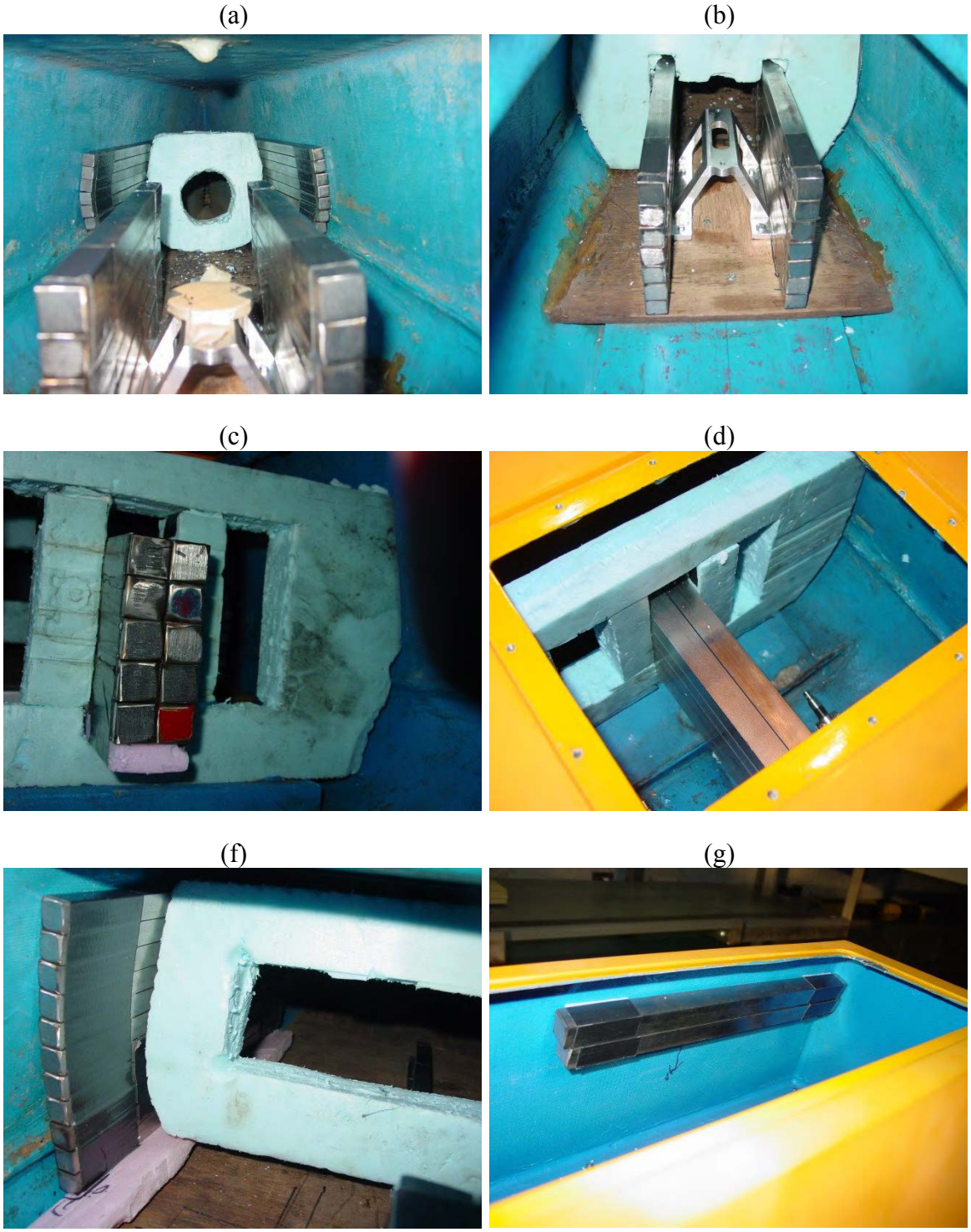


Figure 2-12 Final placement of ballast at (a) bow, (b) mid-bow, (c) mid-stern, (d) mid-stern, (f) stern, and (g) superstructure.

## 2.3 Data Reduction Equations

FORTRAN programs are used on a Windows PC to process the data in batches. Raw data files contain time histories of analog voltage outputs from each measurement device. Zero-point and run-point data files are read and the analog voltages are converted to engineering units with the zero-point correction applied.

### 2.3.1 Free-stream Air Velocity Distribution

The free stream air velocity distribution is measured by sampling velocity over a specified grid which is later described in section 2.4.1. The sample pressure differential sensed by each pitot probe is calculated using

$$\Delta p_i = \left(V_{p_i} - \bar{V}_{0,p}\right) c_{tran} \rho_{al} g \tag{2.25}$$

where $V_{p_i}$ is the sample voltage output of the pressure transducer and signal conditioner system, $\bar{V}_{0,p}$ is the average zero point voltage acquired without wind, $c_{tran}$ is the calibration coefficient which converts voltage to height of fluid used in calibration, $\rho_{al}$ is the density of alcohol that is used as the fluid in calibration, and $g$ is the acceleration due to gravity. Each sample velocity is calculated using the pitot tube equation

$$U_{W_i} = \sqrt{\frac{2(\Delta p_i)}{\rho_a}} \tag{2.26}$$

where $\Delta p_i$ is the sample pressure differential given in (2.25) and $\rho_a$ is the density of air. The average of the velocity time history at each grid point is

$$\bar{U}_W = \frac{1}{N} \sum_{i=1}^{N} U_{W_i} \tag{2.27}$$

where $N$ is number of samples at each grid point and $U_{W_i}$ is the sample velocity in (2.26). The standard deviation of the velocity time history at each grid point is

$$RMS = \sqrt{\frac{1}{N-1} \sum_{i=1}^{N} \left(U_{W_i} - \bar{U}_W\right)^2} \tag{2.28}$$

where $N$ is number of samples at each grid point, $U_{W_i}$ is the sample velocity in (2.26) and $\overline{U}_W$ is the average of velocity time history at each grid point in (2.27). The spatial average of the grid point velocity time history averages is

$$\mu_{\overline{U}_W} = \frac{1}{N}\sum_{i=1}^{N} \overline{U}_{W_i} \tag{2.29}$$

where $N$ is number of grid points and $\overline{U}_{W_i}$ is the average of velocity time history at each grid point in (2.27). The spatial average of the grid point velocity time history standard deviations is

$$\mu_{RMS} = \frac{1}{N}\sum_{i=1}^{N} RMS_i \tag{2.30}$$

where $N$ is number of grid points and $RMS_i$ is the standard deviation of velocity time history at each grid point in (2.28). The variation, or spatial standard deviation of the grid point velocity time history averages in percent of spatial average, is

$$\sigma_{\overline{U}_W} = \frac{100}{\mu_{\overline{U}_W}}\sqrt{\frac{1}{N-1}\sum_{i=1}^{N}(\overline{U}_{W_i} - \mu_{\overline{U}_W})^2} \tag{2.31}$$

where $N$ is number of grid points, $\overline{U}_{W_i}$ is the average of velocity time history at each grid point in (2.27), and $\mu_{\overline{U}_W}$ is the spatial average of grid point velocity time history averages in (2.29). The spatial standard deviation of the grid point velocity time history standard deviations in percent of spatial average is

$$\sigma_{RMS} = \frac{100}{\mu_{\overline{U}_W}}\sqrt{\frac{1}{N-1}\sum_{i=1}^{N}(RMS_i - \mu_{RMS})^2} \tag{2.32}$$

where $N$ is number of grid points, $RMS_i$ is the standard deviation of velocity time history at each grid point in (2.28), $\mu_{RMS}$ is the spatial average of grid point velocity time history standard deviations in (2.30), and $\mu_{\overline{U}_W}$ is the spatial average of grid point velocity time history averages in (2.29).

### 2.3.2 Straight Ahead Test

The total resistance of the model due to water and wind is

$$R_T = F_x = c_{F_x}\left(\overline{V}_{F_x} - \overline{V}_{0,F_x}\right) - D_{mount} \tag{2.33}$$

where $F_x$ is the $x$-component of force measured by the load cell (minus the 3DOF mount drag), $c_{F_x}$ is the laod cell $x$-component calibration coefficient, $\bar{V}_{F_x}$ is the load cell time-averaged $x$-component output voltage over the steady portion of the carriage run, $\bar{V}_{0,F_x}$ is the laod cell time-averaged zero point measurement taken before the carriage run, and $D_{mount}$ is the drag force due to the 3DOF mount determined from the procedure outlined in Appendix A. The total resistance coefficient is defined as

$$C_T = \frac{R_T}{\frac{1}{2}\rho_w {U_C}^2 S} \tag{2.34}$$

where $R_T$ is the total resistance (2.33), $\rho_w$ is the density of water according to the temperature taken at the time of the experiment, $U_C$ is carriage speed, and $S$ is the static wetted surface area (underwater portion only) of the model. The drag coefficient of the above water portion of the model is given by

$$C_D = \frac{D}{\frac{1}{2}\rho_a {\mu_{\bar{U}_W}}^2 A_{proj}} \tag{2.35}$$

where $D$ is the drag force due to wind on the above water portion of the model which is simply the difference between the resistance from corresponding cases with and without wind, $\rho_a$ is the density of air according to the temperature taken at the time of the experiment, $\mu_{\bar{U}_W}$ is the headwind velocity relative to the ship (2.30), and $A_{proj}$ is the projected area of the above water portion of the model onto the $y$-$z$ plane. Non-dimensional and dimensional model static sinkage are given by the following equations

$$z = c_z\left(\bar{V}_z - \bar{V}_{0,z}\right)/L \tag{2.36a}$$

$$z_{mm} = c_z\left(\bar{V}_z - \bar{V}_{0,z}\right) \tag{2.36b}$$

respectively, where $c_z$ is the 3DOF mount heave potentiometer calibration coefficient, $\bar{V}_z$ is the heave potentiometer time-averaged output voltage over the steady portion of the carriage run, $\bar{V}_{0,z}$ is the heave potentiometer time-averaged zero point measurement taken before the carriage run, and $L$ is the ship length. Static trim is given by

$$\theta = c_\theta\left(\bar{V}_\theta - \bar{V}_{0,\theta}\right) \tag{2.37}$$

where $c_\theta$ is the 3DOF mount pitch potentiometer calibration coefficient, $\bar{V}_\theta$ is the heave potentiometer time-averaged output voltage over the steady portion of the carriage run, and $\bar{V}_{0,\theta}$ is the pitch potentiometer time-averaged zero point measurement taken before the carriage run.

### 2.3.3 Static PMM Test

Non-zero sway velocity results in non-zero sway force and yaw moment. Thus, the *x* and *y*-component of the total force and total *z*-moment imparted to the model in the ship-fixed coordinate system are measured. Inertial forces and moments are not imparted by the model for static tests therefore the load cell only measures the hydrodynamic forces and moment

$$X = F_x = c_{F_x}\left(\bar{V}_{F_x} - \bar{V}_{0,F_x}\right) - D_{mount}\cos\psi \tag{2.38a}$$

$$Y = F_y = c_{F_y}\left(\bar{V}_{F_y} - \bar{V}_{0,F_y}\right) + D_{mount}\sin\psi \tag{2.38b}$$

$$N = M_z = c_{M_z}\left(\bar{V}_{M_z} - \bar{V}_{0,M_z}\right) \tag{2.38c}$$

where $X$, $Y$, and $N$ are hydrodynamic forces and moment, respectively, $F_x$, $F_y$, and $M_z$ are the forces (with 3DOF mount drag correction applied) and moment measured by the load cell, respectively, $c$ and $\bar{V}$ are corresponding calibration coefficients and average voltage outputs explained in section 2.3.2, and $D_{mount}$ is the drag force due to the 3DOF mount determined from the procedure outlined in Appendix A. In addition to static sinkage and trim described in section 2.3.2, the non-zero heel and drift angle are given by

$$\phi = c_\phi\left(\bar{V}_\phi - \bar{V}_{0,\phi}\right) \tag{2.39}$$

$$\beta = \psi = c_\psi \bar{V}_\psi \tag{2.40}$$

where $c$ and $\bar{V}$ are corresponding calibration coefficients and average voltage outputs explained in section 2.3.2. Note that $\beta$ does not have a zero point correction because setting $\beta = 0$ before every zero-point acquisition and then resetting to the test value before the run-point acquisition would be impractical. Making appropriate adjustments

to the potentiometer pulley drive cable ensures that $\psi$ contains no offset voltage at $\beta = 0$. For the purpose of non-dimensionalization $L$, $L/U$, and $\frac{1}{2}\rho L^2 T$ are used as the respective characteristic scales for length, time, and mass, where $L$ is the ship length, $U$ is the ship advance speed, $\rho$ is density of water, and $T$ is the draft of the ship, which follows the *Prime-system* of SNAME. Non-dimensional sway velocity, forces, and moment are

$$v' = \frac{v}{U} \tag{2.41a}$$

$$X' = \frac{X}{1/2\rho U^2 LT} \tag{2.41b}$$

$$Y' = \frac{Y}{1/2\rho U^2 LT} \tag{2.41c}$$

$$N' = \frac{N}{1/2\rho U^2 L^2 T} \tag{2.41d}$$

For simplicity, the prime symbol will be omitted for the remainder of the thesis. To determine hydrodynamic derivatives, mathematical models for hydrodynamic forces and moment acting on a ship are given by Abkowitz, 1964. By using the simplified motion equations (2.3) – (2.6), Abkowitz's mathematical models obtained from a 3rd-order Taylor Series expansion can be reduced to determine the hydrodynamic derivatives of interest. For static drift they are

$$X = X_* + X_{vv} v^2 \tag{2.42a}$$

$$Y = Y_v v + Y_{vvv} v^3 \tag{2.42b}$$

$$N = N_v v + N_{vvv} v^3 \tag{2.42c}$$

Static drift tests are performed over a range of drift angle $\beta$ and data is curve-fitted to polynomial functions (with a least squares method) following the mathematical model (2.42):

$$y = A + Bx^2;\ y = X;\ x = v \tag{2.43a}$$

$$y = Ax + Bx^3;\ y = Y, N;\ x = v \tag{2.43b}$$

Then the respective hydrodynamic derivatives are simply

$$X_*, Y_v, N_v = A \tag{2.44a}$$

$$X_{vv}, Y_{vvv}, N_{vvv} = B \tag{2.44b}$$

### 2.3.4 Dynamic PMM Test

Yoon (2009) presents methodology for obtaining hydrodynamic derivatives of DTMB model 5512 from PMM tests. With the model and test conditions being similar and by using the same PMM carriage system, the same methodology for analyzing forces, moment, and motions harmonics and obtaining hydrodynamic derivatives will be used herein. Time histories of prescribed motions ($y$ and $\psi$) and responses ($z$, $\theta$, $\phi$, $F_x$, $F_y$, and $M_z$) are of interest for dynamic tests and are later treated with harmonic analysis. They are measured as

$$y_i = c_y\left(V_{y_i} - \bar{V}_{0,y}\right) \tag{2.45a}$$

$$\psi_i = c_\psi V_{\psi_i} \tag{2.45b}$$

$$z_i = c_z\left(V_{z_i} - \bar{V}_{0,z}\right) \tag{2.45c}$$

$$\theta_i = c_\theta\left(V_{\theta_i} - \bar{V}_{0,\theta}\right) \tag{2.45d}$$

$$\phi_i = c_\phi\left(V_{\phi_i} - \bar{V}_{0,\phi}\right) \tag{2.45e}$$

$$F_{x_i} = c_{F_x}\left(V_{F_{x_i}} - \bar{V}_{0,F_x}\right) - D_{mount}\cos\psi_i \tag{2.45f}$$

$$F_{y_i} = c_{F_y}\left(V_{F_{y_i}} - \bar{V}_{0,F_y}\right) + D_{mount}\sin\psi_i \tag{2.45g}$$

$$M_{z_i} = c_{M_z}\left(V_{M_{z_i}} - \bar{V}_{0,M_z}\right) \tag{2.45h}$$

where *i* represents the variable at a single sample and point in the time history, $c$ and $\bar{V}$ are corresponding calibration coefficients and average voltage outputs explained in section 2.3.2, and $D_{mount}$ is the drag force due to the 3DOF mount determined from the procedure outlined in Appendix A. Note that for yaw and drift cases superimposed drift angle, $\beta$, is not recorded by the DA. It is simply set to the desired static value by

adjusting the model position relative to the PMM drive system using a rotary scale on the strongback.

The addition of lateral motion causes the load cell to measure forces and moment due to the inertia of the ship and 3DOF mount in addition to the hydrodynamic force on the ship. Nondimensional hydrodynamic forces and moment are found by correcting for inertia

$$X = \frac{F_x + m_M(\dot{u} - vr) + m_{mount}(\dot{u} - vr - x_{G,mount}r^2)}{1/2\rho(u^2+v^2)LT} \tag{2.46b}$$

$$Y = \frac{F_y + m_M(\dot{v} - ur) + m_{mount}(\dot{v} + ur + x_{G,mount}\dot{r})}{1/2\rho(u^2+v^2)LT} \tag{2.46c}$$

$$N = \frac{M_z + I_z\dot{r} + I_{z,mount}\dot{r} + m_{mount}(x_{G,mount}(\dot{v} + ur))}{1/2\rho(u^2+v^2)L^2T} \tag{2.46d}$$

where $m_M$ is the mass of the ship, $m_{mount}$ is the mass of the 3DOF mount, $x_{G,mount}$ is the non-zero position of the 3DOF mount center of gravity, $I_z$ is the yaw moment of the inertia of the ship, and $I_{z,mount}$ is the of inertia of the 3DOF mount about the yaw axis. $I_{z,mount}$ and $x_{G,mount}$ are measured prior to data reduction using the procedure outlined in Appendix A. The ship and mount inertia are treated separately so that the ship inertia force can be used for further analysis. Surge, sway, and yaw velocities and accelerations in (2.46) are computed using equations for PMM motions described by (2.4), (2.5), and (2.6).

PMM motions introduce acceleration terms to the mathematical model for hydrodynamic sway force and yaw moment. The simplified mathematical model for pure sway is

$$X = X_* + X_{vv}v^2 \tag{2.47a}$$

$$Y = Y_{\dot{v}}\dot{v} + Y_v v + Y_{vvv}v^3 \tag{2.47b}$$

$$N = N_{\dot{v}}\dot{v} + N_v v + N_{vvv}v^3 \tag{2.47c}$$

Notice that sway velocity derivatives $X_*$, $X_{vv}$, $Y_v$, $Y_{vvv}$, $N_v$, and $N_{vvv}$ can be determined from pure sway tests as well as from static drift tests. Dynamic test data, however, are often known as being frequency-dependent and thus sway velocity derivatives determined from static drift tests are preferred (van Leeuwen, 1964). For pure yaw the hydrodynamic derivatives of interest are a function of yaw rate and acceleration:

$$X = X_* + X_{rr}r^2 \tag{2.48a}$$

$$Y = Y_{\dot{r}}\dot{r} + Y_r r + Y_{rrr}r^3 \tag{2.48b}$$

$$N = N_{\dot{r}}\dot{r} + N_r r + N_{rrr}r^3 \tag{2.48c}$$

Sway and yaw cross-coupled derivatives are of interest for yaw and drift tests:

$$X = X_* + X_{vv}v^2 + X_{rr}r^2 + X_{vr}vr \tag{2.49a}$$

$$Y = Y_v v + Y_{vvv}v^3 + Y_{\dot{r}}\dot{r} + Y_r r + Y_{rrr}r^3 + Y_{vrr}vr^2 + Y_{rvv}rv^2 \tag{2.49b}$$

$$N = N_v v + N_{vvv}v^3 + N_{\dot{r}}\dot{r} + N_r r + N_{rrr}r^3 + N_{vrr}vr^2 + N_{rvv}rv^2 \tag{2.49b}$$

As outlined in Yoon (2009), harmonic forms of the above mathematical models can be obtained by substituting equations for PMM motion (2.4), (2.5), and (2.6). A Fourier-series (FS) reconstruction of the raw data time histories yields the sine and cosine harmonics of the measured data. Sine and cosine harmonics $X_0$, $X_{Sn}$, $X_{Cn}$, $Y_0$, $Y_{Sn}$, $Y_{Cn}$, $N_0$, $N_{Sn}$, and $N_{Cn}$ for $n$ = 1, 2, or 3 are defined to be relative to time $t$ = 0 when sway motion crosses $y$ = 0 going from positive to negative. The hydrodynamic derivatives are then found by curve-fitting these measured harmonics into the harmonics form of the mathematical models following Yoon (2009). The expressions for the harmonics curve-fits given by the mathematical models are summarized in Table 2-6.

Table 2-6 Harmonics Forms of Mathematical Models for Forces and Moment.

Pure sway models:

$$X = X_0 + X_{C2}\cos 2\omega t$$
$$Y = Y_{C1}\cos \omega t + Y_{S1}\sin \omega t + Y_{C3}\cos 3\omega t$$
$$N = N_{C1}\cos \omega t + N_{S1}\sin \omega t + N_{C3}\cos 3\omega t$$

| $X$ model | $Y$ model | $N$ model |
|---|---|---|
| $X_0 = X_* + \frac{1}{2}X_{vv}v_{max}^2$ | $Y_{C1} = -\left(Y_v v_{max} + \frac{3}{4}Y_{vvv}v_{max}^3\right)$ | $N_{C1} = -\left(N_v v_{max} + \frac{3}{4}N_{vvv}v_{max}^3\right)$ |
| $X_{C2} = \frac{1}{2}X_{vv}v_{max}^2$ | $Y_{S1} = Y_{\dot{v}}\dot{v}_{max}$ | $N_{S1} = N_{\dot{v}}\dot{v}_{max}$ |
| | $Y_{C3} = -\frac{1}{4}Y_{vvv}v_{max}^3$ | $N_{C3} = -\frac{1}{4}N_{vvv}v_{max}^3$ |

Pure yaw models:

$$X = X_0 + X_{C2}\cos 2\omega t$$
$$Y = Y_{S1}\sin \omega t + Y_{C1}\cos \omega t + Y_{S3}\sin 3\omega t$$
$$N = N_{S1}\sin \omega t + N_{C1}\cos \omega t + N_{S3}\sin 3\omega t$$

| $X$ model | $Y$ model | $N$ model |
|---|---|---|
| $X_0 = X_* + \frac{1}{2}X_{rr}r_{max}^2$ | $Y_{S1} = Y_r r_{max} + \frac{3}{4}Y_{rrr}r_{max}^3$ | $N_{S1} = N_r r_{max} + \frac{3}{4}N_{rrr}r_{max}^3$ |
| $X_{C2} = -\frac{1}{2}X_{rr}r_{max}^2$ | $Y_{C1} = Y_{\dot{r}}\dot{r}_{max}$ | $N_{C1} = N_{\dot{r}}\dot{r}_{max}$ |
| | $Y_{S3} = -\frac{1}{4}Y_{rrr}r_{max}^3$ | $N_{S3} = -\frac{1}{4}N_{rrr}r_{max}^3$ |

Yaw and drift models:

$$X = X_0 + X_{S1}\sin \omega t + X_{C2}\cos 2\omega t$$
$$Y = Y_{S1}\sin \omega t + Y_{C1}\cos \omega t + Y_{C2}\cos 2\omega t + Y_{S3}\sin 3\omega t$$
$$N = N_{S1}\sin \omega t + N_{C1}\cos \omega t + N_{C2}\cos 2\omega t + N_{S3}\sin 3\omega t$$

| $X$ model | $Y$ model | $N$ model |
|---|---|---|
| $X_0 = X_* + X_{vv}v^2 + \frac{1}{2}X_{rr}r_{max}^2$ | $Y_0 = Y_v v + Y_{vvv}v^3 + \frac{1}{2}Y_{vrr}vr_{max}^2$ | $N_0 = N_v v + N_{vvv}v^3 + \frac{1}{2}N_{vrr}vr_{max}^2$ |
| $X_{S1} = X_{vr}vr_{max}$ | $Y_{S1} = Y_r r_{max} + \frac{3}{4}Y_{rrr}r_{max}^3 + Y_{rvv}r_{max}v^2$ | $N_{S1} = N_r r_{max} + \frac{3}{4}N_{rrr}r_{max}^3 + N_{rvv}r_{max}v^2$ |
| $X_{C2} = -\frac{1}{2}X_{rr}r_{max}^2$ | $Y_{C1} = Y_{\dot{r}}\dot{r}_{max}$ | $N_{C1} = N_{\dot{r}}\dot{r}_{max}$ |
| | $Y_{C2} = -\frac{1}{2}Y_{vrr}vr_{max}^2$ | $N_{C2} = -\frac{1}{2}N_{vrr}vr_{max}^2$ |
| | $Y_{S3} = -\frac{1}{4}Y_{rrr}r_{max}^3$ | $N_{S3} = -\frac{1}{4}N_{rrr}r_{max}^3$ |

## 2.4 Measurement Systems and Calibration Procedures

### 2.4.1 Free-stream Air Velocity Distribution

Free-stream air axial velocity measurements are performed using eight pitot-static probes mounted to a common rack that is attached to a 2D automated Velmex traverse system. This traverse system is fixed to the strongback and is designed to survey axial velocities in *x*-planes upstream of the model. The entire system is shown in Fig. 2-13 along with survey plane locations. Each *x*-plane is split into four zones that cover the outlet area of the wind carriage. Each zone consists of flow corresponding to two fans. A schematic can be seen in Fig. 2-14 (a). The pitot-static probes sample axial velocity at 640 grid points that make up each surveyed *x*-plane. The grid is shown in Fig. 2-14 (b). The eight pitot-static probes are oriented vertically in relation to one another on the rack which is cycled through ten upper positions and ten lower positions within each zone, with a region of overlap coverage located around the vertical center of each zone. This overlap region corresponds to the densely spaced portion of the grid shown in Fig. 2-14 (b). Each of the two traverses that move the rack of pitot-static probes about the *x*-planes are powered by step motors which are controlled by a twin axis Velmex controller. The controller is connected to a PC via serial cable and communication occurs through LabView. Displacement is known through the relationship of motor steps per rotation and the thread pitch of the traverse drive screw. 200 steps corresponds to 1.0 mm of displacement. Pressure sensed by each pitot-static probe is transmitted to its own Validyne model DP15 differential pressure transducer via Tygon tubing. Combination amplifier and signal conditioners are used in conjunction with each of the transducers to send analog output voltage to a 16 channel analog-to-digital (AD) converter, which in conjunction with the PC make up the data acquisition system (DA). Each pitot-static probe, pressure transducer, and amplifier and signal conditioner are calibrated together as a system using a Rouse Manometer. T-fittings in the Tygon tubing connect the

manometer in parallel with the pitot-static probe so that the same pressure differential sensed by the pitot-static probe is also sensed by the manometer. Each pitot probe is placed in the wind stream. The manometer reading is noted while transducer output voltage is being recorded by DA. Performing this procedure at varying wind speeds gives a relationship of manometer working fluid height to transducer output voltage. Manometer working fluid height is then converted to pressure, and then to velocity using (2.25) and (2.26), respectively. The plumbing response of the pressure measurement system is a function of the speed of sound, tubing length, and the ratio of transducer cavity volume to volume contained within the tubing:

$$f_n = \frac{c}{2\pi L\sqrt{\frac{1}{2}+\frac{Q}{aL}}} \tag{2.50}$$

where $Q$ is the DP15 transducer cavity volume, $L$ is the tubing length, $a$ is the tubing cross-sectional area, and $c$ is the speed of sound in air. Refer to Fig. 2-15 for an illustration. The usable system response is usually equal to approximately 20% of the plumbing response frequency $f_n$ (Hz). With $f_n$ = 39.7 Hz the usable system response is approximately 7.9 Hz.

Initially the traverse mounted pitot-static system is mounted as close to the wind carriage outlet as possible using the hardware available at the time. This location corresponds to the surveys taken at $x$ = -0.13. In order to provide fan controller dial setting set points for full wind and half wind conditions, the relationship between wind speed and fan controller master dial setting need be roughly described. Performing surveys over the grid of 640 points at multiple fan controller dial settings is an ideal but overambitious method of obtaining this relationship. A simpler method suffices. The vertically oriented rack of eight pitot-static probes is placed at the vertical and horizontal center of a zone. With the carriage stationary, the 16 channel AD converter is used in conjunction with LabView to record pressure transducer analog output voltages. Data is sampled for 30 seconds at a rate of 100 Hz at each fan controller master dial setting

ranging from zero to the maximum of 1000 then back down to zero with finer increments near 1000 due to the observed non-linear relationship. This process is repeated for each of the four zones. When data from each zone is averaged a rough relationship between velocity and master dial setting is found and thus dial settings for wind conditions are chosen.

Free-stream air velocity distribution surveys begin once dial settings are chosen for each wind condition. An initial round of surveys is performed to determine if the spatial variation $\sigma_{\bar{U}_W}$ of the velocity distribution given in (2.31) warrants the adjustment of individual fans or installation or removal of flow altering screens. This round of surveys also serves to identify any changes in the velocity distribution between surveys taken with the wind carriage stationary ($Fr$ = 0) and the wind carriage moving ($Fr$ = 0.2). During this round of surveys hardware is added allowing the capability to survey at $x$ = 0 which coincides with the FP of the model and $x$ = -0.33 which coincides with the wind carriage outlet exit plane. Surveying the free-stream air velocity distribution at the three planes is needed to observe how the air stream evolves as it exits the wind carriage and approaches the model. This investigation also provides insight needed for modeling the air-inlet boundary condition in the complementary CFD computations. A second and final round of surveys is performed once flow adjustments are made.

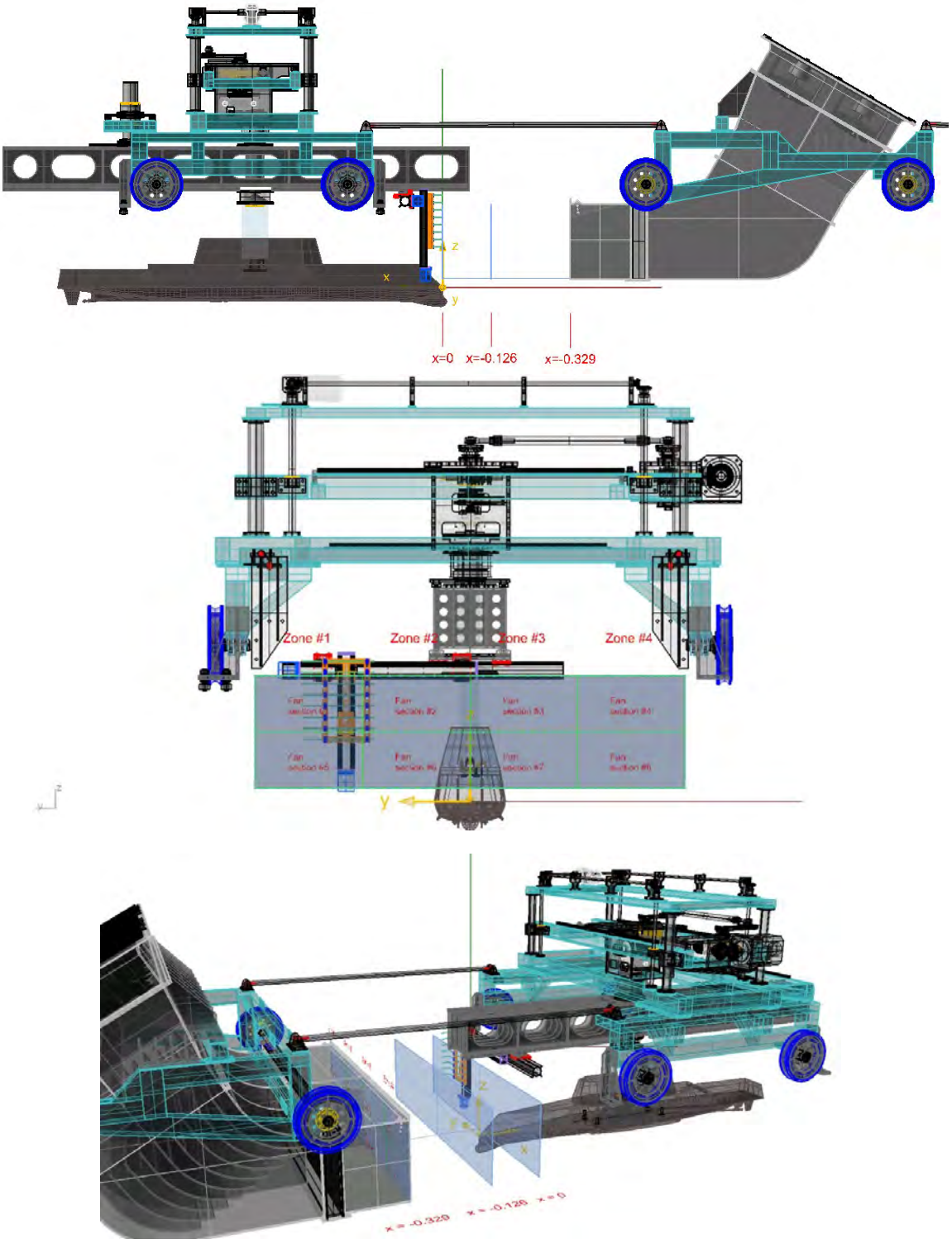


Figure 2-13 Side elevation (top), end view (middle), and perspective (bottom) of carriages, pitot rack, and measurement grid planes. Model and mount are not installed during surveys; just shown for reference. Wind carriage outlet is located at $x$ = -0.33.

(a)

(b)

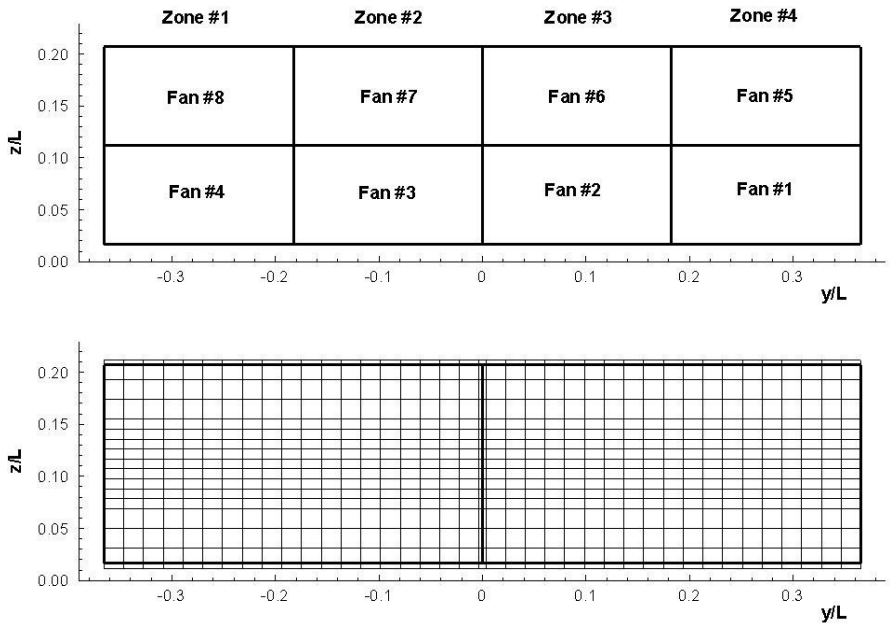


Figure 2-14 Scehmatic of wind carriage outlet showing (a) fan contribution sections of outlet and (b) measurement grid for surveys with the thick black lines representing outlet walls. Positive $x$-direction is out of the page. Fans spin clockwise.

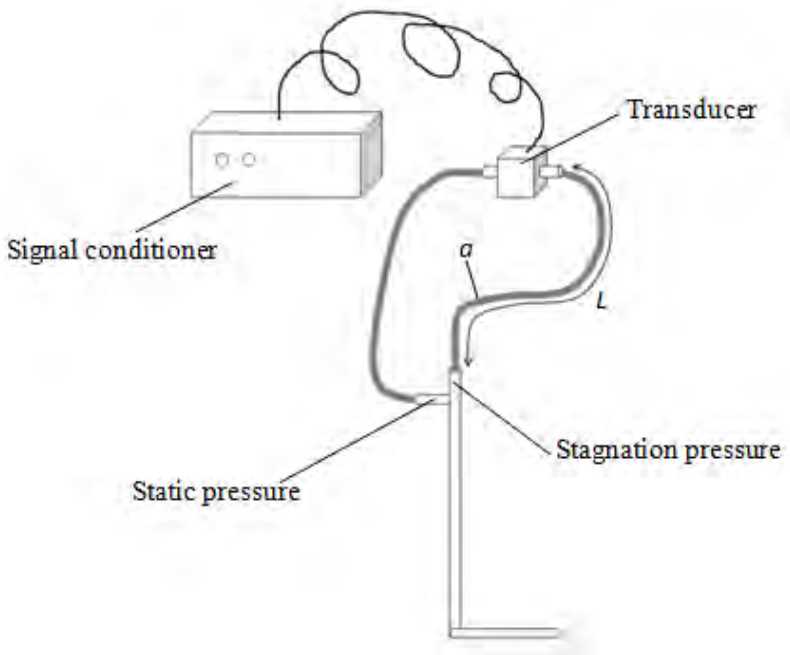


Figure 2-15 Schematic of pitot probe, pressure transducer, and signal conditioner.

### 2.4.2 Straight Ahead and PMM Tests

A 16 channel AD converter is used to read analog voltages from all measurement devices. The first six channels read the output of the Izumi six-component strain-gage type load cell with a 6 channel Izumi amplifier and signal conditioner unit. The maximum ranges for forces and moments are 500 N for $F_x$, $F_y$, and $F_z$ and 50 N-m, 50 N-m, and 200 N-m for $M_x$, $M_y$, and $M_z$, respectively. Forces and moments not used in data reduction are measured to monitor the operation of the load cell. The load cell combination amplifiers and signal conditioners are periodically calibrated using an internal calibration function. The load cell itself is factory calibrated.

The next six channels of the AD converter are used to read motions data $U_C$, $y$, $z$, $\phi$, $\theta$, and $\psi$. The drive carriage's speed circuit uses a wheel mounted encoder to measure and report $U_C$ as a 1:1 output voltage. The details of $U_C$ measurement are presented in Longo and Stern, (2005). $y$, $z$, $\phi$, $\theta$, and $\psi$ are measured using rotary potentiometers and a separate Izumi 6 channel amplifier and signal conditioner unit. The cable driven potentiometers measuring sway motion $y$ and yaw motion $\psi$ are built into the PMM carriage and are calibrated using physical scales affixed to the sway and yaw mechanisms. Sway motion is calibrated over the maximum range of ± 500 mm. Yaw motion is calibrated by measuring the displacement of the strongback's rear support slide at a known distance from the yaw axis to determine yaw displacement through the range of ± 28°. As previously stated, yaw motion does not receive a zero point correction during data reduction therefore ensuring $\psi$ contains no offset voltage at $\beta = 0$ is necessary by making appropriate adjustments to the potentiometer pulley drive cable. The potentiometers for pitch $\theta$, heave $z$, and roll $\phi$ are built into the 3DOF mount which is shown in Fig. 2-16. The heave potentiometer is cable driven and is bench calibrated using a Velmex traverse to provide known linear displacements. The pitch and roll potentiometers are affixed to the gimbal assembly and are gear driven. The drive gears consist of a spring loaded opposing double toothed design used to eliminate gear

backlash, which is necessary for measuring very small angles at their centers of rotation. Pitch and roll potentiometers are bench calibrated using a digital precision angle finder with resolution 0.05°. As previously stated, for yaw and drift tests the superimposed drift angle $\beta$ is not recorded by the DA. A rotary scale on the strong back and yaw platter interface with 1° resolution is used with the scale affixed to the strongback rear support slide offering further precision.

The remaining four channels of the 16 channel AD converter are used to monitor wind velocity at four of the grid points established in the free-stream air velocity distribution surveys. During straight ahead tests the 2D traverse system and pitot probe rack are left in place for convenience and wind velocity is measured using 4 of the pitot probes positioned at grid points on the FP plane circled in blue in Fig. 2-17. The 2D traverse system is removed for static and dynamic PMM tests due to interference with the ship and the wake of the pitot probe rack. The pitot probes are repositioned at spread out locations at the wind carriage outlet plane at grid points circled in red in Fig. 2-17.

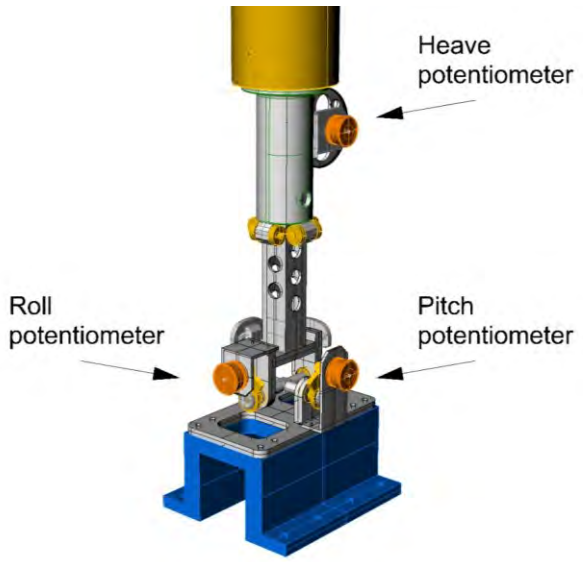


Figure 2-16 Schematic of heave staff and gimbal assembly showing rotary potentiometers for pitch, heave, and roll measurement.

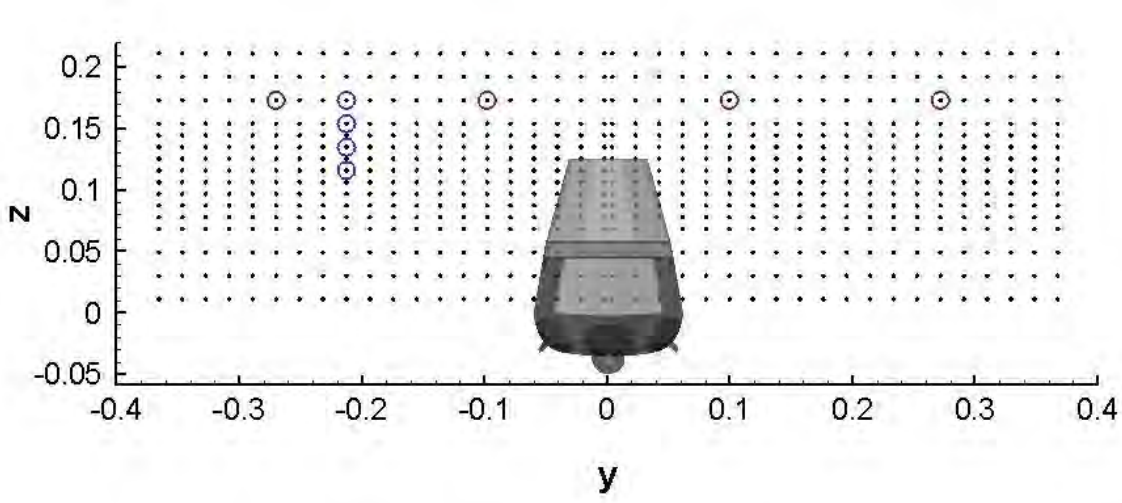


Figure 2-17 Wind speed monitored at grid points circled in blue for straight ahead tests and at grid points circled in red for static and dynamic PMM tests.

## 2.5 Data Acquisition

### 2.5.1 Free-stream Air Velocity Distribution

Procedures for performing free-stream axial velocity distribution surveys with stationary carriage are as follows. The rack of pitot probes is placed at the starting position of a zone. With the wind carriage fans turned off a zero point voltage acquisition is performed for 30 seconds at 100 Hz. The wind carriage fans are then turned on using the master dial according to the wind condition desired. Once data acquisition is begun, LabView uses an input file containing prescribed traverse movements necessary to cover the grid points in the zone. The rack of pitot probes samples for 30 seconds at 100 Hz covering eight grid points. LabView then automatically signals the traverses to position the rack of pitot probes over the next eight grid points in the zone. After two seconds of settling time the rack samples at these grid points for 30 seconds. This process is repeated until all of the grid points in the zone have been sampled. The wind carriage fans are then turned off. When air flow ceases

another zero point voltage acquisition is performed for 30 seconds. An average of the two zero point voltages is subtracted from run point voltages in data reduction to compensate for any drift experienced by transducer voltage outputs. Using the sway movement of the strongback in conjunction with the horizontal traverse allows for the entire wind carriage outlet to be surveyed. Manual reconfiguration of the traverse system and re-alignment is required between sampling each zone. During the first round of surveys, stationary carriage surveys are performed at $x$ = 0, -0.13, and -0.33 $x$-planes for full wind condition and only $x$ = -0.13 for half wind condition. When performing surveys with moving carriage only two rack positions can be sampled per carriage run due to the limited length of the towing tank. All moving carriage surveys are performed at $Fr$ = 0.2. This speed is slow enough to allow for traverse movements and 10 second sampling times for each rack position. A slower carriage speed would be less representative of the intended $Fr$ range of testing and a faster speed would cut sampling times too short. Moving carriage surveys are performed only at $x$ = -0.13 for full wind condition and half wind condition. No moving carriage surveys are performed for second round of surveys.

### 2.5.2 Straight Ahead and Static PMM Tests

Zero-point voltages from all 16 channels of data are sampled for 15 seconds at a sampling rate of 100 Hz prior to each carriage run. Water and air temperature, barometric pressure, and humidity, are noted. If performing a case with wind the wind carriage fans are then powered to produce the desired wind condition. Once the fans reach a steady speed the carriage is accelerated monotonically to the target $U_C$ value. Acceleration occurs before any free surface disturbances due to the wind can reach upstream into the model's future path. Once steady carriage speed is reached the DA is signaled to begin recording the run-point voltages of measured variables at 100 Hz with LabView. The sampling time depends on carriage speed with care taken to ensure the

full length of the towing tank is utilized for optimal convergence. The carriages are returned to the home position for the next measurement with 15 minute intervals between tests to ensure a calm free surface. If performing static drift tests $\beta$ may be changed at this time.

### 2.5.3 Dynamic PMM Test

Data acquisition for dynamic PMM test is the same as static tests with the exception of adding the PMM motions. The PMM frequency is specified in the user interface of the PMM control software on a dedicated PC. Ramp up time is specified to be 10 seconds. Sway and yaw amplitude are physically set on the scotch-yoke mechanism of the PMM carriage. The sway position is centered at $y = 0$ before every zero-point acquisition. If performing pure yaw tests the model is set at its yaw amplitude at this time. Superimposed $\beta$ is set as well if performing yaw and drift tests. The wind carriage fans and PMM motions are started so that they both reach steady state at about the same time. Once this occurs the carriage is accelerated to the target $U_C$ value. For cases with large PMM amplitudes the carriage must be accelerated slightly earlier to prevent large sway and yaw amplitudes from creating too much agitation and violent model reactions. Once carriage speed is steady the DA is triggered to record data.

## 2.6 Statistical Convergence and Uncertainty Analysis

Fast Fourier Transforms (FFT) of all data are performed and presented with time histories as a means of identifying peak frequencies due to noise or motions. A separate set of tests is performed to identify peak frequencies in forces and moment data due to excitation of the load cell and 3DOF mount natural frequencies from noise of carriage vibrations and PMM induced vibrations. The model is not installed and only the 3DOF mount is attached to the load cell. It is possible to measure the effect of model natural frequencies if the model remains installed but is tested with the water absent. Performing this test with the model in air, however, is not possible due to the fragile construction of

the 3DOF mount. Test conditions are shown in Table 2-7. Group A focuses on effects of the PMM drive servo motor. The carriage is stationary with sway and yaw amplitudes set to zero while data is acquired with the PMM motor operating at one of three of the frequencies represented in dynamic test conditions. Sway and yaw motions are added in Group B to observe the effect of imparting sinusoidal motion to the load cell and mount. The three amplitudes listed correspond to the three PMM frequencies tested, respectively. Carriage speed is added in Group C to observe the effect of the carriage moving at the three corresponding carriage speeds. Each condition is repeated twice. Fig. 2-18 shows the results of each test. Generally, peak frequencies are shared between $F_x$, $F_y$, and $M_z$. The lower frequencies due to the actual motions seen in groups B and C are clearly separate from the high frequency noise of the PMM motor see in group A. The high frequency energy is boosted when carriage speed is added as seen in group C.

Stationarity tests are performed on all straight ahead time history data as a means of analyzing statistical convergence of static tests. Bendat (1966) presents two non-parametric statistical procedures known as 'Run test' and Trend tests.' Yoon (2009) presents methodology for applying them both to static and dynamic PMM tests which is used herein. Both stationarity tests withhold four important assumptions that are summarized by Yoon (2009):

> 1) If the data of interest are stationary, then the statistical properties computed for each sequence of short time intervals will not vary significantly from on time interval to the next; 2) Verification of weak stationarity (time invariance of the mean and autocorrelation function) will be acceptable; 3) The sample record of data to be investigated is very long compared to the random fluctuations of the data time history; 4) If the mean square value (or variance) of the data of interest is stationary, then the autocorrelation function for the data is also stationary.

For both stationarity tests the time histories are divided into $N = 20$ equal time intervals with the interval size depending on the sampling time. A mean value ($\bar{x}_1$, $\bar{x}_2$, $\bar{x}_3$, … , $\bar{x}_N$) and variance ($\overline{x_1^2}$, $\overline{x_2^2}$, $\overline{x_3^2}$, … , $\overline{x_N^2}$) for each interval are then computed. The 'Run test' is more effective for detecting fluctuating trends and does so by counting the

number of times each interval's mean and variance change sign about the global mean and variance. The number of occurrences is denoted as $r$. If $r$ falls outside the acceptance region[1] of $6 \leq r \leq 15$ at the 5% level of significance then the hypothesis of stationarity is rejected. The 'Trend test' is more effective for detecting monotonic trends and does so by counting the number of times each interval's mean and variance is less than all other previous intervals' mean and variance. The number of occurrences is denoted as $A$. If $A$ falls outside the acceptance region of $64 \leq A \leq 125$ at the 5% level of significance then the hypothesis of stationarity is rejected. Tables of $r$ and $A$ for measured data are presented in Chapter 4.

Due to time constrains of the present study uncertainty analysis (UA) is postponed as future work. Instead, standard deviations of repeat tests are analyzed and presented as percentages and displayed as error bars in graphical figures. Observed asymmetry about the $xz$-plane for static PMM tests is quantified as the difference

$$D_{asym} = \frac{100}{\mathrm{r}_m}|\mathrm{r} - \mathrm{r}_m| \tag{2.51}$$

where r is the measured data and $\mathrm{r}_m$ is the mean data value between positive and negative $\beta$. In traditional uncertainty analysis $D_{asym}$ is included in the conceptual bias which is not included in the total bias limit of the total uncertainty because it is not considered part of the measurement error. Rather, it is a measured and observed real effect due to anomalies in geometry and/or flow conditions.

Table 2-7 Noise Test Conditions.

| Group | $U_C$ (m/s) | $y_{max}$ (mm) | $\psi_{max}$ (°) | $f_e$ (Hz) |
|---|---|---|---|---|
| A | 0 | 0 | 0 | 0.109, 0.14, 0.228 |
| B | 0 | 253, 340, 228 | 8.9, 10.3, 8.4 | 0.109, 0.14, 0.228 |
| C | 1.111, 1.667, 2.222 | 253, 340, 228 | 8.9, 10.3, 8.4 | 0.109, 0.14, 0.228 |

[1] The acceptance region is obtained from statistics tables (e.g. Bendat 1966, pp. 170 – 171)

Group A: No model, $U_C = 0$, $y_{max} = 0$, $\psi_{max} = 0$

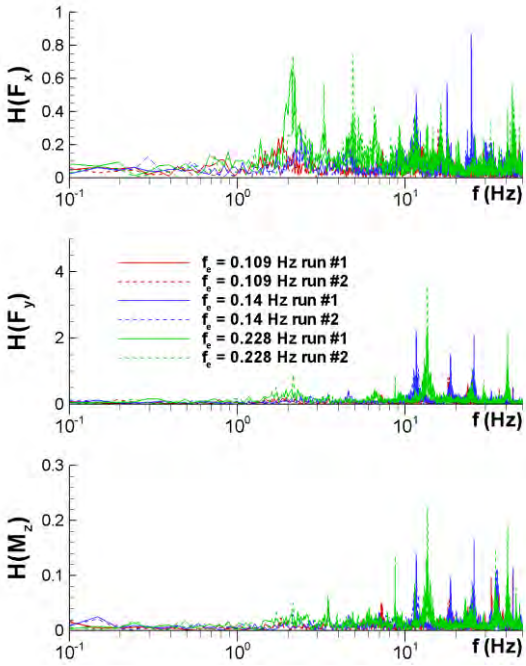


Group B: No model, $U_C = 0$, $y_{max} \neq 0$, $\psi_{max} \neq 0$

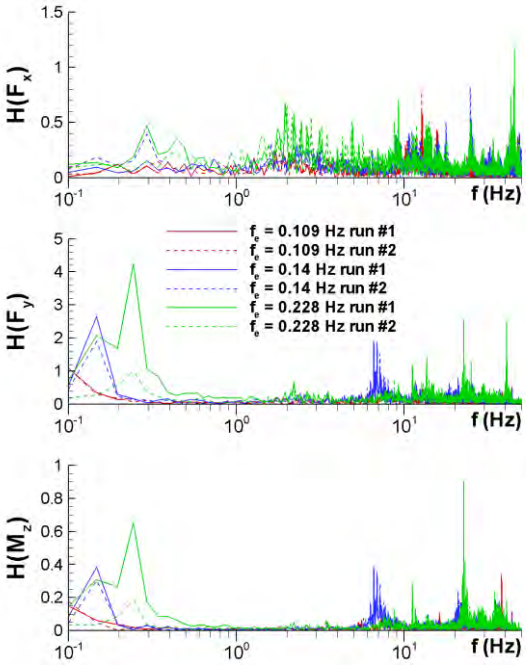


Group C: No model, $U_C \neq 0$, $y_{max} \neq 0$, $\psi_{max} \neq 0$

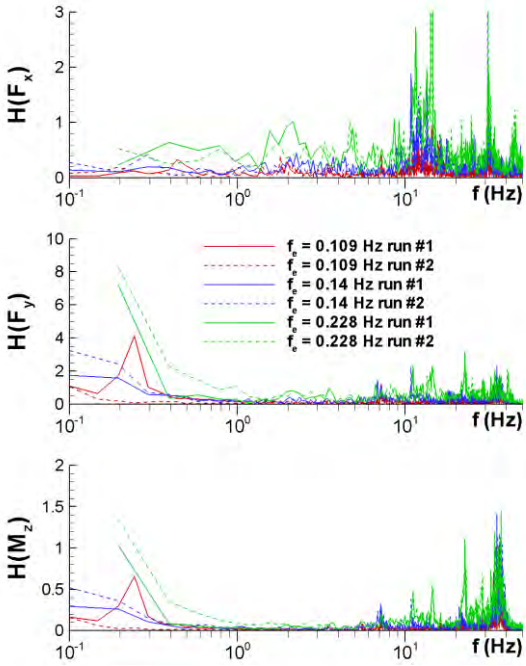


Figure 2-18 Noise test results: FFT for $F_x$, $F_y$, and $M_z$. Groups A shows noise sources from PMM motor, group B shows added noise sources due to motions, and group C shows added noise sources from mechanical vibrations due to carriage speed.

# CHAPTER 3. FREE-STREAM AIR VELOCITY DISTRIBUTION

The relationship of air axial velocity (2.29) and variation (2.31) vs. fan controller master dial setting is shown for each zone in Fig. 3-1 (a). This relationship is used to determine a rough master dial setting for the half wind case. Data is obtained by positioning the rack of pitot probes vertically at the center of each zone and sampling velocity and is not part of the surveys. The master output voltage of the fan controller is also noted at each master dial setting. Air velocity can be seen plotted vs. fan controller master output voltage in Fig. 3-1 (b). This relationship appears to be linear for most of the dial setting range. For the initial round of surveys the dial setting for the half wind condition is chosen to be 925 whereas the master dial setting for the full wind condition is 1000.

Reduced data from (2.29), (2.30), (2.31), and (2.32) are summarized in Table 3-1 for initial round of surveys. Velocity contours are displayed as percentage of the global mean $(\overline{U}_{W_i} - \mu_{\overline{U}_W})/\mu_{\overline{U}_W}$ (%) and turbulence contours are displayed as a percentage of the global mean $RMS_i/\mu_{\overline{U}_W}$ (%) in Fig. 3-2 and Fig. 3-3, respectively. All velocity is reported relative to the carriage mounted pitot probes and thus relative to the ship model. Data obtained from the grid points on the outer edge of the grid as well as points in the second row from the top are omitted from statistical calculations. These locations correspond to areas where high turbulence exists due to interaction with boundaries and mimics jet flow. It is assumed that the model is far enough away from these locations that this turbulence effect can be neglected and any data from these grid points would skew the statistical data used to describe wind imparted onto the model. The high turbulence can be seen as large $RMS$ values on the outer edge of the measurement domain in Fig. 3-3. The large $RMS$ at these locations can also be seen in the velocity time histories from pitot probes #1 and #2 shown in Fig. 3-4. Survey 9 taken at $x$ = -0.33 (directly aft of wind carriage outlet) lacks high turbulence on most of the outer edge

because the tips of the pitot probes are nearly touching the face of the wind carriage outlet or are outside the direct air stream at these locations. This effect can also be seen in Fig. 3-2 as strips of near zero velocity on the top and bottom of the measurement domain.

All surveys from the initial round display inconsistent average velocities $\sigma_{\bar{U}_W}$ between zones which is the first indication that individual fan adjustments are needed to improve uniformity between zones. For all of these surveys the average $RMS$ values from (2.30) are just under 5% of mean flow velocity. Acceptable $RMS$ values for typical wind tunnels vary around 0.1%. Variation $\sigma_{\bar{U}_W}$ is also quite large around 10%. These large discrepancies are likely due to the fact that the wind carriage design is quite far from even a standard open-circuit wind tunnel design. The practical limitations of the towing tank and carriage system require a compact and mobile construction which forces the designer to omit important design features associated with open-circuit wind tunnels. Typical wind tunnels are lengthy and posses carefully tuned geometries that are designed to minimize or control boundary layer effects, unsteadiness, and turbulence. For instance, honeycomb structures and screens are generally placed before the contraction to decrease incoming lateral velocity fluctuations. The contraction then increases velocity while stretching out longitudinal vortex lines. This stretching effectively reduces axial velocity fluctuations and decreases any small scale turbulence caused by honeycombs or screens. The wind carriage, however, has honeycombs and a screen placed just upstream of the outlet. The contraction co-functions as an elbow (containing vanes) placed immediately downstream of the eight fans and *before* the honeycombs. With the axial fans generating large amounts of turbulence just upstream of the contraction, the air stream has little means of dissipating turbulent energy. The non-ideal wind carriage construction may also explain the peaks in local velocity seen in Fig. 3-2.

Surveys listed in Table 3-1 are numbered by the order in which they are taken. Surveys #1 through #3 serve as test and tune efforts and are not listed due to erroneous

data. Surveys #4 and #6 are performed to determine the difference in velocity distribution caused by the carriage moving at speed ($Fr$ = 0.2) vs. stationary for the full wind condition. Surveys #5 and #7 serve the same purpose but for the half wind condition. Global relative wind velocity $\mu_{\bar{U}_W}$ is 0.4% lower with the carriage moving for the full wind condition and 0.3% higher with the carriage moving for the half wind condition. From this it can be concluded that the change in relative wind velocity $\mu_{\bar{U}_W}$ due to carriage speed is due to scatter and the amount is negligible. Surveys #9, #6, and #8 describe how the air stream evolves at it approaches the ship at locations $x$ = -0.33, -0.13, and 0, respectively. Velocity tends to decrease away from the carriage outlet while turbulence increases. The increased turbulent mixing decreases variation $\sigma_{\bar{U}_W}$ which is expected.

The initial round of surveys reveals that adjustments to the screens and individual fans are needed in order to lower the variation and thus obtain more flow uniformity. The velocity contour of survey #8 in Fig. 3-2 shows the areas circled in red that need adjustment. Fan #5 is turned down to decrease the velocity in the region circled at the upper right. Screen sections are removed along the long horizontal region of low velocity circled along the bottom third of the outlet. A new master dial setting of 904 is chosen for the half wind condition in attempt to make the half wind condition's velocity closer to half the velocity of the full wind condition. Surveys #14, #15, #17, and #18 serve to re-characterize the flow after alterations are made. Having concluded that carriage speed does not cause noticeable changes in relative wind velocity, moving surveys are not re-taken. Results are shown in Table 3-2. Velocity contours, $RMS$ contours, and pitot probe velocity time histories are shown in Figures 3-5, 3-6, and 3-7, respectively. Although global velocity decreases slightly, variation has been decreased significantly to approximately 6-7% at the FP plane while turbulence remains relatively unchanged at approximately 4.5%. Global relative wind velocities $\sigma_{\bar{U}_W}$ for the half wind and full wind condition at the FP plane $x$ = 0 are used to define the nominal wind speed values for the

experiment. The half and full wind conditions are defined to have relative velocities 4.786 and 9.380 m/s, respectively. Dimensional and non-dimensional wind speeds relative to the ship and relative to Earth are listed in Table 3-3 for full wind tests and Table 3-4 for half wind tests at every tested $Fr$ value. Full scale wind speeds at $Fr$ = 0.2 correspond to Beaufort numbers 10 and 12 for half wind and full wind, respectively, with full wind simulating strong hurricane scale wind speeds. Note that wind speed is scaled in referenced to ship speed. Reynolds scaling is disregarded due to inherent arbitrary levels of turbulence in the generated air stream as well as in a real ship environment. It is important to note that non-dimensional wind speed relative to Earth $\left(\mu_{\bar{U}_W} - U_C\right)/U_C$ is the quantity that the CFDShip-Iowa V4.5 uses to specify wind speed.

Table 3-1 Summary of wind carriage surveys taken before fan and screen adjustments.

| Survey No. | Wind speed setting | Quantity | $x$ | Zone 1 | Zone 2 | Zone 3 | Zone 4 | Global |
|---|---|---|---|---|---|---|---|---|
| 9 | Full ($Fr = 0$) | $\mu_{\bar{U}_W}$ (m/s) | -0.33 | 9.954 | 9.657 | 9.552 | 10.323 | 9.858 |
| | | $\mu_{RMS}$ (m/s) | | 0.367 | 0.409 | 0.379 | 0.364 | 0.381 |
| | | $\mu_{RMS}/\mu_{\bar{U}_W}$ | | 3.7% | 4.2% | 4.0% | 3.5% | 3.9% |
| | | $\sigma_{\bar{U}_W}$ | | ***9.3%*** | ***13.2%*** | ***12.5%*** | ***10.7%*** | ***11.9%*** |
| | | $\sigma_{RMS}$ | | ***1.0%*** | ***1.2%*** | ***1.3%*** | ***0.8%*** | ***1.1%*** |
| 6 | Full ($Fr = 0$) | $\mu_{\bar{U}_W}$ (m/s) | -0.13 | 9.375 | 9.208 | 9.139 | 9.858 | 9.383 |
| | | $\mu_{RMS}$ (m/s) | | 0.393 | 0.363 | 0.375 | 0.405 | 0.383 |
| | | $\mu_{RMS}/\mu_{\bar{U}_W}$ | | 4.2% | 3.9% | 4.1% | 4.1% | 4.1% |
| | | $\sigma_{\bar{U}_W}$ | | ***10.4%*** | ***9.9%*** | ***8.8%*** | ***10.2%*** | ***10.3%*** |
| | | $\sigma_{RMS}$ | | ***1.2%*** | ***0.7%*** | ***0.8%*** | ***0.9%*** | ***0.9%*** |
| 8 | Full ($Fr = 0$) | $\mu_{\bar{U}_W}$ (m/s) | 0 | 9.341 | 9.274 | 9.171 | 9.844 | 9.398 |
| | | $\mu_{RMS}$ (m/s) | | 0.471 | 0.427 | 0.397 | 0.429 | 0.430 |
| | | $\mu_{RMS}/\mu_{\bar{U}_W}$ | | 5.0% | 4.6% | 4.3% | 4.4% | 4.6% |
| | | $\sigma_{\bar{U}_W}$ | | ***9.1%*** | ***9.2%*** | ***7.9%*** | ***10.5%*** | ***9.6%*** |
| | | $\sigma_{RMS}$ | | ***1.5%*** | ***1.2%*** | ***1.2%*** | ***1.1%*** | ***1.3%*** |
| 4 | Full ($Fr = 0.2$) | $\mu_{\bar{U}_W}$ (m/s) | -0.13 | 9.383 | 9.113 | 9.093 | 9.831 | 9.342 |
| | | $\mu_{RMS}$ (m/s) | | 0.439 | 0.435 | 0.421 | 0.457 | 0.437 |
| | | $\mu_{RMS}/\mu_{\bar{U}_W}$ | | 4.7% | 4.8% | 4.6% | 4.6% | 4.7% |
| | | $\sigma_{\bar{U}_W}$ | | ***8.9%*** | ***9.2%*** | ***9.3%*** | ***10.0%*** | ***9.9%*** |
| | | $\sigma_{RMS}$ | | ***1.3%*** | ***1.0%*** | ***1.0%*** | ***1.0%*** | ***1.1%*** |
| 7 | Half ($Fr = 0$) | $\mu_{\bar{U}_W}$ (m/s) | -0.13 | 5.396 | 5.280 | 5.233 | 5.766 | 5.410 |
| | | $\mu_{RMS}$ (m/s) | | 0.244 | 0.212 | 0.224 | 0.256 | 0.233 |
| | | $\mu_{RMS}/\mu_{\bar{U}_W}$ | | 4.5% | 4.0% | 4.3% | 4.4% | 4.3% |
| | | $\sigma_{\bar{U}_W}$ | | ***10.4%*** | ***10.0%*** | ***9.8%*** | ***9.5%*** | ***10.6%*** |
| | | $\sigma_{RMS}$ | | ***1.4%*** | ***0.8%*** | ***0.7%*** | ***1.0%*** | ***1.1%*** |
| 5 | Half ($Fr = 0.2$) | $\mu_{\bar{U}_W}$ (m/s) | -0.13 | 5.429 | 5.322 | 5.211 | 5.769 | 5.424 |
| | | $\mu_{RMS}$ (m/s) | | 0.243 | 0.233 | 0.239 | 0.274 | 0.247 |
| | | $\mu_{RMS}/\mu_{\bar{U}_W}$ | | 4.5% | 4.4% | 4.6% | 4.7% | 4.6% |
| | | $\sigma_{\bar{U}_W}$ | | ***9.2%*** | ***9.4%*** | ***9.4%*** | ***10.3%*** | ***10.3%*** |
| | | $\sigma_{RMS}$ | | ***1.2%*** | ***0.9%*** | ***0.9%*** | ***1.1%*** | ***1.1%*** |

Note: Outside edge and 2nd row from top grid points omitted from statistical calculations.

Table 3-2 Summary of wind carriage surveys taken after fan and screen adjustments.

| Survey No. | Wind speed setting | Quantity | *x* | Zone 1 | Zone 2 | Zone 3 | Zone 4 | Global |
|---|---|---|---|---|---|---|---|---|
| 17 | Full ($Fr = 0$) | $\mu_{\bar{U}_W}$ (m/s) | -0.33 | 9.830 | 9.554 | 9.675 | 9.797 | 9.706 |
| | | $\mu_{RMS}$ (m/s) | | 0.384 | 0.405 | 0.387 | 0.347 | 0.382 |
| | | $\mu_{RMS}/\mu_{\bar{U}_W}$ | | 3.9% | 4.2% | 4.0% | 3.5% | 3.9% |
| | | $\sigma_{\bar{U}_W}$ | | ***8.9%*** | ***12.9%*** | ***11.2%*** | ***9.4%*** | ***10.8%*** |
| | | $\sigma_{RMS}$ | | ***1.1%*** | ***1.1%*** | ***1.3%*** | ***0.7%*** | ***1.1%*** |
| 15 | Full ($Fr = 0$) | $\mu_{\bar{U}_W}$ (m/s) | -0.13 | 9.408 | 9.127 | 9.203 | 9.371 | 9.271 |
| | | $\mu_{RMS}$ (m/s) | | 0.415 | 0.384 | 0.367 | 0.372 | 0.384 |
| | | $\mu_{RMS}/\mu_{\bar{U}_W}$ | | 4.4% | 4.2% | 4.0% | 4.0% | 4.1% |
| | | $\sigma_{\bar{U}_W}$ | | ***7.4%*** | ***8.0%*** | ***6.9%*** | ***7.2%*** | ***7.4%*** |
| | | $\sigma_{RMS}$ | | ***1.0%*** | ***0.7%*** | ***0.7%*** | ***0.8%*** | ***0.8%*** |
| 14 | Full ($Fr = 0$) | $\mu_{\bar{U}_W}$ (m/s) | 0 | 9.476 | 9.342 | 9.308 | 9.406 | 9.380 |
| | | $\mu_{RMS}$ (m/s) | | 0.465 | 0.411 | 0.389 | 0.408 | 0.417 |
| | | $\mu_{RMS}/\mu_{\bar{U}_W}$ | | 4.9% | 4.4% | 4.2% | 4.3% | 4.4% |
| | | $\sigma_{\bar{U}_W}$ | | ***6.7%*** | ***7.1%*** | ***5.9%*** | ***7.1%*** | ***6.7%*** |
| | | $\sigma_{RMS}$ | | ***1.6%*** | ***0.9%*** | ***1.2%*** | ***1.1%*** | ***1.3%*** |
| 18 | Half ($Fr = 0$) | $\mu_{\bar{U}_W}$ (m/s) | 0 | 4.831 | 4.695 | 4.745 | 4.887 | 4.786 |
| | | $\mu_{RMS}$ (m/s) | | 0.243 | 0.229 | 0.219 | 0.234 | 0.231 |
| | | $\mu_{RMS}/\mu_{\bar{U}_W}$ | | 5.0% | 4.9% | 4.6% | 4.8% | 4.8% |
| | | $\sigma_{\bar{U}_W}$ | | ***6.6%*** | ***7.4%*** | ***7.1%*** | ***7.5%*** | ***7.3%*** |
| | | $\sigma_{RMS}$ | | ***1.7%*** | ***1.4%*** | ***1.2%*** | ***1.1%*** | ***1.3%*** |

Note: Outside edge and 2nd row from top grid points omitted from statistical calculations.

Table 3-3 Relative and absolute wind speeds for full wind speed tests.

| *Fr* | Ship speed relative to Earth $U_C$ (m/s) | Wind speed relative to ship $\mu_{\bar{U}_W}$ (m/s) | Wind speed relative to Earth $\mu_{\bar{U}_W} - U_C$ (m/s) | $\frac{\mu_{\bar{U}_W}}{U_C}$ | $\frac{\mu_{\bar{U}_W} - U_C}{U_C}$ |
|---|---|---|---|---|---|
| 0.000 | 0.000 | 9.380 | 9.380 | - | - |
| 0.050 | 0.278 | 9.380 | 9.102 | 33.776 | 32.776 |
| 0.100 | 0.555 | 9.380 | 8.825 | 16.888 | 15.888 |
| 0.138 | 0.766 | 9.380 | 8.614 | 12.245 | 11.245 |
| 0.150 | 0.833 | 9.380 | 8.547 | 11.259 | 10.259 |
| 0.200 | 1.111 | 9.380 | 8.269 | 8.444 | 7.444 |
| 0.250 | 1.389 | 9.380 | 7.991 | 6.755 | 5.755 |
| 0.280 | 1.555 | 9.380 | 7.825 | 6.031 | 5.031 |
| 0.300 | 1.666 | 9.380 | 7.714 | 5.629 | 4.629 |
| 0.350 | 1.944 | 9.380 | 7.436 | 4.825 | 3.825 |
| 0.364 | 2.022 | 9.380 | 7.358 | 4.639 | 3.639 |
| 0.400 | 2.222 | 9.380 | 7.158 | 4.222 | 3.222 |
| 0.410 | 2.277 | 9.380 | 7.103 | 4.119 | 3.119 |

Table 3-4 Relative and absolute wind speeds for half wind speed tests.

| *Fr* | Ship speed relative to Earth $U_C$ (m/s) | Wind speed relative to ship $\mu_{\bar{U}_W}$ (m/s) | Wind speed relative to Earth $\mu_{\bar{U}_W} - U_C$ (m/s) | $\frac{\mu_{\bar{U}_W}}{U_C}$ | $\frac{\mu_{\bar{U}_W} - U_C}{U_C}$ |
|---|---|---|---|---|---|
| 0.000 | 0.000 | 4.786 | 4.786 | - | - |
| 0.050 | 0.278 | 4.786 | 4.508 | 17.233 | 16.233 |
| 0.100 | 0.555 | 4.786 | 4.231 | 8.617 | 7.617 |
| 0.138 | 0.766 | 4.786 | 4.020 | 6.248 | 5.248 |
| 0.150 | 0.833 | 4.786 | 3.953 | 5.744 | 4.744 |
| 0.200 | 1.111 | 4.786 | 3.675 | 4.308 | 3.308 |
| 0.250 | 1.389 | 4.786 | 3.397 | 3.447 | 2.447 |
| 0.280 | 1.555 | 4.786 | 3.231 | 3.077 | 2.077 |
| 0.300 | 1.666 | 4.786 | 3.120 | 2.872 | 1.872 |
| 0.350 | 1.944 | 4.786 | 2.842 | 2.462 | 1.462 |
| 0.364 | 2.022 | 4.786 | 2.764 | 2.367 | 1.367 |
| 0.400 | 2.222 | 4.786 | 2.564 | 2.154 | 1.154 |
| 0.410 | 2.277 | 4.786 | 2.509 | 2.102 | 1.102 |

(a)

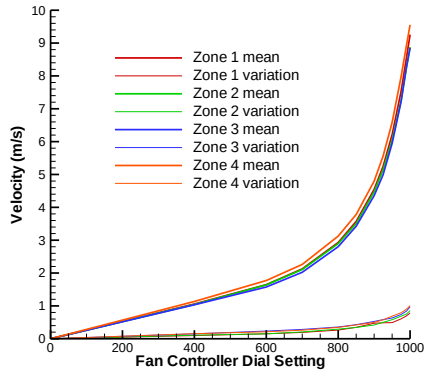


(b)

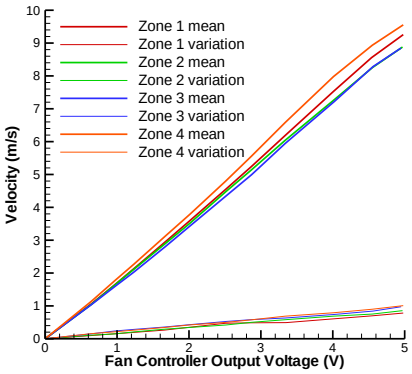


Figure 3-1 $\mu_{\bar{U}_W}$ and $\sigma_{\bar{U}_W}$ vs. (a) fan controller master dial setting and (b) fan controller master output voltage for four zones. $y$-coordinate rack positions are -0.289, -0.099, 0.099, 0.289 for zones 1, 2, 3, 4, respectively. The center of the pitot rack is $z = 0.11$.

---

Note: Data was taken before fan and screen adjustments.

Survey #9
$x$ = -0.33
Full wind speed
$Fr$ = 0

Survey #6
$x$ = -0.13
Full wind speed
$Fr$ = 0

Survey #8
$x$ = 0
Full wind speed
$Fr$ = 0

Survey #4
$x$ = -0.13
Full wind speed
$Fr$ = 0.2

Survey #7
$x$ = -0.13
Half wind speed
$Fr$ = 0

Survey #5
$x$ = -0.13
Half wind speed
$Fr$ = 0.2

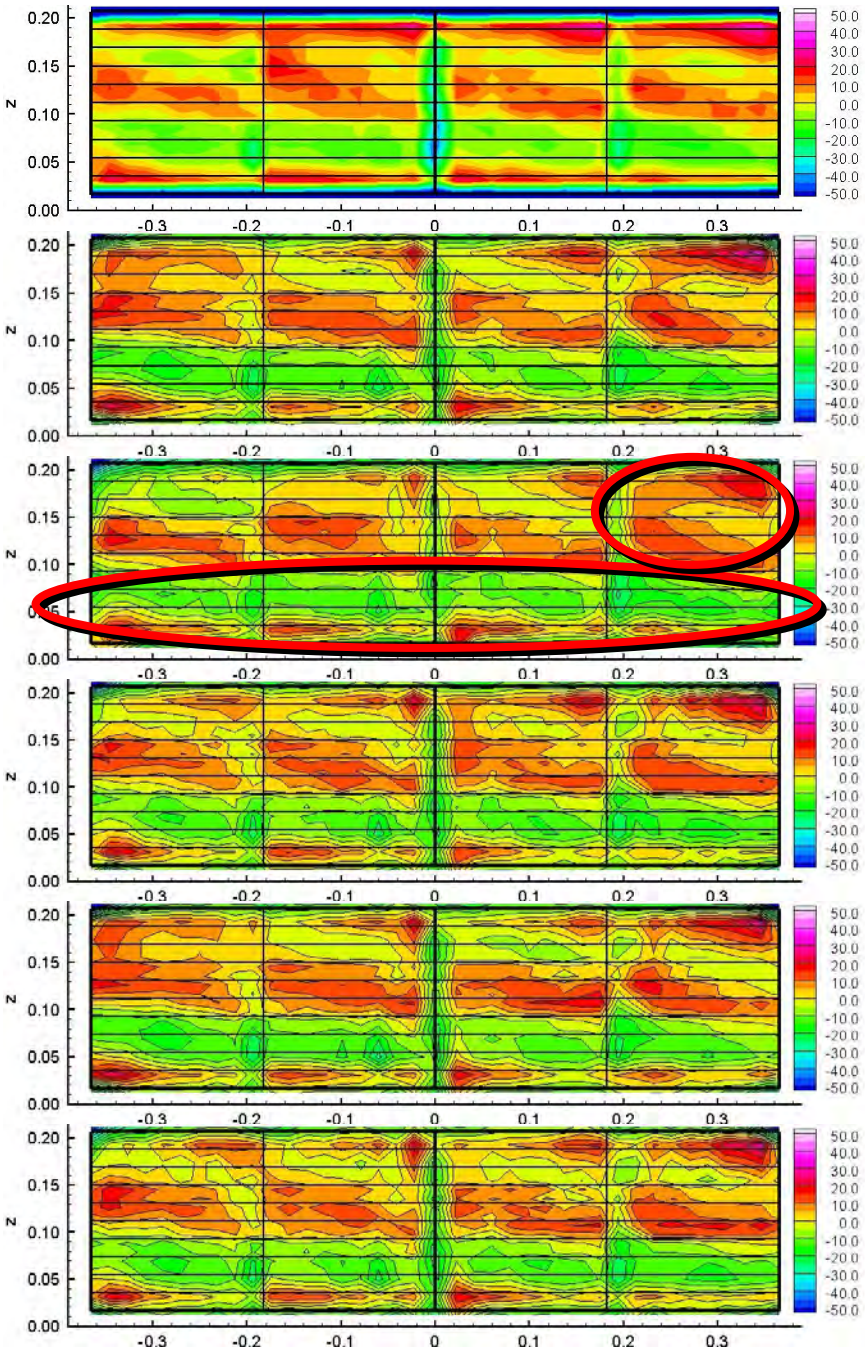


Figure 3-2 Axial velocity data expressed as $(\bar{U}_{W_i} - \mu_{\bar{U}_W})/\mu_{\bar{U}_W}$ (%) for surveys taken before fan and screen adjustments. Medium thick lines represent internal vane locations. Problem areas are circled in red.

Survey #9
$x$ = -0.33
Full wind speed
$Fr$ = 0

Survey #6
$x$ = -0.13
Full wind speed
$Fr$ = 0

Survey #8
$x$ = 0
Full wind speed
$Fr$ = 0

Survey #4
$x$ = -0.13
Full wind speed
$Fr$ = 0.2

Survey #7
$x$ = -0.13
Half wind speed
$Fr$ = 0

Survey #5
$x$ = -0.13
Half wind speed
$Fr$ = 0.2

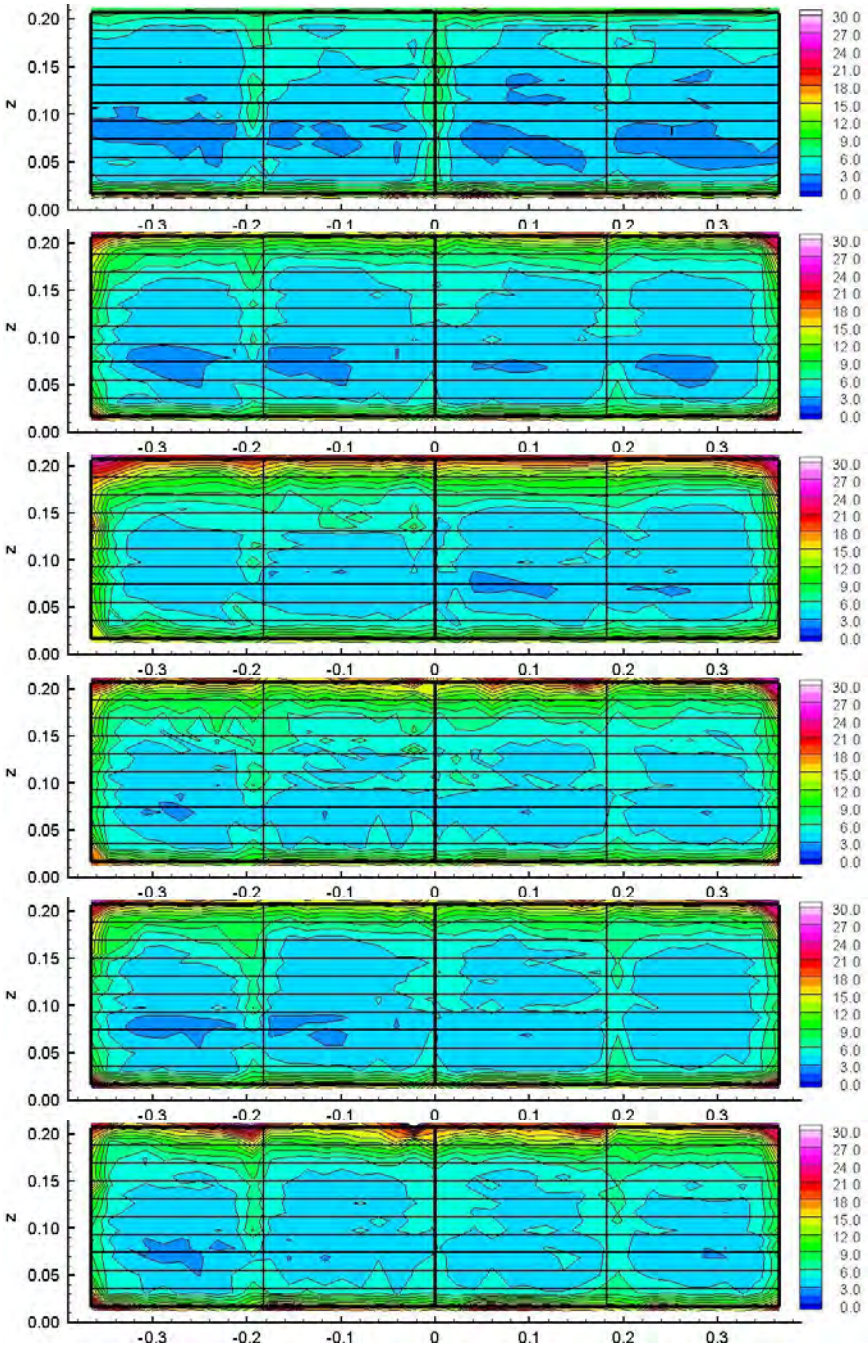


Figure 3-3 Axial velocity $RMS$ data expressed as $RMS_i/\mu_{\bar{U}_W}$ (%) for surveys taken before fan and screen adjustments. Medium thick lines represent internal vane locations.

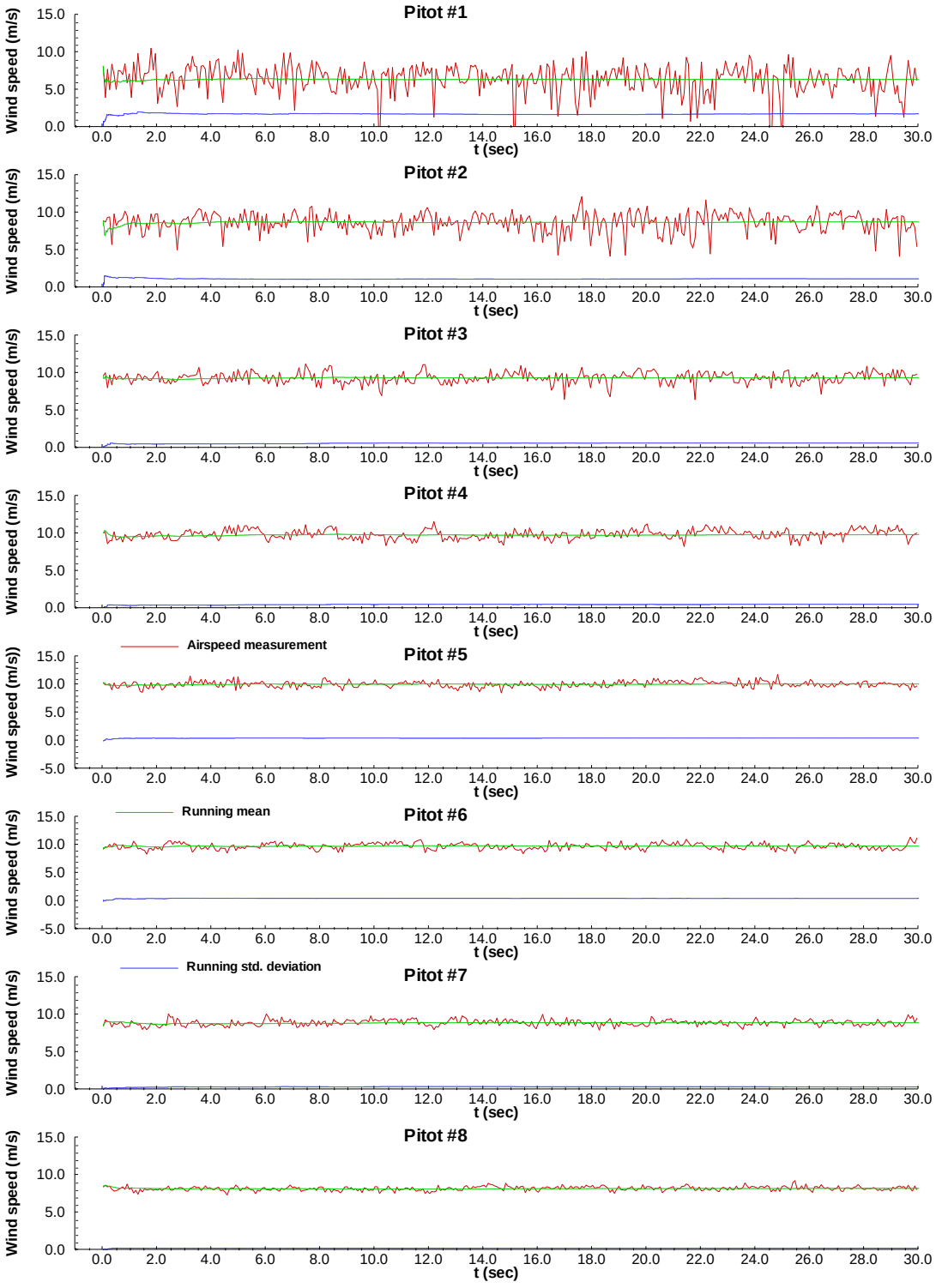


Figure 3-4 Wind measurement at one of 80 rack positions in the measurement grid at $x = 0$ for full speed wind setting and stationary carriage (survey #8) before fan and screen adjustments. Plot shows axial wind speed $U_W$, running mean, and running $RMS$ time histories.

Survey #17
$x$ = -0.33
Full wind speed
$Fr$ = 0

Survey #15
$x$ = -0.13
Full wind speed
$Fr$ = 0

Survey #14
$x$ = 0
Full wind speed
$Fr$ = 0

Survey #18
$x$ = 0
Half wind speed
$Fr$ = 0

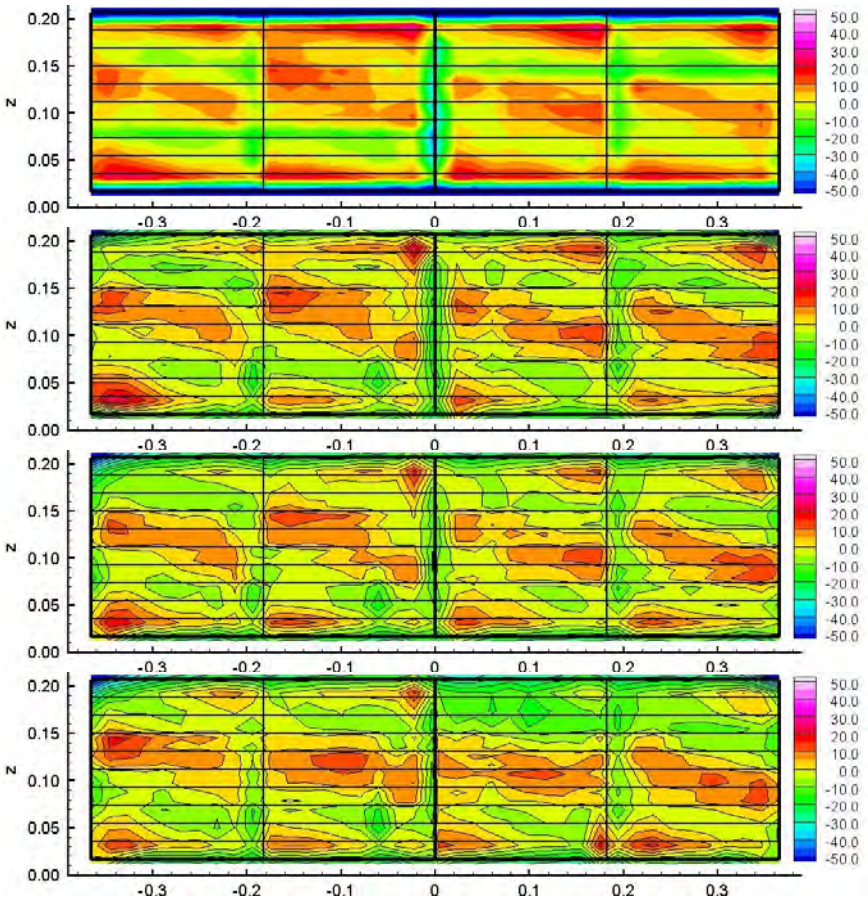


Figure 3-5 Axial velocity data expressed as $(\bar{U}_{W_i} - \mu_{\bar{U}_W})/\mu_{\bar{U}_W}$ (%) for surveys taken after fan and screen adjustments. Medium thick lines represent internal vane locations.

Survey #17
$x$ = -0.33
Full wind speed
$Fr$ = 0

Survey #15
$x$ = -0.13
Full wind speed
$Fr$ = 0

Survey #14
$x$ = 0
Full wind speed
$Fr$ = 0

Survey #18
$x$ = 0
Half wind speed
$Fr$ = 0

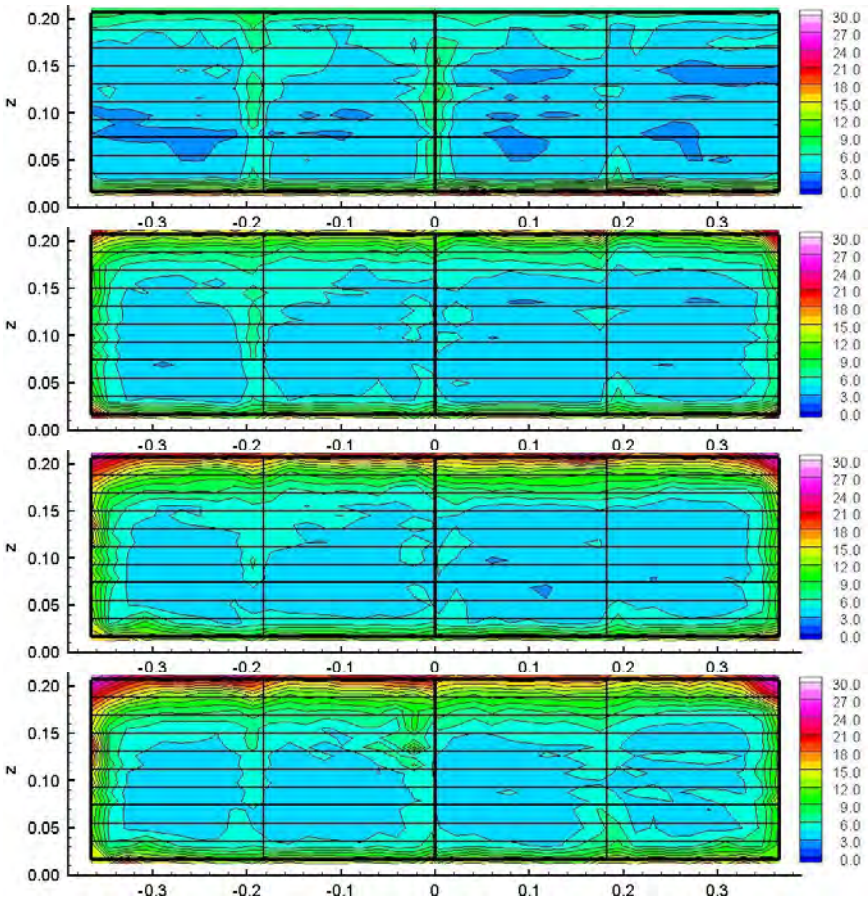


Figure 3-6 Axial velocity $RMS$ data expressed as $RMS_i/\mu_{\bar{U}_W}$ (%) for surveys taken after fan and screen adjustments. Medium thick lines represent internal vane locations.

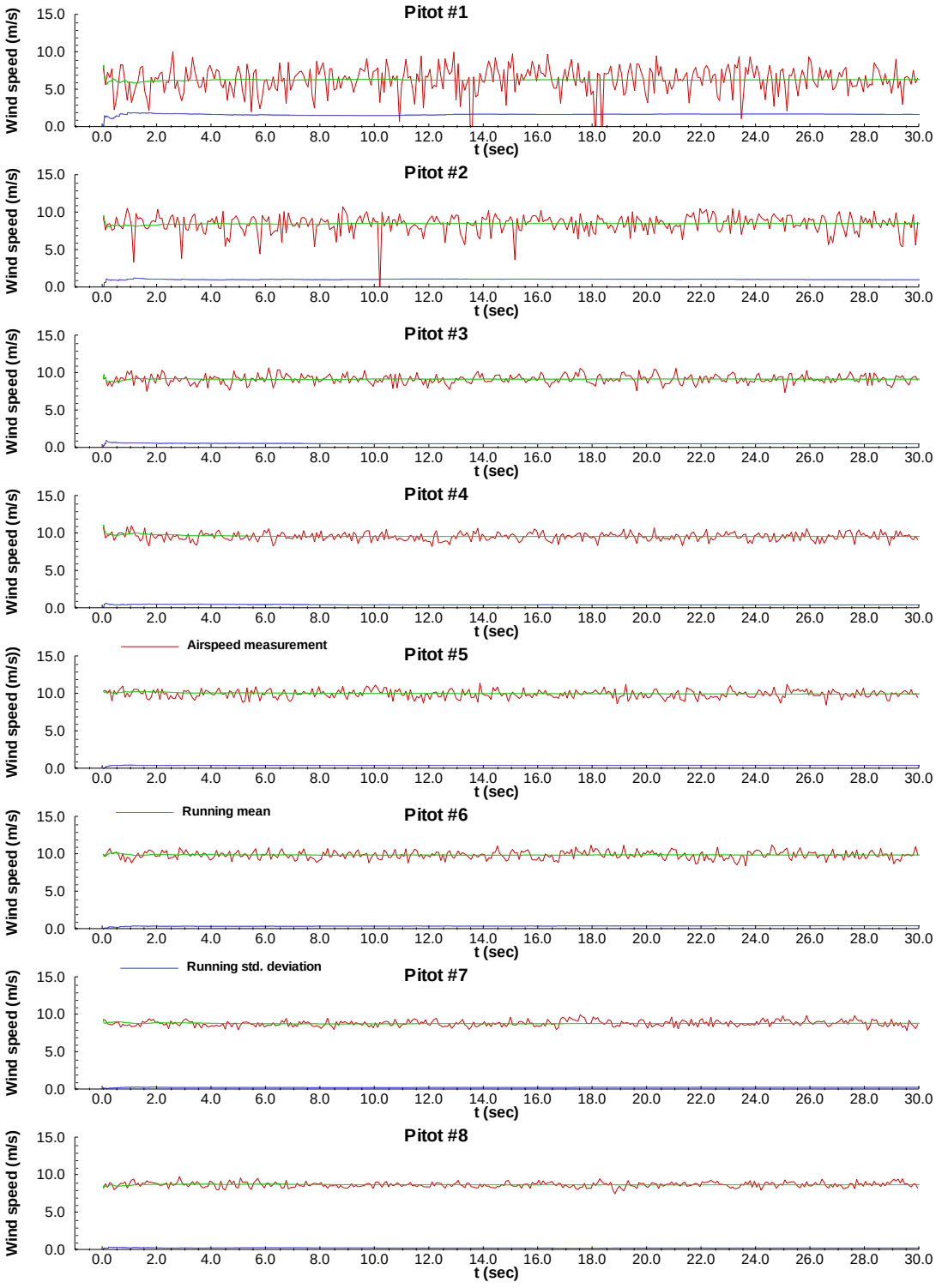


Figure 3-7 Wind measurement at one of 80 rack positions in the measurement grid at $x = 0$ for full speed wind setting and stationary carriage (survey #8) after fan and screen adjustments. Plot shows axial wind speed $U_W$, running mean, and running $RMS$ time histories.

# CHAPTER 4. STRAIGHT AHEAD TEST

Total resistance, $R_T$, and resistance coefficient, $C_T$, for all measured data is compared to existing data in Fig. 4-1. Sinkage, $z$, and trim, $\theta$, for all measured data is compared to existing data in Fig. 4-2. Existing data sets for model 5613 include resistance tests from OU, INSEAN, and three IIHR CFD data sets. Tests at OU were conducted using the same fully appended model as the present study but with the rudders uninstalled. INSEAN conducted resistance tests with a bare hull model of length $L$ = 3.305 m and therefore the presented $R_T$ has been scaled down by the cube of the model's length ratio. Sinkage and trim are not available from INSEAN. One IIHR CFD data set uses a bare hull geometry. A second uses the same bare hull geometry with the addition of bilge keels (BK) while the third uses a fully appended geometry but without propellers, struts, and shafts (i.e with BK and rudders). The skeg is considered part of the hull and present for all data sets.

Resistance, sinkage, and trim are compared between facilities for cases without wind in Tables 4-1, 4-2, and 4-3, respectively, to examine the effects of appendages. Trends are shown in Fig. 4-3. Data from OU is used as the benchmark as the model geometry is identical with the exception of uninstalled rudders. Note that for the remainder of the thesis, percentages representing effects of appendages or wind are reported with sign indicating direction of effect according to the applicable sign convention (i.e., positive sign indicates the effect is in the positive direction). Conversely, errors of complementary CFD data relative to EFD data are reported in percentages referenced absolutely to zero (i.e., positive sign indicates CFD over predicts with data magnitude further from zero than EFD data magnitude). Total resistance shows good agreement and is approximately 5% higher than OU data for low to mid-range $Fr$ values while increasing for higher $Fr$ values. The difference is assumed to be the effect of the rudders. In general, the resistance from the third IIHR CFD data set with rudders

but without propellers, struts, and shafts lies between measured and OU resistance which is expected. The bare hull CFD data set generally agrees with INSEAN bare hull resistance for low to mid-range $Fr$ values with resistance being significantly lower than appended cases (approximately 20%). The measured sinkage and trim data reveals trends suggesting that the addition of rudders causes the stern of the ship to be pulled down which increases trim (bow up) and decreases sinkage (ship down), although CFD sinkage trends do not closely agree with EFD at high $Fr$ values. Sinkage and trim difference percentages are large at small $Fr$ values because of near zero sinkage and trim values. Another possibility for the discrepancy between the measured sinkage and OU sinkage is the effect of tank width. The OU tank width of 7.8 m ($20B$) is significantly larger than the IIHR tank width of 3.048 m ($7.9B$).

The effects of wind on total resistance, sinkage, and trim are summarized in Tables 4-4, 4-5, and 4-6, respectively, and are shown in Fig. 4-3 with a fourth set of IIHR CFD data corresponding to the fully appended complimentary cases with full, half, and without wind for $Fr$ = 0.2, 0.3, and 0.4. As expected, wind effects on resistance are much higher with decreasing ship speed due to the constant ship-relative wind velocity. At $Fr$ = 0.2 the full wind condition increases total resistance by 46%. The CFD total resistance generally agrees with errors up to 7.2%. CFD over predicts resistance in cases without wind with error magnitude increasing as $Fr$ increases and under predicts the increase in resistance due to wind. The increase in resistance due to wind is plotted in Fig. 4-4 (a) and is obtained by subtracting the total resistance from cases without wind from total resistance from cases with wind to give a net drag of the above-water portion of the ship. The wind speed to drag relationship exhibits expected bluff body quadratic behavior (i.e. doubling wind speed quadruples drag, or in this case, scaling wind speed by 1.96 increases drag by the factor $1.96^2 = 3.84$). The drag magnitude tends to decrease (but maintains quadratic scaling) with high $Fr$ values for EFD *and* CFD data sets even though the wind velocity relative to the ship for each wind condition is constant for all

ship speeds. Wind velocity monitored at four locations is shown for each carriage run in Fig. 4-5 and confirms constant overall wind behavior for each wind condition. The reduction in wind drag at higher ship speeds may be explained by the large sinkage and trim values of up to 14 mm and 0.5°, respectively, at the highest ship speeds. As ship speed increases, the model is pulled down exposing less frontal projected area to the air stream, and the wedge-shaped bow is raised which may deflect more of the air stream from stagnating on the ship superstructure. The drag coefficient $C_D$ from (2.35) based on relative wind speed and the projected frontal area of the portion of the ship above water is given for repeat tests and for each wind condition in Table 4-7 along with values from complimentary CFD cases. $C_D$ values from EFD tend to lie slightly above 0.3 whereas CFD values tend to lie slightly below 0.3 suggesting that model 5613 is relatively streamline when compared to other ship types listed by Hoerner (1965).

Trends in sinkage and trim due to wind are not as obvious. Data without wind subtracted from data with wind can be seen on the left of Fig. 4-4 (b) and (c) for sinkage and trim, respectively. The difference for the half wind condition exhibits scatter about zero suggesting the half wind condition has a negligible effect on sinkage and trim. The difference for the full wind condition appears to scatter about slightly higher values than the half wind condition which suggests the effect of the full wind condition may be observed but is largely inconsequential. Detailed views of sinkage and trim repeat test average data points at $Fr$ = 0.2, 0.3, and 0.4 are shown in the right of Fig. 4-4 (b) and (c) with error bars representing standard deviations of 10 repeat tests. The inherent scatter in sinkage and trim data is obvious with data points lying within each other's standard deviations. There is, however, a marginally detectable trend due to wind that is more obvious at the lower ship speeds $Fr$ = 0.2 and 0.3. Wind tends to cause lift which can be seen as increases in sinkage (ship up). Increases in pitch due to wind are extremely small compared to the standard deviations but the underlying trend is that wind increases pitch (bow up) which may be due to stagnation on the superstructure and perhaps lift on the

bow resulting in a positive pitch moment. The wind induced sinkage and trim difference percentages provided in Tables 4-5 and 4-6, respectively, carry little meaning due to near zero data values and large scatter.

Standard deviation percentages from repeat tests are shown in Table 4-8. Carriage speed demonstrates good repeatability with standard deviation percentages much less than 1%. $F_x$ repeatability is also good with maximum standard deviation percentages around 1% at lower $Fr$ values and are comparable between wind conditions which is another indication of wind velocity repeatability. Time histories of $F_x$ raw data at each $Fr$ value and wind condition are shown in Fig. 4-6. Large amounts of high frequency noise are present due to vibrations caused by carriage speed, as was observed in PMM noise tests. The running averages, however, exhibit steady constant behavior. Time histories of sinkage and trim for each $Fr$ value and wind condition are shown in Fig. 4-7 and 4-8, respectively, and are characterized by high frequency noise superimposed onto large transient oscillatory motion. It is obvious that the large oscillatory motion caused by abrupt carriage acceleration is largely under-damped and would require an exceptionally long towing tank to converge. This is the main reason for the large scatter in sinkage and trim data, especially at high ship speeds where only a few periods of oscillation are recorded, in which the running average is more dependent on the point in time data acquisition is begun. As a result, and because of the near zero values, standard deviation percentages for repeat tests shown in Table 4-8 are quite large. Averaging over integer amounts of periods would be a more tailored method of data processing but its application is difficult for the present study due to the observed noise and non-stationarity (discussed below). Another large source of error contributing to scatter in sinkage and trim data is the alignment of the towing tank rails relative to the water free surface. Movement of the rails relative to the free surface is recorded by the pitch, heave, and roll potentiometers as error in pitch, heave, and roll measurements because the 3DOF mount is suspended by the PMM carriage which rides on the rails.

Heave measurement is affected the most because changes in rail elevation cause corresponding heave staff displacements relative to the 3DOF mount. Rail alignment measurements performed at IIHR indicate the rails change elevation on the order of 1 mm over the length of the tank which is a relatively large fraction of the model's dynamic range in sinkage. Pitch and/or roll measurements are affected when the PMM carriage exhibits any incline relative to the free surface due to rail misalignment, especially when maximum measured pitch angles are only as large as 0.5°. It is likely that much of the high frequency noise in pitch measurements is due to porpoising vibration of the PMM carriage caused by imperfections in the wheels and rails.

Stationarity test results are summarized in Tables 4-9, 4-10, and 4-11 for cases without wind, half wind, and full wind, respectively. Occasional failures of $U_C$ at very low speeds are likely due to lengthy run times presenting opportunity for swings in drive motor voltage. $F_x$ exhibits almost no failures of either test which was observed as steady running averages in the time histories. The majority of the sinkage data variance and some trim data variance fail both tests. This is expected due to the oscillatory and transient nature seen in the time histories where monotonic trends can even be seen superimposed on top of the oscillations for the mid to high $Fr$ values, particularly for sinkage which is undoubtedly due to rail elevation changes.

The archival straight ahead data discussed above is in fact a second data set acquired after an initial round of straight ahead tests. The initial round was performed without the use of the yaw guide portion of the 3DOF mount due to its fabrication extending beyond the desired schedule. In its place a temporary rod fixed to the strongback and passing through a slotted hole in a plate attached to the ship bow was used as a means of supporting the ship in yaw (see Fig. B-1 in Appendix B). The initial round neglected the effect of the rod and plate on wind and also did not account for the drag of the 3DOF mount and thus the processed data is not archival but is presented in Appendix B to demonstrate work performed to confirm the operation of the DA.

Table 4-1 Effects of appendages on total resistance.

| $Fr$ | IIHR EFD fully appended $R_T$ (N) | OU EFD fully appended w/o rudders % IIHR | INSEAN EFD bare hull w/o BK % IIHR | IIHR CFD fully appended w/o prop, struts, shafts % IIHR | IIHR CFD bare hull w/BK % IIHR | IIHR CFD bare hull w/o BK % IIHR |
|---|---|---|---|---|---|---|
| 0.05 | 0.34 | -0.7 | 1.3 | | 83.6 | 28.3 |
| 0.10 | 1.28 | -6.4 | -21.2 | | 10.8 | -7.9 |
| 0.138 | 2.38 | | | | -6.2 | -16.7 |
| 0.15 | 2.81 | -5.0 | -21.7 | | -6.8 | -18.9 |
| 0.20 | 4.66 | -2.0 | -20.7 | | -8.6 | -17.8 |
| 0.25 | 7.16 | 0.3 | -18.7 | -3.0 | -8.9 | -16.6 |
| 0.28 | 9.31 | | -17.0 | | -10.6 | -17.7 |
| 0.30 | 11.08 | -2.3 | -17.4 | -3.7 | -12.9 | -19.2 |
| 0.35 | 16.23 | -5.1 | -21.8 | -3.6 | -15.0 | -21.2 |
| 0.364 | 18.07 | | | | -15.9 | -22.5 |
| 0.40 | 24.56 | -10.1 | -18.1 | -7.7 | -19.4 | -25.5 |
| 0.41 | 26.35 | | -17.9 | | -20.1 | -26.0 |

Table 4-2 Effects of appendages on sinkage.

| $Fr$ | IIHR EFD fully appended $z$ (mm) | OU EFD fully appended w/o rudders % IIHR | INSEAN EFD bare hull w/o BK % IIHR | IIHR CFD fully appended w/o prop, struts, shafts % IIHR | IIHR CFD bare hull w/BK % IIHR | IIHR CFD bare hull w/o BK % IIHR |
|---|---|---|---|---|---|---|
| 0.05 | 0.2 | -118.0 | | | -116.0 | -143.1 |
| 0.10 | -0.4 | 28.3 | | | -1.3 | -37.7 |
| 0.0138 | -0.9 | | | | 0.0 | -3.5 |
| 0.15 | -1.1 | 23.4 | | | 5.6 | 0.9 |
| 0.20 | -2.3 | 18.7 | | | 10.0 | 6.1 |
| 0.25 | -3.8 | 5.6 | | 9.0 | 8.1 | 6.5 |
| 0.28 | -5.4 | | | | 13.0 | 11.8 |
| 0.30 | -6.2 | 6.6 | | 10.7 | 10.7 | 9.7 |
| 0.35 | -9.4 | 11.9 | | 14.2 | 14.6 | 13.2 |
| 0.364 | -10.6 | | | | 15.7 | 15.7 |
| 0.40 | -13.3 | 8.1 | | 16.1 | 16.1 | 17.6 |
| 0.41 | -14.0 | | | | 17.9 | 18.5 |

Table 4-3 Effects of appendages on trim.

| $Fr$ | IIHR EFD fully appended $\theta$ (°) | OU EFD fully appended w/o rudders % IIHR | INSEAN EFD bare hull w/o BK % IIHR | IIHR CFD fully appended w/o prop, struts, shafts % IIHR | IIHR CFD bare hull w/BK % IIHR | IIHR CFD bare hull w/o BK % IIHR |
|---|---|---|---|---|---|---|
| 0.05 | -0.026 | 124.9 | | | 225.0 | 147.6 |
| 0.10 | -0.012 | -25.2 | | | 300.9 | 125.5 |
| 0.0138 | -0.015 | | | | 157.0 | 52.5 |
| 0.15 | -0.019 | -20.9 | | | 157.2 | 32.5 |
| 0.20 | -0.024 | -100.0 | | | 65.8 | -23.4 |
| 0.25 | -0.046 | -55.0 | | 35.1 | 60.1 | 13.3 |
| 0.28 | -0.029 | | | | 69.2 | -12.9 |
| 0.30 | -0.006 | -684.4 | | 202.3 | 57.7 | -304.9 |
| 0.35 | 0.015 | -702.7 | | 421.7 | 62.7 | -110.1 |
| 0.364 | 0.078 | | | | -47.0 | -91.1 |
| 0.40 | 0.379 | -60.6 | | -4.0 | -52.3 | -64.8 |
| 0.41 | 0.466 | | | | -48.8 | -57.4 |

Table 4-4 Effects of wind on total resistance.

| $Fr$ | IIHR EFD fully appended w/o wind $R_T$ (N) | IIHR EFD fully appended half wind % w/o wind | IIHR EFD fully appended full wind % w/o wind | IIHR CFD fully appended w/o wind $R_T$ (N), (% error) | IIHR CFD fully appended half wind % w/o (% error) | IIHR CFD fully appended full wind % w/o (% error) |
|---|---|---|---|---|---|---|
| 0.05 | 0.34 | 182.6 | 668.1 | | | |
| 0.10 | 1.28 | 46.9 | 176.1 | | | |
| 0.0138 | 2.38 | 22.5 | 93.7 | | | |
| 0.15 | 2.81 | 18.2 | 78.1 | | | |
| 0.20 | 4.66 | 12.1 | 45.9 | 4.94 (6.1) | 9.1 (3.3) | 35.4 (-1.5) |
| 0.25 | 7.16 | 8.5 | 33.0 | | | |
| 0.28 | 9.31 | 5.9 | 24.6 | | | |
| 0.30 | 11.08 | 5.3 | 18.8 | 11.88 (7.2) | 3.5 (5.4) | 14.2 (3.0) |
| 0.35 | 16.23 | 1.5 | 10.6 | | | |
| 0.364 | 18.07 | 2.2 | 10.7 | | | |
| 0.40 | 24.56 | 1.9 | 6.2 | 25.85 (5.3) | 1.3 (4.6) | 5.2 (4.3) |
| 0.41 | 26.35 | 1.2 | 5.2 | | | |

Table 4-5 Effects of wind on sinkage.

| $Fr$ | IIHR EFD fully appended w/o wind $z$ (mm) | IIHR EFD fully appended half wind % w/o wind | IIHR EFD fully appended full wind % w/o wind | IIHR CFD fully appended w/o wind $z$ (mm), (% error) | IIHR CFD fully appended half wind % w/o (% error) | IIHR CFD fully appended full wind % w/o (% error) |
|---|---|---|---|---|---|---|
| 0.05 | 0.2 | -265.2 | 30.1 | | | |
| 0.10 | -0.4 | 93.7 | 137.0 | | | |
| 0.0138 | -0.9 | -9.4 | -30.9 | | | |
| 0.15 | -1.1 | 14.7 | -17.8 | | | |
| 0.20 | -2.3 | 7.3 | 15.7 | -2.3 (0.4) | 7.2 (0.5) | 16.4 (-0.4) |
| 0.25 | -3.8 | -0.2 | 11.0 | | | |
| 0.28 | -5.4 | 8.8 | 4.4 | | | |
| 0.30 | -6.2 | 0.6 | 1.8 | -6.0 (-3.2) | 1.3 (-3.8) | 1.7 (-3.1) |
| 0.35 | -9.4 | 0.7 | 9.9 | | | |
| 0.364 | -10.6 | 2.0 | 4.7 | | | |
| 0.40 | -13.3 | -0.2 | 0.9 | -12.6 (-5.2) | -1.2 (-4.2) | 2.4 (-6.7) |
| 0.41 | -14.0 | 0.6 | 5.9 | | | |

Table 4-6 Effects of wind on trim.

| $Fr$ | IIHR EFD fully appended w/o wind $\theta$ (°) | IIHR EFD fully appended half wind % w/o wind | IIHR EFD fully appended full wind % w/o wind | IIHR CFD fully appended w/o wind $\theta$ (°), (% error) | IIHR CFD fully appended half wind % w/o (% error) | IIHR CFD fully appended full wind % w/o (% error) |
|---|---|---|---|---|---|---|
| 0.05 | -0.026 | 7.0 | 116.3 | | | |
| 0.10 | -0.012 | -42.2 | 64.3 | | | |
| 0.0138 | -0.015 | 15.5 | -5.1 | | | |
| 0.15 | -0.019 | -8.8 | 33.5 | | | |
| 0.20 | -0.024 | -7.9 | 37.4 | -0.024 (-1.7) | -8.0 (-1.7) | 36.9 (-1.0) |
| 0.25 | -0.046 | -5.2 | 26.9 | | | |
| 0.28 | -0.029 | -24.4 | 46.4 | | | |
| 0.30 | -0.006 | 42.4 | 222.9 | -0.006 (-3.3) | 43.3 (-4.9) | 222.5 (-3.5) |
| 0.35 | 0.015 | 29.7 | 176.0 | | | |
| 0.364 | 0.078 | 9.8 | 32.9 | | | |
| 0.40 | 0.379 | 0.9 | 0.1 | 0.351 (-7.4) | 12.4 (3.1) | 11.3 (2.9) |
| 0.41 | 0.466 | -3.5 | -2.8 | | | |

Table 4-7 Above water wind $C_D$ based on frontal area of ONRT.

| Source | | Relative to ship $\frac{\mu_{\bar{U}_W}}{U_S}$ | Relative to Earth $\frac{\mu_{\bar{U}_W} - U_s}{U_S}$ | $C_D$ EFD | $C_D$ CFD |
|---|---|---|---|---|---|
| IIHR | $Fr$ = 0.2 | 8.444 | 7.444 | 0.33 | 0.27 |
| | | 4.308 | 3.308 | 0.34 | 0.27 |
| | $Fr$ = 0.3 | 5.629 | 4.629 | 0.33 | 0.26 |
| | | 2.872 | 1.872 | 0.37 | 0.25 |
| | $Fr$ = 0.4 | 4.222 | 3.222 | 0.24 | 0.21 |
| | | 2.154 | 1.154 | 0.29 | 0.20 |
| IIHR CFD[1)] | $Fr$ = 0.2 | 8 | 7 | N/A | 0.30 |
| Hoerner[2)] (not ONRT specific) | | | | 0.17 – 1.22 | |

[1)] Mousaviraad, S. M., Carrica, P. M., Huang, J., and Stern, F., 2008, "CFD Prediction of Ship Response to Severe Ocean Waves and Wind", Proc. 27th Symposium on Naval Hydrodynamics, Seoul, Korea.

[2)] Hoerner, Sighard F., "Fluid Dynamic Drag," 2nd Edition, New York City, 1965, pp 11-8.

Table 4-8 Standard deviations from straight ahead repeat tests in percent of mean.

| Condition | Wind | $s_{Fr}$ (%) | $s_{R_T}$ (%) | $s_z$ (%) | $s_\theta$ (%) |
|---|---|---|---|---|---|
| Fr = 0.2 | none | 0.27 | 0.63 | 11.78 | 29.16 |
| | half | 0.16 | 1.19 | 12.99 | 29.19 |
| | full | 0.18 | 1.06 | 11.22 | 70.93 |
| Fr = 0.3 | none | 0.12 | 1.27 | 2.81 | 220.31 |
| | half | 0.16 | 0.83 | 2.73 | 360.97 |
| | full | 0.09 | 0.67 | 7.24 | 208.23 |
| Fr = 0.4 | none | 0.09 | 0.84 | 1.95 | 1.51 |
| | half | 0.07 | 0.45 | 2.18 | 2.06 |
| | full | 0.08 | 0.89 | 5.27 | 2.54 |

Table 4-9 Tests for stationarity without wind.

| | Run Test, $r$ †$(6 \le r \le 15$ for $N = 20)$ | | | | | | | | Trend Test, $A$ †$(64 \le A \le 125$ for $N = 20)$ | | | | | | | |
|---|---|---|---|---|---|---|---|---|---|---|---|---|---|---|---|---|
| | $\bar{x}$ | | | | $\overline{x^2}$ | | | | $\bar{x}$ | | | | $\overline{x^2}$ | | | |
| $Fr$ | $U_C$ | $F_x$ | $z$ | $\theta$ | $U_C$ | $F_x$ | $z$ | $\theta$ | $U_C$ | $F_x$ | $z$ | $\theta$ | $U_C$ | $F_x$ | $z$ | $\theta$ |
| 0.050 | 16 | 13 | 8 | 9 | 9 | 11 | 6 | 11 | 70 | 90 | 82 | 90 | 106 | 117 | 145 | 119 |
| 0.100 | 4 | 11 | 6 | 8 | 10 | 7 | 9 | 7 | 43 | 90 | 68 | 116 | 131 | 85 | 119 | 97 |
| 0.138 | 8 | 12 | 6 | 6 | 10 | 10 | 4 | 8 | 57 | 101 | 45 | 98 | 93 | 115 | 110 | 113 |
| 0.150 | 8 | 12 | 5 | 14 | 10 | 10 | 6 | 8 | 60 | 91 | 63 | 84 | 89 | 106 | 101 | 119 |
| **0.200** | **10** | **12** | **6** | **10** | **10** | **7** | **5** | **6** | **60** | **93** | **48** | **96** | **108** | **108** | **135** | **125** |
| 0.250 | 14 | 14 | 16 | 16 | 12 | 11 | 10 | 6 | 70 | 79 | 73 | 97 | 82 | 102 | 135 | 124 |
| 0.280 | 12 | 12 | 12 | 12 | 10 | 6 | 10 | 6 | 87 | 85 | 71 | 75 | 93 | 102 | 136 | 124 |
| **0.300** | **11** | **11** | **10** | **12** | **10** | **7** | **10** | **6** | **67** | **92** | **75** | **87** | **93** | **105** | **137** | **125** |
| 0.350 | 15 | 11 | 7 | 7 | 16 | 10 | 10 | 8 | 86 | 96 | 71 | 94 | 102 | 75 | 122 | 117 |
| 0.364 | 10 | 13 | 6 | 7 | 16 | 10 | 11 | 10 | 71 | 86 | 60 | 107 | 95 | 54 | 117 | 80 |
| **0.400** | **12** | **11** | **5** | **6** | **10** | **7** | **5** | **6** | **87** | **105** | **68** | **103** | **102** | **118** | **127** | **131** |
| 0.410 | 8 | 11 | 5 | 5 | 11 | 9 | 8 | 10 | 112 | 103 | 58 | 119 | 96 | 81 | 129 | 84 |

† Acceptance region at the 5% level of significance.

Red: Outside the acceptance region.

**Bold**: Average of 10 repeat tests.

Table 4-10 Tests for stationarity with half wind.

| | Run Test, $r$ †$(6 \le r \le 15$ for $N = 20)$ | | | | | | | | Trend Test, $A$ †$(64 \le A \le 125$ for $N = 20)$ | | | | | | | |
|---|---|---|---|---|---|---|---|---|---|---|---|---|---|---|---|---|
| | $\bar{x}$ | | | | $\overline{x^2}$ | | | | $\bar{x}$ | | | | $\overline{x^2}$ | | | |
| $Fr$ | $U_C$ | $F_x$ | $z$ | $\theta$ | $U_C$ | $F_x$ | $z$ | $\theta$ | $U_C$ | $F_x$ | $z$ | $\theta$ | $U_C$ | $F_x$ | $z$ | $\theta$ |
| 0.000 | 14 | 4 | 4 | 2 | 11 | 5 | 13 | 3 | 89 | 145 | 84 | 168 | 78 | 113 | 84 | 72 |
| 0.050 | 9 | 12 | 11 | 8 | 10 | 10 | 13 | 8 | 90 | 84 | 88 | 119 | 92 | 75 | 112 | 76 |
| 0.100 | 6 | 15 | 5 | 13 | 6 | 6 | 8 | 5 | 46 | 102 | 75 | 61 | 111 | 137 | 109 | 126 |
| 0.138 | 12 | 13 | 6 | 12 | 9 | 12 | 9 | 8 | 65 | 85 | 85 | 83 | 110 | 109 | 110 | 115 |
| 0.150 | 10 | 11 | 3 | 14 | 9 | 12 | 4 | 14 | 70 | 82 | 70 | 111 | 104 | 85 | 103 | 91 |
| **0.200** | **10** | **11** | **5** | **10** | **11** | **7** | **5** | **6** | **60** | **96** | **64** | **93** | **114** | **107** | **123** | **127** |
| 0.250 | 13 | 17 | 13 | 15 | 13 | 7 | 9 | 9 | 94 | 83 | 74 | 105 | 88 | 74 | 126 | 95 |
| 0.280 | 11 | 13 | 12 | 13 | 10 | 7 | 12 | 7 | 94 | 98 | 92 | 99 | 113 | 90 | 119 | 110 |
| **0.300** | **11** | **11** | **10** | **12** | **10** | **6** | **10** | **6** | **72** | **88** | **72** | **84** | **97** | **117** | **133** | **138** |
| 0.350 | 15 | 10 | 7 | 7 | 8 | 15 | 11 | 11 | 97 | 103 | 80 | 89 | 81 | 102 | 125 | 123 |
| 0.364 | 10 | 15 | 6 | 7 | 9 | 8 | 7 | 6 | 111 | 98 | 76 | 93 | 101 | 115 | 131 | 145 |
| **0.400** | **12** | **10** | **5** | **6** | **10** | **8** | **8** | **8** | **89** | **103** | **75** | **103** | **107** | **104** | **130** | **120** |
| 0.410 | 12 | 13 | 4 | 5 | 12 | 5 | 8 | 8 | 100 | 97 | 62 | 95 | 87 | 106 | 116 | 111 |

† Acceptance region at the 5% level of significance.

Red: Outside the acceptance region.

**Bold**: Average of 10 repeat tests.

Table 4-11 Tests for stationarity with full wind.

| | Run Test, $r$ †$(6 \le r \le 15$ for $N = 20)$ | | | | | | | | Trend Test, $A$ †$(64 \le A \le 125$ for $N = 20)$ | | | | | | | |
|---|---|---|---|---|---|---|---|---|---|---|---|---|---|---|---|---|
| | $\bar{x}$ | | | | $\overline{x^2}$ | | | | $\bar{x}$ | | | | $\overline{x^2}$ | | | |
| $Fr$ | $U_C$ | $F_x$ | $z$ | $\theta$ | $U_C$ | $F_x$ | $z$ | $\theta$ | $U_C$ | $F_x$ | $z$ | $\theta$ | $U_C$ | $F_x$ | $z$ | $\theta$ |
| 0.000 | 10 | 8 | 6 | 11 | 13 | 9 | 7 | 5 | 94 | 140 | 94 | 87 | 78 | 93 | 91 | 74 |
| 0.050 | 11 | 12 | 7 | 10 | 11 | 7 | 6 | 11 | 98 | 106 | 60 | 92 | 120 | 101 | 45 | 85 |
| 0.100 | 2 | 11 | 7 | 11 | 6 | 10 | 4 | 9 | 42 | 85 | 80 | 99 | 115 | 101 | 63 | 92 |
| 0.138 | 5 | 13 | 5 | 11 | 9 | 11 | 3 | 10 | 57 | 98 | 89 | 68 | 91 | 139 | 131 | 137 |
| 0.150 | 6 | 13 | 5 | 11 | 10 | 9 | 10 | 8 | 48 | 79 | 69 | 85 | 131 | 105 | 71 | 95 |
| **0.200** | **10** | **12** | **6** | **12** | **10** | **7** | **9** | **6** | **66** | **107** | **68** | **83** | **117** | **107** | **111** | **130** |
| 0.250 | 8 | 15 | 9 | 15 | 8 | 9 | 8 | 8 | 64 | 104 | 88 | 95 | 119 | 95 | 143 | 123 |
| 0.280 | 10 | 11 | 7 | 13 | 13 | 6 | 6 | 6 | 65 | 92 | 78 | 107 | 96 | 68 | 112 | 108 |
| **0.300** | **10** | **12** | **9** | **11** | **10** | **6** | **11** | **7** | **66** | **99** | **60** | **83** | **108** | **116** | **134** | **145** |
| 0.350 | 15 | 10 | 7 | 7 | 10 | 8 | 10 | 10 | 89 | 82 | 87 | 75 | 91 | 127 | 128 | 128 |
| 0.364 | 11 | 7 | 6 | 7 | 11 | 8 | 9 | 9 | 101 | 92 | 70 | 79 | 103 | 66 | 129 | 107 |
| **0.400** | **12** | **10** | **5** | **6** | **10** | **7** | **8** | **8** | **88** | **102** | **70** | **105** | **99** | **71** | **126** | **94** |
| 0.410 | 12 | 12 | 4 | 5 | 9 | 8 | 9 | 14 | 65 | 106 | 57 | 94 | 77 | 63 | 101 | 86 |

† Acceptance region at the 5% level of significance.

Red: Outside the acceptance region.

**Bold**: Average of 10 repeat tests.

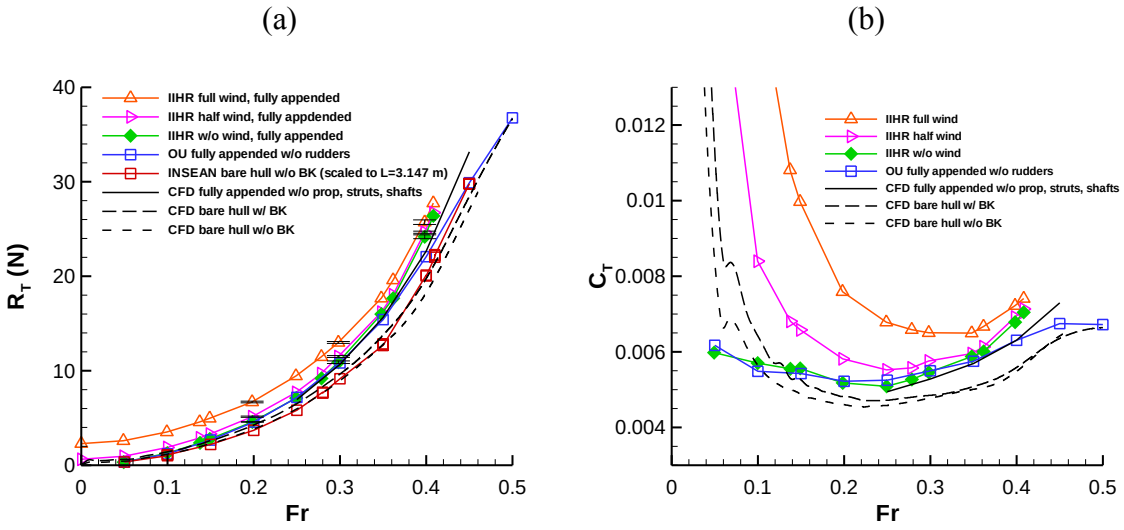


Figure 4-1 Comparison between all straight ahead data: (a) $R_T$ and (b) $C_T$.

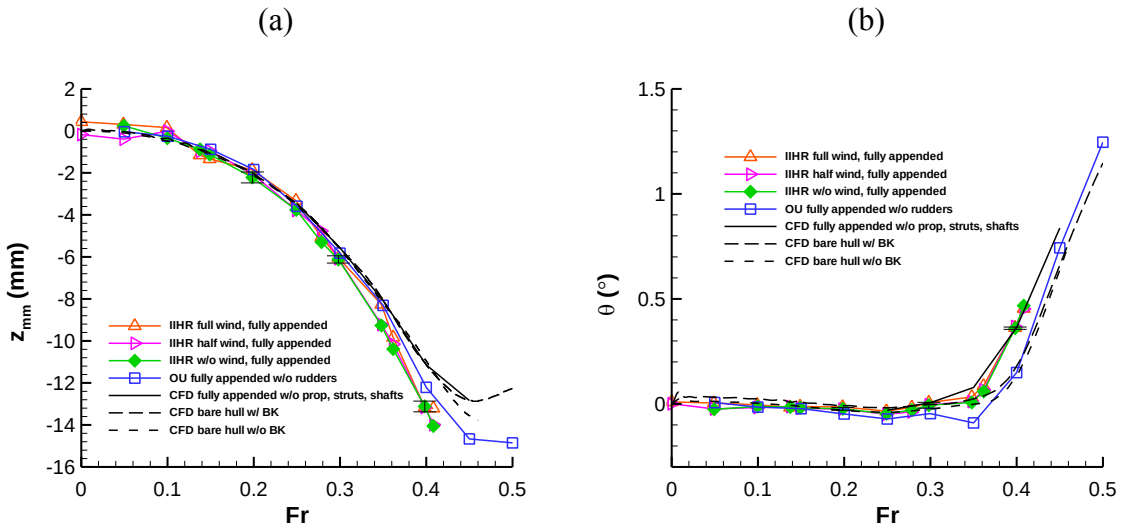


Figure 4-2 Comparison between all straight ahead data: (a) sinkage and (b) trim.

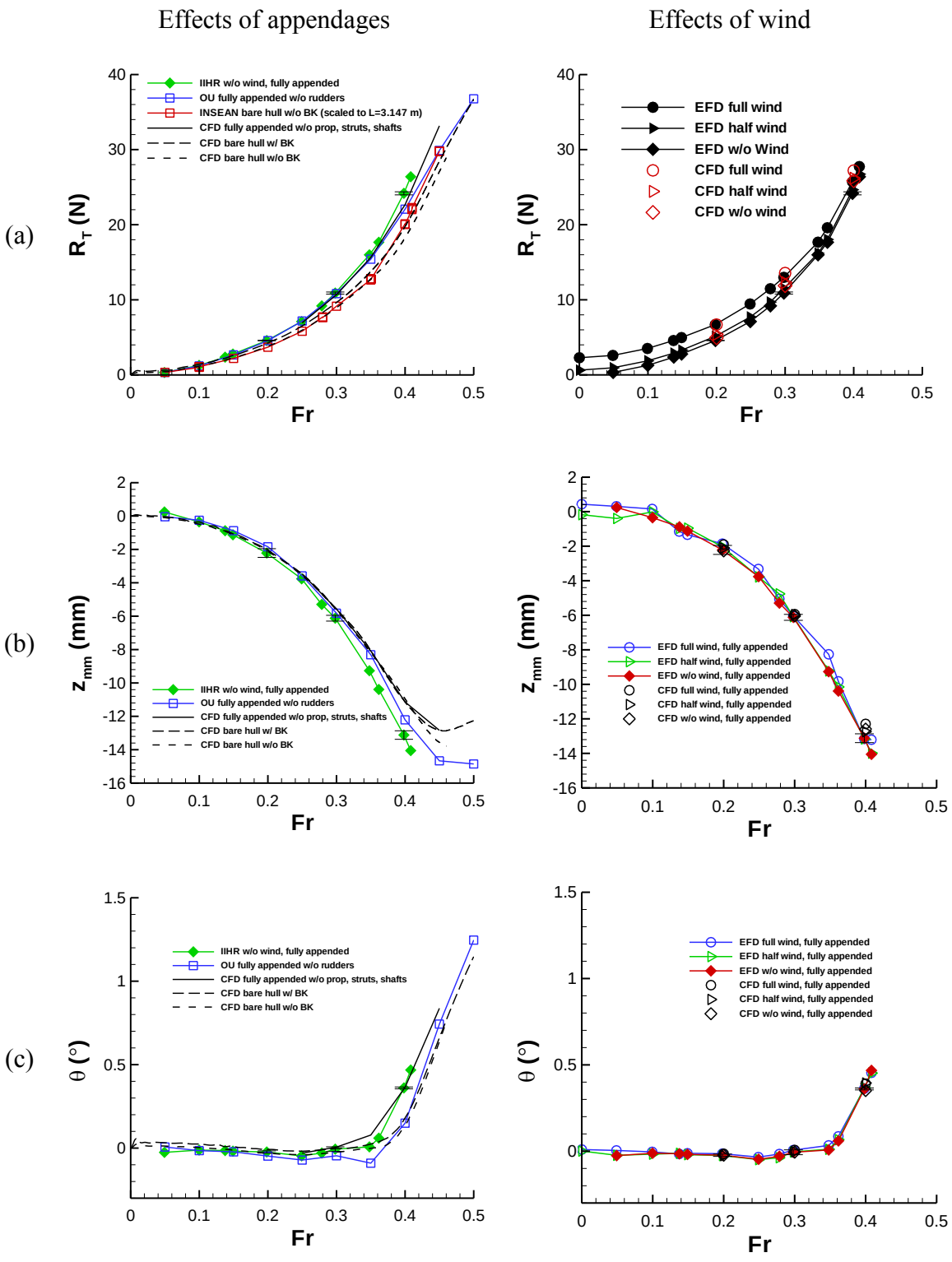


Figure 4-3 Effects of appendages (left) and wind (right): (a) total resistance, (b) sinkage, and (c) trim.

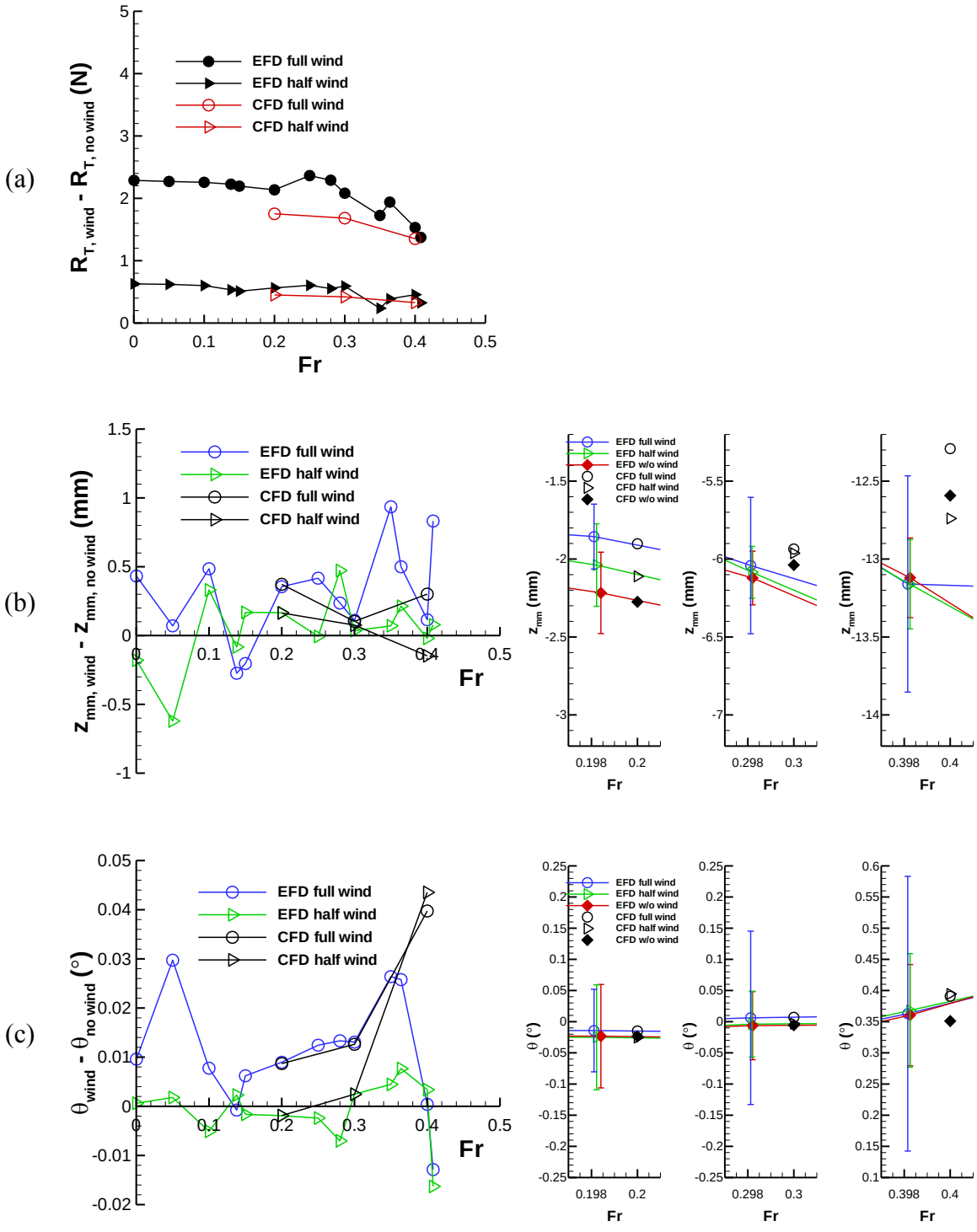


Figure 4-4 No wind data subtracted from data with wind (left) and detailed view of static values (right) vs *Fr* for (a) total resistance, (b) sinkage, and (c) trim.

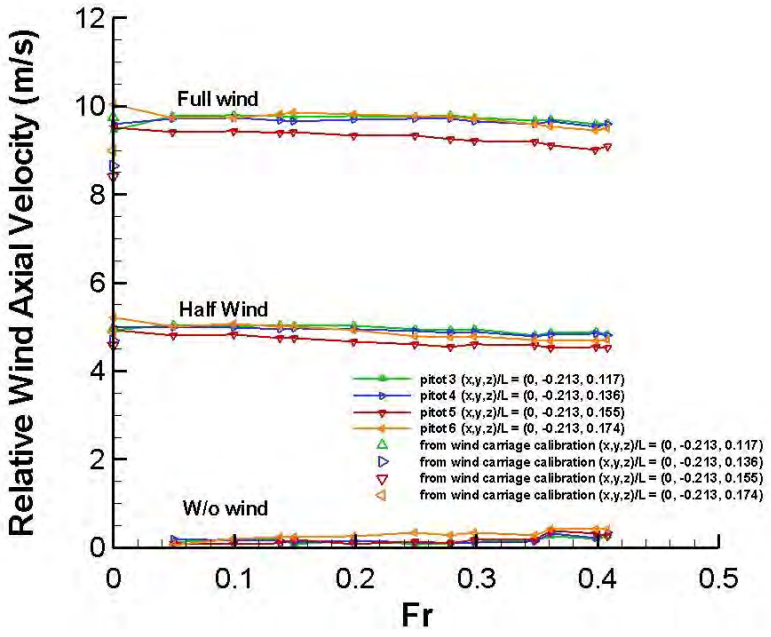


Figure 4-5 Wind axial velocities relative to ship from pitots 3, 4, 5, and 6.

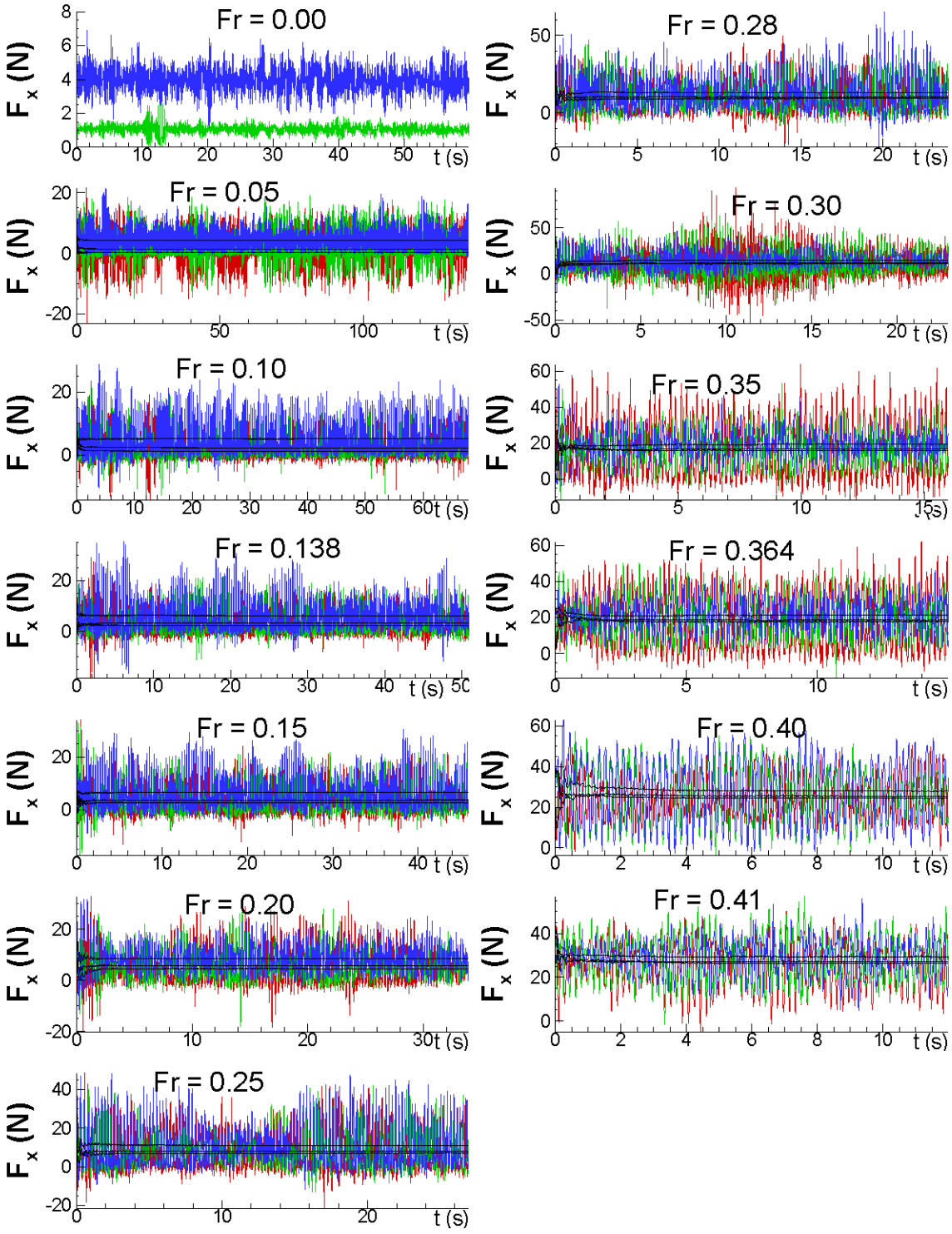


Figure 4-6 Time histories of raw $F_x$ for all $Fr$. Color codes; red: w/o wind, green: half wind, blue: full wind, black: running average. Includes 3DOF mount drag.

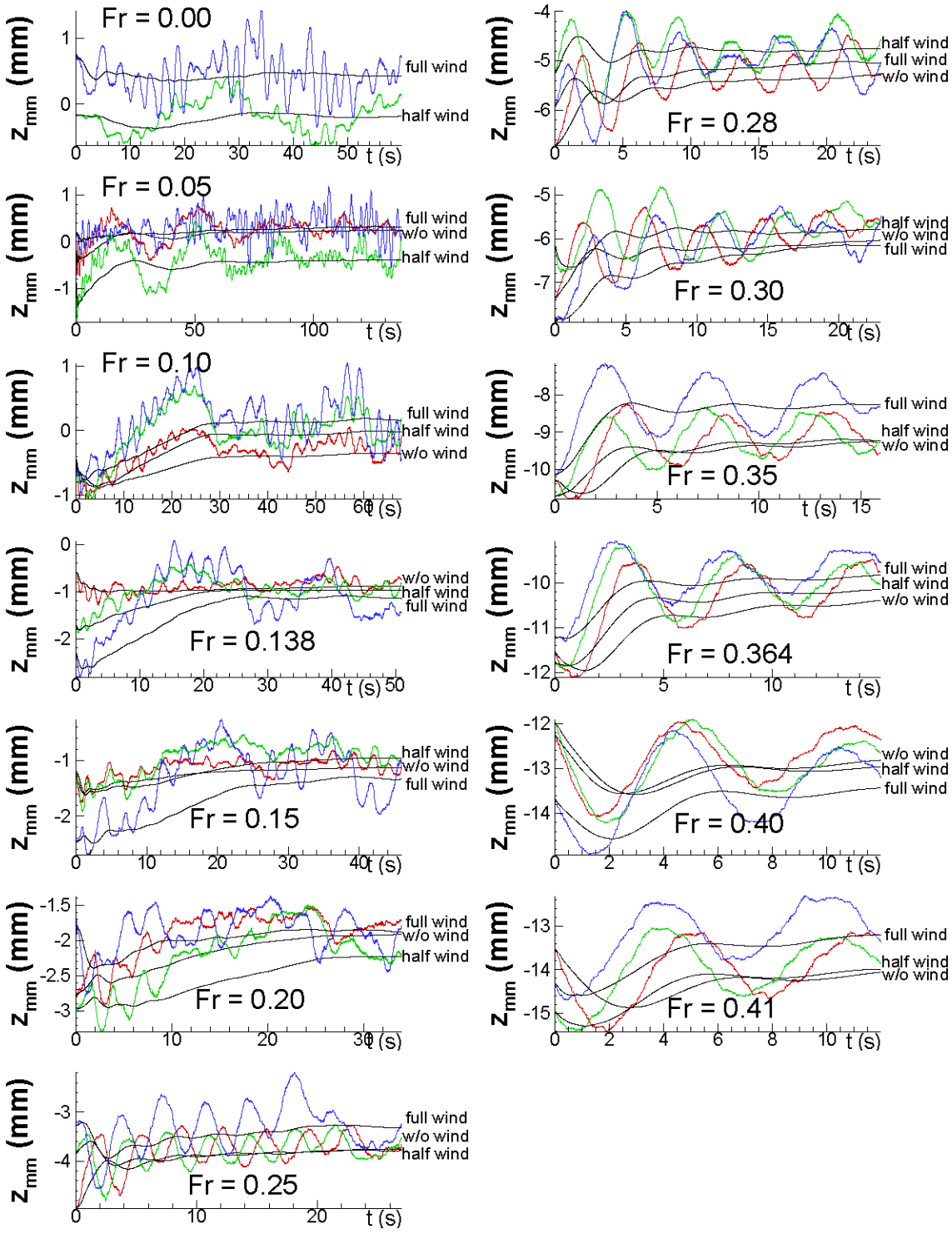


Figure 4-7 Time histories of sinkage for all $Fr$. Color codes; red: w/o wind, green: half wind, blue: full wind, black: running average.

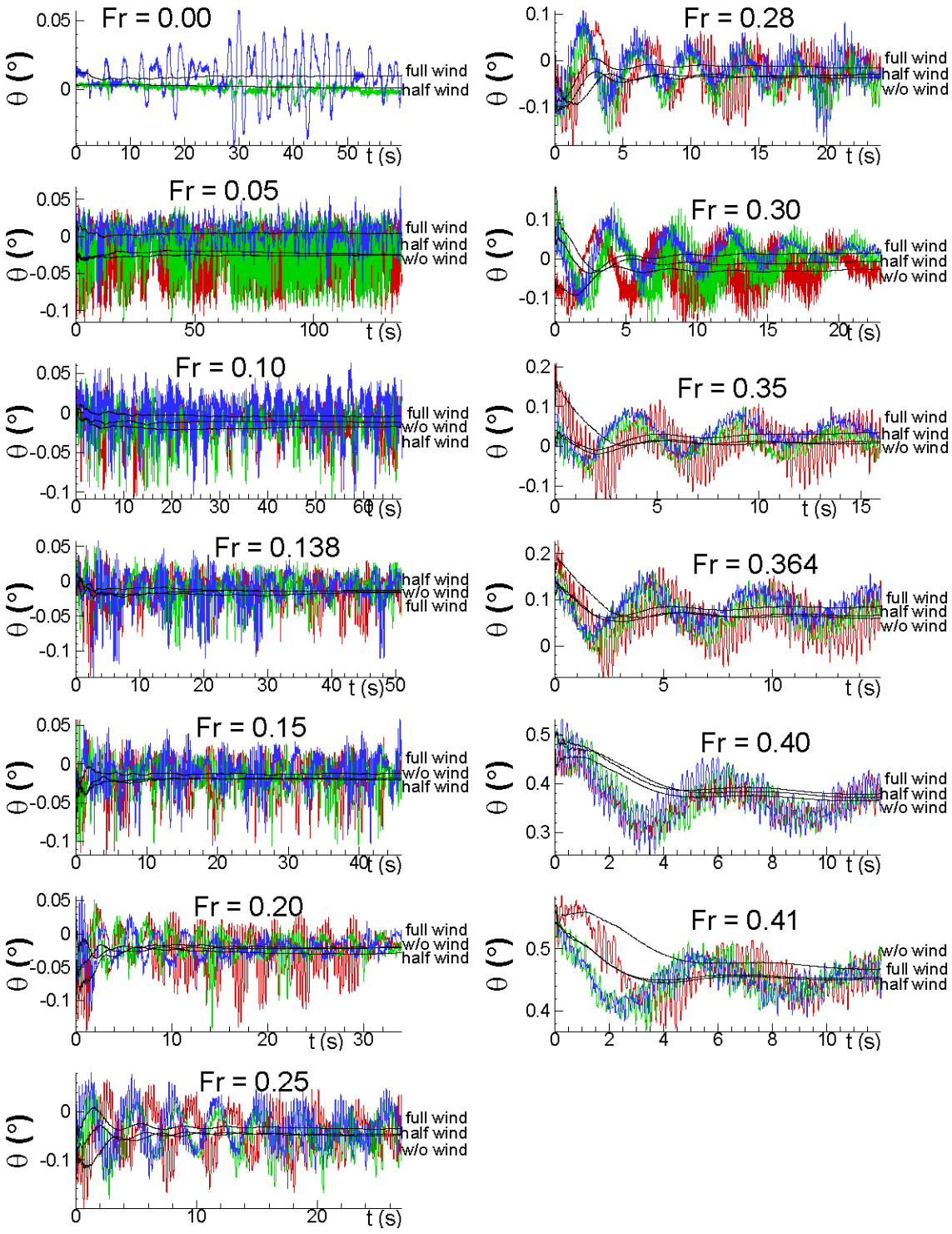


Figure 4-8 Time histories of trim for all $Fr$. Color codes; red: w/o wind, green: half wind, blue: full wind, black: running average.

# CHAPTER 5. STATIC PMM TEST

All measured forces, moment, and motions data is shown in Fig. 5-1. Note that all presented $F_x$ and $F_y$ in the present chapter already have the 3DOF mount drag correction applied. Forces and moment exhibit quadratic scaling with wind speed, as expected, with wind increasing $F_x$, $F_y$, and $M_z$ magnitudes. At repeat test conditions $Fr$ = 0.2 and $\beta$ = -9.3° the half wind condition increases $F_x$, $F_y$, and $M_z$ by 12%, 11%, and 10%, respectively, whereas the full wind condition increases $F_x$, $F_y$, and $M_z$ by 42%, 40%, and 37%, respectively. As in straight ahead tests the relative effect of wind on forces and moment decreases at higher $Fr$. The magnitudes of the wind effects drop at $Fr$ = 0.4 as well. Non-dimensional forces and moment are shown in Fig. 5-2. The effects of drift angle $\beta$ on wind effects, forces, moment and motions are as follows. With $F_x$ depending on $\cos\beta$ and test values for $\beta$ being relatively small, $\beta$ has a negligible effect on wind contribution to $F_x$ but does affect $F_y$ and $M_z$ due to their cubic nature and more sensitive dependence on $\sin\beta$. Effects of wind on sinkage and trim are slightly more pronounced with non-zero $\beta$ than in straight ahead tests. There may be a larger effective planform area contributing to more lift on the ship, counteracting the observed increased sinkage (ship down) due to non-zero $\beta$. Projected frontal area of the ship also increases with non-zero $\beta$ contributing to increased responses in pitch due to wind, although pitch magnitudes decrease with non-zero $\beta$. The model tends to heel to its leading side when towed at oblique angle $\beta$. Observed roll angles increases with $\beta$. Wind counteracts this response, decreasing roll magnitudes by as much as 1.8° for slower ship speeds.

Standard deviation percentages for repeat tests at $Fr$ = 0.2 with $\beta$ = -9.3° and $Fr$ = 0.4 with $\beta$ = -3.7° are listed in Table 5-1. Standard deviations for imposed $Fr$ and $\beta$ are all much less than 1%. $F_x$ exhibits similar repeatability to straight ahead tests with standard deviations around 1% whereas $F_y$ standard deviations are just above 1%. $M_z$

standard deviations range from 1.5 – 2%. With test values for $\beta$ being relatively small and $F_y$ and $M_z$ being proportional to $\sin\beta$ it follows that $F_y$ and $M_z$ should be more sensitive than $F_x$ (proportional to $\cos\beta$) to small scatter in $\beta$. Sinkage magnitudes increase with non-zero $\beta$ so standard deviation percentages are smaller than straight ahead tests at less than 2%. Non-zero $\beta$ decreases trim magnitudes at high ship speeds so standard deviation percentages increase relative to straight ahead tests. Roll standard deviations are all approximately 2% with ship speed and wind having seemingly no effect on repeatability.

Noticeable asymmetry exists in forces, moment, and motions as was the case for Yoon (2009) using the same facility and carriage system but with DTMB model 5512. $D_{asym}$ for nondimensional forces and moment and motions are summarized in Table 5-2. Asymmetry in $X$ is largest for small ship speeds and generally does not exceed 11%. Cases with small $\beta$ exhibit very large asymmetry for anti-symmetric variables such as $Y$ and $N$ due to unexpected non-zero $F_y$, and $M_z$ occuring at $\beta$ = 0°. Initially it is thought that $\beta$ set points are misaligned by a constant value. Upon close inspection of $\beta$ intercepts for $F_y$ and $M_z$, however, $F_y$ = 0 for all conditions when $\beta$ = -0.3° but $M_z$ = 0 for all conditions when $\beta$ = 0.6°. These conflicting offsets suggest that misalignment in $\beta$ is unlikely and that the offset is likely due to some other imperfection. Asymmetry cannot be caused by any unintended wind non-uniformity because cases without wind exhibit asymmetry and the addition of wind does not change trends in asymmetry. Observed small asymmetries in static heel support these statements. Non-perfect hull form construction or non-perfect mount positioning and attachment within the model may be to blame. To obtain archival data suitable for CFD validation it is necessary to correct for symmetry by averaging the data values from negative and positive $\beta$ cases. Static drift hydrodynamic derivatives are then found from the symmetry-corrected forces and moment data. Symmetry-corrected non-dimensional hydrodynamic forces and moment data are fitted to the polynomial mathematical models in (2.42) with data points and

polynomial fits plotted in Fig. 5-3. Forces and moment data fit the mathematical model quite well. The effect of wind diminishes with increasing speed. Hydrodynamic derivatives are found via (2.43) and (2.44) and are listed in Table 5-3. Effects of wind on hydrodynamic derivatives are presented in Table 5-4. The maximum effect of wind on linear derivatives occurs at $Fr = 0.2$ with $X_*$, $Y_v$, and $N_v$ affected up to 46.5%, 41.2%, and 62.2%, respectively, and consistently decreases with increasing ship speeds. The observed effect of wind on non-linear derivatives generally differs between ship speeds. It should be noted that non-linear derivatives found from curve fits are generally less reliable at increased ship speeds due to the smaller ranges of tested $\beta$ which exhibit weak non-linearity near $\beta = 0$. Symmetry-corrected motions data are fitted to polynomials and are presented in Fig. 5-4. Time histories and FFT of representative cases are shown in Figures 5-5 through 5-10.

Table 5-1 Standard deviations from static drift repeat tests in percent of mean.

| Condition | Wind | $s_{Fr}$ (%) | $s_{\beta}$ (%) | $s_{F_x}$ (%) | $s_{F_y}$ (%) | $s_{M_z}$ (%) | $s_z$ (%) | $s_{\theta}$ (%) | $s_{\phi}$ (%) |
|---|---|---|---|---|---|---|---|---|---|
| $Fr$ = 0.2 $\beta$ = -9.3° | none | 0.20 | 0.33 | 0.98 | 1.15 | 1.49 | 1.87 | 12.29 | 2.04 |
| | half | 0.18 | 0.32 | 0.72 | 1.29 | 1.88 | 1.48 | 14.21 | 2.64 |
| | full | 0.20 | 0.33 | 1.04 | 1.18 | 1.47 | 1.76 | 32.15 | 2.21 |
| $Fr$ = 0.4 $\beta$ = -3.7° | none | 0.19 | 0.57 | 0.87 | 1.55 | 1.91 | 1.13 | 4.02 | 2.16 |
| | half | 0.12 | 0.56 | 1.12 | 1.00 | 1.54 | 1.78 | 4.51 | 1.76 |
| | full | 0.07 | 0.56 | 0.70 | 1.32 | 1.58 | 1.53 | 3.39 | 1.99 |

Table 5-2 Asymmetry for static drift tests.

| | | | $D_{asym} = \frac{100}{\mathrm{r_m}}\lvert \mathrm{r} - \mathrm{r}_m \rvert$ (%) | | | | | | |
|---|---|---|---|---|---|---|---|---|---|
| $Fr$ | $\beta_m$ (°) | Wind | $\beta$ | $X$ | $Y$ | $N$ | $z$ | $\theta$ | $\phi$ |
| 0.2 | 11.67 | none | 0.12 | 10.58 | 2.04 | 3.70 | 1.19 | 12.01 | 1.27 |
| | 11.67 | half | 0.15 | 10.83 | 0.93 | 5.41 | 5.09 | 3.51 | 0.62 |
| | 11.67 | full | 0.15 | 11.02 | 0.36 | 4.46 | 4.34 | 17.55 | 0.30 |
| | 9.35 | none | 0.15 | 7.80 | 1.38 | 7.34 | 4.73 | 28.93 | 0.49 |
| | 9.36 | half | 0.13 | 8.33 | 1.34 | 6.84 | 2.97 | 15.46 | 0.33 |
| | 9.36 | full | 0.13 | 8.40 | 0.96 | 4.99 | 1.94 | 2.40 | 0.69 |
| | 7.00 | none | 0.22 | 7.02 | 2.31 | 10.08 | 4.80 | 18.58 | 0.08 |
| | 7.01 | half | 0.24 | 6.74 | 0.72 | 10.34 | 4.65 | 14.70 | 2.53 |
| | 7.01 | full | 0.25 | 6.06 | 0.87 | 9.28 | 3.67 | 53.24 | 7.31 |
| | 4.62 | none | 1.20 | 4.88 | 0.61 | 17.84 | 12.16 | 31.58 | 4.99 |
| | 4.62 | half | 1.31 | 4.57 | 0.23 | 16.96 | 4.19 | 25.07 | 4.59 |
| | 4.62 | full | 1.33 | 4.76 | 1.59 | 12.31 | 0.62 | 900.13 | 3.67 |
| | 2.37 | none | 0.62 | 2.01 | 10.77 | 32.15 | 4.07 | 34.80 | 0.53 |
| | 2.35 | half | 1.54 | 1.93 | 8.06 | 31.90 | 1.05 | 48.92 | 1.60 |
| | 2.35 | full | 1.62 | 2.06 | 7.00 | 23.71 | 3.01 | 3011.53 | 12.32 |
| 0.3 | 7.03 | none | 0.16 | 6.80 | 3.24 | 5.41 | 0.50 | 1.72 | 2.83 |
| | 7.03 | half | 0.15 | 6.18 | 2.87 | 7.19 | 1.56 | 9.70 | 1.50 |
| | 7.03 | full | 0.15 | 5.46 | 2.10 | 7.12 | 3.74 | 10.07 | 0.86 |
| | 4.63 | none | 1.32 | 4.35 | 2.41 | 15.19 | 0.98 | 122.91 | 2.15 |
| | 4.63 | half | 1.27 | 4.25 | 2.52 | 14.53 | 3.23 | 3.89 | 1.78 |
| | 4.63 | full | 1.28 | 3.39 | 2.24 | 14.17 | 3.59 | 6.87 | 0.95 |
| | 2.36 | none | 1.68 | 2.02 | 7.85 | 26.56 | 5.09 | 5.66 | 0.85 |
| | 2.36 | half | 1.67 | 1.77 | 8.10 | 26.83 | 1.61 | 23.54 | 1.79 |
| | 2.36 | full | 1.78 | 1.60 | 7.67 | 25.38 | 0.76 | 2.22 | 2.43 |
| 0.4 | 3.77 | none | 0.44 | 1.73 | 5.74 | 12.53 | 1.83 | 7.81 | 2.88 |
| | 3.78 | half | 0.01 | 3.05 | 6.90 | 11.75 | 2.17 | 7.21 | 2.95 |
| | 3.77 | full | 0.47 | 2.45 | 6.96 | 12.02 | 1.85 | 5.26 | 3.43 |
| | 2.38 | none | 2.08 | 2.11 | 6.71 | 26.71 | 0.37 | 8.02 | 0.69 |
| | 2.38 | half | 2.04 | 1.81 | 6.35 | 26.55 | 0.98 | 6.60 | 2.34 |
| | 2.38 | full | 2.07 | 1.31 | 7.57 | 26.19 | 0.79 | 6.46 | 1.04 |
| | 0.90 | none | 3.98 | 0.69 | 21.38 | 69.98 | 1.52 | 1.01 | 2.06 |
| | 0.90 | half | 4.07 | 1.41 | 23.80 | 73.55 | 0.42 | 0.70 | 5.79 |
| | 0.90 | full | 4.21 | 0.99 | 21.81 | 68.96 | 0.01 | 2.23 | 2.15 |

Table 5-3 Hydrodynamic Derivatives (Static Drift).

| | $Fr$ = 0.2 | | | $Fr$ = 0.3 | | | $Fr$ = 0.4 | | |
|---|---|---|---|---|---|---|---|---|---|
| Derivative | none | half | full | none | half | full | none | half | full |
| $X_*$ | -0.0213 | -0.0240 | -0.0312 | -0.0227 | -0.0238 | -0.0269 | -0.0275 | -0.0285 | -0.0294 |
| $X_{vv}$ | -0.0989 | -0.1003 | -0.1092 | -0.1425 | -0.1442 | -0.1455 | -0.4074 | -0.2001 | -0.2621 |
| $Y_v$ | -0.3453 | -0.3818 | -0.4876 | -0.3397 | -0.3610 | -0.4062 | -0.3918 | -0.3959 | -0.4028 |
| $Y_{vvv}$ | -1.8173 | -1.9616 | -2.3337 | -3.6514 | -2.9669 | -3.4653 | -6.4683 | -7.0826 | -10.3429 |
| $N_v$ | -0.0576 | -0.0663 | -0.0934 | -0.0800 | -0.0846 | -0.0935 | -0.0957 | -0.09653 | -0.0991 |
| $N_{vvv}$ | -0.8345 | -0.8027 | -0.6676 | -1.0225 | -0.7295 | -0.6444 | -1.9064 | -1.9085 | -1.9430 |

Table 5-4 Effects of Wind on Hydrodynamic Derivatives (Static Drift).

| | $Fr$ = 0.2 | | $Fr$ = 0.3 | | $Fr$ = 0.4 | |
|---|---|---|---|---|---|---|
| Derivative | half | full | half | full | half | full |
| $X_*$ | -12.7 % | -46.5 % | -4.8 % | -18.5 % | -3.6 % | -6.9 % |
| $X_{vv}$ | -1.4 % | -10.4 % | -1.2 % | -2.1 % | 50.9 % | 35.7 % |
| $Y_v$ | -10.6 % | -41.2 % | -6.3 % | -19.6 % | -1.0 % | -2.8 % |
| $Y_{vvv}$ | -7.9 % | -28.4 % | 18.7 % | 5.1 % | -9.5 % | -59.9 % |
| $N_v$ | -15.1 % | -62.2 % | -5.7 % | -16.9 % | -0.9 % | -3.6 % |
| $N_{vvv}$ | 3.8 % | 20.0 % | 28.7 % | 37.0 % | -0.1 % | -1.9 % |

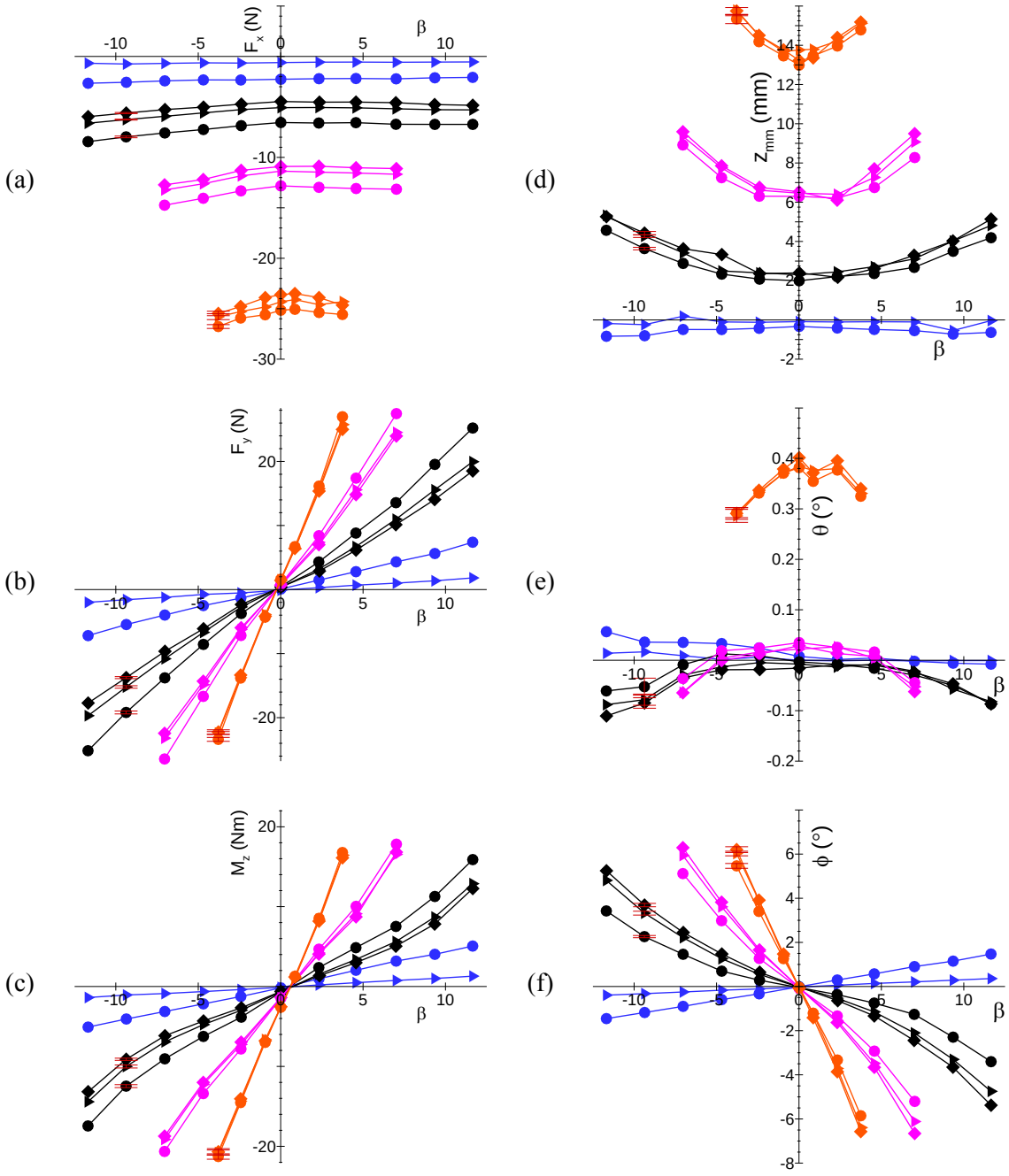


Figure 5-1 Static drift test results in physical units: (a) $F_x$, (b) $F_y$, (c) $M_z$, (d) $z_{mm}$, (e) $\theta$, (f) $\phi$, respectively. Symbols: ♦ w/o wind, ▶ half wind, ● full wind. Color codes; blue: $Fr = 0$, black: $Fr = 0.2$, pink: $Fr = 0.3$, orange: $Fr = 0.4$.

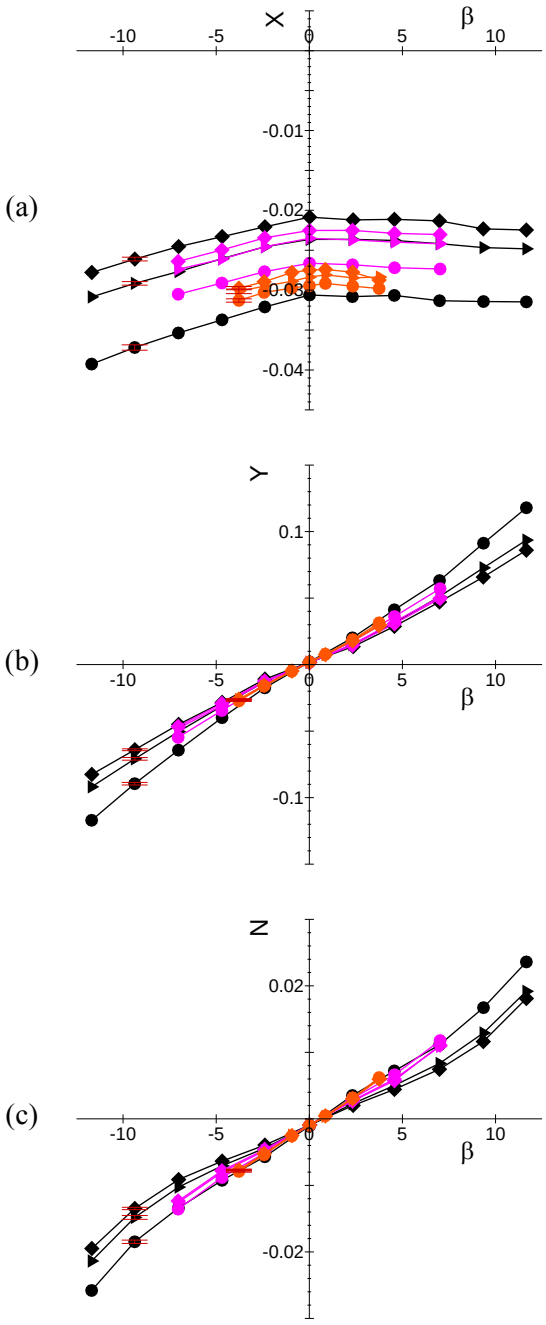


Figure 5-2 Nondimensional forces and moment data for static drift test: (a) *X*, (b) *Y*, (c) *N*, respectively. Symbols: ♦ w/o wind, ▶ half wind, ● full wind. Color codes; blue: $Fr = 0$, black: $Fr = 0.2$, pink: $Fr = 0.3$, orange: $Fr = 0.4$

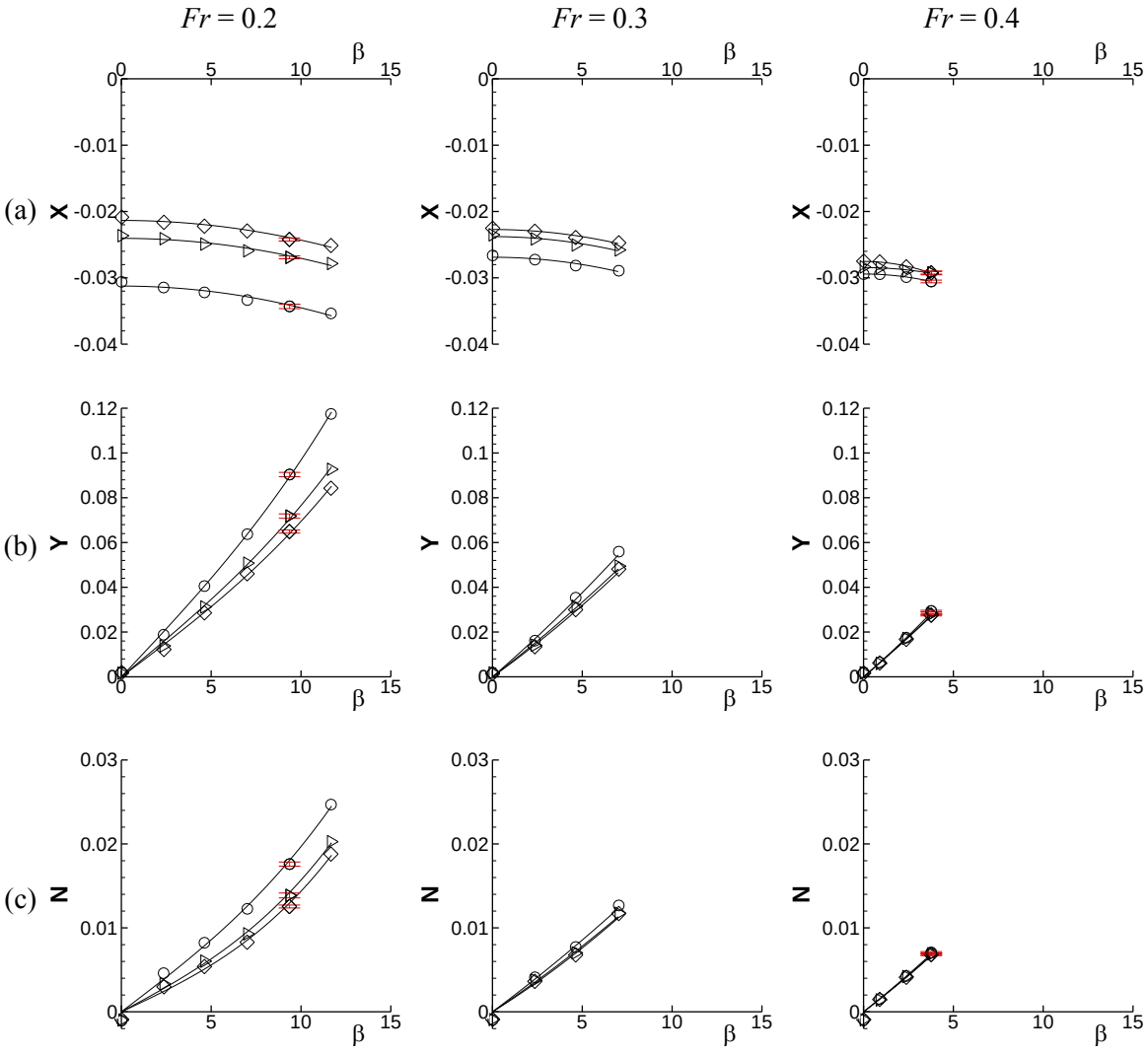


Figure 5-3 Nondimensional forces and moment data for static drift test (corrected for symmetry) at $Fr = 0.2$ (left), 0.3 (center), and 0.4 (right): (a) $X$, (b) $Y$, and (c) $N$. Symbols: ♦ w/o wind, ► half wind, ● full wind.

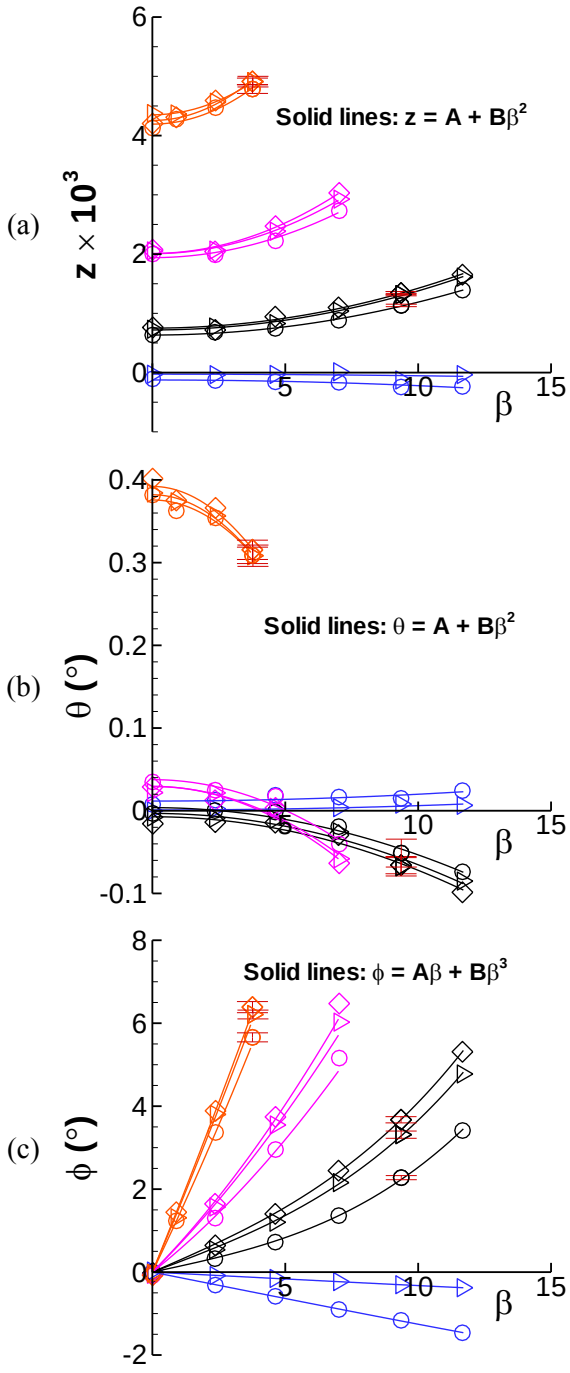


Figure 5-4 Motions data for static drift tests (corrected for symmetry: (a) $z$, (b) $\theta$, and (c) $\phi$. Color codes; blue: $Fr = 0$, black: $Fr = 0.2$, pink: $Fr = 0.3$, orange: $Fr = 0.4$.

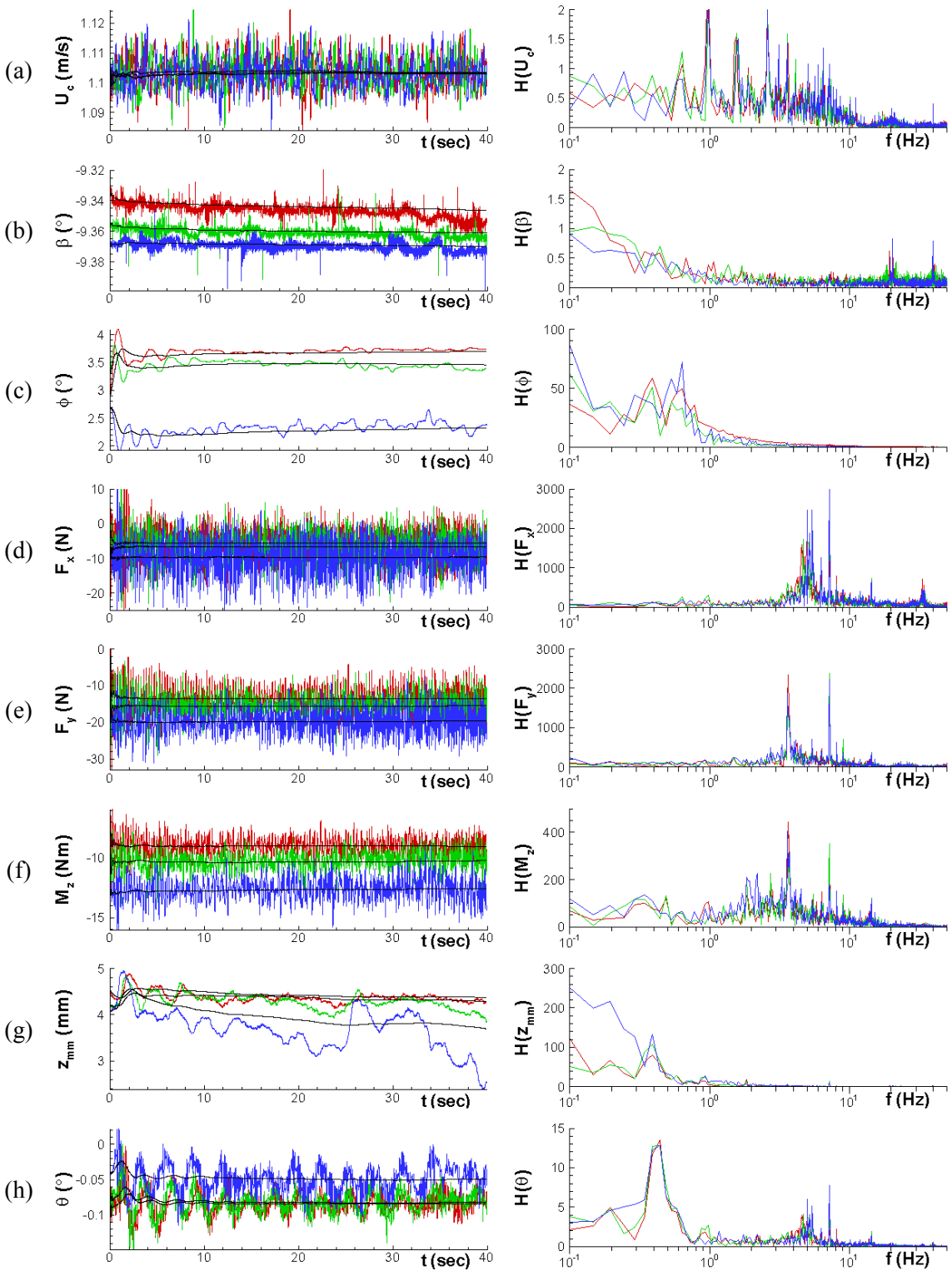


Figure 5-5 Time history (left) and FFT (right) of static drift test data with $Fr = 0.2$ and $\beta = -9.3°$: (a) $U_C$, (b) $\beta$, (c) $\phi$, (d) $F_x$, (e) $F_y$, (f) $M_z$, (g) $z_{mm}$, and (h) $\theta$. Colors; red; w/o wind, green: half wind, blue: full wind, black: running average.

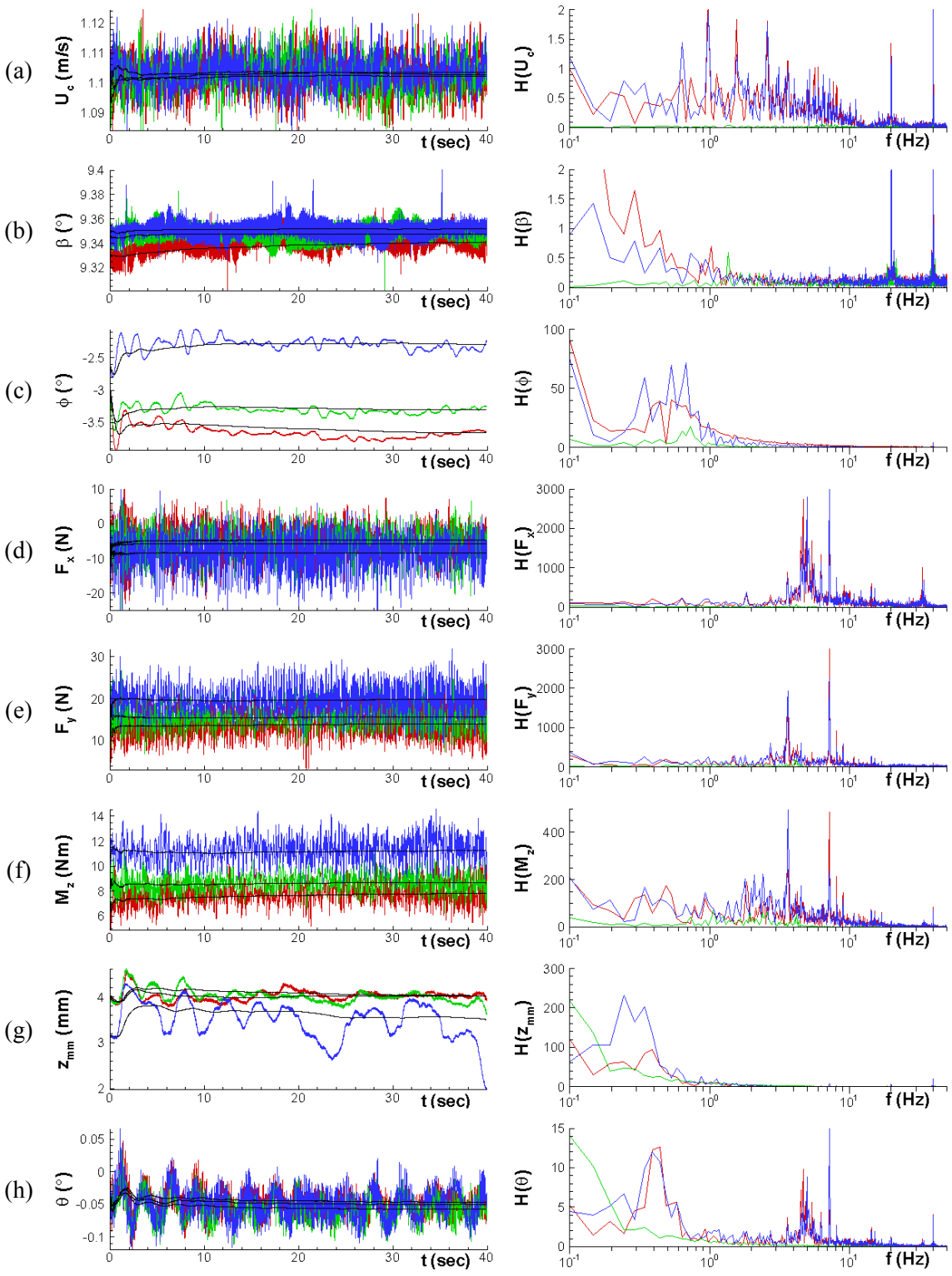


Figure 5-6 Time history (left) and FFT (right) of static drift test data with $Fr = 0.2$ and $\beta = 9.3°$: (a) $U_C$, (b) $\beta$, (c) $\phi$, (d) $F_x$, (e) $F_y$, (f) $M_z$, (g) $z_{mm}$, and (h) $\theta$. Colors; red; w/o wind, green: half wind, blue: full wind, black: running average

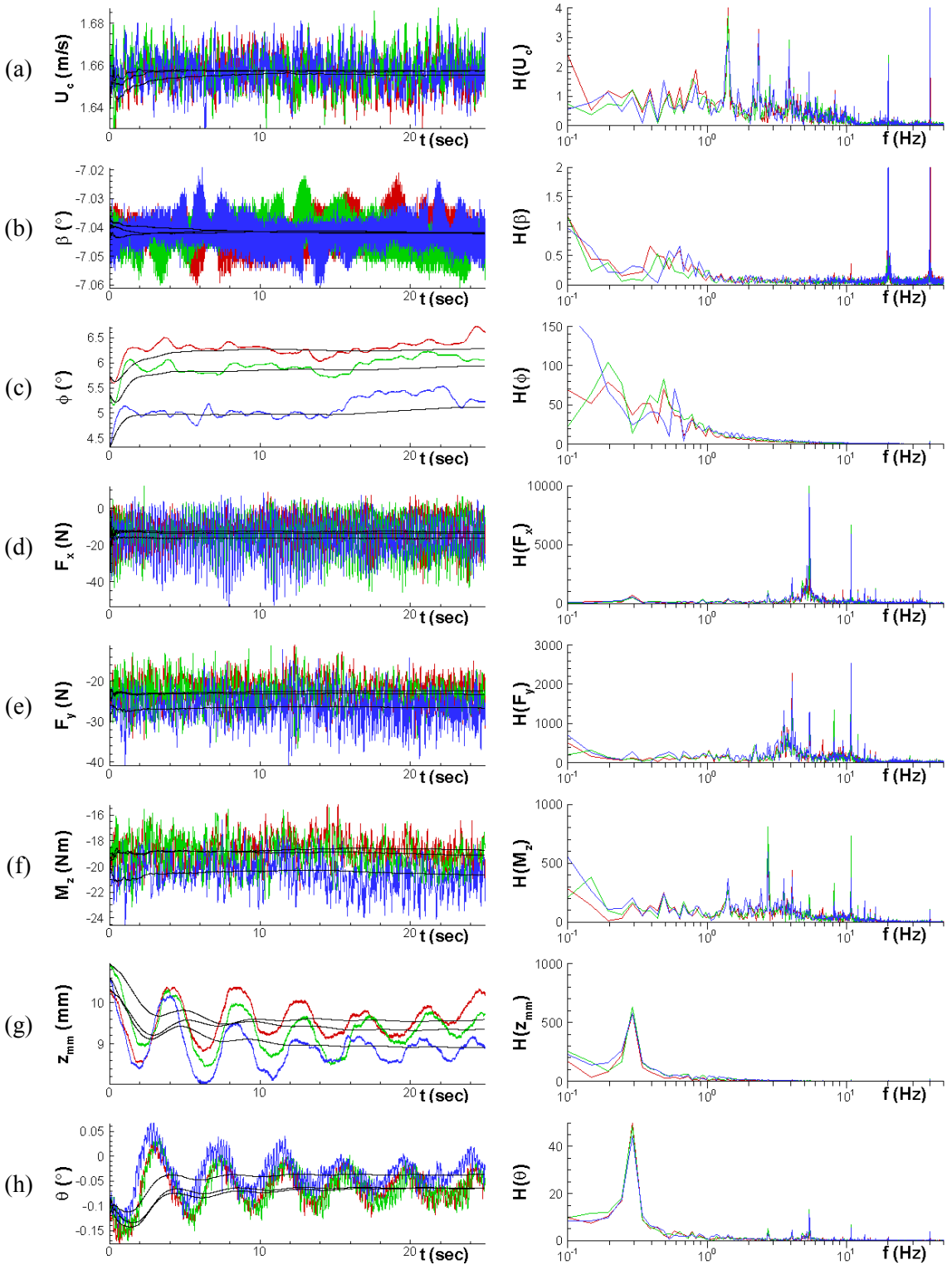


Figure 5-7 Time history (left) and FFT (right) of static drift test data with $Fr = 0.3$ and $\beta = -7°$: (a) $U_C$, (b) $\beta$, (c) $\phi$, (d) $F_x$, (e) $F_y$, (f) $M_z$, (g) $z_{mm}$, and (h) $\theta$. Colors; red; w/o wind, green: half wind, blue: full wind, black: running average.

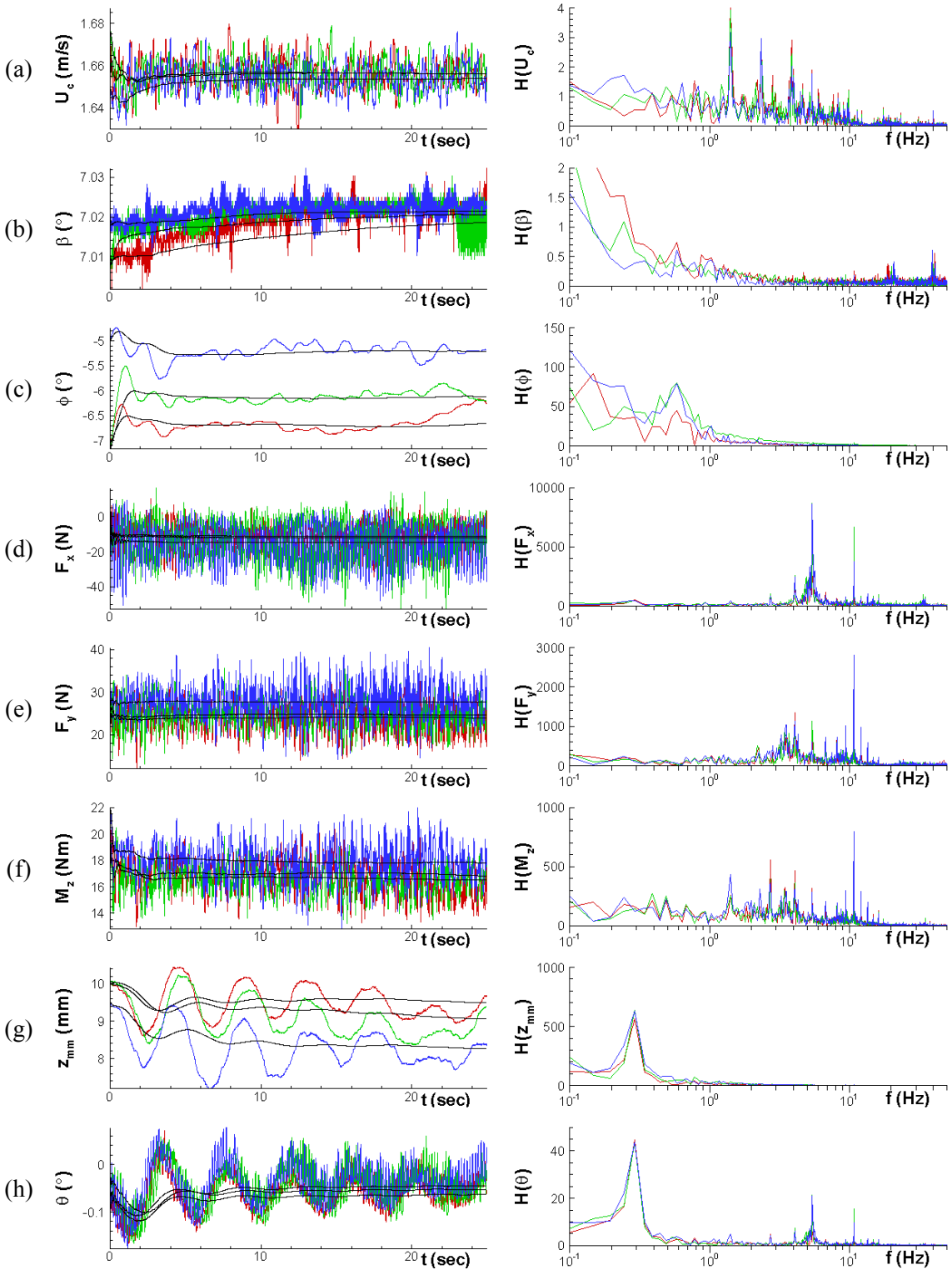


Figure 5-8 Time history (left) and FFT (right) of static drift test data with $Fr = 0.3$ and $\beta = 7°$: (a) $U_C$, (b) $\beta$, (c) $\phi$, (d) $F_x$, (e) $F_y$, (f) $M_z$, (g) $z_{mm}$, and (h) $\theta$. Colors; red; w/o wind, green: half wind, blue: full wind, black: running average

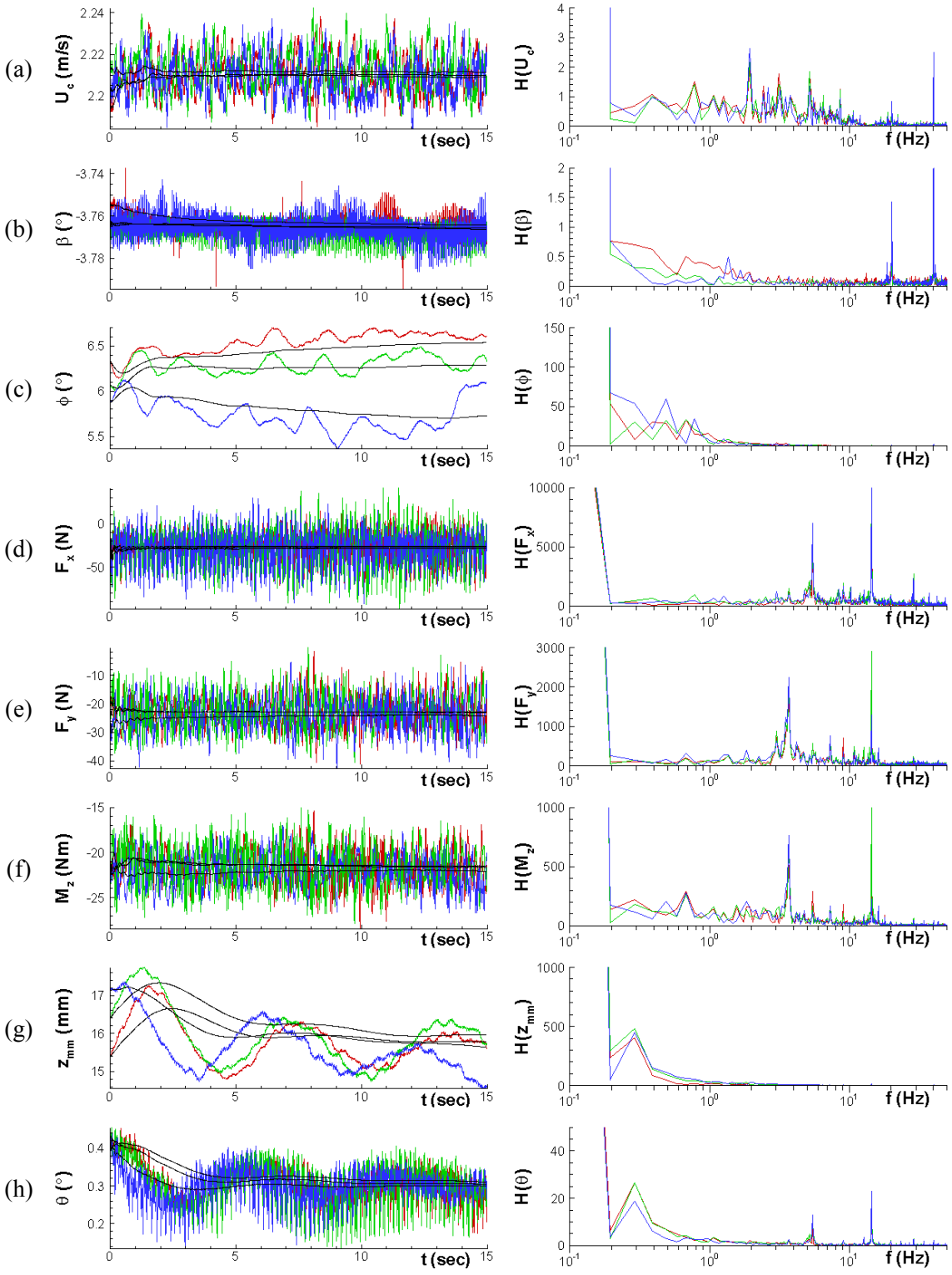


Figure 5-9 Time history (left) and FFT (right) of static drift test data with $Fr = 0.4$ and $\beta = -3.7°$: (a) $U_C$, (b) $\beta$, (c) $\phi$, (d) $F_x$, (e) $F_y$, (f) $M_z$, (g) $z_{mm}$, and (h) $\theta$. Colors; red; w/o wind, green: half wind, blue: full wind, black: running average.

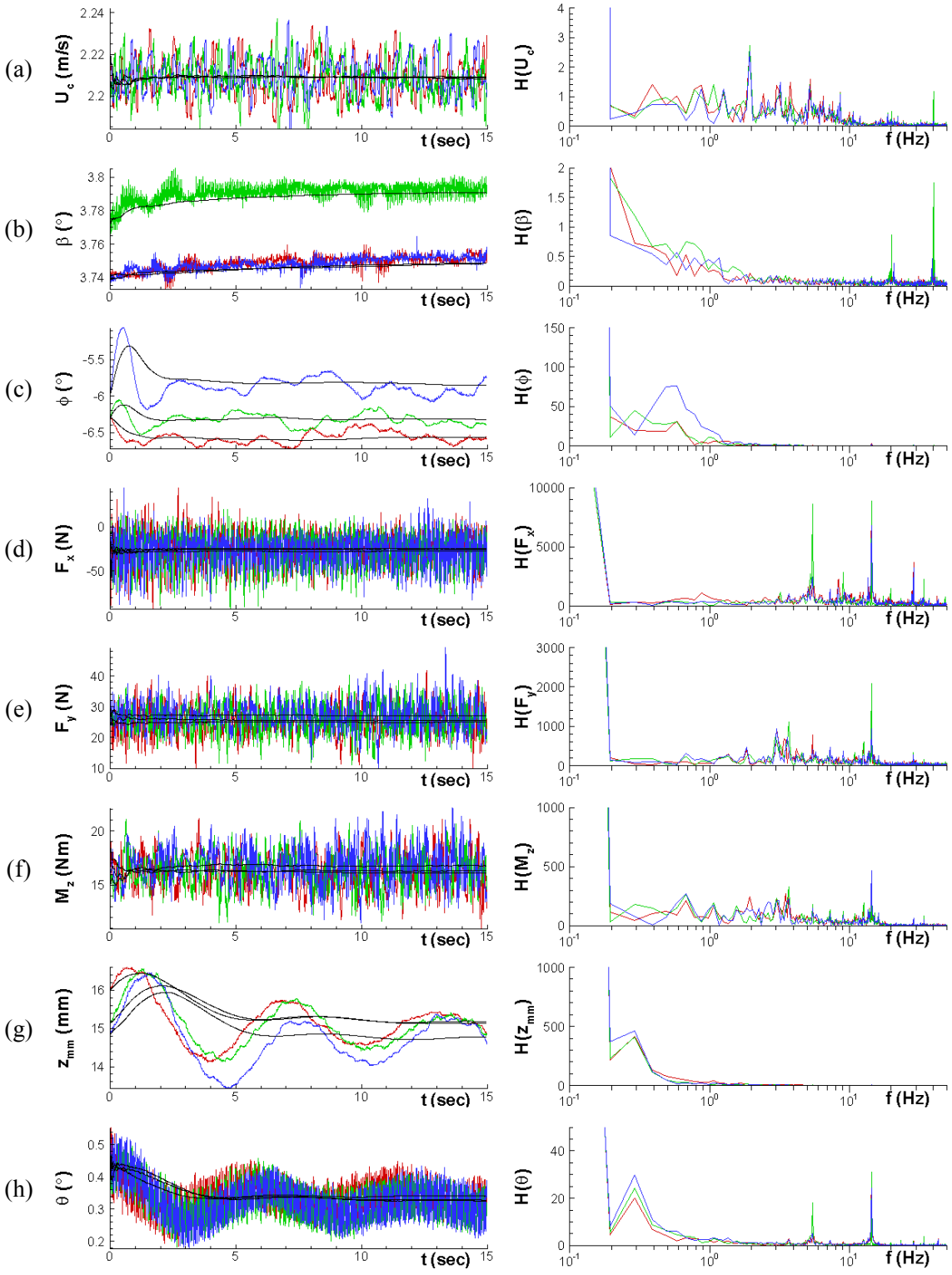


Figure 5-10 Time history (left) and FFT (right) of static drift test data with $Fr = 0.4$ and $\beta = 3.7°$: (a) $U_C$, (b) $\beta$, (c) $\phi$, (d) $F_x$, (e) $F_y$, (f) $M_z$, (g) $z_{mm}$, and (h) $\theta$. Colors; red; w/o wind, green: half wind, blue: full wind, black: running average.

# CHAPTER 6. DYNAMIC PMM TEST

It is important to note an inherent flaw in using PMM tests to measure hydrodynamic derivatives in water with wind which is as follows. PMM tests are designed to acquire hydrodynamic derivatives by measuring the change in response of forces and moments to controlled changes in one independent (state) variable, such as $v$ for static drift and pure sway, and $r$ for pure yaw. The problem arises when wind introduces additional changing parameters. For pure sway tests, the continuously changing drift angle relative to water is different than the drift angle relative to wind due to differing wind and water streamwise velocities. For instance, in the pure sway case of $v_{max}/U_C$ = 0.174, $\beta_{max}$ relative to water is $\tan^{-1}(v_{max}/U_C)$ = 10°. Undergoing this pure sway motion with the full wind condition, $\beta_{max}$ relative to wind is then $\tan^{-1}\left(v_{max}/\mu_{\bar{U}_W}\right)$ = 1.2°. As with pure sway tests, pure yaw tests are defined relative to the water in which yaw rate $r$ is continuously changing and $v = \beta = 0$ at all times. Relative to wind, however, the ship is not undergoing pure yaw. The wind drift angle is continuously changing in addition to yaw rate because wind speed and water speed are not equal. It would not be surprising then, to see that hydrodynamic derivatives are extremely dependent on wind speed and direction. Considering the above arguments, hydrodynamic derivatives found using traditional PMM methods for combined wind and water applications do not constitute true maneuvering coefficients. Nevertheless, it is still quite useful to analyze the effect of wind on hydrodynamic derivatives as a means to gain insight about ship response due to wind.

As a consequence of measuring dynamic forces and moment with a load cell, the measured forces and moment consist of contributions from both hydrodynamic forces and the inertia forces imparted by the acceleration of the ship and 3DOF mounts' mass. (2.46) is used to separate the hydrodynamic contributions from the inertia contributions. Hydrodynamic forces and moment time histories are expressed in FS harmonic forms up

to $6^{th}$-order using the method outlined by Yoon (2009). The necessary sine and cosine harmonic amplitudes are thus obtained. Following the 'multiple run' (MR) method, the sine and cosine harmonic amplitudes are then curve-fitted into the harmonic forms of (2.47), (2.48), and (2.49) in order to obtain hydrodynamic derivatives from the curve-fit polynomial coefficients following Yoon (2009). Two versions of the 'MR' method are used to calculate hydrodynamic derivatives. The first version curve-fits $0^{th}$- or $1^{st}$-order (low-order) forces and moment harmonics such as $X_0$, $Y_0$, $Y_{C1}$, $Y_{S1}$, $N_0$, $N_{C1}$, and $N_{S1}$ to determine both linear and non-linear derivatives and is referred to as the '$MR_L$' method. Alternatively, the second method curve-fits $2^{nd}$- or $3^{rd}$-order (high-order) harmonics such as $X_{C2}$, $Y_{C2}$, $Y_{C3}$, $Y_{S3}$, $N_{C2}$, $N_{C3}$, and $N_{S3}$ to determine only non-linear derivatives and is referred to as the '$MR_H$' method. Repeat test standard deviations of forces and moment harmonics are listed in Tables 6-1, 6-2, and 6-3 for pure sway, pure yaw, and yaw and drift tests, respectively. In general, the higher order harmonics show rather large standard deviations. This suggests that the large scatter in the higher order harmonics may cause curve-fits from the '$MR_H$' method to be less accurate and thus the '$MR_L$' method may be preferred. Linear and non-linear hydrodynamic derivatives determined from the '$MR_L$' method are presented in Tables 6-4, 6-5, and 6-6 for cases without wind, with half wind, and with full wind, respectively. Non-linear hydrodynamic derivatives determined from the '$MR_H$' method are presented in Tables 6-7, 6-8, and 6-9 for cases without wind, with half wind, and with full wind, respectively. Discussion of derivatives and the curve fits used to determine them is continued below. Refer to Table 2-6 for a summary of mathematical models used for the curve-fits.

Fig. 6-1 contains forces and moment harmonics data and the necessary curve-fits for pure sway tests. Symmetry-corrected static drift data is also presented in Fig. 6-1 (a), (c), and (f) as $X_0$, $Y_{C1}$, and $N_{C1}$ harmonics, respectively, for means of comparison. $X_0$, $Y_{C1}$, and $N_{C1}$ harmonics are not directly comparable between static drift and pure sway data due to motions but should be similar. It is important to notice a fundamental difference

in the effects of wind between static drift and pure sway data, which is as follows. In pure sway tests the wind and water $y$-velocities with respect to the ship are both equal to each other no matter the difference in wind and water streamwise velocities because sway motion is perpendicular to both flows. This means that wind should have little to no effect on $Y$ and $N$ amplitudes for pure sway tests, which can be seen in Fig. 6-1. For static drift tests, however, the model is towed at a constant oblique angle to the wind and water. Here, wind and water $y$-velocities with respect to the ship are no longer equal because the ship is no longer oriented with zero heading relative to the differing steamwise velocities of wind and water. This effect can be seen as the clear separation between wind conditions for $Y_{C1}$ and $N_{C1}$ trends from static drift tests in Fig. 6-1 (b) and (f) whereas pure sway trends tend to overlap between wind conditions. This implies that the wind's effect on sway velocity derivatives $X_*$, $X_{vv}$, $Y_v$, $Y_{vvv}$, $N_v$, and $N_{vvv}$ is fundamentally different between static drift and pure sway tests. The difference leads one to question which test yields the correct derivatives, i.e., which test undergoes a more realistic situation in regards to wind direction. A ship undergoing an arbitrary trajectory likely does not experience wind that continually changes direction in accordance to the ship's heading as is simulated with pure sway tests. Therefore, static drift tests may be the more realistic situation when testing wind's effect on sway velocity derivatives. Unfortunately, pure sway tests are the only practical means of analyzing the effect of wind on sway acceleration derivatives $Y_{\dot{v}}$ and $N_{\dot{v}}$ regardless of the apparent artificiality of the imposed wind direction. As a consequence of the maintained zero heading, wind has no obvious effects on all sway derivatives except $X_*$ and $X_{vv}$.

Fig. 6-2 contains forces and moment harmonics data and the necessary curve-fits for pure yaw tests with $Fr$ = 0.2. Curve fits of $X_0$ and effects of wind are as expected. $Y_{S1}$ values are unexpectedly positive when comparing to negative values from pure yaw tests on model 5512 by Yoon (2009). Curve-fits for both models exhibit negative curvature which suggests sign errors are improbable. As a result, $Y_r$ is positive for model

5613 and negative for model 5512 and both models have negative $Y_{rrr}$. An explanation for the discrepancy in $Y_r$ sign is proposed in later discussion. $Y_{S1}$ values are visibly increased by wind which increases $Y_r$ up to 15% and increases $Y_{rrr}$ magnitude by 14%. With $Y_{S1}$ originating from the velocity terms of the mathematical model in (2.48) it follows that the wind increases the 'damping' force imparted by the flow. $N_{S1}$ values, and thus $N_r$ and $N_{rrr}$, are unaffected by wind. $Y_{C1}$ describes the 'added mass' force imparted by the inertia of the flow as it originates from the acceleration terms of (2.48). It can be seen that wind significantly increases the 'added-mass' force causing $Y_{\dot{r}}$ to increase up to 152%. $N_{C1}$ and thus $N_{\dot{r}}$ are similarly affected. Forces and moment harmonics data and the necessary curve fits for pure yaw tests with $Fr$ = 0.3 and 0.4 are shown in Figures 6-3 and 6-4, respectively. Note that harmonics are subject to more scatter at higher ship speeds and wind effects become less distinguishable.

Fig. 6-5 contains forces and moment harmonics data and the necessary curve-fits for yaw and drift tests. Zeroth harmonics of forces and moment are compared with static drift time-averaged values for comparison. Again, although in general agreement, the dynamic motions cause trends to exhibit slightly larger magnitudes than static drift values. Harmonics for pure yaw cases with the same yaw rate of $r$ = 0.3 are also shown as constants in applicable plots. Yaw and drift trends should approach the pure yaw data as $v$ approaches zero. Low-order harmonics $X_0$, $Y_{S1}$, $N_{S1}$, $Y_{C1}$, and $N_{C1}$ show good agreement. Higher-order harmonics such as $X_{C2}$ and $Y_{S3}$ show somewhat acceptable agreement but repeat tests exhibit large scatter. Similar behavior is observed for model 5512 by Yoon (2009). The only $X$-force hydrodynamic derivative of interest for yaw and drift tests is sway and yaw cross-coupled $X_{vr}$ which is determined by the linear curve-fit of $X_{S1}$ harmonics. The observed scatter and poor curve fit, however, propagate to large uncertainty in $X_{vr}$ and thus to the observed wind effect on $X_{vr}$. Zeroth harmonics $Y_0$ and $N_0$ show very coherent trends with good curve fits. As a result, $Y_{vrr}$ and $N_{vrr}$ values are well trusted and the effects of wind are apparent. Wind affects $Y_{vrr}$ up to 1650% and

$N_{vrr}$ up to 56%. $Y_{S1}$ and $N_{S1}$ harmonics also exhibit good curve-fits but with smaller effects due to wind with $Y_{rvv}$ affected up to 26% and $N_{rvv}$ is seemingly unaffected.

Figures 6-6, 6-7, and 6-8 show raw and FS-reconstructed time histories and FFT of pure sway forces, moment, and motions for cases with $\beta_{max}$ = 2°, 4°, and 10°, respectively. Differences in phase between wind conditions are merely due to arbitrary initiation of data acquisition. Notice that FS-reconstructions of forces and moment appear to be representative of the raw data. $z_{mm}$ is the only motion that exhibits discrepancy between the FS-reconstruction and raw data which is likely due to transient error from carriage rail misalignments. Zero heading must be maintained for pure sway tests but $\psi$ undergoes oscillations of ±0.05° due to the inherent play in the scotch-yoke. This may explain for any unexpected zeroth harmonic offsets that occur. Primary frequencies for $F_x$, $z_{mm}$, and $\theta$ must be twice the PMM frequency which is most easily seen in time histories for pure yaw cases. Raw and FS-reconstructed time histories and FFT of pure yaw forces, moment, and motions are shown in Figures 6-9, 6-10, 6-11, 6-12, 6-13, and 6-14 for representative cases with $Fr$ = 0.2 and $r_{max}$ = 0.3, $Fr$ = 0.2 and $r_{max}$ = 0.75, $Fr$ = 0.3 and $r_{max}$ = 0.3, $Fr$ = 0.3 and $r_{max}$ = 0.6, $Fr$ = 0.4 and $r_{max}$ = 0.3, and $Fr$ = 0.4 and $r_{max}$ = 0.45, respectively. These correspond to the repeat test cases ($r_{max}$ = 0.3) and cases with highest yaw rate for each tested $Fr$ value. Figures 6-15, 6-16, and 6-17 show raw and FS-reconstructed time histories and FFT of yaw and drift forces, moment, and motions for cases with $\beta$ = -2°, -4°, and -10°, respectively.

Fig 6-18 displays single period FS-reconstructed hydrodynamic, inertia, and total forces and moment time histories for pure sway tests. The inertia forces and moment are predicted using the prescribed ship accelerations and thus follow a simple sine form. Hydrodynamic forces and moment are revealed when the inertia forces and moment are subtracted from the total (measured) data. The ship undergoes zero acceleration in the $x$-direction for pure sway tests so $F_x$ does not show any inertia contribution. Inertia $F_y$ is considerable and lags hydrodynamic $F_y$ in phase. The effect of inertia on $M_z$ is zero for

pure sway tests because the ship is towed from its center of gravity. Analyzing the decomposition of measured forces and moment into hydrodynamic and inertia components is most important for pure yaw cases because it is here that the measured data defies results from similar PMM tests by Yoon (2009) with model 5512. Figures 6-19, 6-20, and 6-21 show these time histories for pure yaw cases with $Fr$ = 0.2, 0.3, and 0.4, respectively. $F_x$ contains a significant inertia contribution due to the slight time dependence of surge velocity. The more interesting observation, however, is in the response of the hydrodynamic component of $F_y$. Notice that the amplitude of the inertia force meets or exceeds the measured total force but leads in phase. This means the calculated hydrodynamic force $Y$ must lag significantly and may have opposite sign of $Y_{S1}$ harmonic amplitude from the expected response observed from model 5512, causing unexpected positive $Y_r$ as discussed previously. For model 5512, maximum hydrodynamic sway force occurs very near maximum sway amplitude (Yoon, 2009) whereas for model 5613 the maximum hydrodynamic sway force occurs slightly before the model approaches $y$ = 0 which corresponds to a phase lag of approximately 90° from model 5512. Araki et al. (2010) of Osaka University (OU) performed a single calm water pure yaw test of model 5613 with $L$ = 2 m, $Fr$ = 0.452 and $r_{max}L/U_C$ = 0.046 at the National Research Institute of Fisheries Engineering (NRIFE), Japan which is close to one of the current test conditions of $Fr$ = 0.4 and $r_{max}L/U_C$ = 0.05 and is thus used for comparison. Fig. 6-22 shows a comparison of the hydrodynamic component $Y$ between OU model 5613 and IIHR model 5613. Notice both data sets are similar in amplitude with phase causing positive $Y$ at $t$ = 0.25 where $y = y_{max}$. For model 5512, $Y$ is negative at this location (Yoon, 2009). Fig 6-23 displays one period of FS-reconstructed hydrodynamic, inertia, and total forces and moment time histories for yaw and drift tests. The effect of wind on zeroth harmonics $Y_0$ and $N_0$ is seen here.

Fig 6-24 displays single period FS-reconstructed motions time histories of prescribed $\beta$ and responses $z_{mm}$, $\theta$, and $\phi$ for pure sway tests. Effects of wind do not

appear to change with increasing $\beta_{max}$ due to maintained zero heading. Wind's effect on pitch and heave motions appears slightly more exaggerated than those of static tests. Figures 6-25, 6-26, and 6-27 show single period FS-reconstructed motions time histories of prescribed $\psi$ and responses $z_{mm}$, $\theta$, and $\phi$ for pure yaw cases with $Fr$ = 0.2, 0.3, and 0.4, respectively. Surprisingly, wind offsets heave motions up to 1 mm which is approximately 20% of the corresponding amplitude. The effect of wind on pitch is miniscule compared to the relatively large amplitudes experienced for cases with $Fr$ = 0.2 although effects increase for higher $Fr$. As expected, wind has the largest effect on roll motion with the full wind condition completely changing the sign of roll magnitudes in $Fr$ = 0.2 cases. For higher ship speeds the wind does not have the strength to overcome water's effect on roll, however, wind significantly reduces roll magnitudes. It follows that the motion whose wind effect is most sensitive to changing $r_{max}$ (and thus $\psi_{max}$) is indeed roll. Fig 6-28 displays single period FS-reconstructed motions time histories of prescribed $\psi$ and responses $z_{mm}$, $\theta$, and $\phi$ for yaw and drift tests. For small $\beta$, motions resemble the pure yaw case of $r_{max}$ = 0.3 with $Fr$ = 0.2 only slightly offset, as they should. As $\beta$ increases, both offsets and amplitudes increase. The ship experience the largest heading of all tests in the case of $\beta$ = -10° with $\psi_{max}$ = -18.9°. As in pure yaw cases, the full wind condition has the strength to shift apparent roll phase by approximately 180° and decreases the magnitude of the offset by approximately 40%.

Asymmetry about the $xz$-plane as observed in static drift tests is also present in dynamic tests and is seen as even-order harmonics present in time histories of anti-symmetric variables such as $Y$, $N$, and $\phi$ and odd-order harmonics present in symmetric variables such as $X$, $z$, and $\theta$. PMM motions tend to exaggerate observed asymmetry as compared to static drift. The relative effect is larger for small amplitude motions. Asymmetry in response motions is most obvious in pitch time histories with peak-to-peak values of the 2$^{nd}$-order harmonic being affected on the order of 0.1°.

Table 6-1 Pure sway repeat test standard deviations of forces and moment FS harmonics in percent of mean.

| Condition | Wind | $s_{X_0}$ (%) | $s_{X_{C2}}$ (%) | $s_{Y_{C1}}$ (%) | $s_{Y_{S1}}$ (%) | $s_{Y_{C3}}$ (%) | $s_{N_{C1}}$ (%) | $s_{N_{S1}}$ (%) | $s_{N_{C3}}$ (%) |
|---|---|---|---|---|---|---|---|---|---|
| $Fr = 0.2$ $\beta_{max} = 10°$ | none | 0.82 | 19.69 | 0.32 | 0.60 | 7.62 | 0.68 | 4.23 | 4.62 |
| | half | 0.57 | 16.69 | 0.71 | 1.17 | 7.76 | 1.35 | 5.94 | 4.14 |
| | full | 0.43 | 112.74 | 1.25 | 1.95 | 17.08 | 2.20 | 5.89 | 5.89 |

Table 6-2 Pure yaw repeat test standard deviations of forces and moment FS harmonics in percent of mean.

| Condition | Wind | $s_{X_0}$ (%) | $s_{X_{C2}}$ (%) | $s_{Y_{S1}}$ (%) | $s_{Y_{C1}}$ (%) | $s_{Y_{S3}}$ (%) | $s_{N_{S1}}$ (%) | $s_{N_{C1}}$ (%) | $s_{N_{S3}}$ (%) |
|---|---|---|---|---|---|---|---|---|---|
| $Fr = 0.2$ $r_{max} = 0.30$ | none | 0.60 | 100.68 | 2.54 | 4.59 | 21.20 | 0.65 | 8.61 | 9.38 |
| | half | 0.64 | 77.46 | 2.19 | 3.02 | 34.88 | 0.66 | 4.92 | 16.70 |
| | full | 0.49 | 663.92 | 1.99 | 1.53 | 71.29 | 0.89 | 3.30 | 8.97 |
| $Fr = 0.3$ $r_{max} = 0.30$ | none | 0.37 | 138.80 | 7.82 | 2.75 | 17.97 | 0.48 | 25.62 | 40.07 |
| | half | 0.39 | 680.61 | 8.78 | 1.87 | 16.84 | 0.77 | 18.27 | 43.03 |
| | full | 0.67 | 869.18 | 7.28 | 1.34 | 34.14 | 0.54 | 11.56 | 37.12 |
| $Fr = 0.4$ $r_{max} = 0.30$ | none | 1.71 | 124.12 | 7.00 | 4.35 | 10.22 | 0.83 | 10.44 | 9.46 |
| | half | 1.55 | 203.65 | 6.84 | 4.48 | 9.75 | 1.14 | 10.48 | 10.45 |
| | full | 2.98 | 228.50 | 6.09 | 3.02 | 11.70 | 0.87 | 6.35 | 11.80 |

Table 6-3 Yaw and drift repeat test standard deviations of forces and moment FS harmonics in percent of mean.

| Condition | Wind | $s_{X_0}$ (%) | $s_{X_{C2}}$ (%) | $s_{Y_0}$ (%) | $s_{Y_{S1}}$ (%) | $s_{Y_{C1}}$ (%) | $s_{Y_{C2}}$ (%) | $s_{Y_{S3}}$ (%) | $s_{N_0}$ (%) | $s_{N_{S1}}$ (%) | $s_{N_{C1}}$ (%) | $s_{N_{C2}}$ (%) | $s_{N_{S3}}$ (%) |
|---|---|---|---|---|---|---|---|---|---|---|---|---|---|
| $Fr = 0.2$ | none | 0.59 | 45.50 | 1.52 | 11.47 | 14.82 | 5.48 | 22.72 | 1.91 | 1.00 | 8.05 | 4.26 | 17.75 |
| $r_{max} = 0.30$ | half | 0.77 | 41.07 | 2.65 | 14.22 | 8.77 | 8.09 | 34.69 | 3.43 | 1.87 | 7.01 | 7.00 | 25.63 |
| $\beta = 10°$ | full | 0.94 | 15.69 | 2.42 | 17.00 | 5.43 | 7.21 | 32.57 | 2.75 | 1.39 | 5.66 | 9.05 | 16.93 |

Table 6-4 Hydrodynamic derivatives w/o wind ($MR_L$ Method).

| Derivative | $Fr$ = 0.2 | Derivative | $Fr$ = 0.2 | $Fr$ = 0.3 | $Fr$ = 0.4 | Derivative | $Fr$ = 0.2 |
|---|---|---|---|---|---|---|---|
| $X_*$ | -0.0210 (0.99) | $X_*$ | -0.0205 (0.96) | -0.0225 (0.99) | -0.0272 (0.99) | | |
| $X_{vv}$ | -0.1553 (1.57) | $X_{rr}$ | -0.0129 | -0.0151 | -0.0332 | $X_{vr}$ | 0.0184 |
| $Y_v$ | -0.3661 (1.06) | $Y_r$ | 0.0551 | 0.0629 | 0.0629 | $Y_{vrr}$ | -0.0758 |
| $Y_{vvv}$ | -2.7708 (1.52) | $Y_{rrr}$ | -0.0590 | -0.1531 | -0.2401 | $Y_{rvv}$ | -0.7496 |
| $N_v$ | -0.0463 (0.80) | $N_r$ | -0.0618 | -0.0682 | -0.0835 | $N_{vrr}$ | -3.0638 |
| $N_{vvv}$ | -0.7627 (0.91) | $N_{rrr}$ | -0.0410 | -0.0749 | -0.1083 | $N_{rvv}$ | -0.9185 |
| $Y_{\dot{v}}$ | -0.1551 | $Y_{\dot{r}}$ | -0.0165 | -0.0249 | -0.0351 | | |
| $N_{\dot{v}}$ | 0.0115 | $N_{\dot{r}}$ | -0.0046 | -0.0043 | -0.0036 | | |

( ): ratio to static drift

Table 6-5 Hydrodynamic derivatives with half wind ($MR_L$ Method).

| Derivative | $Fr$ = 0.2 | Derivative | $Fr$ = 0.2 | $Fr$ = 0.3 | $Fr$ = 0.4 | Derivative | $Fr$ = 0.2 |
|---|---|---|---|---|---|---|---|
| $X_*$ | -0.0233 (0.97) | $X_*$ | -0.0233 (0.97) | -0.0234 (0.98) | -0.0287 (1.01) | | |
| $X_{vv}$ | -0.1676 (1.67) | $X_{rr}$ | -0.0118 | -0.0165 | -0.0179 | $X_{vr}$ | 0.0126 |
| $Y_v$ | -0.3715 (0.97) | $Y_r$ | 0.0584 | 0.0671 | 0.0652 | $Y_{vrr}$ | -0.9971 |
| $Y_{vvv}$ | -2.7644 (1.41) | $Y_{rrr}$ | -0.0599 | -0.1720 | -0.2411 | $Y_{rvv}$ | -0.8613 |
| $N_v$ | -0.0481 (0.73) | $N_r$ | -0.0619 | -0.0671 | -0.0834 | $N_{vrr}$ | -3.5978 |
| $N_{vvv}$ | -0.7221 (0.90) | $N_{rrr}$ | -0.0417 | -0.0833 | -0.1034 | $N_{rvv}$ | -0.9227 |
| $Y_{\dot{v}}$ | -0.1549 | $Y_{\dot{r}}$ | -0.0223 | -0.0275 | -0.0363 | | |
| $N_{\dot{v}}$ | 0.0115 | $N_{\dot{r}}$ | -0.0057 | -0.0044 | -0.0038 | | |

( ): ratio to static drift

Table 6-6 Hydrodynamic derivatives with full wind ($MR_L$ Method).

| Derivative | $Fr$ = 0.2 | Derivative | $Fr$ = 0.2 | $Fr$ = 0.3 | $Fr$ = 0.4 | Derivative | $Fr$ = 0.2 |
|---|---|---|---|---|---|---|---|
| $X_*$ | -0.0306 (0.98) | $X_*$ | -0.0311 (1.00) | -0.0269 (1.00) | -0.0293 (1.00) | | |
| $X_{vv}$ | -0.1951 (1.79) | $X_{rr}$ | -0.0118 | -0.0130 | -0.0201 | $X_{vr}$ | 0.0120 |
| $Y_v$ | -0.3512 (0.72) | $Y_r$ | 0.0632 | 0.0724 | 0.0682 | $Y_{vrr}$ | -1.3265 |
| $Y_{vvv}$ | -4.0527 (1.74) | $Y_{rrr}$ | -0.0674 | -0.1755 | -0.2634 | $Y_{rvv}$ | -0.9430 |
| $N_v$ | -0.0456 (0.49) | $N_r$ | -0.0620 | -0.0671 | -0.0818 | $N_{vrr}$ | -4.7794 |
| $N_{vvv}$ | -0.9369 (1.40) | $N_{rrr}$ | -0.0422 | -0.0822 | -0.1076 | $N_{rvv}$ | -0.8672 |
| $Y_{\dot{v}}$ | -0.1567 | $Y_{\dot{r}}$ | -0.0415 | -0.0377 | -0.0407 | | |
| $N_{\dot{v}}$ | 0.0110 | $N_{\dot{r}}$ | -0.0096 | -0.0067 | -0.0047 | | |

( ): ratio to static drift

Table 6-7 Hydrodynamic derivatives w/o wind ($MR_H$ Method).

| Derivative | $Fr$ = 0.2 | Derivative | $Fr$ = 0.2 | $Fr$ = 0.3 | $Fr$ = 0.4 | Derivative | $Fr$ = 0.2 |
|---|---|---|---|---|---|---|---|
| $X_{vv}$ | -0.0581 (0.37) | $X_{rr}$ | -0.0009 (0.07) | -0.0139 (0.92) | -0.0136 (0.41) | | |
| $Y_{vvv}$ | -1.8478 (0.67) | $Y_{rrr}$ | -0.1165 (1.97) | -0.1582 (1.03) | -0.2720 (1.13) | $Y_{vrr}$ | -0.7691 (10.15) |
| $N_{vvv}$ | -1.2407 (1.63) | $N_{rrr}$ | -0.0696 (1.70) | -0.1109 (1.48) | -0.1123 (1.04) | $N_{vrr}$ | -0.1880 (0.06) |

( ): ratio to $MR_L$

Table 6-8 Hydrodynamic derivatives with half wind ($MR_H$ Method).

| Derivative | $Fr$ = 0.2 | Derivative | $Fr$ = 0.2 | $Fr$ = 0.3 | $Fr$ = 0.4 | Derivative | $Fr$ = 0.2 |
|---|---|---|---|---|---|---|---|
| $X_{vv}$ | -0.0543 (0.32) | $X_{rr}$ | -0.0019 (0.16) | -0.0126 (0.76) | -0.0129 (0.72) | | |
| $Y_{vvv}$ | -1.7406 (0.63) | $Y_{rrr}$ | -0.1211 (2.02) | -0.1289 (0.75) | -0.2969 (1.23) | $Y_{vrr}$ | -0.8221 (0.82) |
| $N_{vvv}$ | -1.2108 (1.68) | $N_{rrr}$ | -0.0693 (1.66) | -0.1059 (1.27) | -0.1174 (1.14) | $N_{vrr}$ | -0.2137 (0.06) |

( ): ratio to $MR_L$

Table 6-9 Hydrodynamic derivatives with full wind ($MR_H$ Method).

| Derivative | $Fr$ = 0.2 | Derivative | $Fr$ = 0.2 | $Fr$ = 0.3 | $Fr$ = 0.4 | Derivative | $Fr$ = 0.2 |
|---|---|---|---|---|---|---|---|
| $X_{vv}$ | -0.0108 (0.06) | $X_{rr}$ | -0.0011 (0.09) | -0.0138 (1.06) | -0.0190 (0.95) | | |
| $Y_{vvv}$ | -1.6942 (0.42) | $Y_{rrr}$ | -0.1052 (1.56) | -0.1239 (0.71) | -0.2909 (1.10) | $Y_{vrr}$ | -0.7373 (0.56) |
| $N_{vvv}$ | -1.1915 (1.27) | $N_{rrr}$ | -0.0699 (1.66) | -0.1110 (1.35) | -0.1255 (1.17) | $N_{vrr}$ | -0.2301 (0.05) |

( ): ratio to $MR_L$

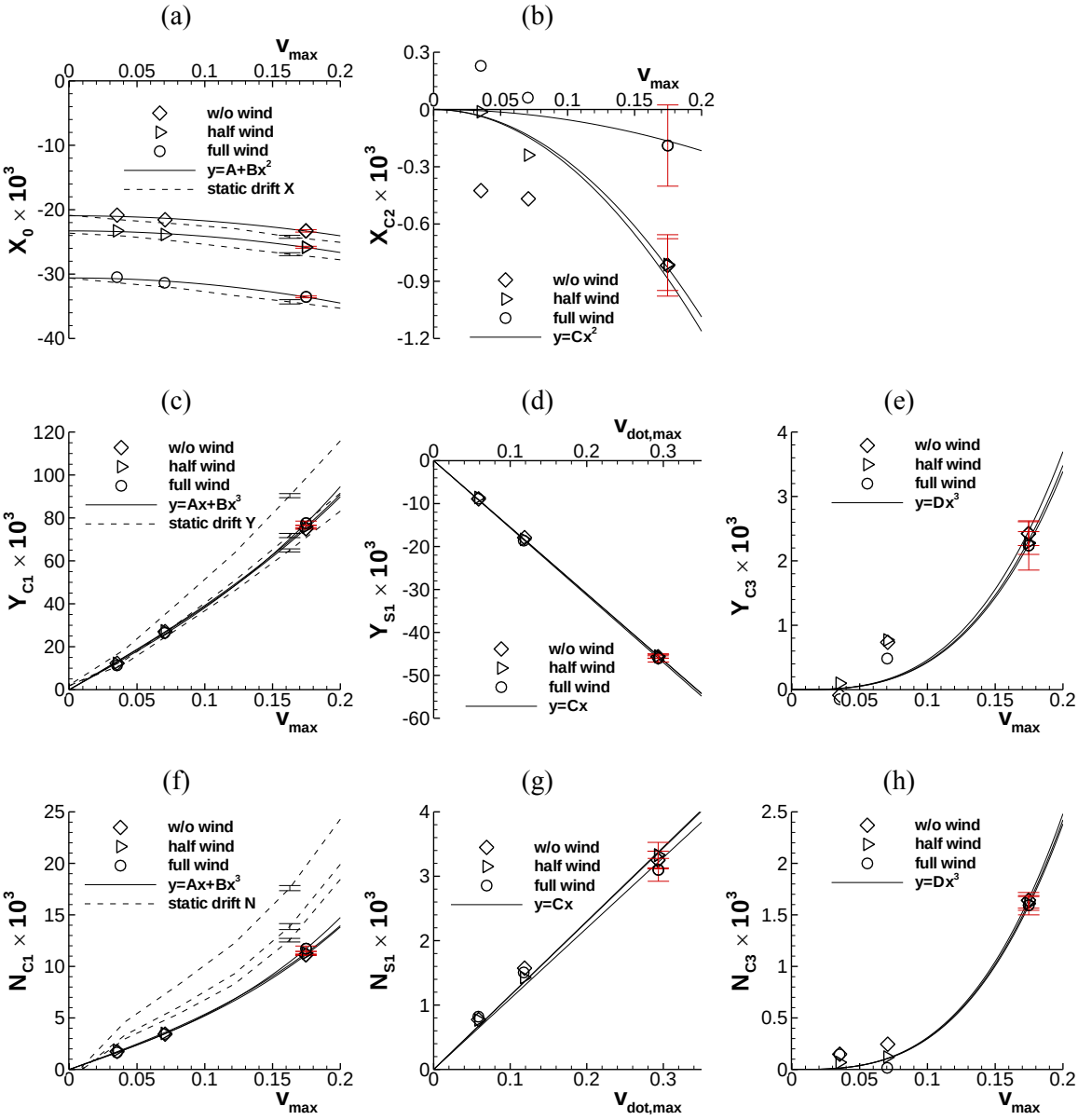


Figure 6-1 Pure sway *X*, *Y*, and *N* data FS harmonics: (a) $X_0$, (b) $X_{C2}$, (c) $Y_{C1}$, (d) $Y_{S1}$, (e) $Y_{C3}$, (f) $N_{C1}$, (g) $N_{S1}$, and (h) $N_{C3}$.

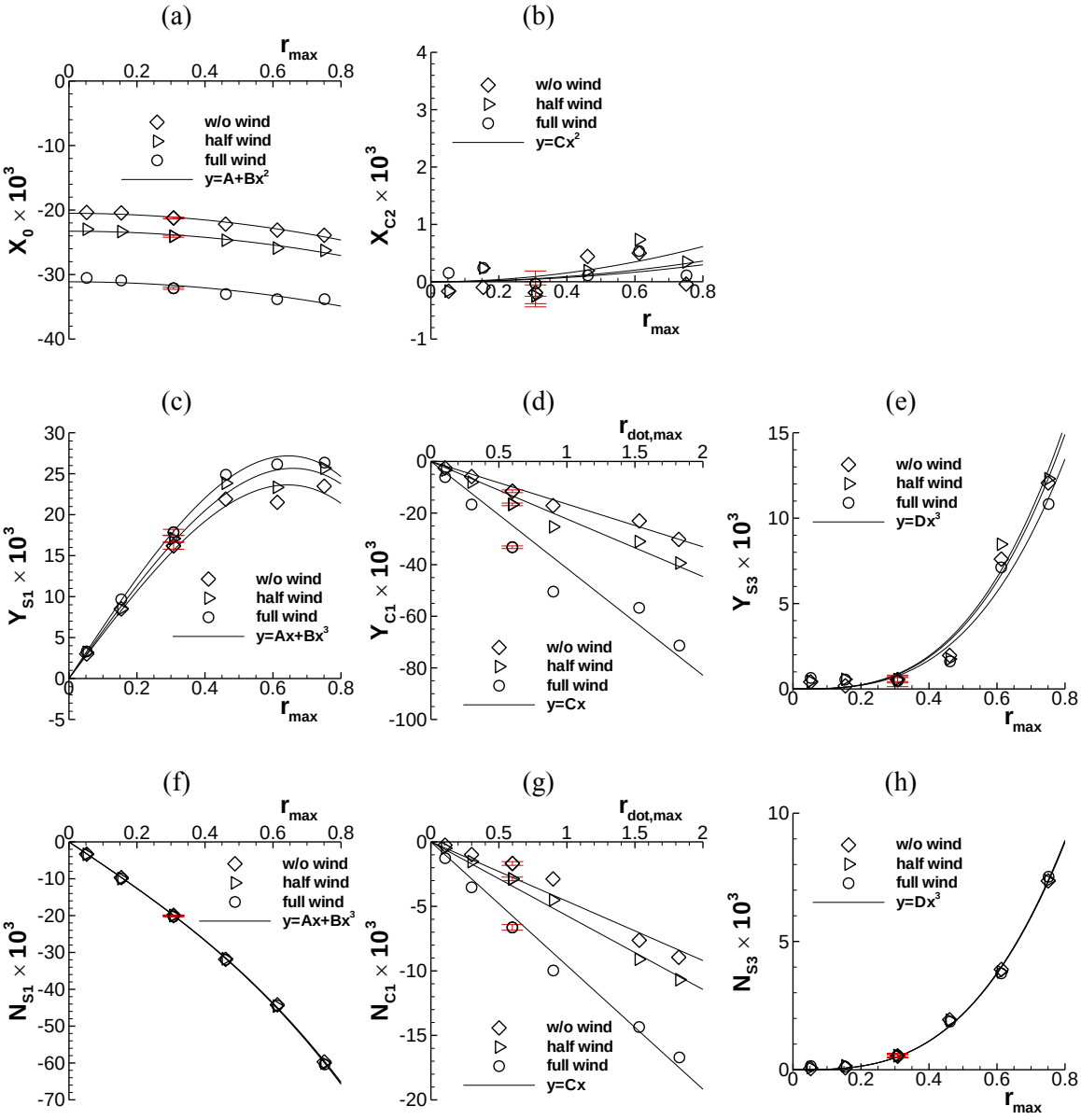


Figure 6-2 Pure yaw *X*, *Y*, and *N* data FS harmonics for $Fr = 0.2$ cases: (a) $X_0$, (b) $X_{C2}$, (c) $Y_{S1}$, (d) $Y_{C1}$, (e) $Y_{S3}$, (f) $N_{S1}$, (g) $N_{C1}$, and (h) $N_{S3}$.

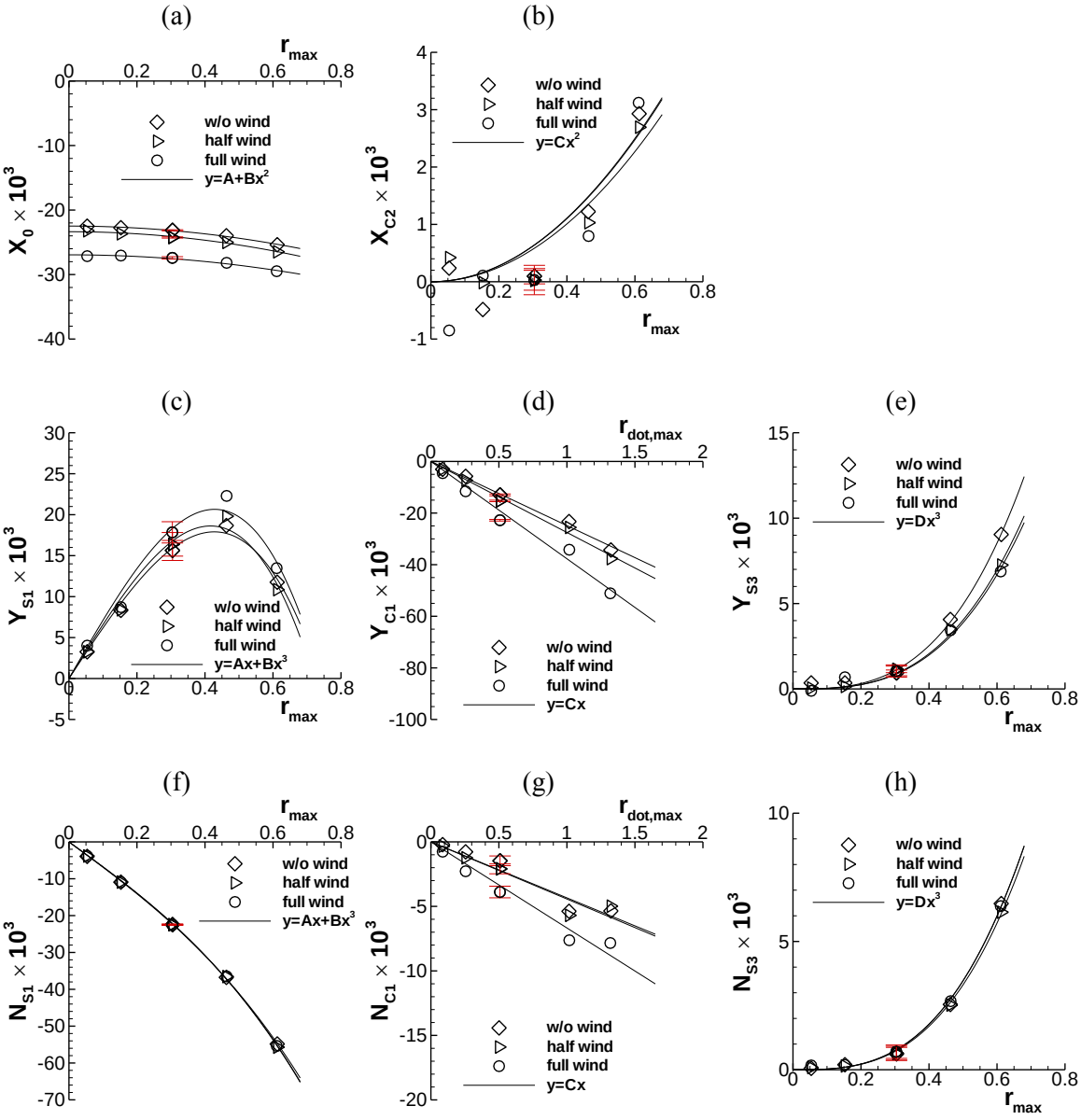


Figure 6-3 Pure yaw *X*, *Y*, and *N* data FS harmonics for $Fr = 0.3$ cases: (a) $X_0$, (b) $X_{C2}$, (c) $Y_{S1}$, (d) $Y_{C1}$, (e) $Y_{S3}$, (f) $N_{S1}$, (g) $N_{C1}$, and (h) $N_{S3}$.

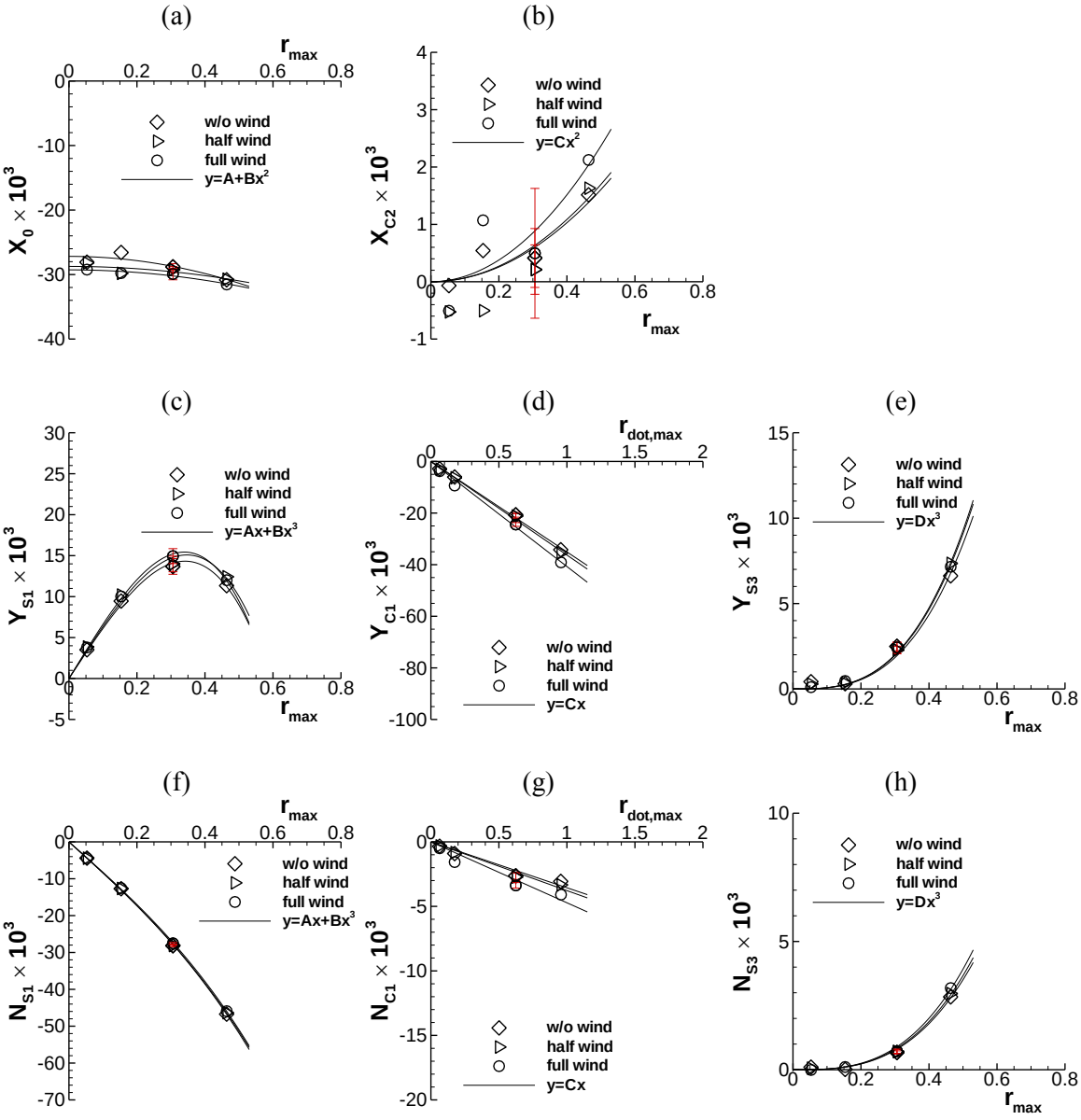


Figure 6-4 Pure yaw *X*, *Y*, and *N* data FS harmonics for $Fr = 0.4$ cases: (a) $X_0$, (b) $X_{C2}$, (c) $Y_{S1}$, (d) $Y_{C1}$, (e) $Y_{S3}$, (f) $N_{S1}$, (g) $N_{C1}$, and (h) $N_{S3}$.

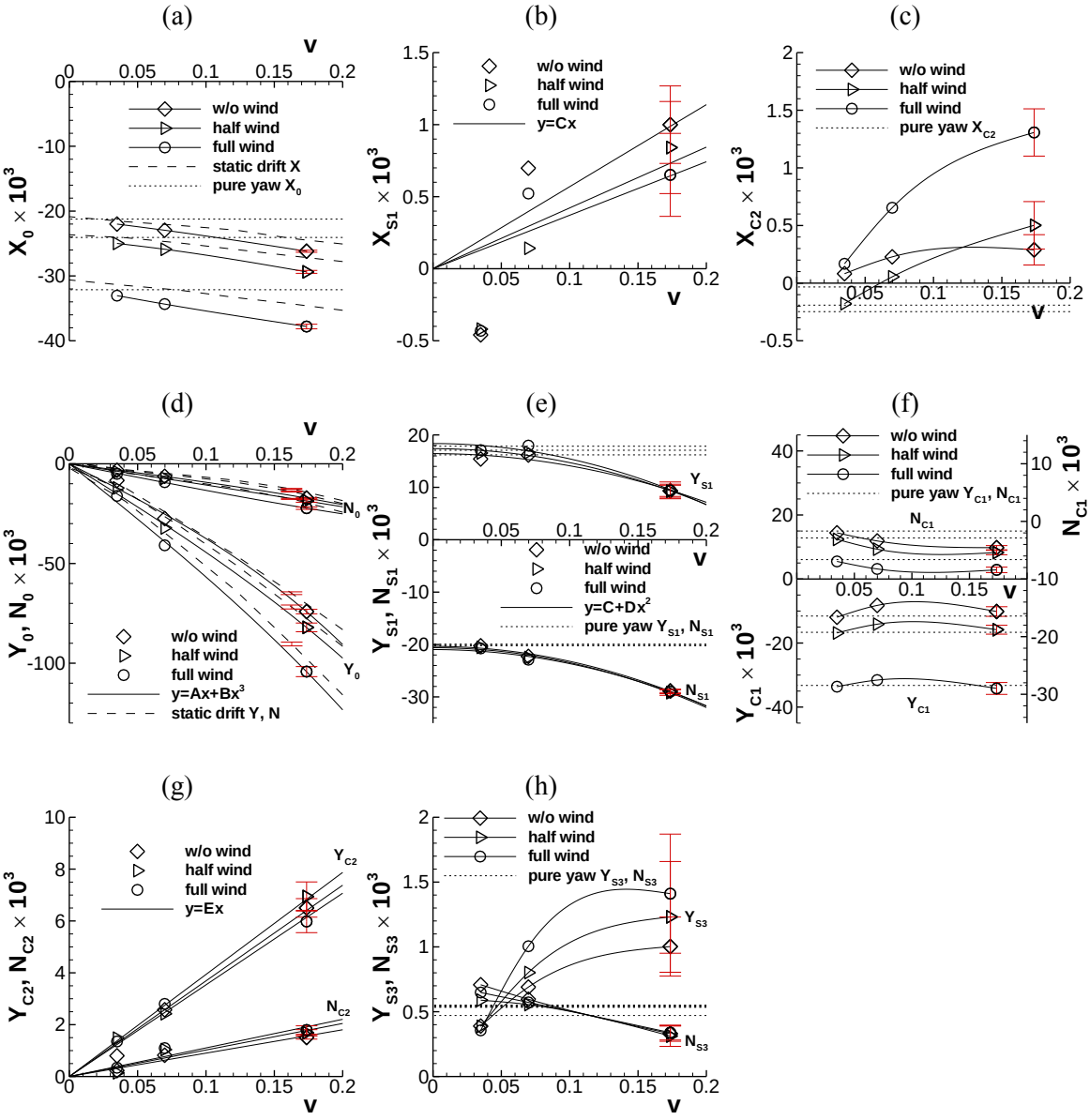


Figure 6-5 Yaw and drift *X*, *Y*, and *N* data FS harmonics: (a) $X_0$, (b) $X_{S1}$, (c) $X_{C2}$, (d) $Y_0$ and $N_0$,(e) $Y_{S1}$ and $N_{S1}$, (f) $Y_{C1}$ and $N_{C1}$, (g) $Y_{C2}$ and $N_{C2}$, and (h) $Y_{S3}$ and $N_{S3}$.

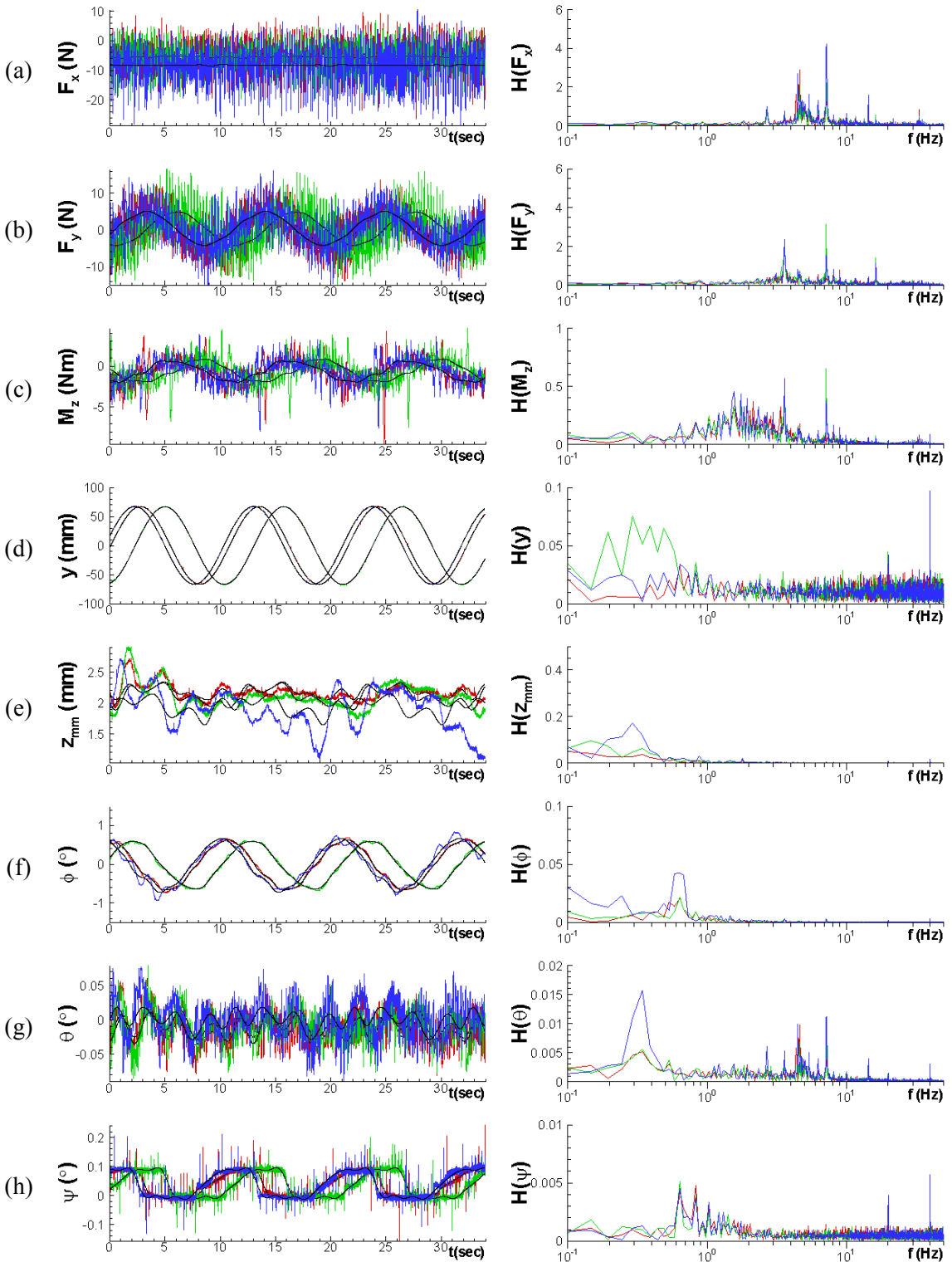


Figure 6-6 Time history (left) and FFT (right) of pure sway test data with $Fr = 0.2$ and $\beta_{max} = 2°$: (a) $F_x$, (b) $F_y$, (c) $M_z$, (d) $y$, (e) $z_{mm}$, (f) $\phi$, (g) $\theta$, and (h) $\psi$. Colors; red: w/o wind, green: half wind, blue: full wind, black: FS-reconstruction.

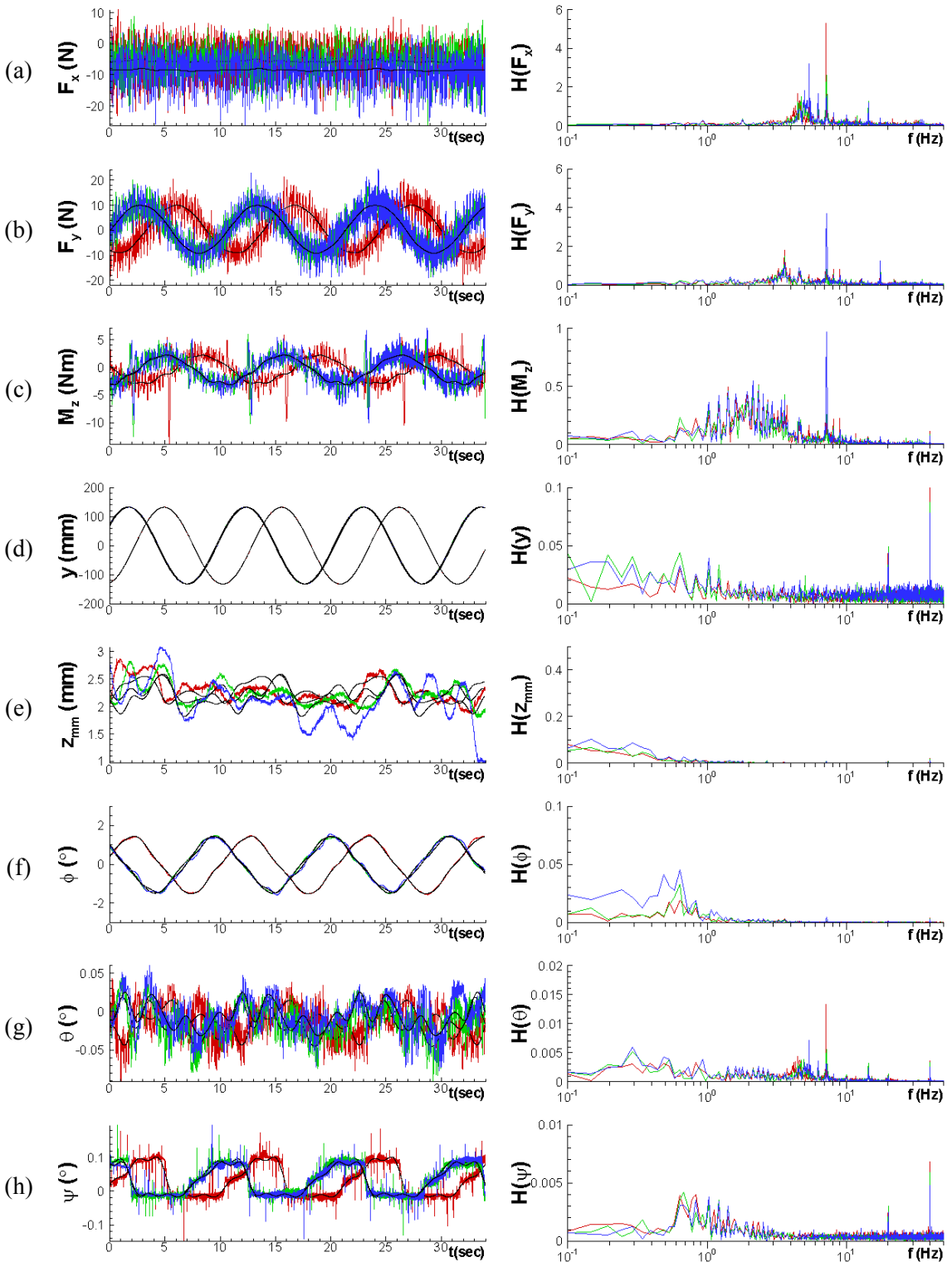


Figure 6-7 Time history (left) and FFT (right) of pure sway test data with $Fr = 0.2$ and $\beta_{max} = 4°$: (a) $F_x$, (b) $F_y$, (c) $M_z$, (d) $y$, (e) $z_{mm}$, (f) $\phi$, (g) $\theta$, and (h) $\psi$. Colors; red: w/o wind, green: half wind, blue: full wind, black: FS-reconstruction.

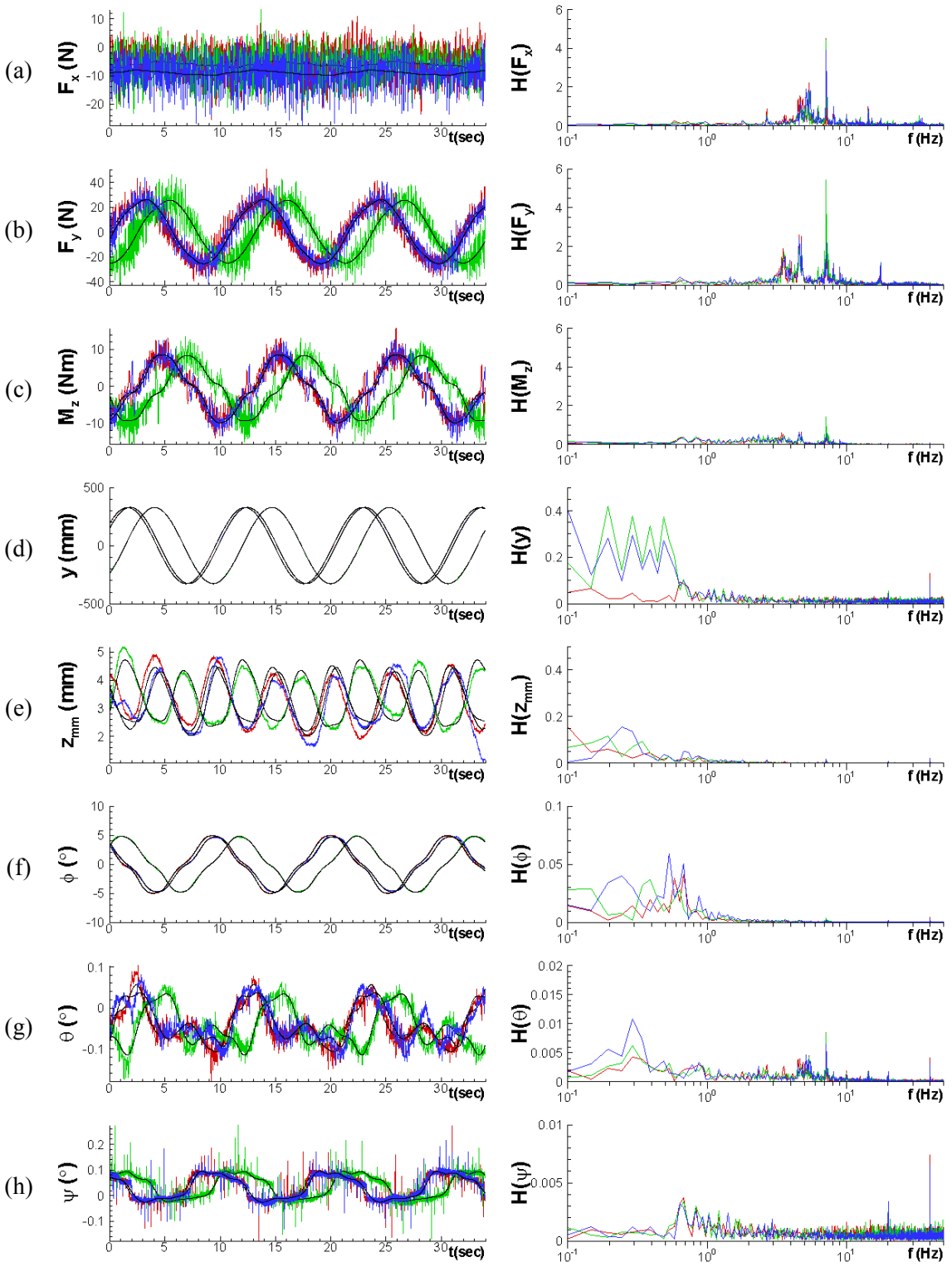


Figure 6-8 Time history (left) and FFT (right) of pure sway test data with $Fr = 0.2$ and $\beta_{max} = 10°$: (a) $F_x$, (b) $F_y$, (c) $M_z$, (d) $y$, (e) $z_{mm}$, (f) $\phi$, (g) $\theta$, and (h) $\psi$. Colors; red: w/o wind, green: half wind, blue: full wind, black: FS-reconstruction.

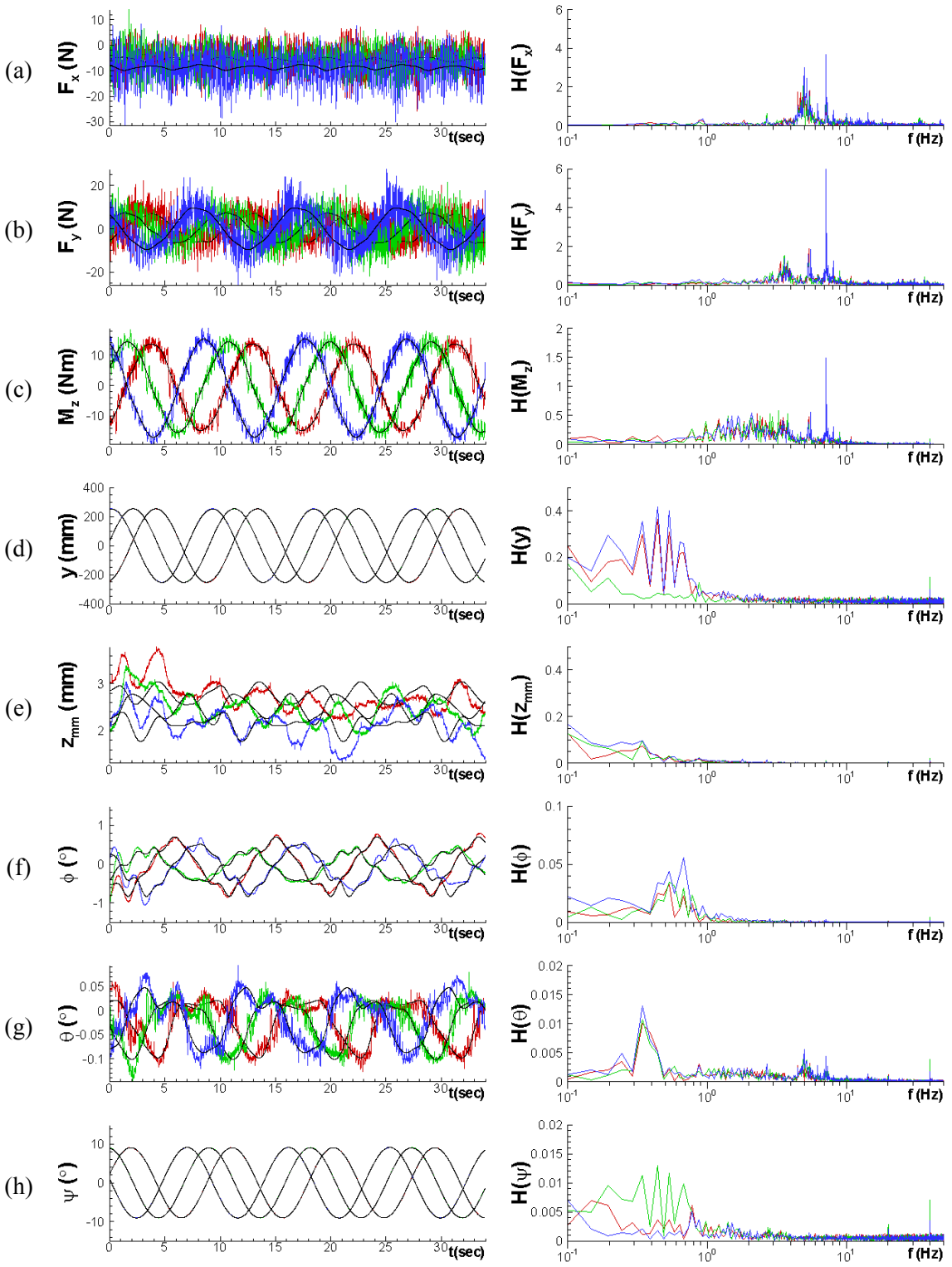


Figure 6-9 Time history (left) and FFT (right) of pure yaw test data with $Fr = 0.2$ and $r_{max} = 0.3$: (a) $F_x$, (b) $F_y$, (c) $M_z$, (d) $y$, (e) $z_{mm}$, (f) $\phi$, (g) $\theta$, and (h) $\psi$. Colors; red: w/o wind, green: half wind, blue: full wind, black: FS-reconstruction.

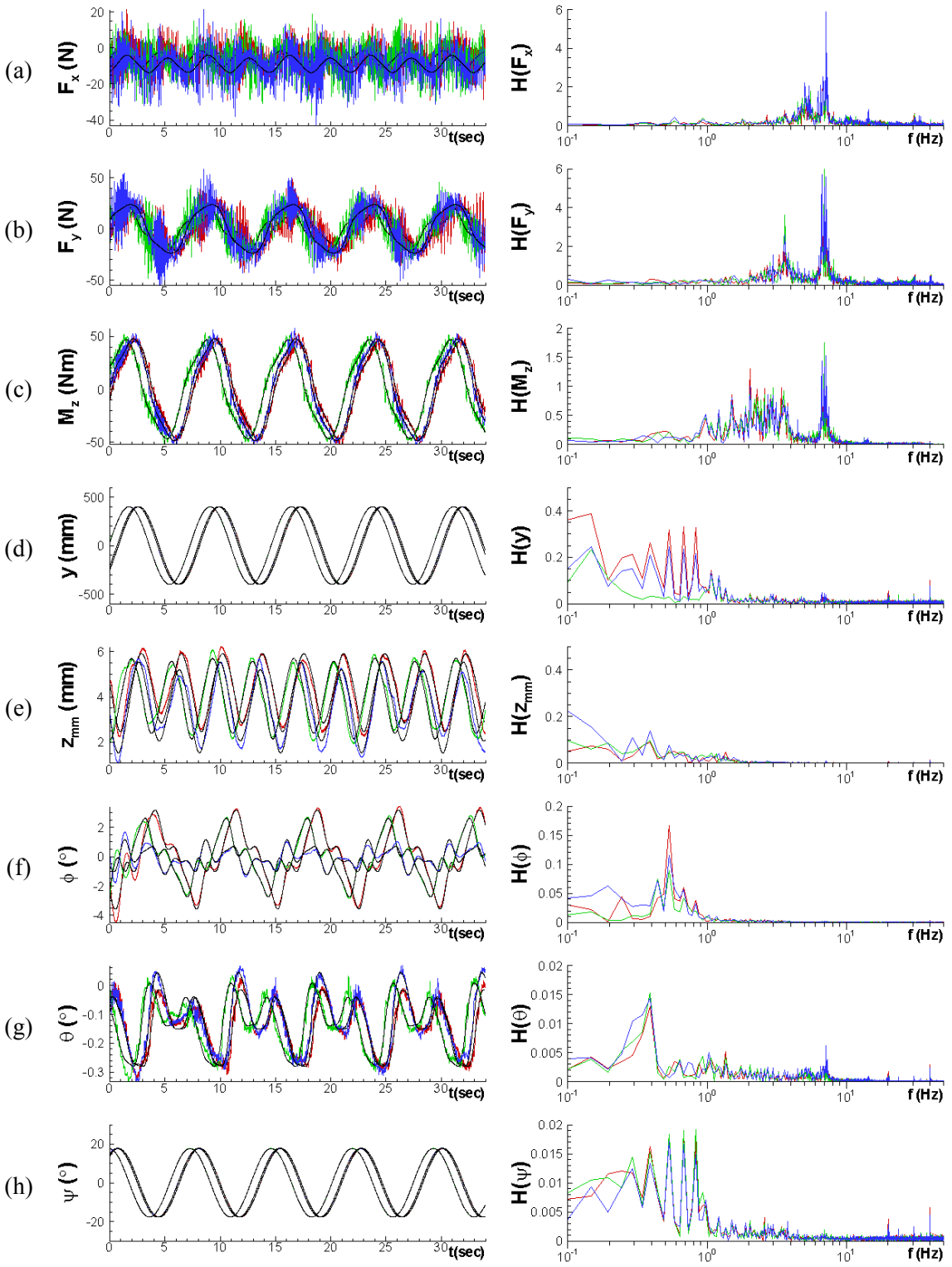


Figure 6-10 Time history (left) and FFT (right) of pure yaw test data with $Fr = 0.2$ and $r_{max} = 0.75$: (a) $F_x$, (b) $F_y$, (c) $M_z$, (d) $y$, (e) $z_{mm}$, (f) $\phi$, (g) $\theta$, and (h) $\psi$. Colors; red: w/o wind, green: half wind, blue: full wind, black: FS-reconstruction.

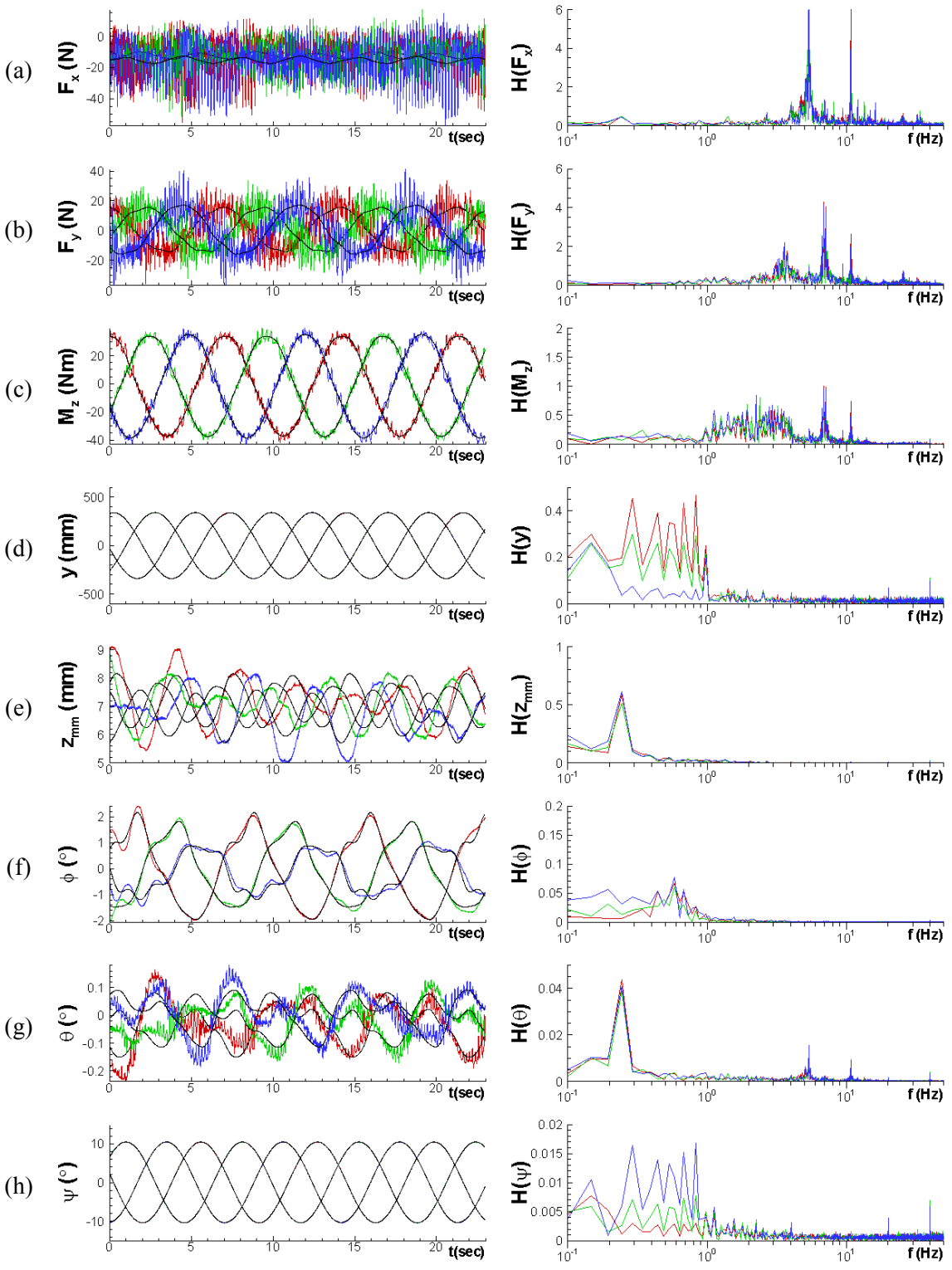


Figure 6-11 Time history (left) and FFT (right) of pure yaw test data with $Fr = 0.3$ and $r_{max} = 0.3$: (a) $F_x$, (b) $F_y$, (c) $M_z$, (d) $y$, (e) $z_{mm}$, (f) $\phi$, (g) $\theta$, and (h) $\psi$. Colors; red: w/o wind, green: half wind, blue: full wind, black: FS-reconstruction.

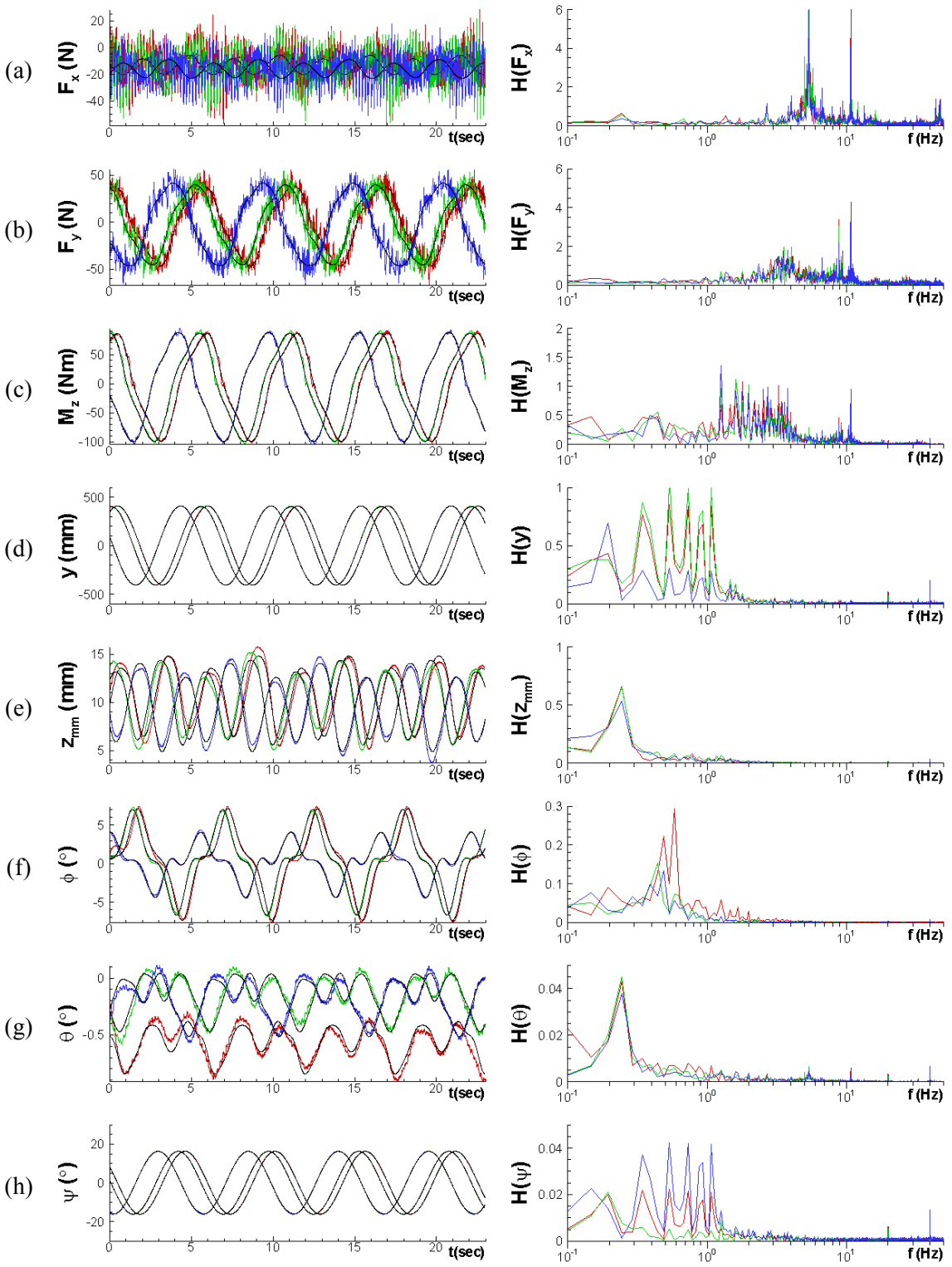


Figure 6-12 Time history (left) and FFT (right) of pure yaw test data with $Fr = 0.3$ and $r_{max} = 0.6$: (a) $F_x$, (b) $F_y$, (c) $M_z$, (d) $y$, (e) $z_{mm}$, (f) $\phi$, (g) $\theta$, and (h) $\psi$. Colors; red: w/o wind, green: half wind, blue: full wind, black: FS-reconstruction.

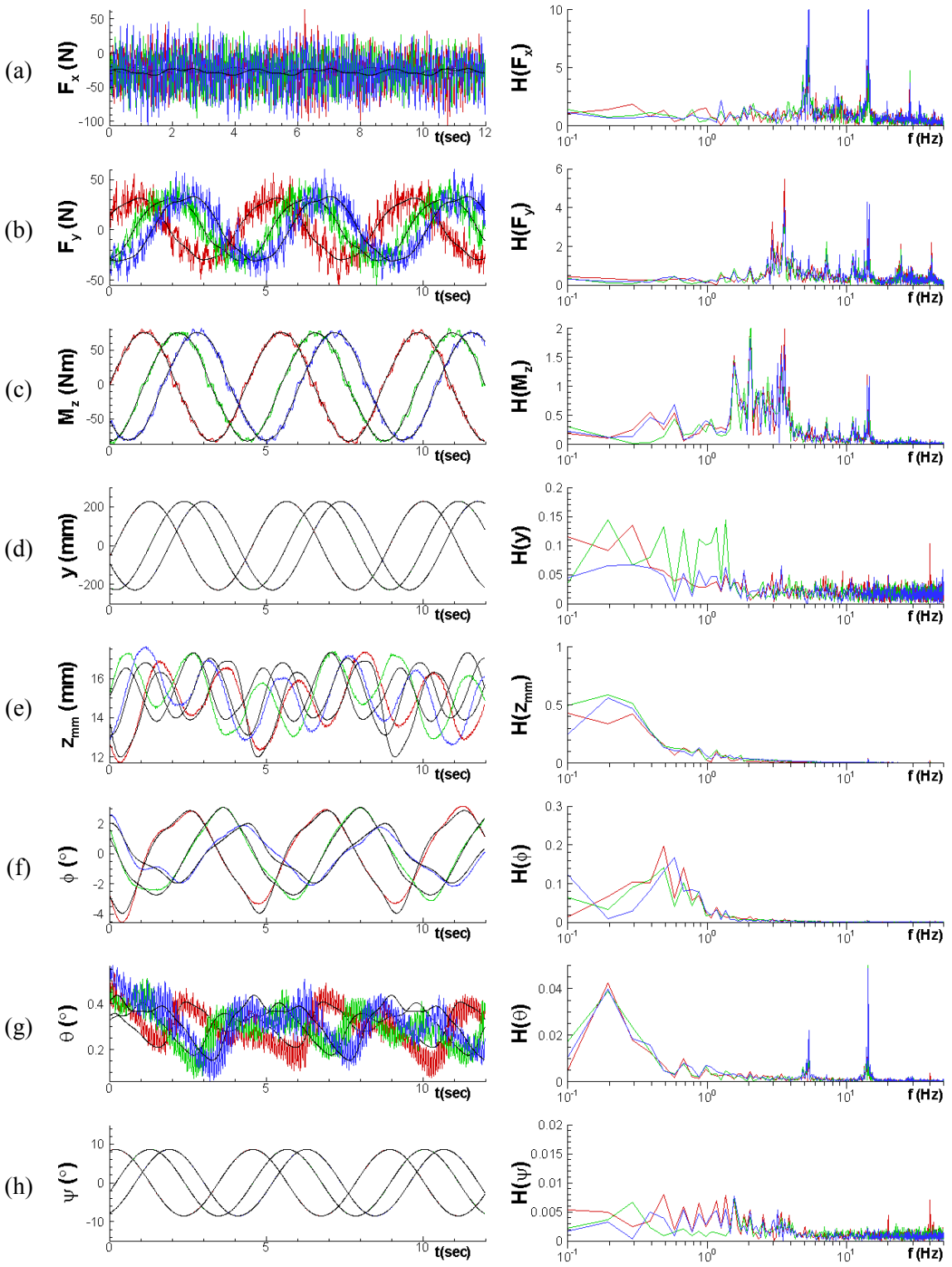


Figure 6-13 Time history (left) and FFT (right) of pure yaw test data with $Fr = 0.4$ and $r_{max} = 0.3$: (a) $F_x$, (b) $F_y$, (c) $M_z$, (d) $y$, (e) $z_{mm}$, (f) $\phi$, (g) $\theta$, and (h) $\psi$. Colors; red: w/o wind, green: half wind, blue: full wind, black: FS-reconstruction.

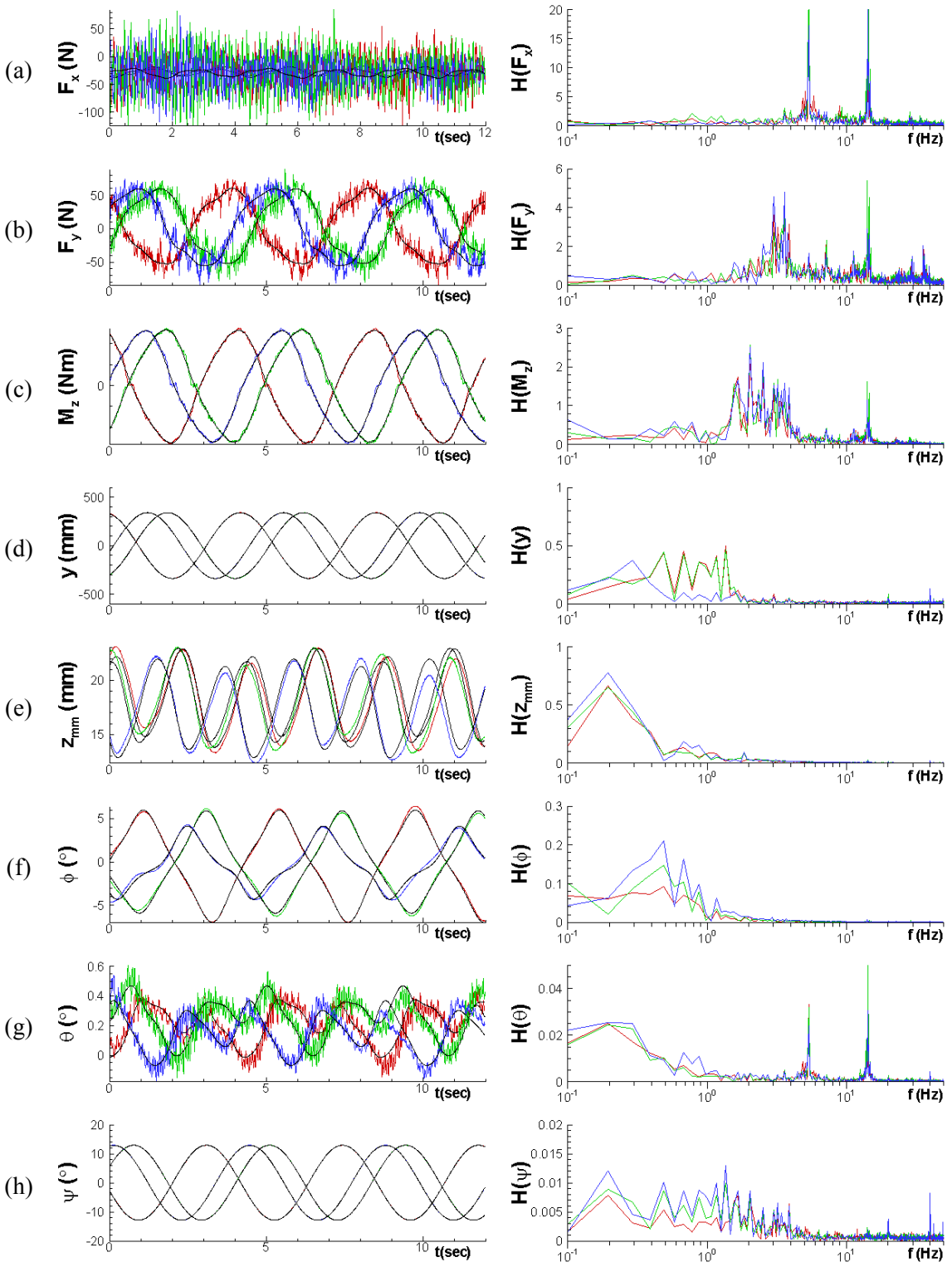


Figure 6-14 Time history (left) and FFT (right) of pure yaw test data with $Fr = 0.4$ and $r_{max} = 0.45$: (a) $F_x$, (b) $F_y$, (c) $M_z$, (d) $y$, (e) $z_{mm}$, (f) $\phi$, (g) $\theta$, and (h) $\psi$. Colors; red: w/o wind, green: half wind, blue: full wind, black: FS-reconstruction.

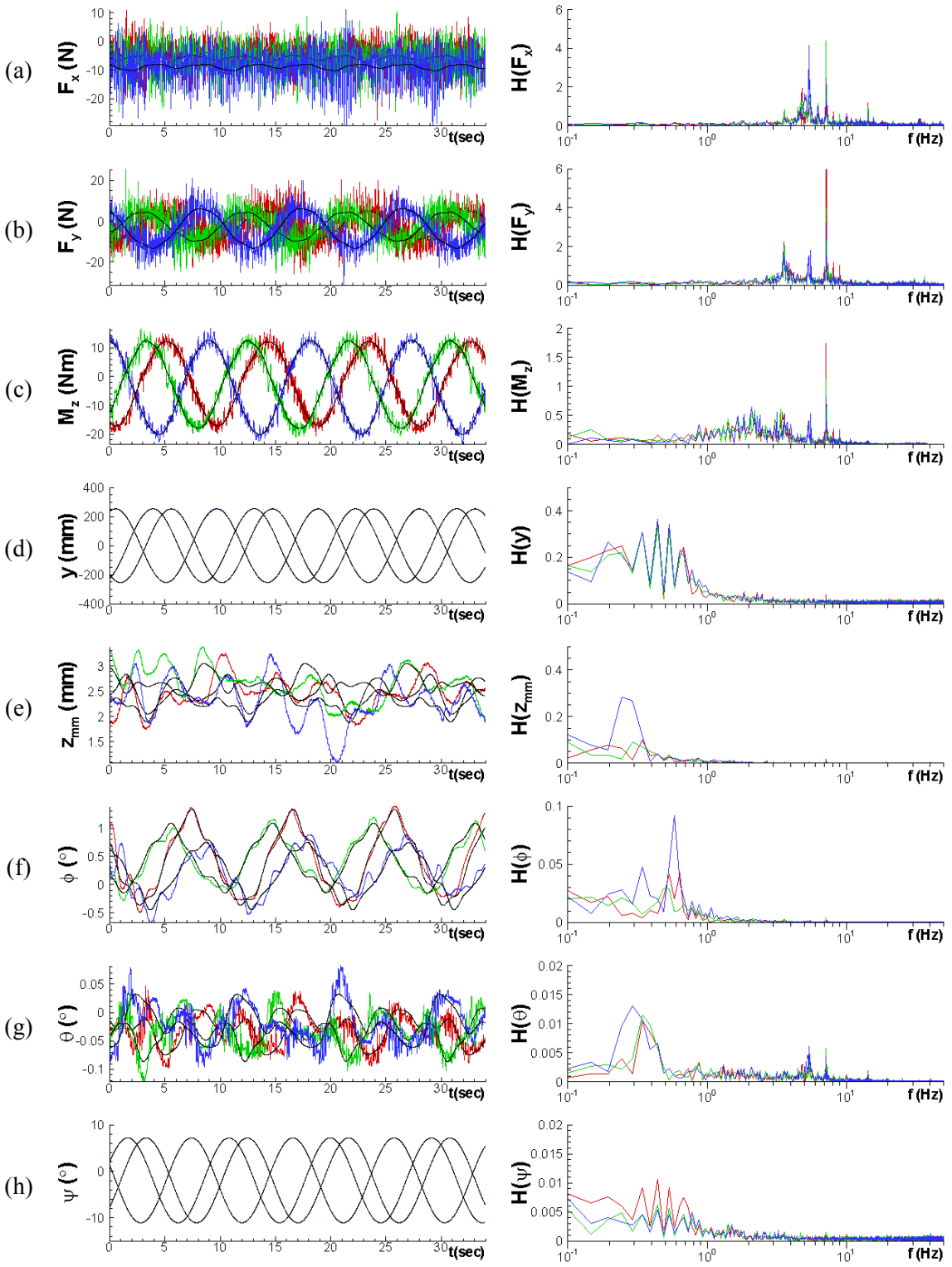


Figure 6-15 Time history (left) and FFT (right) of yaw and drift test data with $\beta$ = -2°: (a) $F_x$, (b) $F_y$, (c) $M_z$, (d) $y$, (e) $z_{mm}$, (f) $\phi$, (g) $\theta$, and (h) $\psi$. Colors; red: w/o wind, green: half wind, blue: full wind, black: FS-reconstruction.

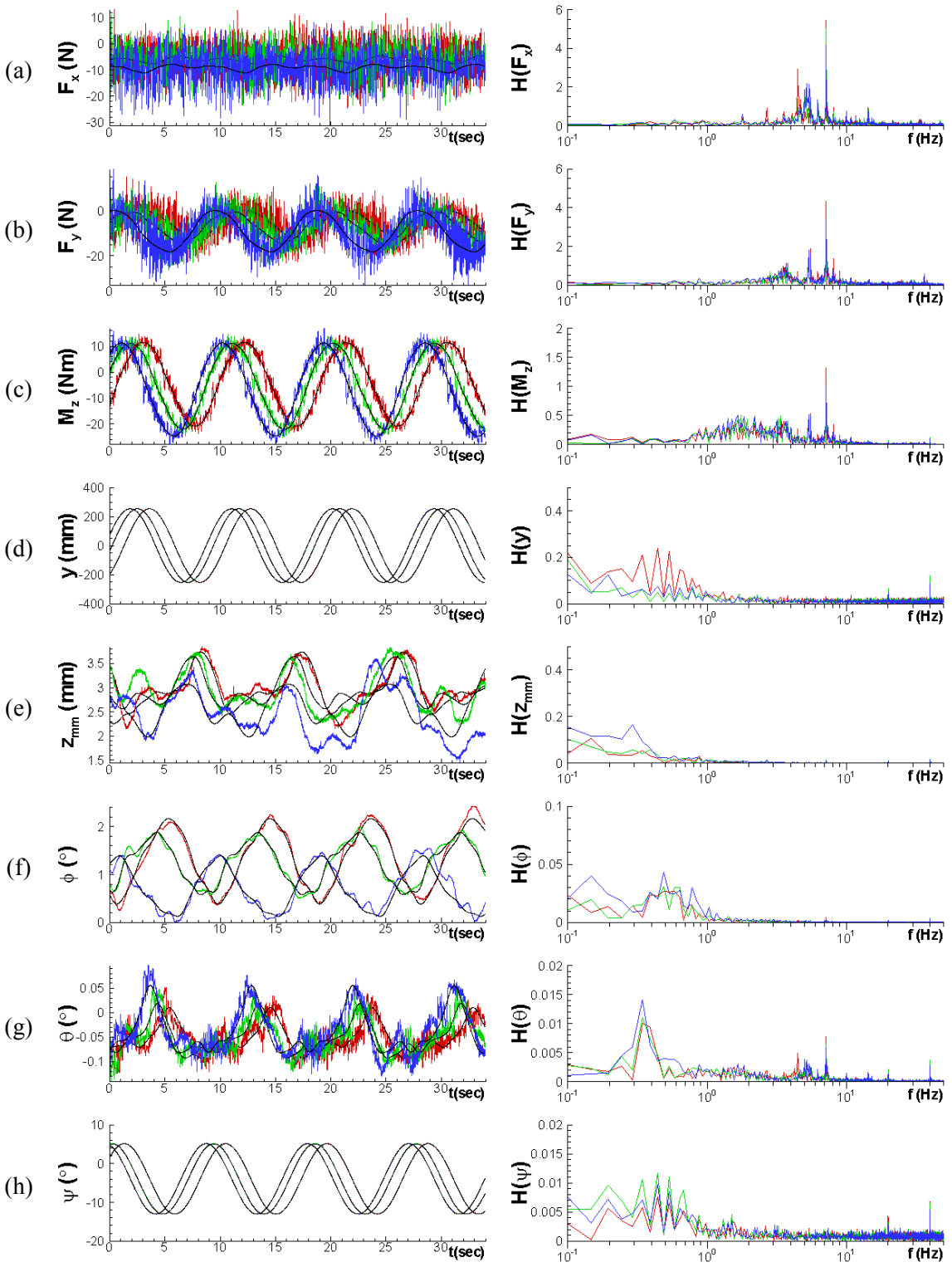


Figure 6-16 Time history (left) and FFT (right) of yaw and drift test data with $\beta$ = -4°: (a) $F_x$, (b) $F_y$, (c) $M_z$, (d) $y$, (e) $z_{mm}$, (f) $\phi$, (g) $\theta$, and (h) $\psi$. Colors; red: w/o wind, green: half wind, blue: full wind, black: FS-reconstruction.

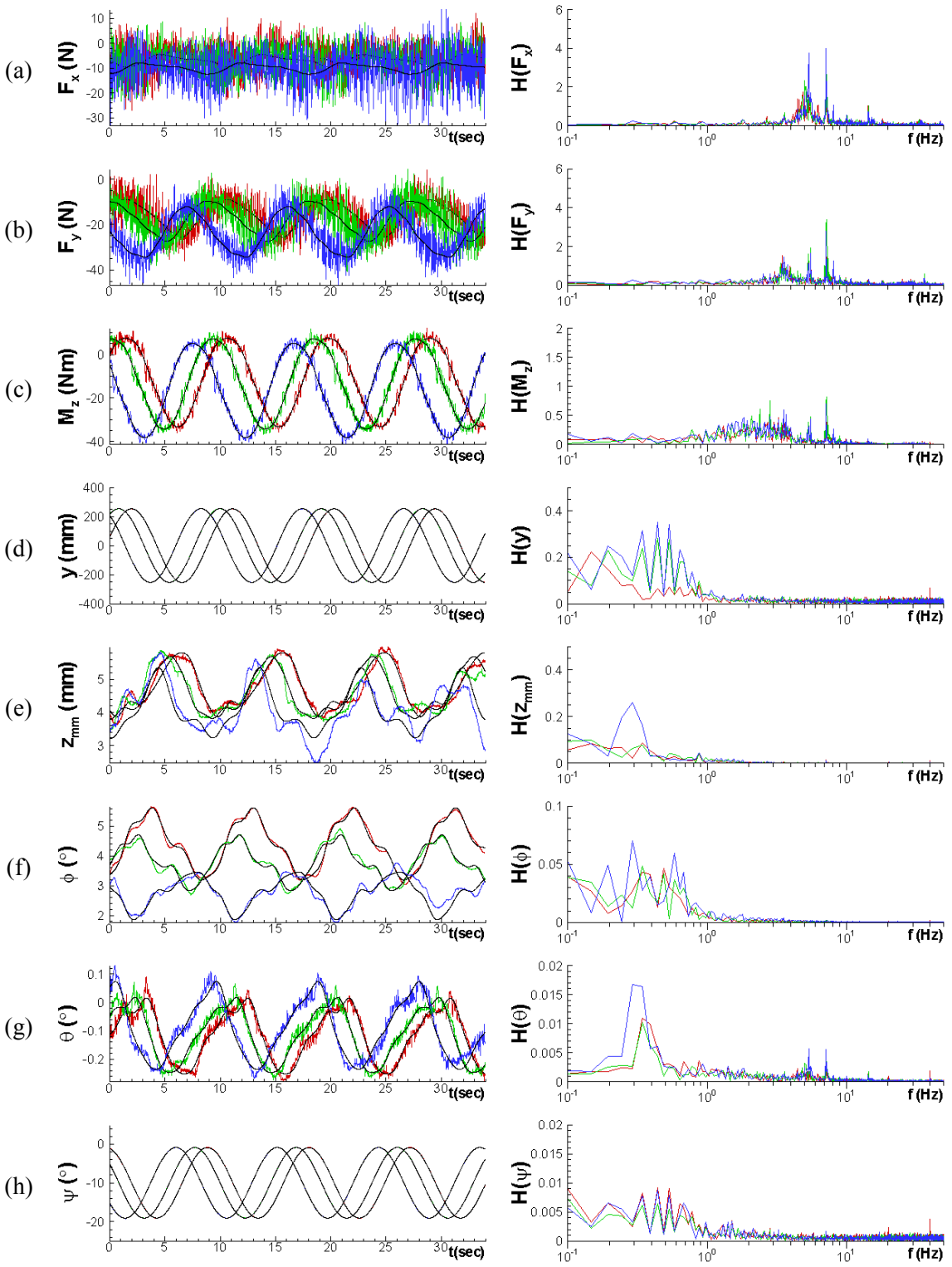


Figure 6-17 Time history (left) and FFT (right) of yaw and drift test data with $\beta$ = -10°: (a) $F_x$, (b) $F_y$, (c) $M_z$, (d) $y$, (e) $z_{mm}$, (f) $\phi$, (g) $\theta$, and (h) $\psi$. Colors; red: w/o wind, green: half wind, blue: full wind, black: FS-reconstruction.

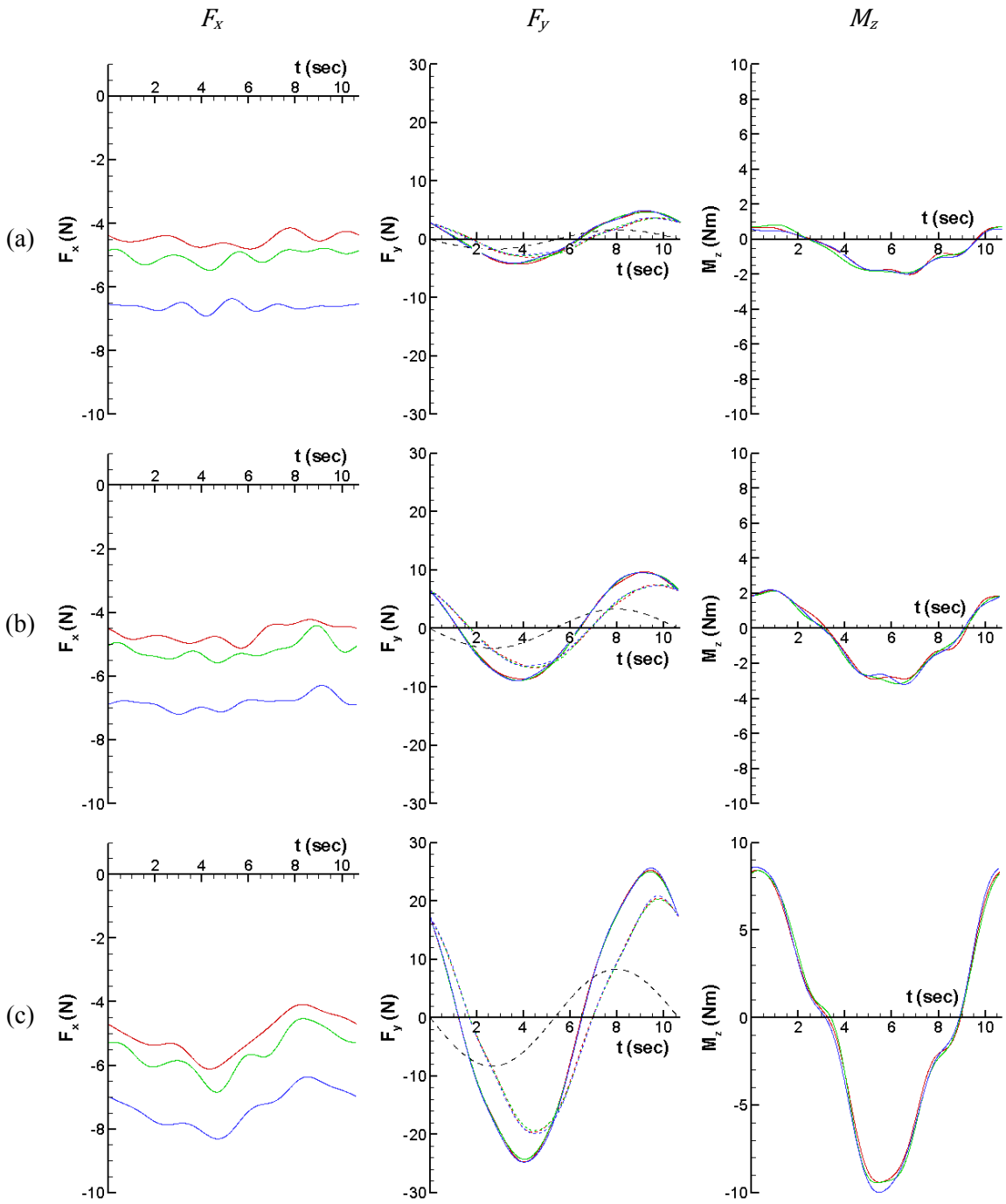


Figure 6-18 FS reconstructed time history of total, inertia, and hydrodynamic $F_x$ (left), $F_y$ (center), and $M_z$ (right) for pure sway tests with $Fr = 0.2$: (a) $\beta_{max} = 2°$, (b) $\beta_{max} = 4°$, and (c) $\beta_{max} = 10°$. Colors, symbols; red: w/o wind, green: half wind, blue: full wind, — total, --- inertia, ⋯ hydrodynamic.

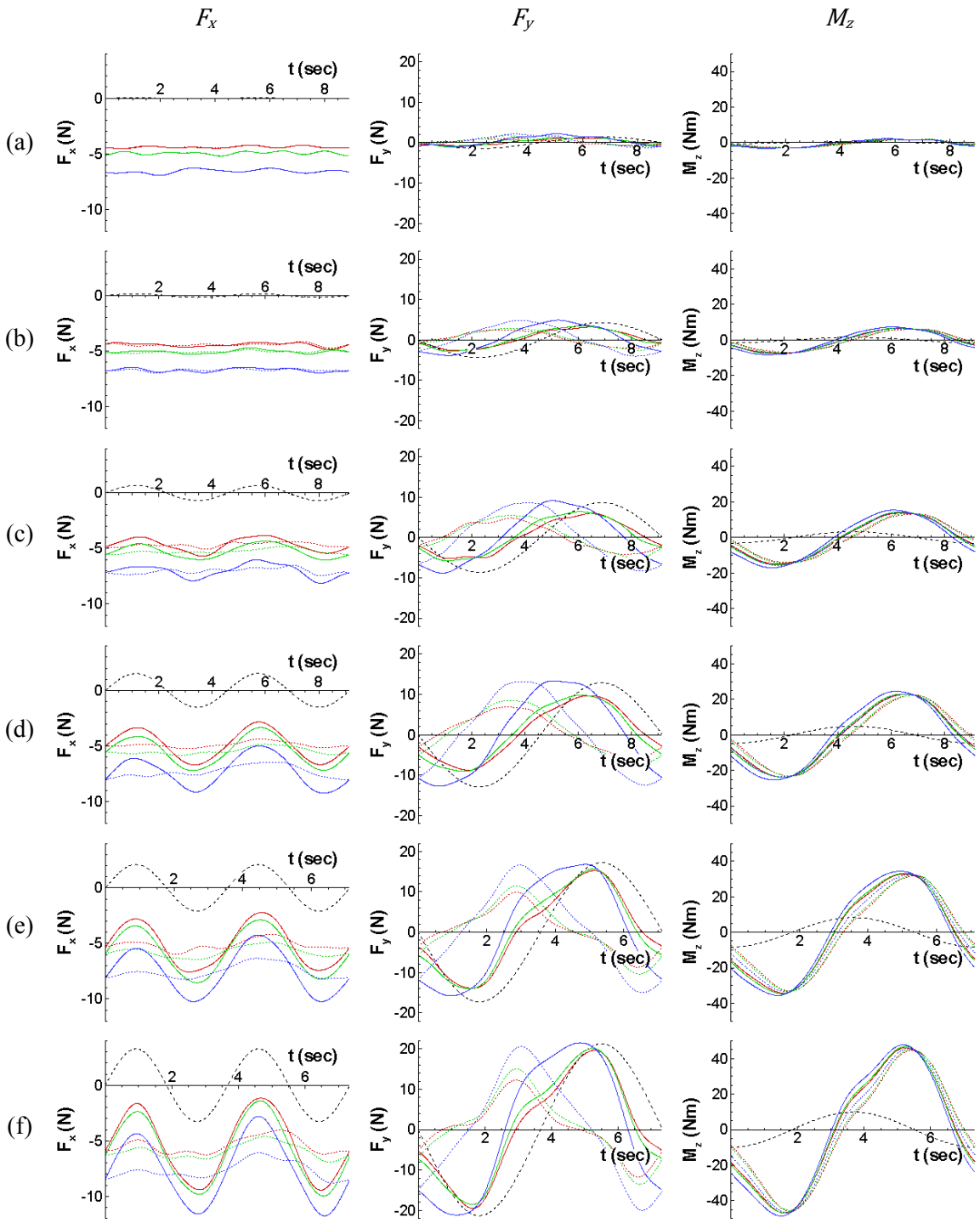


Figure 6-19 FS reconstructed time history of total, inertia, and hydrodynamic $F_x$ (left), $F_y$ (center), and $M_z$ (right) for pure yaw tests with $Fr = 0.2$: (a) $r_{max} = 0.05$, (b) $r_{max} = 0.15$, (c) $r_{max} = 0.3$, (d) $r_{max} = 0.45$, (e) $r_{max} = 0.6$, and (f) $r_{max} = 0.75$. Colors, symbols; red: w/o wind, green: half wind, blue: full wind, — total, --- inertia, ⋯ hydrodynamic.

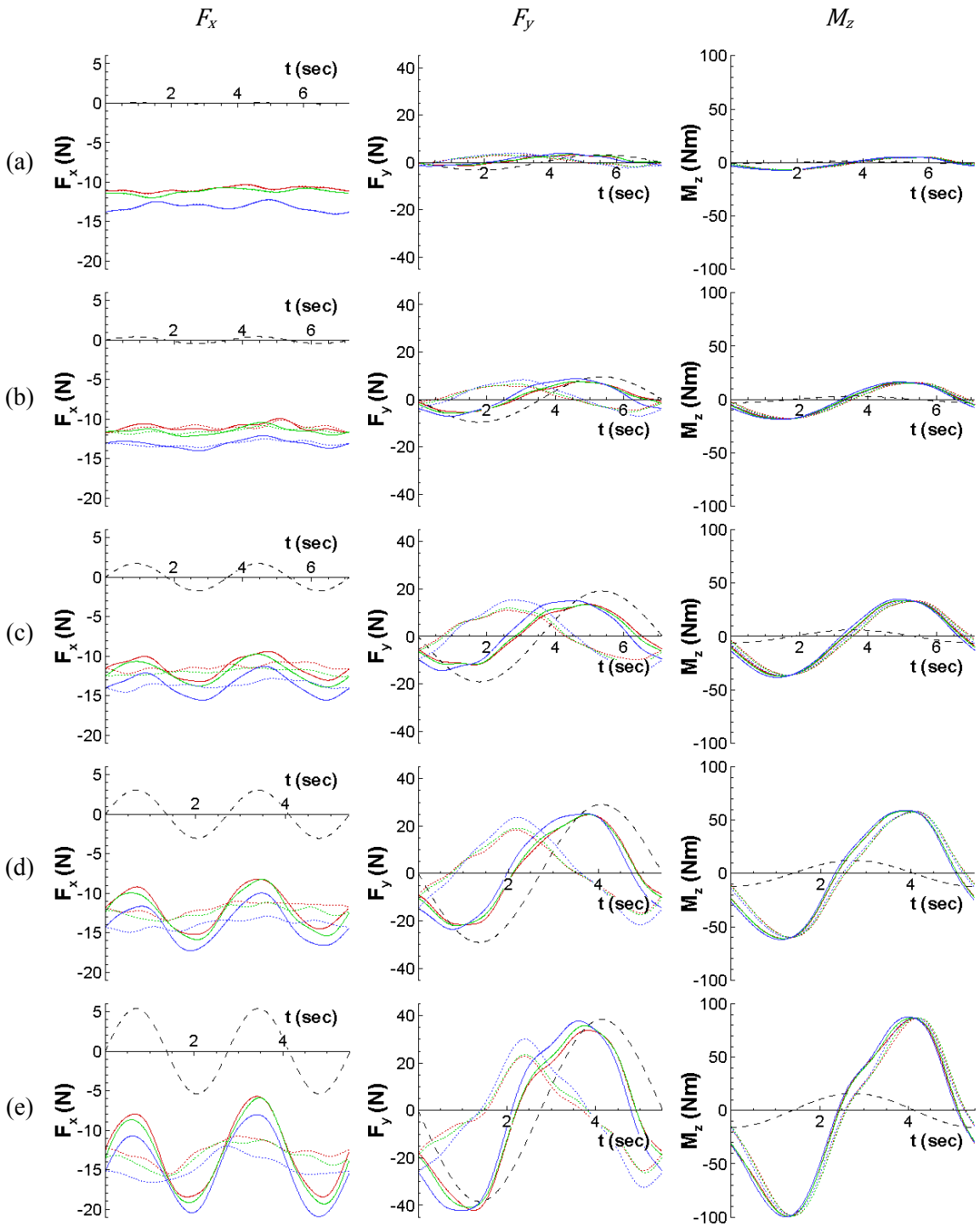


Figure 6-20 FS reconstructed time history of total, inertia, and hydrodynamic $F_x$ (left), $F_y$ (center), and $M_z$ (right) for pure yaw tests with $Fr = 0.3$: (a) $r_{max} = 0.05$, (b) $r_{max} = 0.15$, (c) $r_{max} = 0.3$, (d) $r_{max} = 0.45$, and (e) $r_{max} = 0.6$. Colors, symbols; red: w/o wind, green: half wind, blue: full wind, — total, --- inertia, ⋯ hydrodynamic.

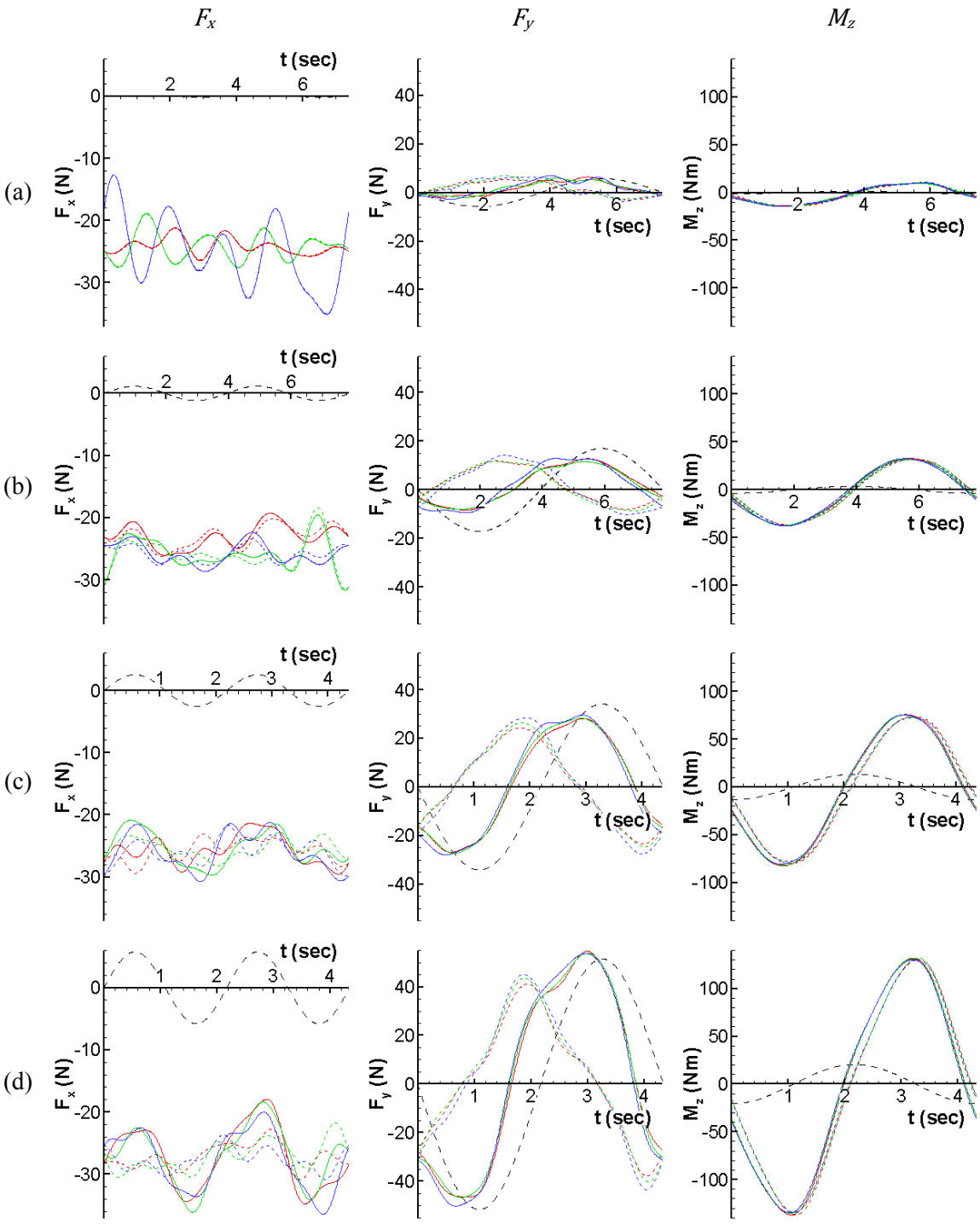


Figure 6-21 FS reconstructed time history of total, inertia, and hydrodynamic $F_x$ (left), $F_y$ (center), and $M_z$ (right) for pure yaw tests with $Fr = 0.4$: (a) $r_{max} = 0.05$, (b) $r_{max} = 0.15$, (c) $r_{max} = 0.3$, and (d) $r_{max} = 0.45$. Colors, symbols; red: w/o wind, green: half wind, blue: full wind, — total, --- inertia, ⋯ hydrodynamic.

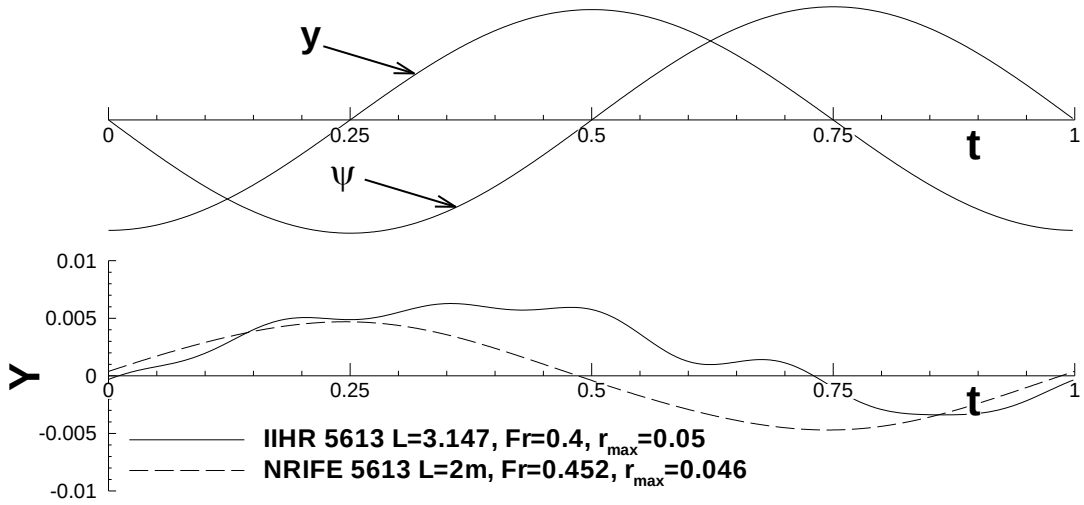


Figure 6-22 Comparison between IIHR and and OU (NRIFE) pure yaw test $Y$-force for similar test conditions. Sway and yaw are shown to provide reference of trajectory.

---

Note: OU data is 1st-order FS reconstruction whereas IIHR data is 6th-order.

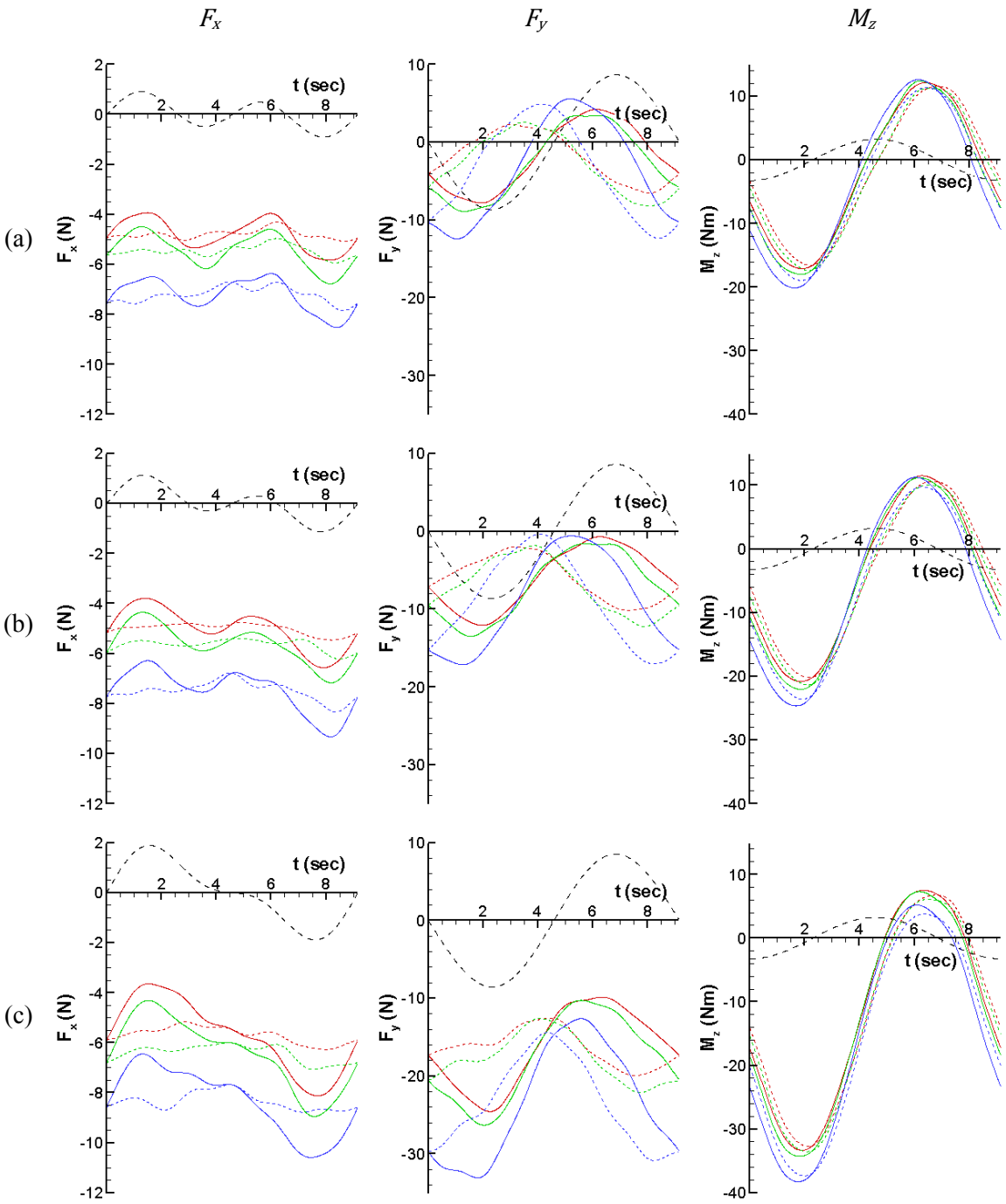


Figure 6-23 FS reconstructed time history of total, inertia, and hydrodynamic $F_x$ (left), $F_y$ (center), and $M_z$ (right) for yaw and drift tests with $Fr = 0.2$ and $r_{max} = 0.3$: (a) $\beta = -2°$, (b) $\beta = -4°$, and (c) $\beta = -10°$. Colors, symbols; red: w/o wind, green: half wind, blue: full wind, — total, --- inertia, ⋯ hydrodynamic.

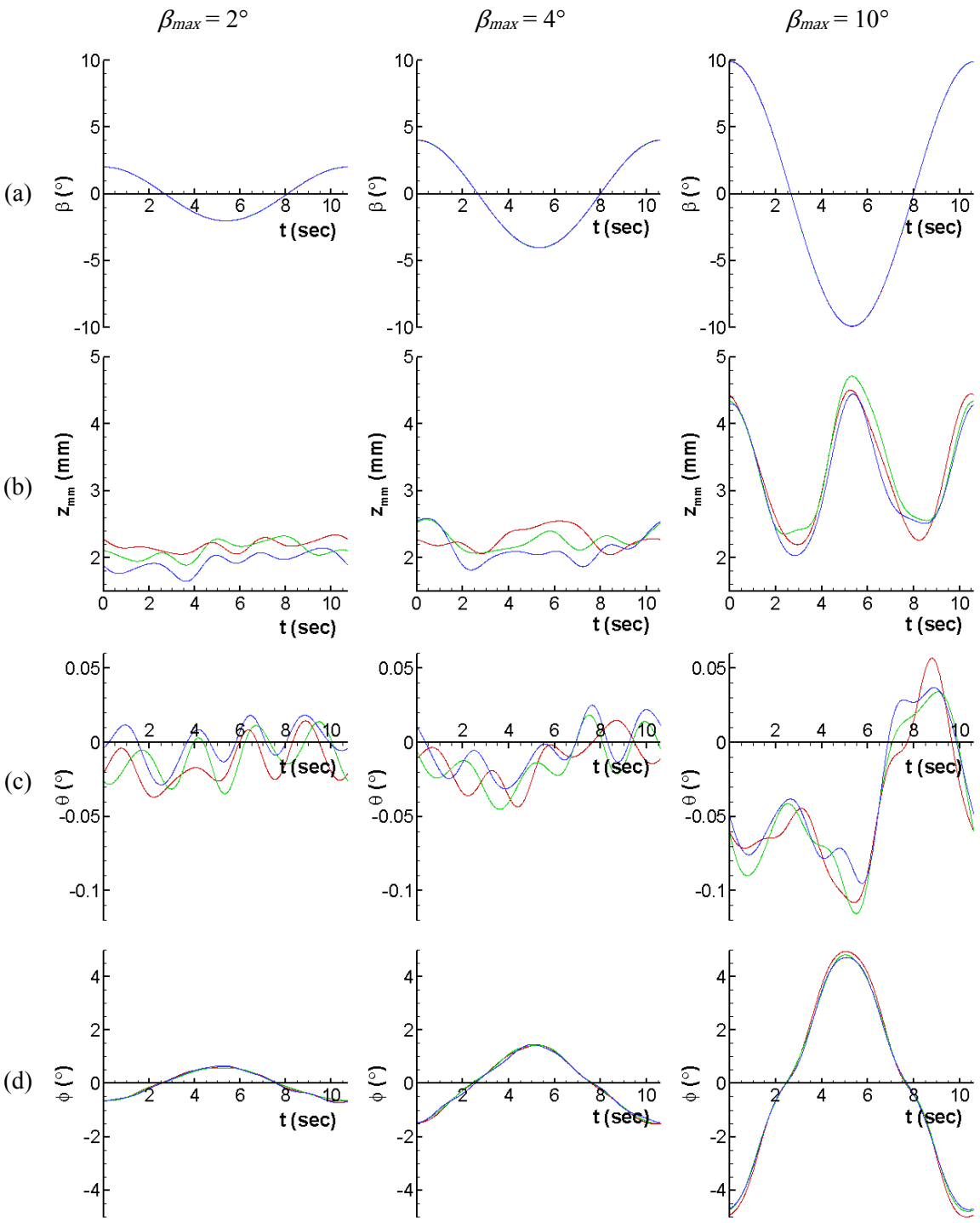


Figure 6-24 FS reconstructed time history of pure sway input (a) $\beta$ and responses (b) $z_{mm}$, (c) $\theta$, and (d) $\phi$ for $\beta_{max}$ = 2° (left), 4° (center), and 10° (right). Colors; red: w/o wind, green: half wind, blue: full wind.

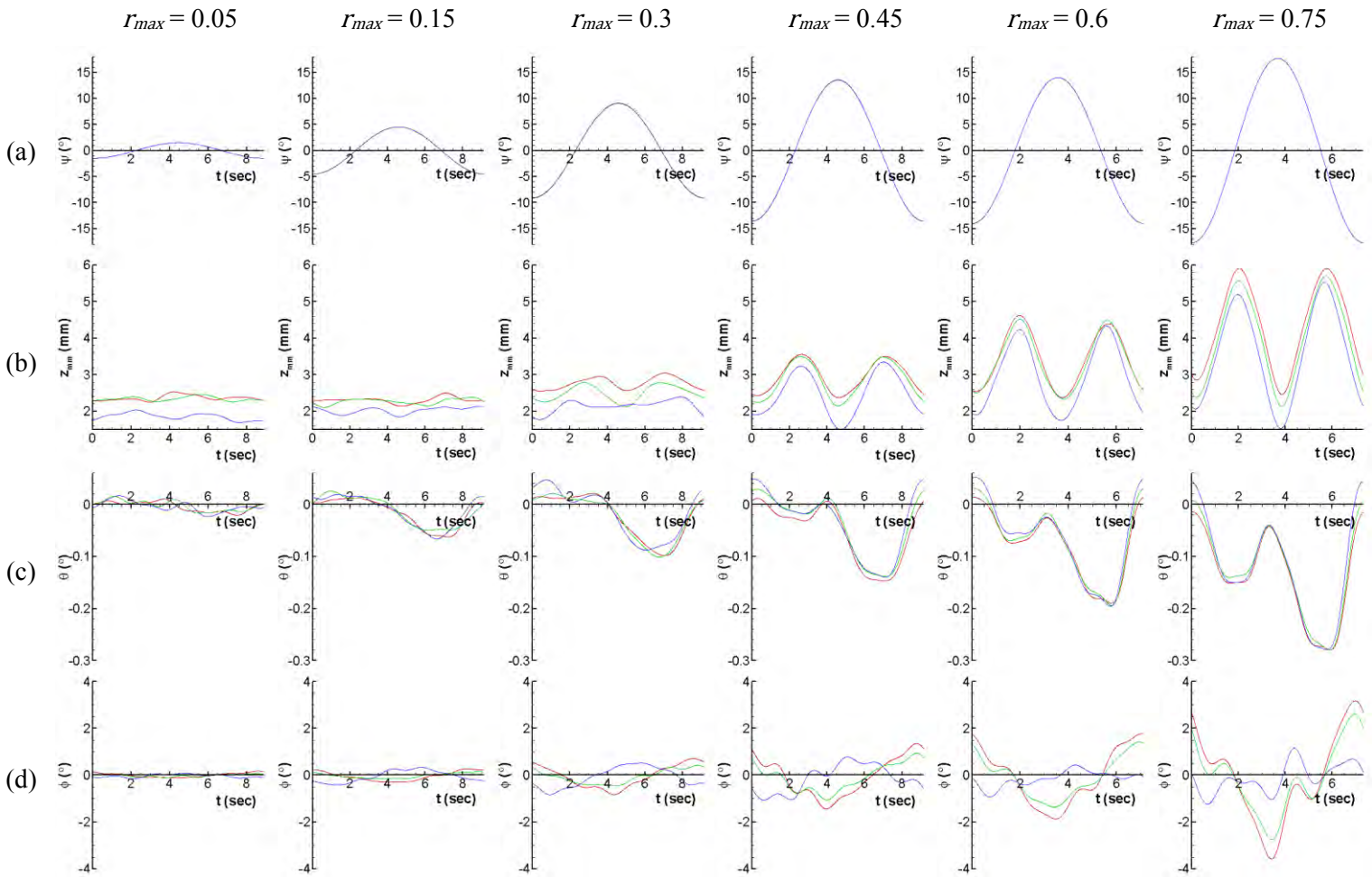


Figure 6-25 FS reconstructed time history of $Fr = 0.2$ pure yaw input (a) $\psi$ and responses (b) $z_{mm}$, (c) $\theta$, and (d) $\phi$ for $r_{max} = 0.05$, 0.15, 0.3, 0.45, 0.6, and 0.75 left to right. Colors; red: w/o wind, green: half wind, blue: full wind.

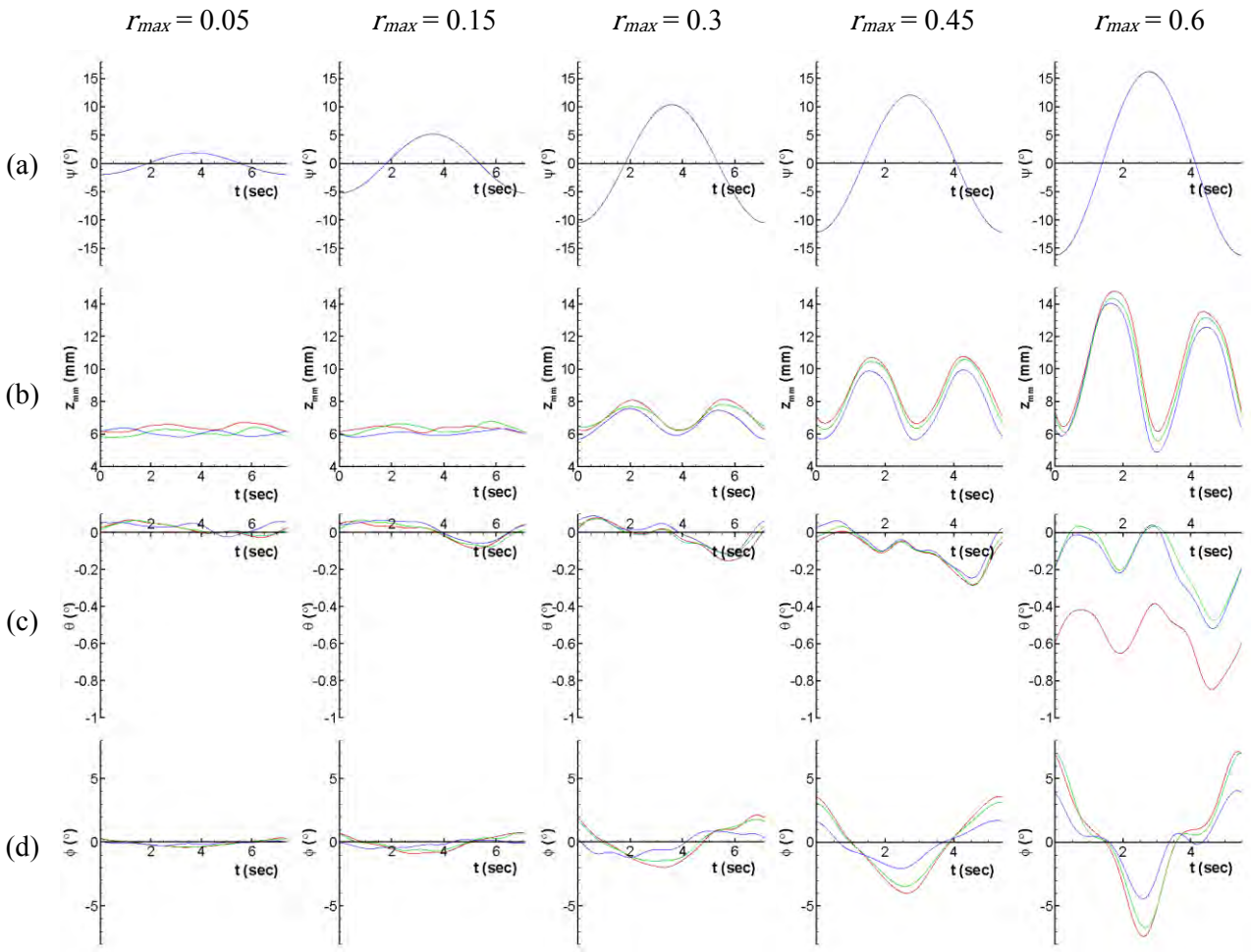


Figure 6-26 FS reconstructed time history of $Fr$ = 0.3 pure yaw input (a) $\psi$ and responses (b) $z_{mm}$, (c) $\theta$, and (d) $\phi$ for $r_{max}$ = 0.05, 0.15, 0.3, 0.45, and 0.6 left to right. Colors; red: w/o wind, green: half wind, blue: full wind.

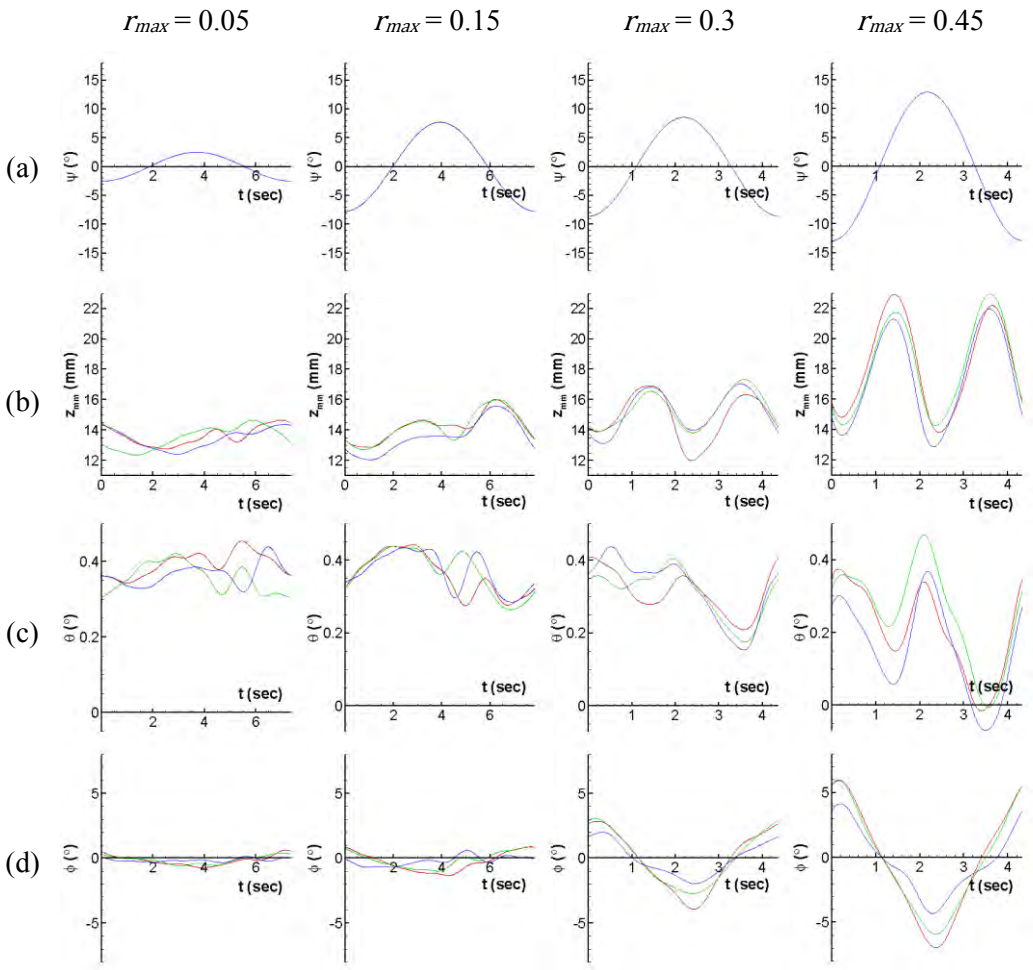


Figure 6-27 FS reconstructed time history of $Fr$ = 0.4 pure yaw input (a) $\psi$ and responses (b) $z_{mm}$, (c) $\theta$, and (d) $\phi$ for $r_{max}$ = 0.05, 0.15, 0.3, and 0.45 left to right. Colors; red: w/o wind, green: half wind, blue: full wind.

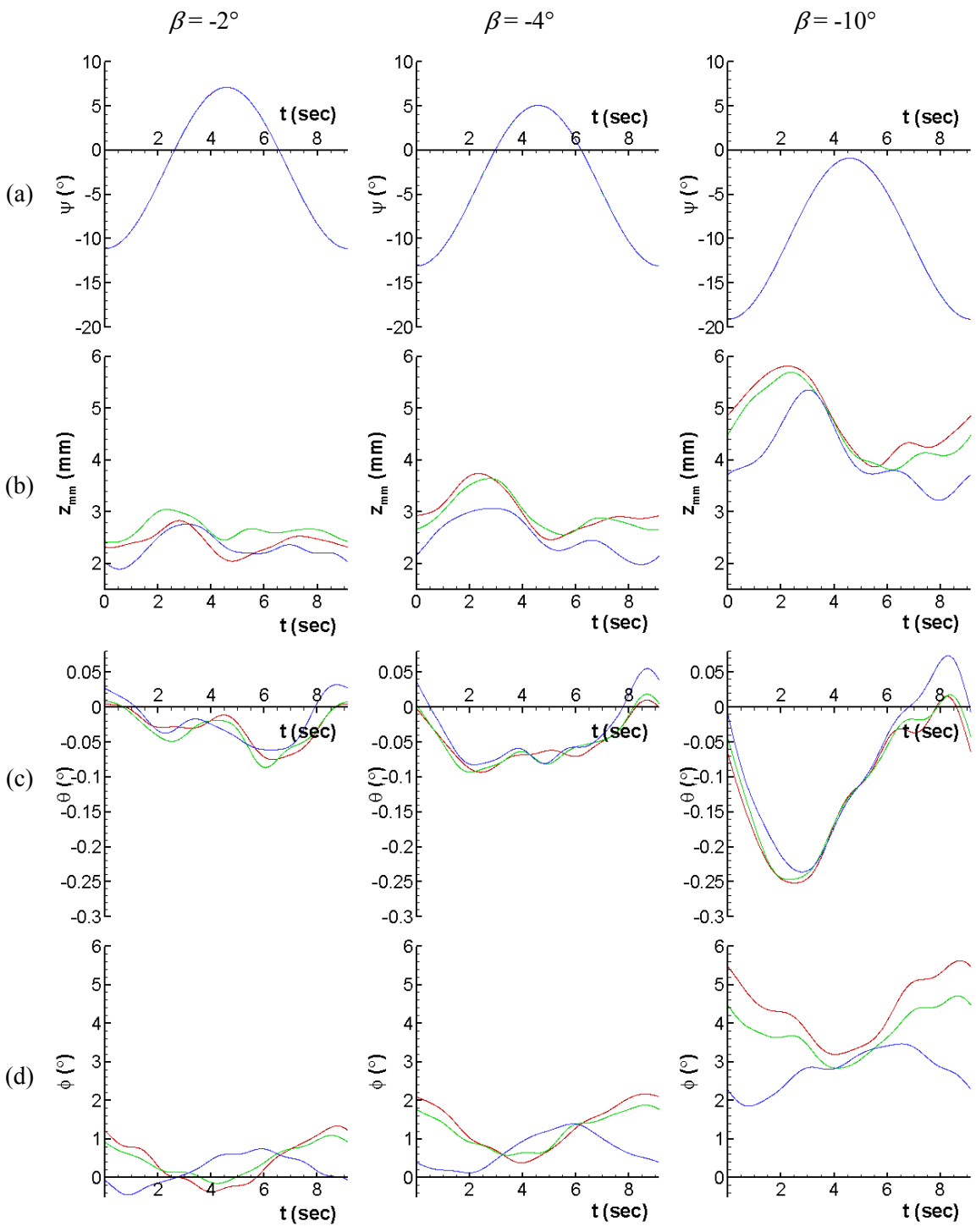


Figure 6-28 FS reconstructed time history of yaw and drift input (a) $\psi$ and responses (b) $z_{mm}$, (c) $\theta$, and (d) $\phi$ for $\beta = 2°$ (left), 4° (center), and 10° (right). Colors; red: w/o wind, green: half wind, blue: full wind.

# CHAPTER 7. CONCLUSION AND FUTURE WORK

Calm water resistance tests and static and dynamic planar motion mechanism (PMM) tests are performed at the IIHR towing tank for ONR Tumblehome model 5613 in three headwind conditions. The effect of wind is analyzed for resistance, static sinkage and trim, static PMM forces, moment, and motions, dynamic forces, moment and motions, and hydrodynamic derivatives. Complimentary CFD computations are in progress during the completion of this thesis and validations of available CFD data are carried out.

Characterization of the free-stream air velocity distribution is performed by surveying the axial velocity at three streamwise planes to observe and document the performance of the custom built wind carriage. The surveys indicate that wind velocity does not change with carriage speed. Adjustments are made to the wind carriage to optimize velocity uniformity. Velocity magnitudes and variation are high upon exiting the wind carriage outlet but the increased turbulent mixing smooths uniformity to more acceptable levels as the wind approaches the model. Maximum uniformity variations are brought to approximately 6-7% while $RMS$ (turbulence) levels are approximately 4.5% at the forward perpendicular (FP) streamwise plane. These values are high when compared to conventional open circuit wind tunnels because flow control is sacrificed for construction purposes. Relative wind speed to ship speed ratio is 7.4 for the $Fr$ = 0.2 full wind condition. Full scale wind speeds at $Fr$ = 0.2 correspond to Beaufort numbers 10 and 12 for half wind and full wind, respectively, with full wind simulating strong hurricane scale wind speeds.

For straight ahead resistance tests without wind, data conforms to other facilities. Appendages have noticeable effects on resistance, sinkage and trim. Wind has a large effect on resistance with nearly constant effect over $Fr$ range due to constant relative wind speed. Total resistance shows reasonable agreement with CFD cases and wind drag

exhibits quadratic scaling with wind speed. The drag coefficient calculated for the portion of the ship above water shows reasonable agreement with literature and CFD. The drag of the 3DOF mount is large in comparison with the drag of the above-water portion of the ship and its effect is hugely consequential in calculating ship drag. Scatter in sinkage and trim data provides difficulty in identified effects of wind. Nonetheless, on average wind tends to lift the ship and increase pitch (bow up) very small amounts. Stationarity tests reveal underlying trends in sinkage and trim due to carriage rail alignment issues.

Wind effects on static PMM tests are large for smaller ship speeds. Drift angles are limited at higher ship speeds due to roll limitations of the 3DOF mount and thus observed wind effects are smaller. The data is corrected for apparent asymmetry and sway hydrodynamic derivatives are found. Surge, sway, and yaw derivatives are largely affected by wind for small ship speeds. Wind effects on Dynamic PMM tests are strongly dependent on the type of test performed. Pure sway tests maintain zero heading and thus wind mainly affects surge force. A large number of pure yaw tests are performed to adequately fit data to the mathematical models and realize the effect of wind with respect to motion parameters and ship speed. As expected, sway force and yaw moment harmonic amplitudes are significantly affected in addition to surge force. Lower-order harmonics and some high-order harmonics fit the mathematical models well. Unexpected sway response reveals a phase shift in the hydrodynamic force compared to another surface combatant, model 5512 (Yoon, 2009). Data from a single pure yaw test performed by Araki et al. (2010) is processed and used to confirm unexpected behavior. Motions data shows roll as being the most sensitive to wind.

Future work for the present study will focus on CFD validations for dynamic tests. Harmonic amplitudes and phases for forces, moment and motions will be compared and the effect of wind on harmonic amplitudes of motions will be more closely analyzed. Detailed flow field information from CFD will be used to explain the flow

physics and ship responses. Uncertainty analysis (UA) following ASME (2005) standard procedures will be performed. Particle Image Velocimetry (PIV) tests are planned to measure velocity fields in streamwise planes over the helicopter deck to validate CFD flow field data.

All EFD and CFD data will be compiled and presented in the conference proceedings of the *29th ONR Symposium on Naval Hydrodynamics* entitled "Complimentary EFD and CFD on Effects of Headwinds on Towing Tank Resistance and PMM Tests for ONR Tumblehome."

It is possible to further process the acquired data and obtain surge hydrodynamic derivatives $X_u$, $X_{uu}$, and $X_{uuu}$ from resistance curves. Similarly, surge and sway cross-coupled derivatives $X_{vvu}$, $Y_{vu}$, $Y_{vuu}$, $N_{vu}$, and $N_{vuu}$ can be obtained from static drift tests because tests were performed at multiple ship speeds. By performing pure yaw tests at multiple ship speeds it follows that surge and yaw cross-coupled derivatives $X_{rru}$, $Y_{ru}$, $Y_{ruu}$, $N_{ru}$, and $N_{ruu}$ can also be found from the acquired data.

It should be noted that the effects of tailwinds could potentially be analyzed by performing the same model tests with the ship installed in the reverse configuration and performing carriage runs in the reverse direction. If the need arises to explore the effects of wind in a more general sense, this option must not be overlooked.

# APPENDIX A. DETERMINATION OF 3DOF MOUNT DRAG AND MASS EFFECT

The following describes the procedures performed to determine the drag of the portion of the 3DOF mount that is exposed to wind and the mass properties of the mount that affect forces and moment data.

The wind drag of the 3DOF mount is referred to as $D_{mount}$ and contributes to measured ship-fixed $F_x$ and $F_y$ in the streamwise direction. A series of measurements is performed to measure $D_{mount}$ using the load cell at all tested $Fr$ values and all three wind conditions for the straight ahead ($\beta = 0$) orientation only. The ship is left in place but is not towed by the 3DOF mount. Instead it is towed by a post at the stern of the ship, far downstream of the mount. This ensures the same flow behavior around the mount while allowing the load cell to only measure the drag force imparted to the exposed portion mount. The gimbal is raised and pinned in place away from its attachment point with a dummy weight standing in to ensure correct displacement. The yaw guide portion of the 3DOF mount remains attached to the model in order to support the ship in sway and yaw. The rail linkage ensures no streamwise force is imparted to the mount by the model. All streamwise force is directed to the stern post which restrains the model about a spherical joint fixed in space. The model is now forced to pitch about this point, however, the effects of ship motions on the drag of the mount are assumed to be negligible. Test setup is shown in Fig. A-1. The study also presents opportunity to measure the effect of removing the pitot rack traverse hardware that is positioned upstream and slightly above the mount. This hardware is left in place for straight ahead tests but must be removed for PMM tests. $D_{mount}$ vs. $Fr$ is plotted for all wind conditions in Fig. A-2. Measurements with the pitot hardware removed are taken at $Fr$ = 0.2, 0.3, and 0.4. As expected, $D_{mount}$ exhibits constant behavior across $Fr$ range with the removal of the pitot hardware only having a measurable effect on $D_{mount}$ at $Fr$ = 0.4 with full wind (about 3% ). The

majority of data points lie within the standard deviations of the 5 repeat tests at $Fr$ = 0.2, 0.3, and 0.4. Therefore the average value of $D_{mount}$ for each wind condition is used as a correction for all measured forces data within the entire experiment. Test conditions without wind use $D_{mount}$ = 0 whereas values for half and full wind conditions are summarized in Table A-1 along with predicted drag using $C_D$ of a cylinder. The predicted drag from a cylinder is up to 5.8% less than the measured drag. The discrepancy is likely due to the cylinder prediction not accounting for the interface of the mount and load cell which consists of a short cylinder of larger diameter and 8 bolt heads. For the full wind condition in straight ahead tests $D_{mount}$ accounts for about 45% of the total wind drag imparted to the ship and mount combined. For static and dynamic PMM tests $F_x$ and $F_y$ are corrected by resolving $D_{mount}$ into ship-fixed $x$- and $y$-directions due to the ship-fixed orientation of the load cell. It is assumed that non-zero $\beta$ and/or motions have a negligible effect on $D_{mount}$.

To ensure that removing the pitot hardware does not affect the wind force on the ship, 5 straight ahead repeat measurements are taken at $Fr$ = 0.2, 0.3, and 0.4 for each wind condition with the ship re-attached to the 3DOF mount and the pitot hardware removed. Fig. A-3 shows data overlaid on original straight ahead $F_x$ data. As expected wind force on the ship is not affected by removal of the pitot hardware.

For dynamic tests the mass properties of the 3DOF mount must be determined so that the contribution of its inertia to the forces and moment measured by the load cell can be determined. With PMM motions the mount only experiences purely lateral displacement and rotation. Therefore, when in motion, its mass contributes inertia forces to measured $F_x$ and $F_y$. The location of the mount's center of gravity is not located at $x$ = 0 and therefore its mass contributes a moment to measured $M_z$. In addition, the mount's moment of inertia about the ship $z$-axis contributes to measured $M_z$. The following describes procedures performed to obtain the mount's mass, center of gravity $x$-location, and moment of inertia about the ship $z$-axis.

The mass of the 3DOF mount is found two ways. First it is measured on a hanging scale with the heave staff removed (the heave staff is considered a point mass at the ship center of gravity). It is then installed on the load cell and $z$-force is measured to confirm mass and operation of the load cell. The $x$-location of the mount's center of gravity is found by measuring the $y$-moment imparted to the load cell with the 3DOF mount installed. The $x$-location is then the moment arm

$$x_{G,mount} = \frac{M_y}{W_{mount}} \tag{A.1}$$

where $M_y$ is the measured $y$-moment and $W_{mount}$ is the weight of the 3DOF mount (with heave staff removed). Load cell $M_y$ operation is confirmed by placing a standard weight on the mount a known $x$-distance from the $z$-axis. $x_{G,mount}$ is confirmed from the digital 3D model using Rhinoceros® software. The mount's $z$-moment of inertia is found by supplying an oscillatory yaw motion via the PMM mechanism and measuring the response $M_z$ at various maximum yaw accelerations. $M_z$ data is FS-reconstructed to find the first harmonic amplitude $M_{z_1}$. Sample raw $M_z$ and FS-reconstruction is shown in Fig. A-4. When $M_{z_1}$ is plotted against maximum yaw acceleration $\dot{r}_{max}$ for each test the slope of the relationship (found using least squares fit) is the mount's $z$-moment of inertia about the ship z-axis. Refer to Fig. A-5. The observed offset in Figures A-4 and A-5 is due to PMM induced noise. The measured mass properties of the 3DOF mount are summarized in Table A-2.

Table A-1 Measured and Predicted Drag of the 3DOF Mount.

| | Average mount drag (N) | Prediction from cylinder (N) |
|---|---|---|
| Half wind | 0.449 | 0.423 (-5.8 %) |
| Full wind | 1.661 | 1.625 (-2.2 %) |

Table A-2 Measured Mass Properties of the 3DOF Mount.

| $m_{mount}$ (kg) | $I_{z,mount}$ (kg·m$^2$) | $x_{G,mount}$ (m) | $y_{G,mount}$ (m) |
|---|---|---|---|
| 8.543 | 0.2879 | 0.09633 | 0 |

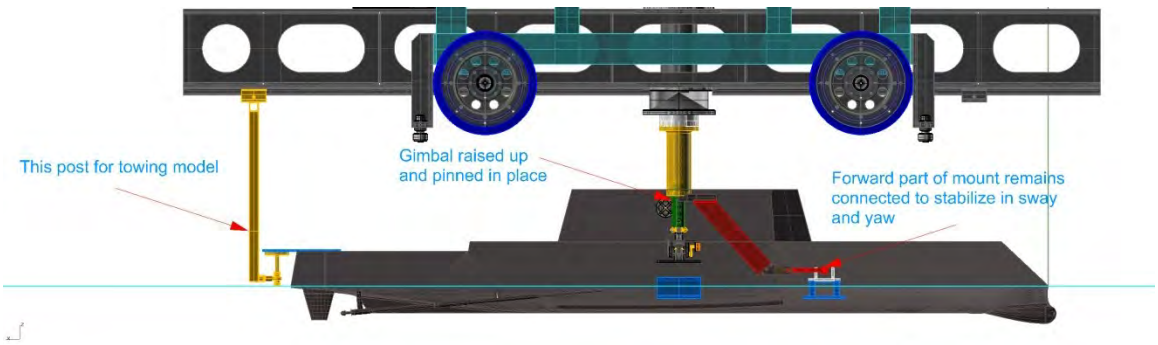


Figure A-1 Test setup for 3DOF mount drag measurement.

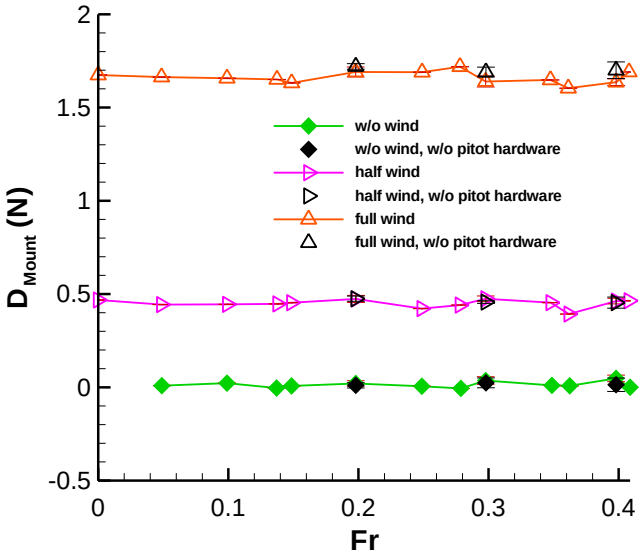


Figure A-2 Drag of the 3DOF mount. The model is present but towed from the strongback instead of the load cell. 5 repeat tests are performed at $Fr$ = 0.2, 0.3, and 0.4.

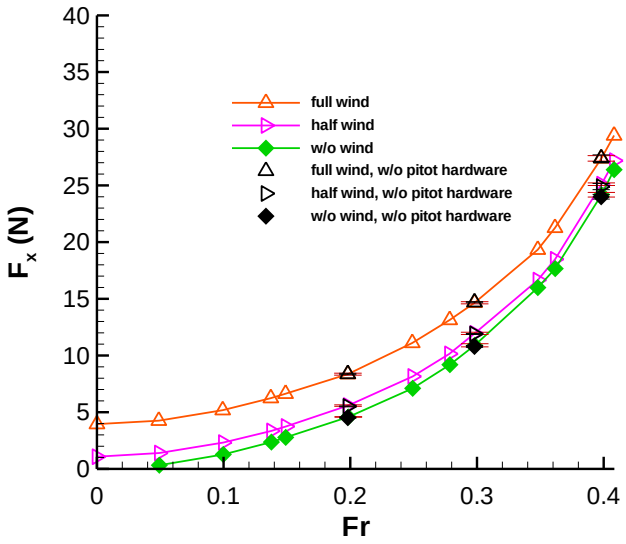


Figure A-3 Comparison of $F_x$ for cases with and without the pitot probe rack traverse hardware. $D_{mount}$ is included. 5 repeat tests are performed at $Fr$ = 0.2, 0.3, and 0.4.

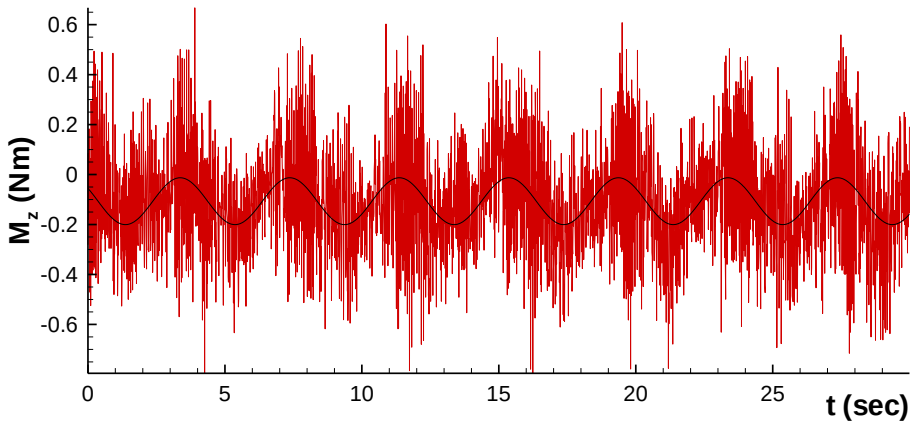


Figure A-4 Sample raw $M_z$ and FS-reconstructed data for $\dot{r}_{max}$ = 0.22 rad/s$^2$.

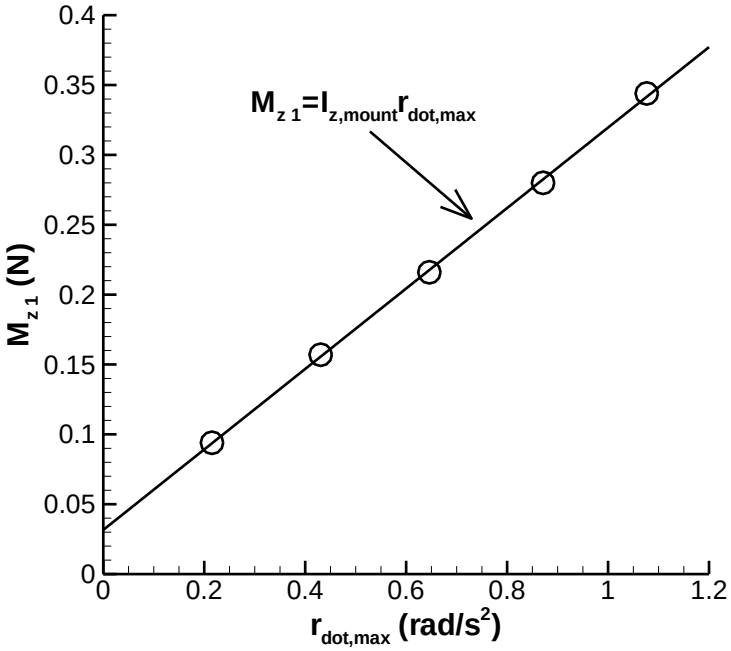


Figure A-5 The slope of $M_{z_1}$ vs. $\dot{r}_{max}$ is the 3DOF mount's $z$-moment of inertia about the ship $z$-axis.

# APPENDIX B. PRELIMINARY STRAIGHT AHEAD TEST

The proceeding straight ahead data is not archival and is used as a means to confirm operation of all data acquisitions systems and data processing procedures. The ship is supported in yaw by a rod passing through a slot in a plate attached to the bow of the ship and is shown in Fig B-1. The data is processed neglecting the effect of the rod and plate and without the 3DOF mount drag correction applied.

Table B-1 Effects of appendages on total resistance.

| *Fr* | IIHR EFD fully appended | OU EFD fully appended w/o rudders | INSEAN EFD bare hull w/o BK | IIHR CFD fully appended w/o prop, struts, rudders | IIHR CFD bare hull w/BK | IIHR CFD bare hull w/o BK |
|---|---|---|---|---|---|---|
| 0.05 | 0.37 N | -9.8 % | -8.0 % | | +66.7 % | +16.4 % |
| 0.10 | 1.26 N | -5.0 % | -15.3 % | | +12.4 % | -6.6 % |
| 0.15 | 2.74 N | -2.7 % | -19.7 % | | -4.5 % | -16.9 % |
| 0.20 | 4.54 N | +0.6 % | -18.6 % | | -6.2 % | -15.7 % |
| 0.25 | 6.74 N | +6.6 % | -13.6 % | +3.0 % | -3.2 % | -11.4 % |
| 0.28 | 9.04 N | | -14.6 % | | -8.0 % | -15.3 % |
| 0.30 | 11.30 N | -4.2 % | -19.0 % | -5.6 % | -14.6 % | -20.8 % |
| 0.35 | 15.83 N | -2.7 % | -19.5 % | -1.2 % | -12.8 % | -19.2 % |
| 0.40 | 23.72 N | -6.9 % | -15.4 % | -4.4 % | -16.5 % | -22.8 % |
| 0.41 | 27.72 N | | -20.1 % | | -23.1 % | -28.6 % |

Table B-2 Effects of appendages on sinkage.

| *Fr* | IIHR EFD fully appended | OU EFD fully appended w/o rudders | INSEAN EFD bare hull w/o BK | IIHR CFD fully appended w/o prop, struts, rudders | IIHR CFD bare hull w/BK | IIHR CFD bare hull w/o BK |
|---|---|---|---|---|---|---|
| 0.05 | -4.20E-06 | -219.3 % | | | -183.6 % | -665.0 % |
| 0.10 | -8.88E-05 | +9.1 % | | | -28.4 % | -74.6 % |
| 0.15 | -3.31E-04 | +15.6 % | | | -4.1 % | -9.2 % |
| 0.20 | -6.71E-04 | +12.9 % | | | +3.5 % | -0.7 % |
| 0.25 | -1.05E-03 | -8.7 % | | -5.0 % | -5.8 % | -7.7 % |
| 0.28 | -1.62E-03 | | | | +8.7 % | +7.5 % |
| 0.30 | -1.97E-03 | +6.0 % | | +10.2 % | +10.1 % | +9.0 % |
| 0.35 | -2.96E-03 | +10.8 % | | +13.1 % | +13.5 % | +12.1 % |
| 0.40 | -4.14E-03 | +6.2 % | | +14.4 % | +14.4 % | +15.9 % |
| 0.41 | -4.63E-03 | | | | +20.3 % | +20.7 % |

Table B-3 Effects of appendages on trim.

| *Fr* | IIHR EFD fully appended | OU EFD fully appended w/o rudders | INSEAN EFD bare hull w/o BK | IIHR CFD fully appended w/o prop, struts, rudders | IIHR CFD bare hull w/BK | IIHR CFD bare hull w/o BK |
|---|---|---|---|---|---|---|
| 0.05 | -0.029 deg | +122.1 % | | | +210.9 % | +142.2 % |
| 0.10 | -0.023 deg | +33.6 % | | | +206.6 % | +113.5 % |
| 0.15 | -0.031 deg | +27.2 % | | | +134.5 % | +59.3 % |
| 0.20 | -0.040 deg | -21.2 % | | | +79.3 % | +25.2 % |
| 0.25 | -0.055 deg | -30.6 % | | +45.3 % | +66.4 % | +27.0 % |
| 0.28 | -0.045 deg | | | | +80.2 % | +27.5 % |
| 0.30 | -0.017 deg | -169.8 % | | +135.2 % | +85.4 % | -39.3 % |
| 0.35 | 0.004 deg | -2446.6 % | | +1931.3 % | +533.5 % | -139.3 % |
| 0.40 | 0.323 deg | -53.8 % | | +12.8 % | -44.0 % | -58.6 % |
| 0.41 | 0.466 deg | | | | -45.4 % | -54.1 % |

Table B-4 Effects of wind on total resistance.

| *Fr* | IIHR EFD fully appended w/o wind | IIHR EFD fully appended half wind | IIHR EFD fully appended full wind | IIHR CFD fully appended w/o wind | IIHR CFD fully appended half wind | IIHR CFD fully appended full wind |
|---|---|---|---|---|---|---|
| 0.05 | 0.37 N | +205.5 % | +777.9 % | | | |
| 0.10 | 1.26 N | +58.0 % | +231.7 % | | | |
| 0.15 | 2.74 N | +25.5 % | +106.9 % | | | |
| 0.20 | 4.54 N | +16.1 % | +64.4 % | | | |
| 0.25 | 6.74 N | +17.3 % | +50.0 % | | | |
| 0.28 | 9.04 N | +8.4 % | +34.1 % | | | |
| 0.30 | 11.30 N | +3.5 % | +22.5 % | | | |
| 0.35 | 15.83 N | +5.7 % | +16.2 % | | | |
| 0.40 | 23.72 N | +2.4 % | +14.0 % | | | |
| 0.41 | 27.72 N | | +1.2 % | | | |

Table B-5 Effects of wind on sinkage.

| *Fr* | IIHR EFD fully appended w/o wind | IIHR EFD fully appended half wind | IIHR EFD fully appended full wind | IIHR CFD fully appended w/o wind | IIHR CFD fully appended half wind | IIHR CFD fully appended full wind |
|---|---|---|---|---|---|---|
| 0.05 | -4.20E-06 | +792.1 % | +3066.5 % | | | |
| 0.10 | -8.88E-05 | +21.3 % | +236.4 % | | | |
| 0.15 | -3.31E-04 | +14.3 % | +18.1 % | | | |
| 0.20 | -6.71E-04 | +5.2 % | +10.2 % | | | |
| 0.25 | -1.05E-03 | -12.8 % | +8.4 % | | | |
| 0.28 | -1.62E-03 | +4.6 % | +8.6 % | | | |
| 0.30 | -1.97E-03 | +0.3 % | +6.9 % | | | |
| 0.35 | -2.96E-03 | -1.7 % | +5.0 % | | | |
| 0.40 | -4.14E-03 | +1.1 % | -2.4 % | | | |
| 0.41 | -4.63E-03 | | +9.2 % | | | |

Table B-6 Effects of wind on trim.

| *Fr* | IIHR EFD fully appended w/o wind | IIHR EFD fully appended half wind | IIHR EFD fully appended full wind | IIHR CFD fully appended w/o wind | IIHR CFD fully appended half wind | IIHR CFD fully appended full wind |
|---|---|---|---|---|---|---|
| 0.05 | -0.029 deg | +28.8 % | +123.9 % | | | |
| 0.10 | -0.023 deg | +30.5 % | +66.1 % | | | |
| 0.15 | -0.031 deg | +31.6 % | +63.8 % | | | |
| 0.20 | -0.040 deg | +4.1 % | +21.9 % | | | |
| 0.25 | -0.055 deg | +11.7 % | +30.9 % | | | |
| 0.28 | -0.045 deg | +12.3 % | +51.5 % | | | |
| 0.30 | -0.017 deg | -39.0 % | +32.8 % | | | |
| 0.35 | 0.004 deg | +497.2 % | +682.8 % | | | |
| 0.40 | 0.323 deg | +1.4 % | +22.5 % | | | |
| 0.41 | 0.466 deg | | -10.7 % | | | |

Table B-7 Above water wind $C_D$ based on frontal area of ONRT.

| Source | Relative to ship $\frac{\mu_{\bar{U}_W}}{U_S}$ | Relative to Earth $\frac{\mu_{\bar{U}_W} - U_s}{U_S}$ | $C_D$ |
|---|---|---|---|
| IIHR CFD ($Fr$ = 0.2) | 8 | 7 | 0.31 |
| IIHR EFD ($Fr$ = 0.2) | 8.44 | 7.44 | 0.45 |
| Hoerner[1)] (not ONRT specific) | | | 0.17 – 1.22 |

[1)] Hoerner, Sighard F., "Fluid Dynamic Drag," 2nd Edition, New York City, 1965, pp 11-8.

Table B-8 Tests for stationarity without wind.

| | Run Test, $r$ †$(6 \leq r \leq 15$ for $N = 20)$ | | | | | | | | Trend Test, $A$ †$(64 \leq A \leq 125$ for $N = 20)$ | | | | | | | |
|---|---|---|---|---|---|---|---|---|---|---|---|---|---|---|---|---|
| | $\bar{x}$ | | | | $\overline{x^2}$ | | | | $\bar{x}$ | | | | $\overline{x^2}$ | | | |
| $Fr$ | $U_C$ | $X$ | $z$ | $\theta$ | $U_C$ | $X$ | $z$ | $\theta$ | $U_C$ | $X$ | $z$ | $\theta$ | $U_C$ | $X$ | $z$ | $\theta$ |
| 0.050 | | | | | | | | | | | | | | | | |
| 0.100 | 12 | 11 | 7 | 11 | 11 | 8 | 7 | 9 | 82 | 99 | 79 | 69 | 113 | 104 | 85 | 97 |
| 0.150 | 8 | 15 | 5 | 14 | 14 | 9 | 8 | 11 | 92 | 94 | 65 | 96 | 100 | 85 | 56 | 84 |
| 0.200 | 5 | 12 | 9 | 4 | 7 | 6 | 11 | 4 | 71 | 94 | 56 | 45 | 63 | 156 | 90 | 155 |
| 0.250 | 8 | 11 | 8 | 11 | 9 | 9 | 11 | 7 | 58 | 81 | 46 | 75 | 111 | 134 | 116 | 128 |
| 0.280 | 9 | 16 | 12 | 11 | 11 | 6 | 12 | 6 | 135 | 97 | 74 | 93 | 100 | 108 | 142 | 127 |
| 0.300 | 6 | 10 | 9 | 9 | 7 | 4 | 13 | 4 | 72 | 103 | 80 | 99 | 106 | 141 | 130 | 146 |
| 0.350 | 8 | 13 | 6 | 4 | 9 | 9 | 8 | 11 | 67 | 101 | 70 | 39 | 103 | 64 | 74 | 55 |
| 0.400 | 4 | 9 | 4 | 4 | 8 | 9 | 7 | 4 | 75 | 104 | 74 | 110 | 118 | 115 | 114 | 143 |
| 0.410 | 9 | 14 | 4 | 4 | 9 | 7 | 8 | 8 | 81 | 81 | 93 | 91 | 90 | 98 | 128 | 129 |

† Acceptance region at the 5% level of significance.

Red: Outside the acceptance region.

Table B-9 Tests for stationarity with half wind.

| | Run Test, $r$ †$(6 \le r \le 15$ for $N = 20)$ | | | | | | | | Trend Test, $A$ †$(64 \le A \le 125$ for $N = 20)$ | | | | | | | |
|---|---|---|---|---|---|---|---|---|---|---|---|---|---|---|---|---|
| | $\bar{x}$ | | | | $\overline{x^2}$ | | | | $\bar{x}$ | | | | $\overline{x^2}$ | | | |
| $Fr$ | $U_C$ | $X$ | $z$ | $\theta$ | $U_C$ | $X$ | $z$ | $\theta$ | $U_C$ | $X$ | $z$ | $\theta$ | $U_C$ | $X$ | $z$ | $\theta$ |
| 0.050 | | | | | | | | | | | | | | | | |
| 0.100 | 8 | 14 | 8 | 8 | 12 | 9 | 11 | 7 | 71 | 103 | 85 | 67 | 120 | 122 | 83 | 120 |
| 0.150 | 7 | 16 | 11 | 9 | 14 | 9 | 9 | 8 | 94 | 99 | 92 | 115 | 115 | 55 | 80 | 50 |
| 0.200 | 8 | 13 | 6 | 10 | 12 | 5 | 10 | 7 | 78 | 93 | 69 | 120 | 124 | 41 | 127 | 66 |
| 0.250 | 6 | 13 | 15 | 14 | 6 | 5 | 9 | 10 | 72 | 99 | 84 | 111 | 95 | 34 | 121 | 63 |
| 0.280 | 5 | 12 | 12 | 11 | 14 | 7 | 12 | 5 | 54 | 87 | 90 | 108 | 99 | 58 | 113 | 69 |
| 0.300 | 9 | 11 | 8 | 10 | 10 | 7 | 10 | 3 | 83 | 77 | 61 | 105 | 129 | 63 | 126 | 61 |
| 0.350 | 8 | 12 | 6 | 6 | 10 | 8 | 10 | 11 | 65 | 70 | 44 | 52 | 106 | 44 | 122 | 55 |
| 0.400 | 8 | 13 | 4 | 4 | 9 | 6 | 11 | 8 | 65 | 87 | 127 | 82 | 110 | 163 | 99 | 151 |
| 0.410 | 9 | 14 | 4 | 4 | 7 | 8 | 8 | 6 | 94 | 105 | 106 | 96 | 74 | 142 | 111 | 151 |

† Acceptance region at the 5% level of significance.

Red: Outside the acceptance region.

Table B-10 Tests for stationarity with full wind.

| | Run Test, $r$ †$(6 \leq r \leq 15$ for $N = 20)$ | | | | | | | | Trend Test, $A$ †$(64 \leq A \leq 125$ for $N = 20)$ | | | | | | | |
|---|---|---|---|---|---|---|---|---|---|---|---|---|---|---|---|---|
| | $\bar{x}$ | | | | $\overline{x^2}$ | | | | $\bar{x}$ | | | | $\overline{x^2}$ | | | |
| $Fr$ | $U_C$ | $X$ | $z$ | $\theta$ | $U_C$ | $X$ | $z$ | $\theta$ | $U_C$ | $X$ | $z$ | $\theta$ | $U_C$ | $X$ | $z$ | $\theta$ |
| 0.050 | | | | | | | | | | | | | | | | |
| 0.100 | 7 | 6 | 6 | 7 | 4 | 10 | 9 | 9 | 86 | 123 | 102 | 53 | 69 | 114 | 99 | 116 |
| 0.150 | 11 | 10 | 6 | 6 | 6 | 6 | 12 | 6 | 106 | 92 | 80 | 119 | 135 | 66 | 106 | 71 |
| 0.200 | 4 | 13 | 11 | 9 | 9 | 3 | 7 | 3 | 150 | 83 | 92 | 112 | 97 | 67 | 114 | 85 |
| 0.250 | 6 | 14 | 12 | 14 | 9 | 8 | 9 | 8 | 55 | 99 | 76 | 108 | 113 | 43 | 65 | 53 |
| 0.280 | 11 | 14 | 6 | 11 | 10 | 2 | 10 | 2 | 65 | 93 | 83 | 115 | 95 | 23 | 80 | 33 |
| 0.300 | 6 | 12 | 8 | 9 | 11 | 2 | 13 | 2 | 71 | 103 | 88 | 114 | 108 | 38 | 89 | 40 |
| 0.350 | 8 | 10 | 7 | 8 | 9 | 6 | 11 | 6 | 62 | 90 | 37 | 69 | 100 | 36 | 95 | 34 |
| 0.400 | 4 | 12 | 5 | 4 | 12 | 3 | 6 | 7 | 113 | 102 | 92 | 127 | 102 | 71 | 112 | 89 |
| 0.410 | 8 | 12 | 4 | 4 | 8 | 6 | 6 | 7 | 42 | 87 | 97 | 78 | 95 | 82 | 127 | 93 |

† Acceptance region at the 5% level of significance.

Red: Outside the acceptance region.

Figure B-1 Rod through slotted hole used a means of supporting the ship in yaw for initial, non-archival round of straight ahead tests. Rod diameter is 0.375 inches.

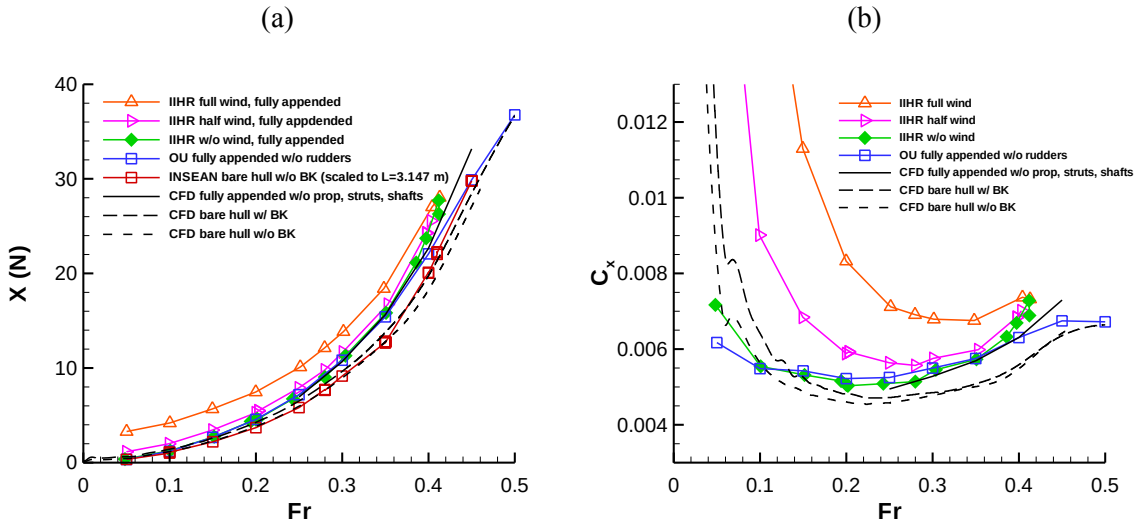


Figure B-2 Comparison between all straight ahead data: (a) $X$ and (b) $C_X$.

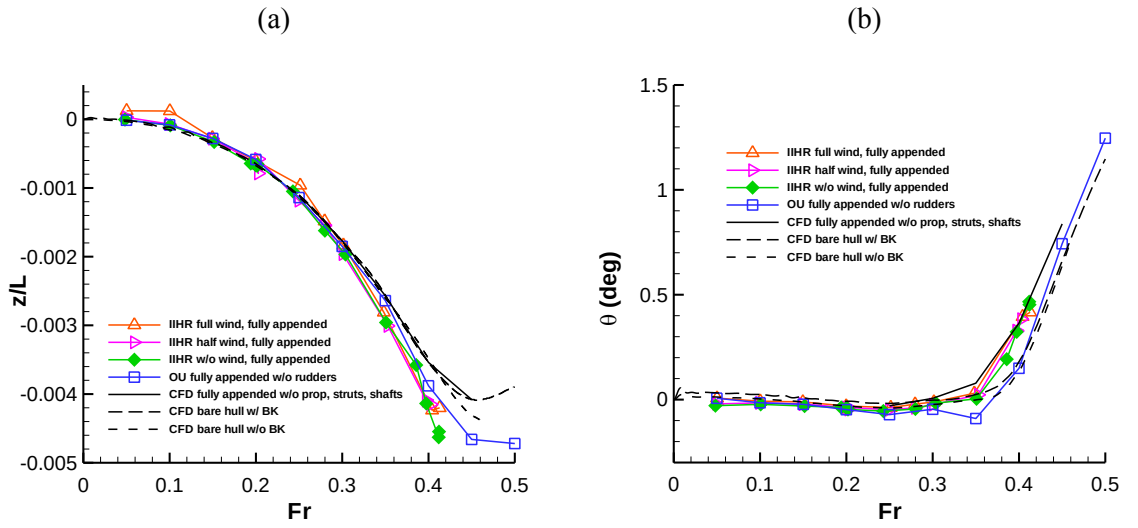


Figure B-3 Comparison between all straight ahead data: (a) sinkage and (b) trim.

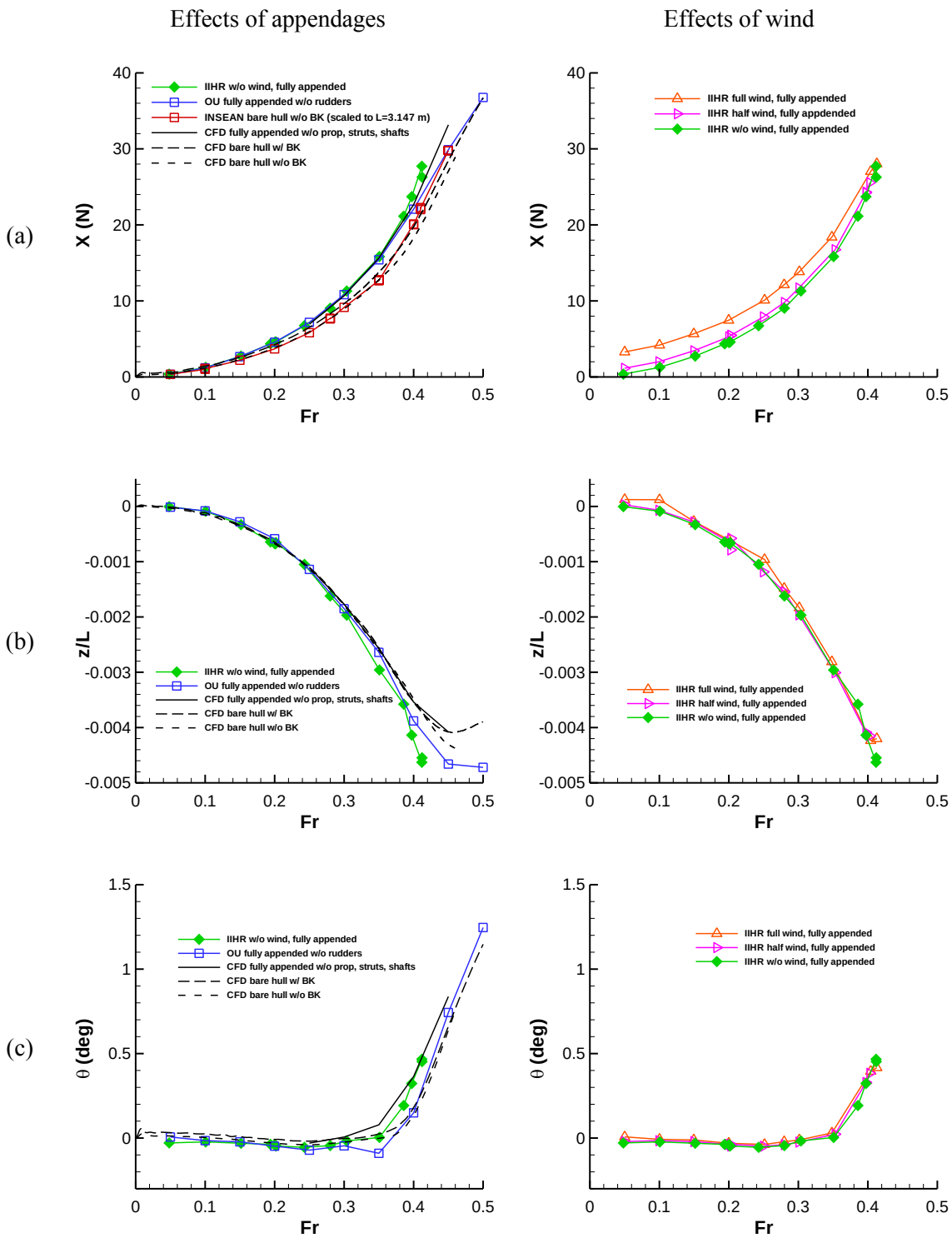


Figure B-4 Effects of appendages (left) and wind (right): (a) *X*, (b) sinkage, and (c) trim.

(a)

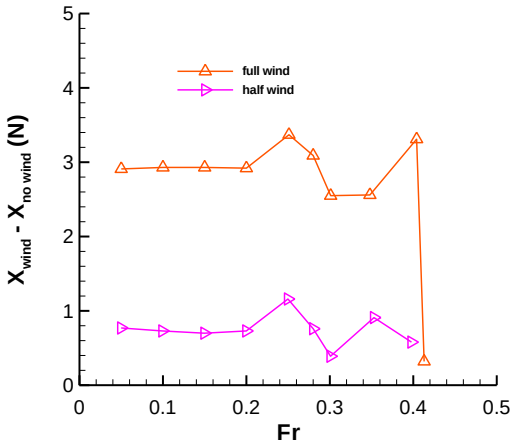


(b)

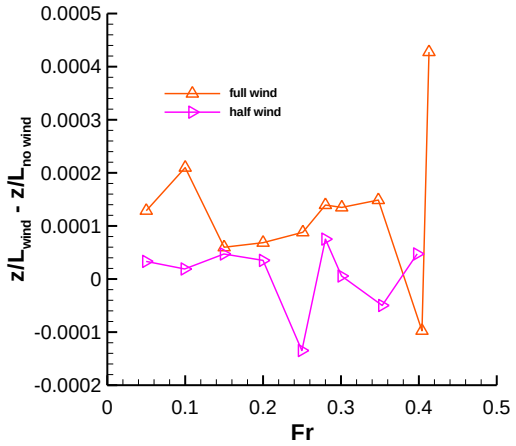


(c)

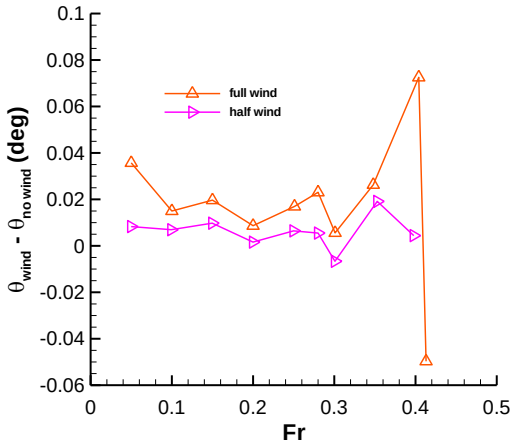


Figure B-5 No wind data subtracted from data with wind vs *Fr* for (a) *X*, (b) sinkage, and (c) trim.

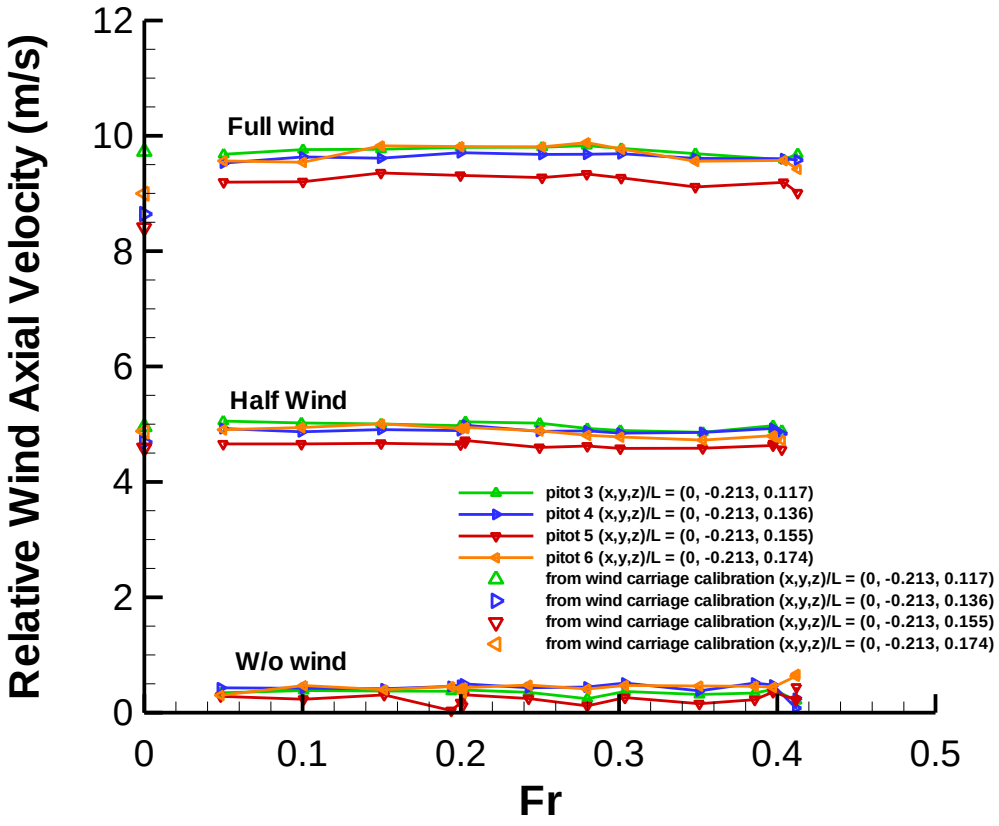


Figure B-6 Wind axial velocities relative to ship from pitots 3, 4, 5, and 6.

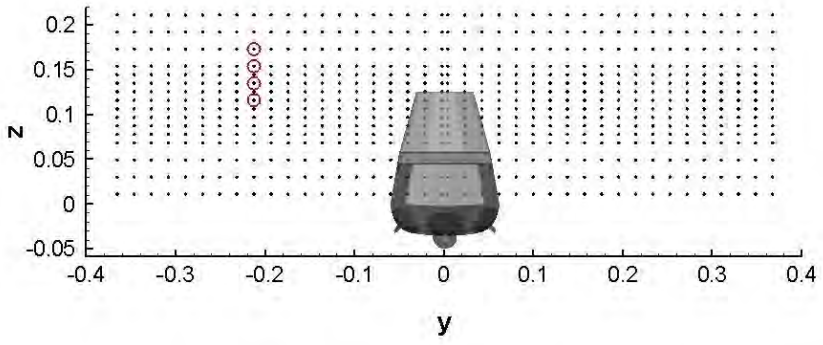


Figure B-7 Wind monitored at 4 grid points circled in red during wind tests.

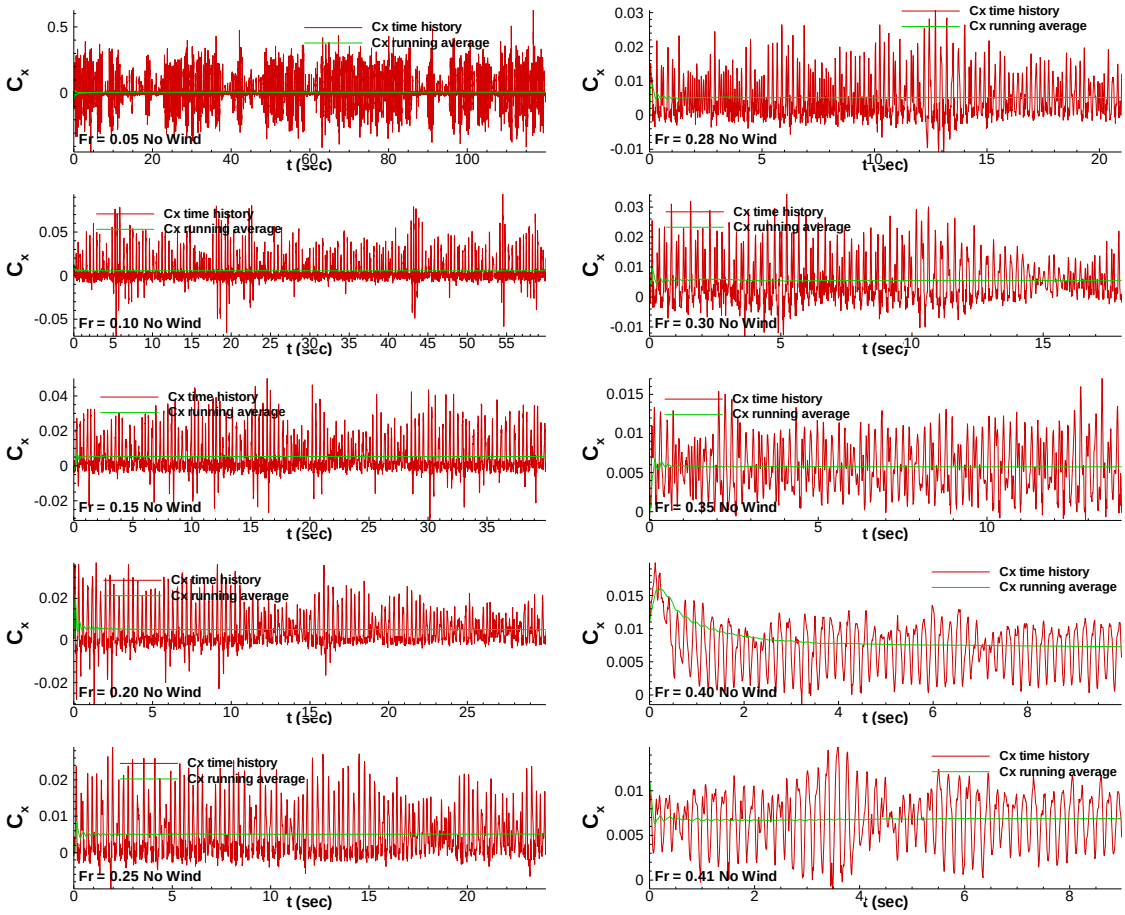


Figure B-8 Time histories of resistance coefficient for range of $Fr$ without wind.

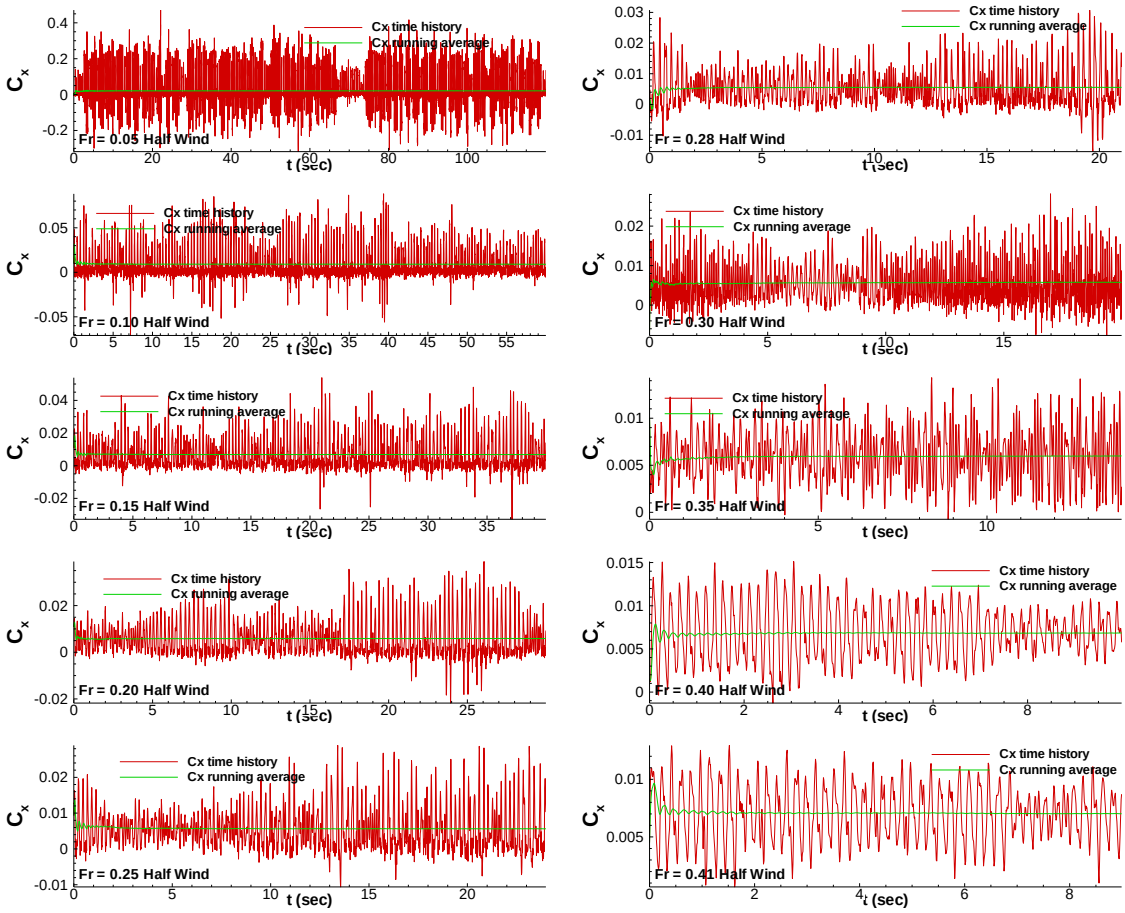


Figure B-9 Time histories of resistance coefficient for range of $Fr$ with half wind.

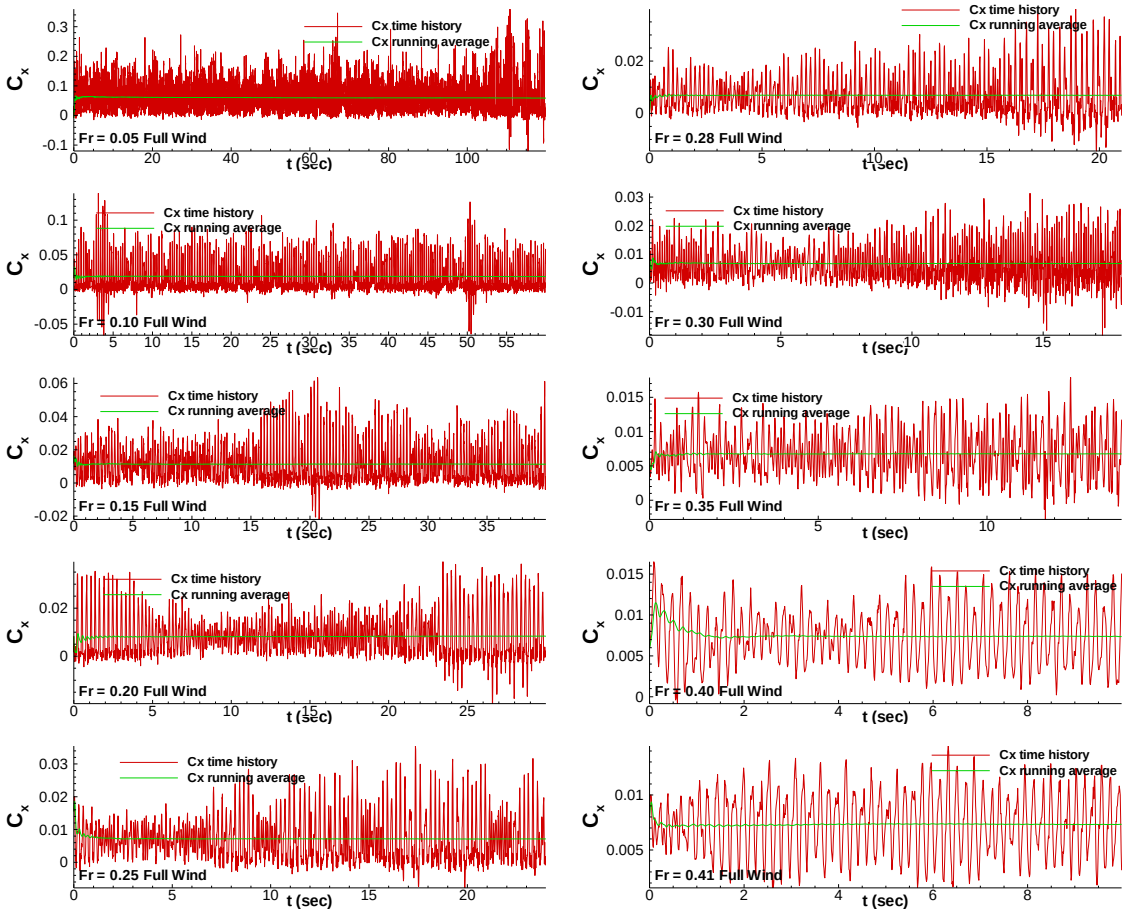


Figure B-10 Time histories of resistance coefficient for range of $Fr$ with full wind.

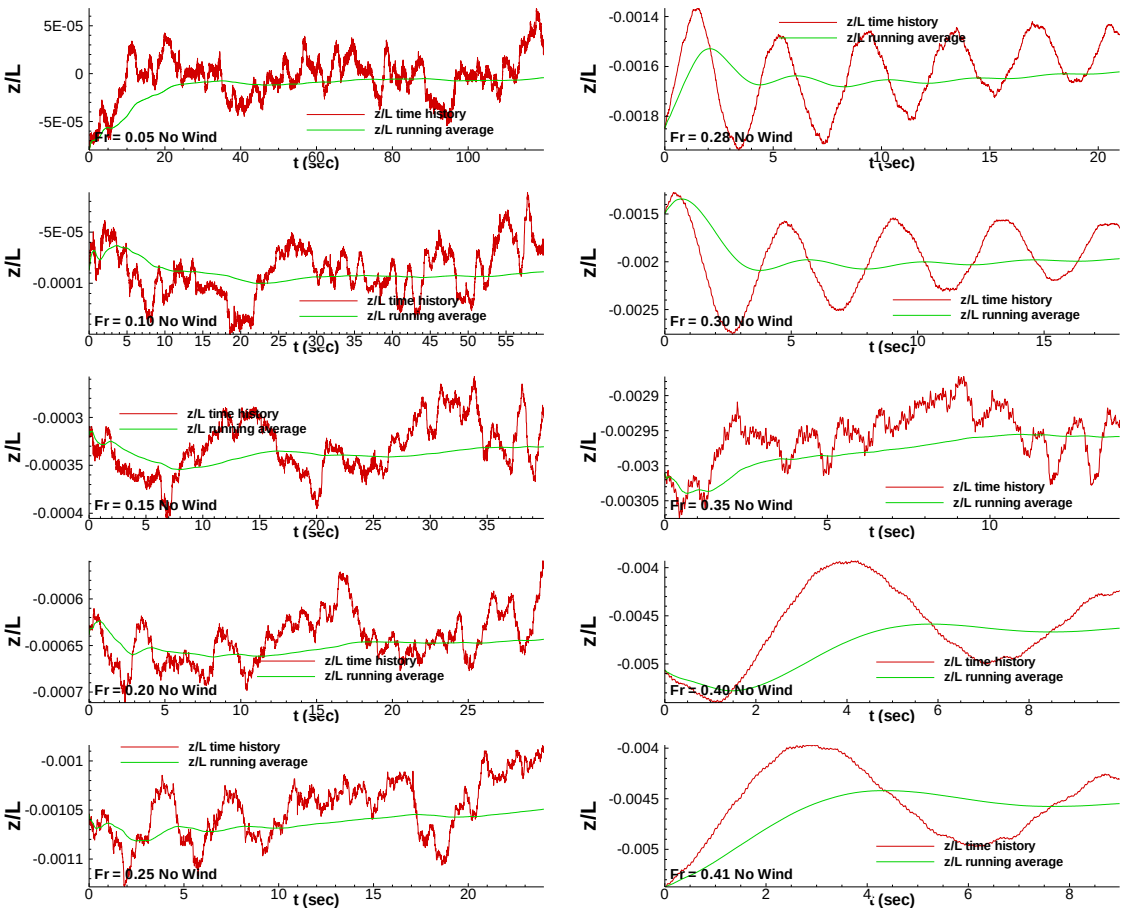


Figure B-11 Time histories of sinkage for range of $Fr$ without wind.

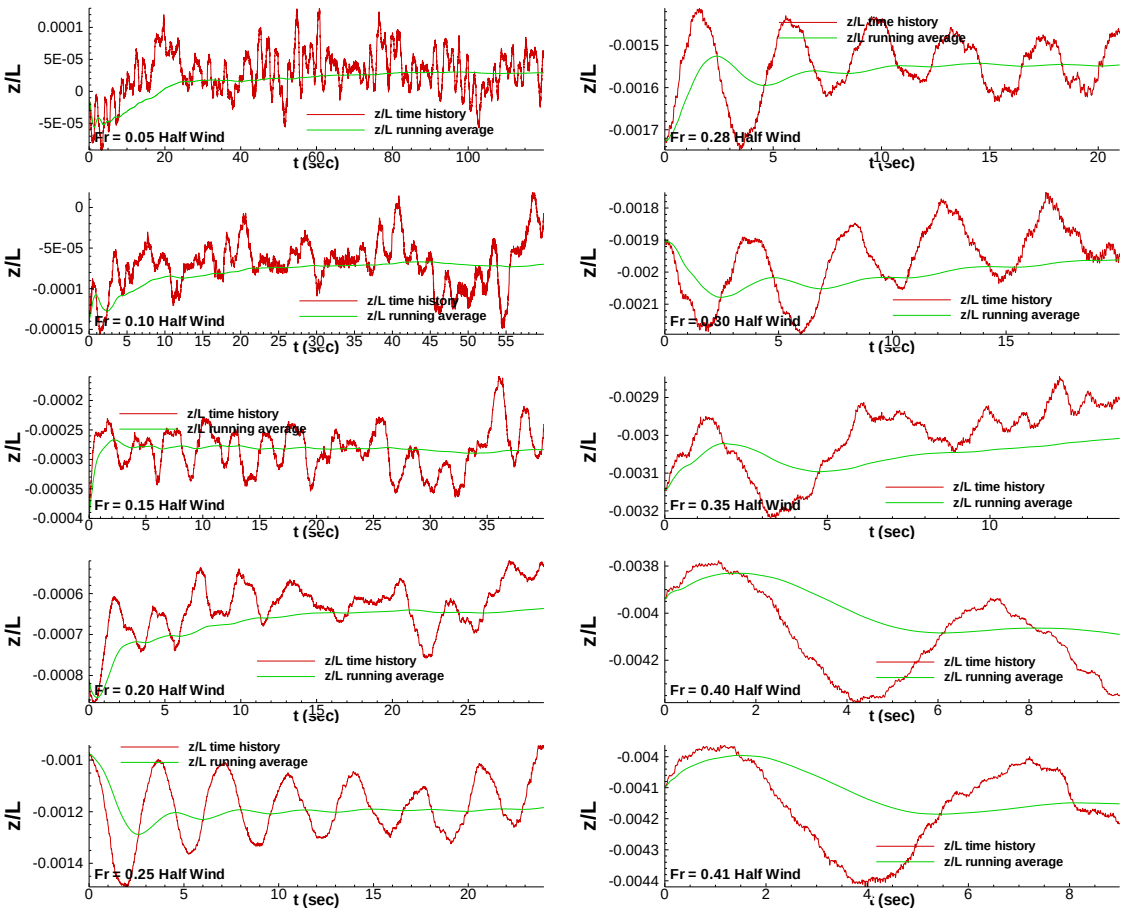


Figure B-12 Time histories of sinkage for range of $Fr$ with half wind.

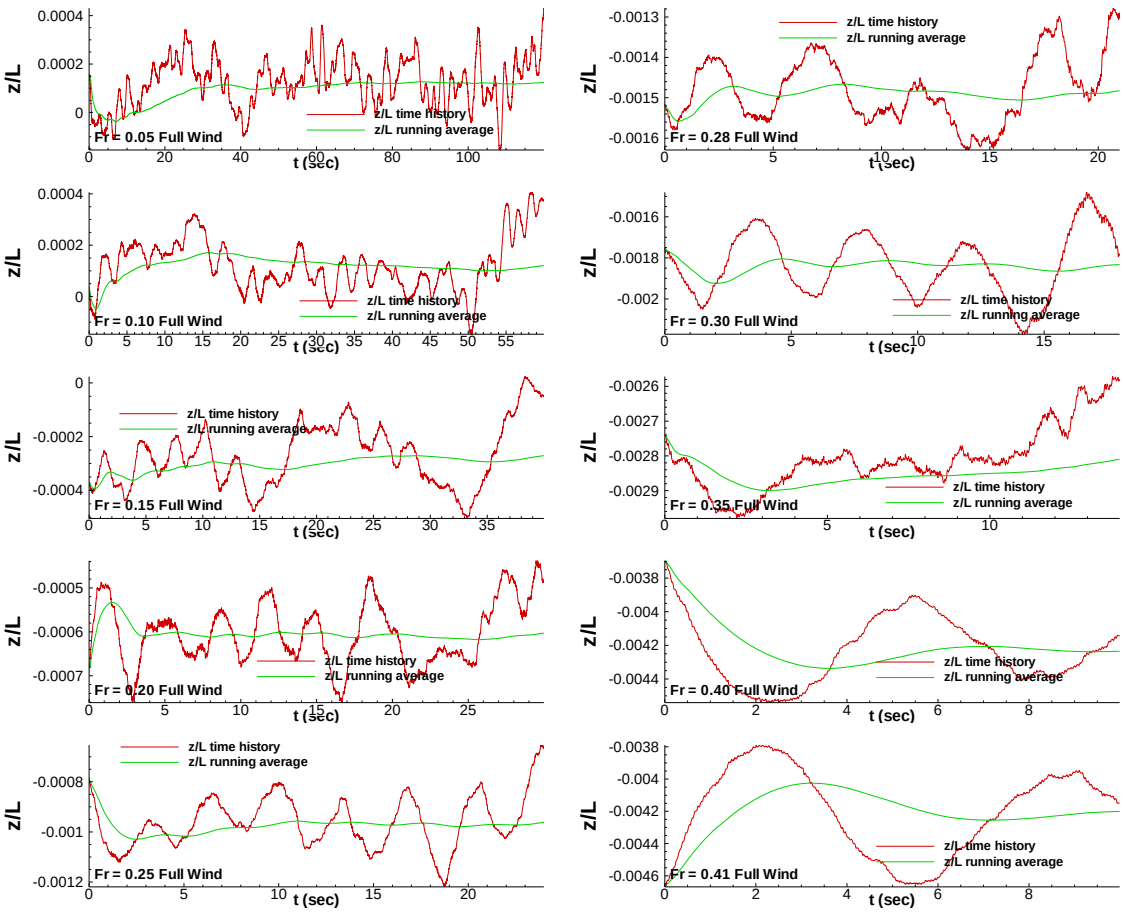


Figure B-13 Time histories of sinkage for range of $Fr$ with full wind.

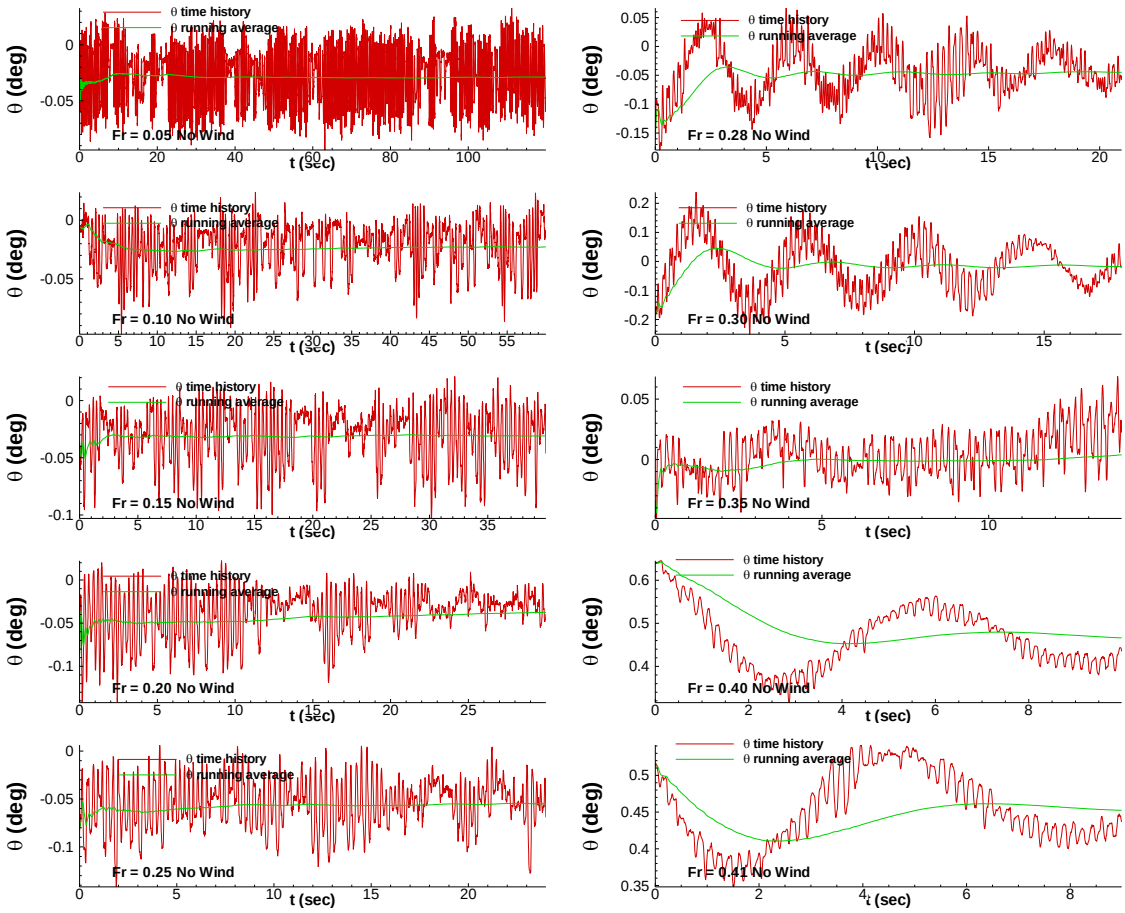


Figure B-14 Time histories of trim for range of $Fr$ without wind.

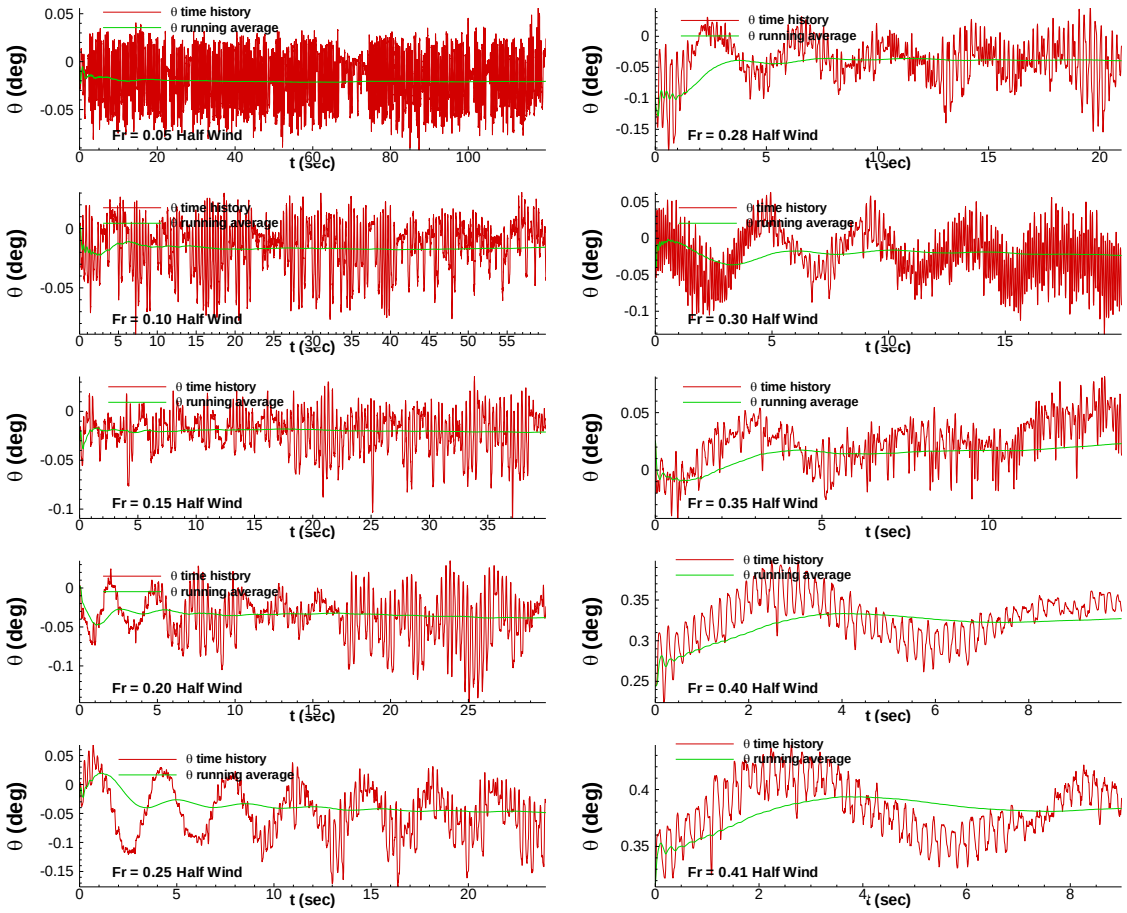


Figure B-15 Time histories of trim for range of $Fr$ with half wind.

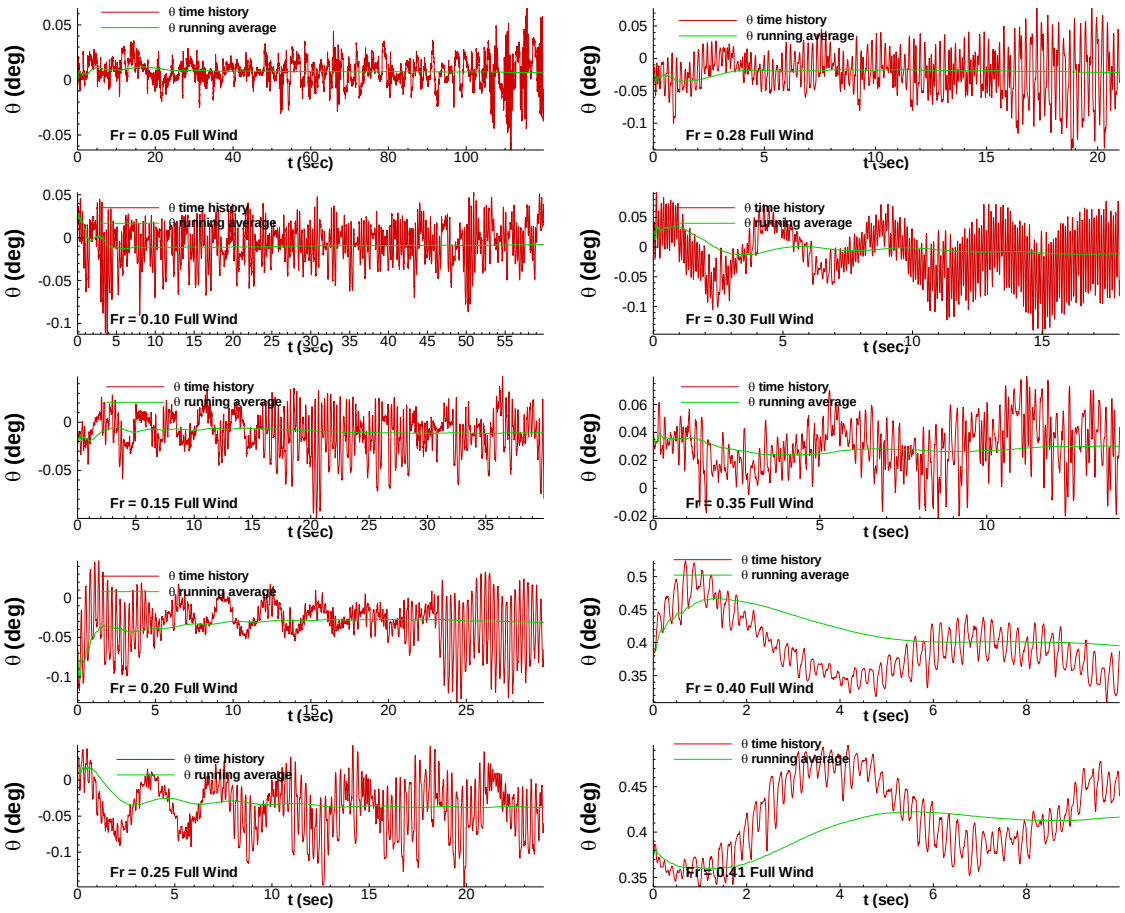


Figure B-16 Time histories of trim for range of *Fr* with full wind.

# REFERENCES

Abkowitz, M. A., 1964, "Lectures on ship hydrodynamics – Steering and maneuvering," Hydro- and Aerodynamics Laboratory Report Hy-5, Lyngby, Denmark.

Araki, M., Umeda, N., Hashimoto, H., and Matsuda, A., 2010, "Broaching Prediction Using an Improved System-Based Approach," Proceedings of the 28th Symposium on Naval Hydrodynamics, Pasadena, California.

Bendat, J. S., and Piersol, A. G., 1966, *Measurement and Analysis of Random Data*, John Wiley and Sons, Inc., New York, USA.

Fujiwara, T., Nimura, T., et al., 2008, "Free Running Model Test on a Large Container Ship Under Wind and Waves at Towing Tank," Journal of the Japan Society of Naval Architects and Ocean Engineers, Vol. 8, pp. 155-162.

Hoerner, Sighard F., "Fluid Dynamic Drag," 2nd Edition, New York City, 1965.

ITTC, 2005, *Proceedings*, 24th International Towing Tank Conference, Edinburgh, Scottland.

ITTC, 2008, *Proceedings*, 25th International Towing Tank Conference, Fukuoka, Japan.

Leeuwen, G. van, 1964, "The Lateral Damping and Added Mass of an Oscillating Ship-Model," Shipbuilding Laboratory, Technical University Delft, Publication No. 23.

Longo, J. and Stern, F., 2005, "Uncertainty Assessment for Towing Tank Tests with Example for Surface Combatant DTMB Model 5415," J. of Ship Research, Vol. 49, No. 01, pp. 55-68.

Mousaviraad, S. M., Carrica, P. M., Huang, J., and Stern, F., 2008, "CFD Prediction of Ship Response to Severe Ocean Waves and Wind," Proceedings of the 27th Symposium on Naval Hydrodynamics, Seoul, Korea.

"Nomenclature for Treating the Motion of a Submerged Body through a Fluid," SNAME Technical and Research Bulletin 1-5, 1952.

Umeda, N., Yamamura, S. et al., 2008, "Extreme Motions of a Tumblehome Hull in Following and Quartering Waves," Proceedings of the 6th Osaka Colloquium on Seakeeping and Stability of Ships, Osaka, pp.437-443.

Yoon, H., 2009, *Phase-Averaged Stereo-PIV Flow Field and Force/Moment/Motion Measurements for Surface Combatant in PMM Maneuvers*. Unpublished doctoral dissertation, University of Iowa, Iowa City, Iowa.